PHASE I REPORT:
DARPA EXOSKELETON PROGRAM

January 2004

Assembled and edited by B. S. Richardson

Other contributors
J. F. Jansen[*]
J. F. Birdwell[*]
A. C. Boynton[†]
H. P. Crowell, III[†]
W. K. Durfee[‡]
J. D. Gongola[§]
S. M. Killough[*]
D. J. Leo[**]
R. F. Lind[*]
L. J. Love[*]
M. Mungiole[†]
F. G. Pin[*]
J. C. Rowe[*]
O. A. Velev[§]
T. Zambrano[§]

[*] Oak Ridge National Laboratory
[†] Army Research Laboratory
[‡] University of Minnesota
[§] AeroVironment, Inc.
[**] Virginia Polytechnic Institute

PHASE I REPORT: DARPA EXOSKELETON PROGRAM

Assembled and edited by B. S. Richardson

Other contributors
J. F. Jansen
J. F. Birdwell
A. C. Boynton
H. P. Crowell, III
W. K. Durfee
J. D. Gongola
S. M. Killough
D. J. Leo
R. F. Lind
L. J. Love
M. Mungiole
F. G. Pin
J. C. Rowe
O. A. Velev
T. Zambrano

TABLE OF CONTENTS

LIST OF FIGURES

LIST OF TABLES

x

LIST OF ACRONYMS

ANOVA – Analysis of Variance

ARL – Army Research Laboratory

BSC – Battery System Controller

CAD – Computer Aided Design

DARPA – Defense Advanced Research Projects Agency

DOF – Degree-of-Freedom

EAP – Electroactive Polymer

EHPA – Exoskeleton for Human Performance Augmentation

HGO – Hip Guidance Orthosis

HKAFO – Hip-Knee-Ankle-Foot Orthosis

ICE – Internal Combustion Engine

LSD – Least Significant Difference

NSK – Nippon Seiko

NiMH – Nickel-Metal-Hydride

ORNL – Oak Ridge National Laboratory

PZN – Lead Zirconate Niobate

PZN-PT – Lead Zirconate Niobate / Lead Titanate

PZT – Lead Zirconate Titanate

RGO – Reciprocating Gait Orthosis

SACH – Solid-Ankle, Cushioned Heel

SMA – Shaped Memory Alloy

VPI – Virginia Polytechnic Institute

ABSTRACT

The Defense Advanced Research Projects Agency (DARPA) inaugurated a program addressing research and development for an Exoskeleton for Human Performance Augmentation in FY!2001. A team consisting of Oak Ridge National Laboratory, the prime contractor, AeroVironment, Inc., the Army Research Laboratory, the University of Minnesota, and the Virginia Polytechnic Institute has recently completed an 18-month Phase I effort in support of this DARPA program. The Phase I effort focused on the development and proof-of-concept demonstrations for key enabling technologies, laying the foundation for subsequently building and demonstrating a prototype exoskeleton.

The overall approach was driven by the need to optimize energy efficiency while providing a system that augmented the operator in as transparent manner as possible (non-impeding). These needs led to the evolution of two key distinguishing features of this team's approach. The first is the "no knee contact" concept. This concept is dependent on a unique Cartesian-based control scheme that uses force sensing at the foot and backpack attachments to allow the exoskeleton to closely follow the operator while avoiding the difficulty of connecting and sensing position at the knee. The second is an emphasis on energy efficiency manifested by an energetic, power, actuation and controls approach designed to enhance energy efficiency as well as a reconfigurable kinematic structure that provides a non-anthropomorphic configuration to support an energy saving long-range march/transport mode.

The enabling technologies addressed in the first phase were controls and sensing, the soft tissue interface between the machine and the operator, the power system, and actuation. The controller approach was implemented and demonstrated on a test stand with an actual operator. Control stability, low operator fatigue, force amplification and the human interface were all successfully demonstrated, validating the controls approach. A unique, lightweight, low profile, multi-axis foot sensor (an integral element of the controls approach) was designed, fabricated, and its performance verified. A preliminary conceptual design of the human coupling and soft tissue interface, based on biomechanics research has been developed along with a test plan to support an iterative design process. The power system concept, a fuel cell hybrid power supply using chemical generated hydrogen, was successfully demonstrated and shown to be able to efficiently meet both steady-state and transient peak loads. Two actuator approaches, a piezoelectric actuator, with theoretical high power densities and an approach based on a high-performance, high-speed electric motor driving a miniature hydraulic pump have been investigated. The first shows great potential but will require further research before reaching that promise. The other approach has been modeled and simulated and shown to provide the possibility for significant energy savings (>30%) and improved power densities in comparison to conventional hydraulics.

Biomechanics analysis and testing were also performed in support of these enabling technologies, to provide a basis for design criteria. An analysis was performed to determine baseline data for initial mechanical design and power supply sizing. Testing conducted to evaluate boot sole thickness found that thickness increases up to two inches could be accommodated without significant impact on human factors issues.

This 18-month long Phase I effort has evaluated key enabling technologies and demonstrated advances in these technologies that have significantly increased the likelihood of building a functional prototype exoskeleton.

INTRODUCTION

The Defense Advanced Research Projects Agency (DARPA) inaugurated a program addressing research and development for an Exoskeleton for Human Performance Augmentation in FY!2001. A team consisting of Oak Ridge National Laboratory, the prime contractor, AeroVironment, Inc., the Army Research Laboratory, the University of Minnesota, and the Virginia Polytechnic Institute has recently completed an 18-month Phase I effort in support of this DARPA program. The Phase I effort focused on the development and proof-of-concept demonstrations for key enabling technologies, laying the foundation for subsequently building and demonstrating a prototype exoskeleton.

The overall approach was driven by the need to optimize energy efficiency while providing a system that augmented the operator in as transparent manner as possible (non-impeding). These needs led to the evolution of two key distinguishing features of this teams approach. The first is the "no knee contact" concept. This concept is dependent on a unique Cartesian-based control scheme that uses force sensing at the foot and backpack attachments to allow the exoskeleton to closely follow the operator while avoiding the difficulty of connecting and sensing position at the knee. The second is an emphasis on energy efficiency manifested by an energetic, power, actuation and controls approach designed to enhance energy efficiency as well as a reconfigurable kinematic structure that provides a non-anthropomorphic configuration to support an energy saving long-range march/transport mode.

The enabling technologies addressed in the first phase were controls and sensing, the soft tissue interface between the machine and the operator, the power system, and actuation. Biomechanics analysis and testing were also performed in support of these enabling technologies, to provide a basis for design criteria. This document describes the advances made in the 18-month long Phase I effort for each of these key enabling technologies and how these advances have increased the likelihood of building a functional prototype exoskeleton.

CONTROLS

APPROACH

The Oak Ridge National Laboratory's (ORNL's) controls approach is based on three requirements: (1) the human operator will perform all the balancing, (2) small amount of force due to the load will be reflected back to the human, and (3) only two physical contact points per leg with the human are allowed. These three requirements necessitate a bilateral force-based controller. While the final exoskeleton system would be composed of arm, torso, and leg structures, the leg structure is the major emphasis of the first phase of the exoskeleton program due to its difficulty and uniqueness and will be the only exoskeleton structure discussed in detail.

While biped control for autonomous robots is still an active research area, its application to an exoskeleton is almost negligible because the balancing capability of the human operator will be utilized by the exoskeleton. The transfer of balancing capability from the operator to the exoskeleton is based on bilateral force reflection. Historically, the major application of bilateral force reflection controls has been for teleoperator (master-slave) systems. There are three general types of control strategies used in a teleoperator system: (1) position-position, (2) position-force, and (3) force-force control. The first control strategy, which was used on the Hardiman, refers to the type of sensory information (in this case positional information) being used in the "outer" feedback loop of both the master and slave. Position-position control is commonly implemented in most teleoperator systems. Two teleoperators built at ORNL in the 1980s, the M2 and the Advanced Servo Manipulators, are examples of this type of control strategy that is common for systems that have kinematically similar master-slave manipulators. For kinematically dissimilar master-slave systems, position-force control is commonly used. For human-amplifier (or extender) type systems, where the master and slave are one integral unit such that the human operator and the manipulator are attached to a common point and bilateral force reflection is the primary performance objective, force-force control is commonly used. Bilateral force feedback for the exoskeleton will not only provide the necessary balancing, but will also allow the human operator to feel any contact with the environment.

ORNL's exoskeleton leg structure is fundamentally based on a "no knee contact" concept, where only sensing at the feet and the backpack is required. Based on past experience with the design and construction of teleoperators and the experience of other researchers in the area of orthotics, the mechanical interface with human tissues have indicated that pressures less than 2 psi can significantly damage skin and human tissues in a few hours. Long-term damage could include potential "pinching" of the tendons and deformation of the muscles such as those in the vicinity of the knee. Based on these observations and measurements, joint-to-joint motion tracking control of the knee utilizing displacement sensing would have difficulties in meeting the objectives of user comfort and non-impeding physical enhancement. To avoid these problems, a unique Cartesian-based control scheme based on force sensing at the foot and backpack attachments that will allow the exoskeleton system to closely follow the human body and thus avoid having to make a physical connection to the human knee and thereby prevent injury to the human operator has been selected by ORNL. The basic concept (again just for the leg) is shown in Fig. 1. The basis for the controls approach and the mechanical design concept are described in more detail in Appendices A and B.
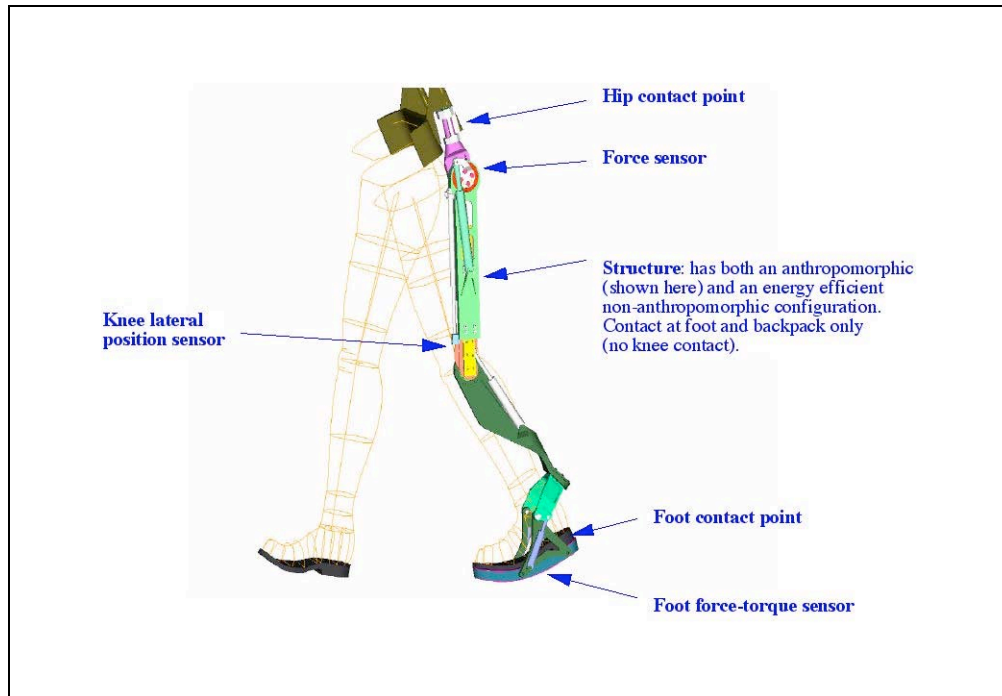
Fig. 1. Leg structure and sensing concept.

QUASI-HYDROSTATIC CONTROL

It was recognized that another control loop would be required to help reduce the energy loss of the system. While the demonstration of this outer loop was not scheduled until Phase 2 of this program, preliminary work was started on a way to efficiently control the energy from the hydraulic pump while still maintaining good overall tracking performance of the inner control loop. This approach is called quasi-hydrostatic control.

The duty cycle associated with an exoskeleton system changes significantly depending on the overall mission being imposed by the operator. In the past, fine hydraulic control has been achieved by means of a constant pressure hydraulic source utilizing a fluid control device such as a servo valve. Analogous to an electrical resistive element, a servo valve is notoriously lossy and can consume at least 1/3 of the overall power generated by the pumping source. Since all of the teams currently working on exoskeleton development are using a hydraulic- or a fluid-based actuation scheme, fine control of hydraulic fluid without incurring significant energy loss is of paramount importance to this program. The quasi-hydrostatic control, a combination of flow control (to reduce losses) and pressure control (to achieve good tracking) has been explored to address this deficiency. The specific advantage of this approach is a large reduction in the peak power required from the pump. The challenge is that the force-force based control problem becomes very nonlinear. As an example, a comparison was made between a conventional constant-pressure control system and the quasi-hydrostatic approach on a single hydraulic cylinder by means of computer simulations. Figures 2 and 3 provide a comparison of the two approaches. The peak power from the constant pressure pump, after the initial transient, is 1,500!W whereas the peak power from the quasi-hydrostatic controlled system is 570!W. The savings is even greater if we consider transients in the system (e.g., the initial transient in Fig.!2).

Just as important, Figs. 4 and 5 show little difference between the two methods in terms of the tracking performance.
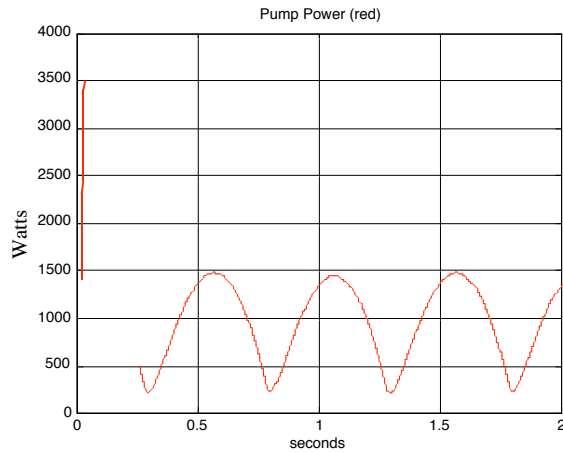
Fig. 2. Power requirement, constant pressure.
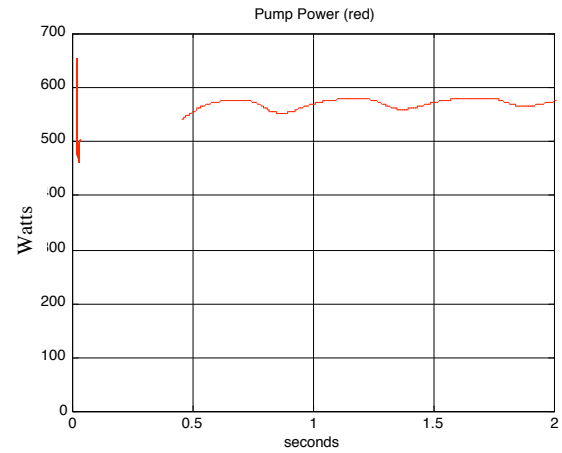
Fig. 3. Power requirement, quasi-hydrostatic.
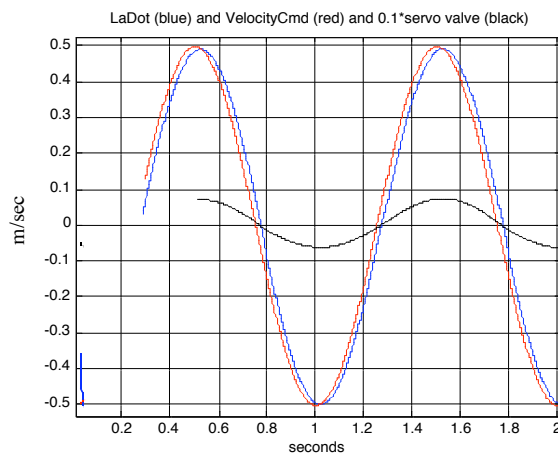
Fig. 4. Tracking, constant pressure.
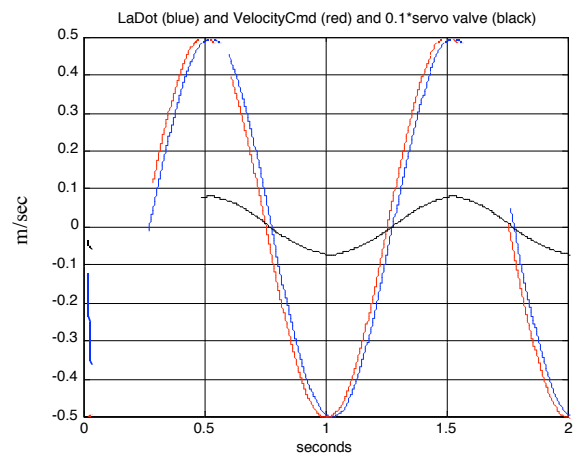
Fig. 5. Tracking, quasi-hydrostatic.

As can be seen from these simulations, a quasi-hydrostatic actuation methodology shows significant improvements in efficiency (maximum actuation power requirements cut in half) without sacrificing tracking performance.

CONTROLS TEST STAND

To demonstrate the control strategy before the construction of the actual exoskeleton, a highly instrumented test stand has been constructed (Figs. 6 and 7). The test stand has two major objectives stemming from the need to extend our understanding of both the biomechanical and engineering issues that will need to be addressed for the practical deployment of a fielded exoskeleton system. Specifically, from a biomechanics perspective, the purpose of this test stand was to:

1) demonstrate and study force contact stability with the environment under sudden impact loads (e.g., foot fall), stumble recovery, hopping scenarios, varying environmental compliance, and backpack load variations;
2) demonstrate and study the overall force-based control strategy when coupled to a human operator;
3) minimize the force interaction between the human and the foot and backpack areas; and
4) investigate minimization of human machine interface induced fatigue by studying (a)!the reduction of drag as a function of increasing the overall bandwidth (response time) of the actuator system, (b)!the use of mechanical compliance to reduce impact forces on the structure, and (c)!human and pack compliance requirements.

Fig. 6. ORNL's test stand.
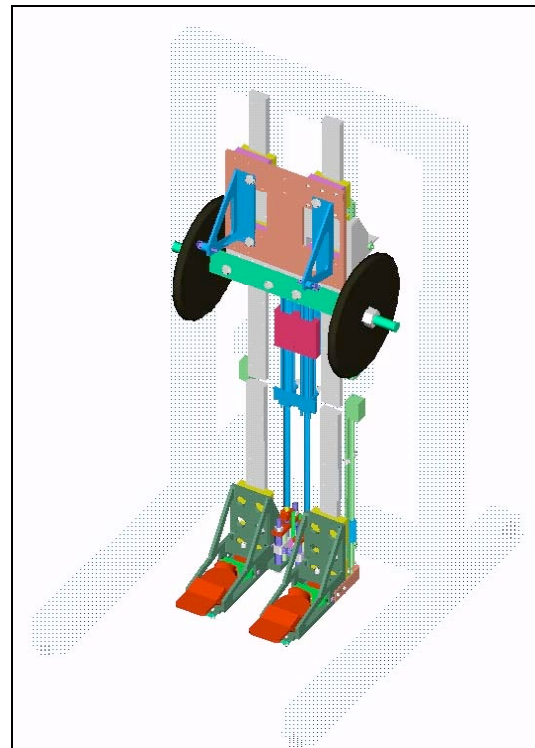
Fig. 7. ORNL's test stand physical layout.

From an engineering perspective, the purpose of the test stand was to:
1) understand the effect that mechanical compliance in series with the actuators (series elastic actuation) has on overall actuator bandwidth (during both small and large motions) and actuator saturation;
2) determine sensor requirements (e.g., dual force-torque sensing at the foot);
3) develop a methodology for tuning of controls settings;
4) minimize bias forces due to sensor degradation/creep; and
5) determine acceptable signal conditioning levels (e.g., dead band and bias loading of foot sensor in preferential direction) for all sensors.

The exoskeleton test stand is uniquely instrumented to measure position, acceleration, and forces at both the feet and the backpack area and is vital to our understanding of all the issues mentioned above. Figure 8 shows the sensor location on the test stand. Data acquisition for the test stand currently can measure data with up to a 1 kHz sample rate. The test stand has an open loop response in excess of 11 Hz, making it almost transparent to the human operator, with the capability to exert mechanical forces of over 1,000 lb. Furthermore, almost any type of passive (and a restricted subset of non-passive) load can be generated and applied to the human operator.
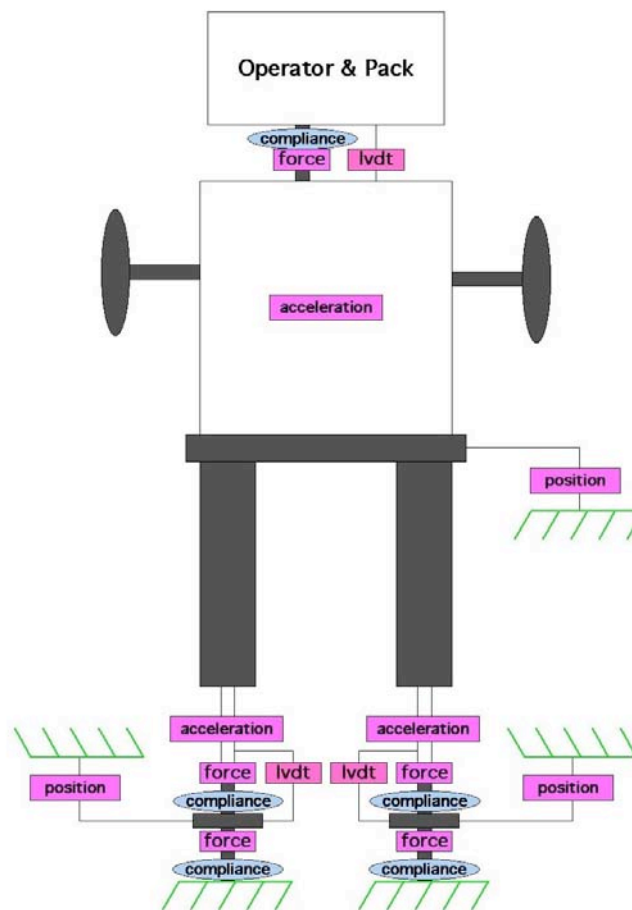
Fig. 8. ORNL's test stand sensor layout.

TEST STAND RESULTS

All of the Phase 1 goals have been met culminating in the demonstration of the force amplification on the test stand with adjustable gains up to 100:1 (Milestones 3.1 and 3.2) showing mass and inertia reduction control. Further, rapid foot contact stability was demonstrated completing Milestone 3.3. The exoskeleton controller approach has been implemented on the test stand and contact stability, low fatigue to operator, force amplification, and human interface at two contact points have all been demonstrated and documented on video which completes Milestones 5.1, 6.1, and 6.2.

FOOT FORCE-TORQUE SENSOR

One of the most critical sensors in the proposed control strategy is the foot sensor (see Fig.!1). Since force sensing at the hip has to sense a limited number of degrees of freedom with relatively low impact loading, the foot sensor was the primary focus for the Phase 1 effort. The challenging aspect of this multi-axis force sensor is that it must conform to the bending of the human foot, withstand high impact loads (3x static loads), have better than a 2000:1 force sensitivity ratio, feel comfortable to the human operator, be integrated into a military style boot, and measure the forces on the human foot when either just the ball or the heel of the foot is in contact with the ground. There are no commercial force sensors that can meet such requirements. To fill this void, ORNL has relied on past experience in designing and building custom, high sensitivity force-torque sensors for high-precision applications as a basis for building a custom foot sensor.

DESCRIPTION

The new foot sensor utilizes two flexible plates that are constrained to maintain similar curvature. The top plate is in contact with the human foot while the bottom plate contacts the ground. The plates are thin and flexible enough so that normal foot flexing is permitted. The upper plate is attached to the human shoe through bindings so that all forces and moments generated by the foot are transmitted to the upper flex plate. The binding connection, which is tight at the ball of the foot, permits a small amount of fore/aft displacement between the foot sole and flex plate at both the heel and toe. This displacement allows normal flexing of the foot without stiffening the boot.

The upper flex plate is connected to the lower (ground contact) flex plate through a number of vertical and horizontal force sensing elements. These connections are designed to transmit the forces to the sensing elements in their sensitive axis while not imposing loads in unmeasured directions. The design of these connections is very important to the overall accuracy of the foot sensor system. A key advantage of this design is that the number of required force sensing elements is reduced since the flex plate carries all the transverse loads (lateral and fore/aft), thus enhancing flexibility of the sensor and allowing for a more compact design.

The first prototype foot force-torque sensor is shown in Fig. 9. This is a 4-axis unit developed specifically for an exoskeleton, including bosses to connect to the exoskeleton ankle frame and a vertical load rating of 1200!lb. This design may be easily adapted to include more axes and for human biomechanical measurement applications (which would not require the 1200!lb vertical load). The Z-axis is defined as perpendicular to the flex plate (corresponds to vertical when standing on level surface) and the X-axis as horizontal pointing to the side with the longitudinal Y-axis pointing to the front (Fig.!10). The prototype foot sensor has four Z-axis force sensors (two at the ball and two at the heel) from which total Z-force (Fz) can be computed as well as X and Y moments (Mx, My). A force sensor along the Y-axis measures fore/aft force (Fy). Figure!10 shows the general arrangement of the strain gage bending beam force sensing elements (see Fig.!11). Figure!12 shows a view of the sensor in the flat configuration (it is 1.75!inches thick including the 0.5-inch rubber padding on the bottom).

Fig. 9. Foot force-torque sensor attached to boot.
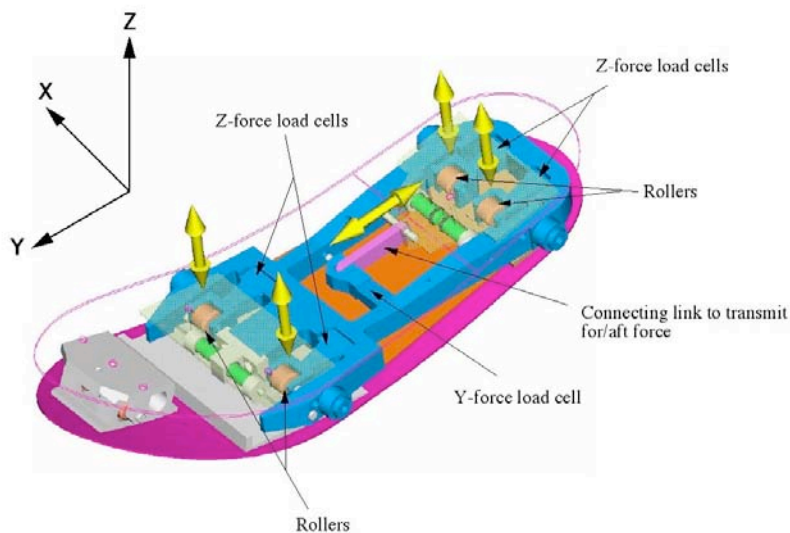
Fig. 10. Sensor force measurements.

In this design, considerable translational displacements occur between the upper and lower flex plates. These relative motions occur primarily in the Y direction and are accommodated by the connections between the upper flex plate and the force sensors that are mounted to the lower flex plate. Z-direction loads imposed on the flexible foot input plate are transmitted to the rigid load sensors through rollers (Fig.!10) that allow significant angular and Y translational motion (with little resistive force) while maintaining stiffness in the load sensitive Z-direction.

Figures 10, 11 and 13 also show the lateral constraint elements that are used to minimize lateral forces on the vertical load cells. This helps assure accuracy of load measurement. The lateral constraint elements behave like ball bearings so that nearly friction-free flexing and translation of the flexible input plate is permitted without lateral movement.
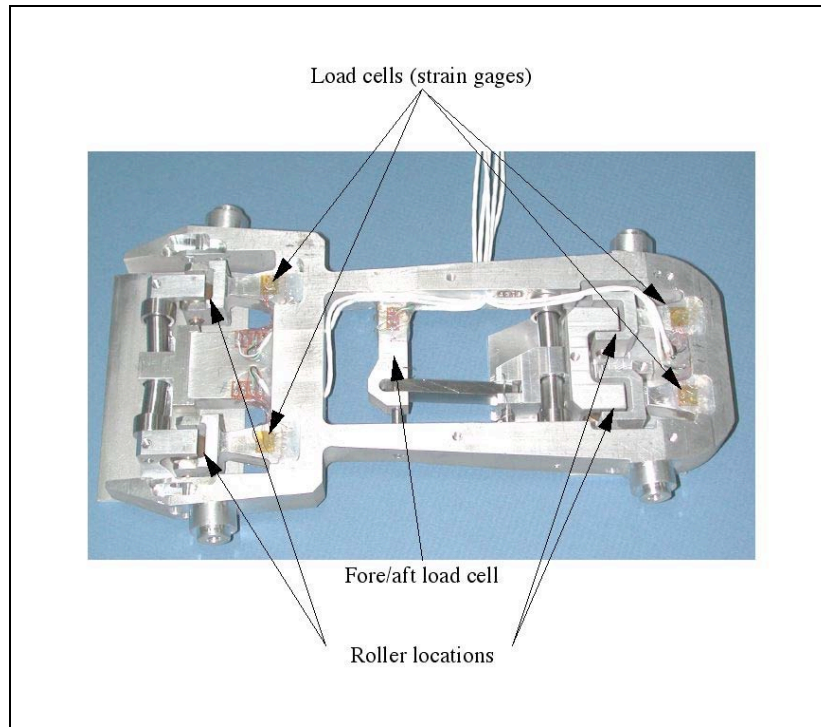
Fig. 11. Prototype foot sensor load cell details (bottom view).
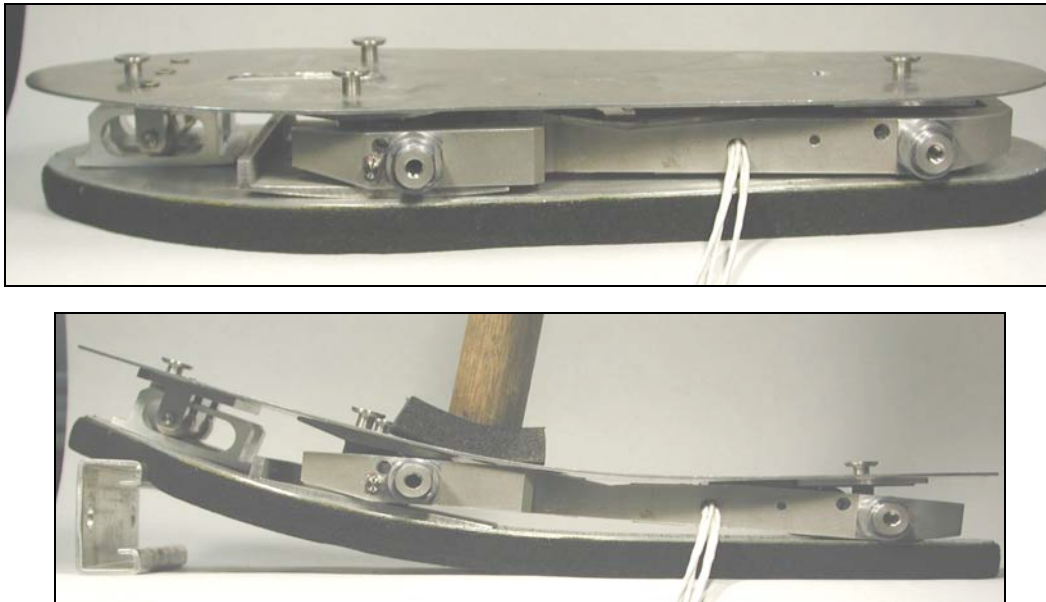
Fig. 12. Force-torque sensor shown flat and flexing.

Bending of the upper flex plate creates loading on the load cells that is not exactly parallel with the sensitive axis. This off-axis force (while small) is not measured but can be computed if the off-axis angle is known. Future versions will include a sensor to measure the degree of bending in the upper flex plate allowing the off-axis components of force created by the angled contact to be calculated and factored into the output results.
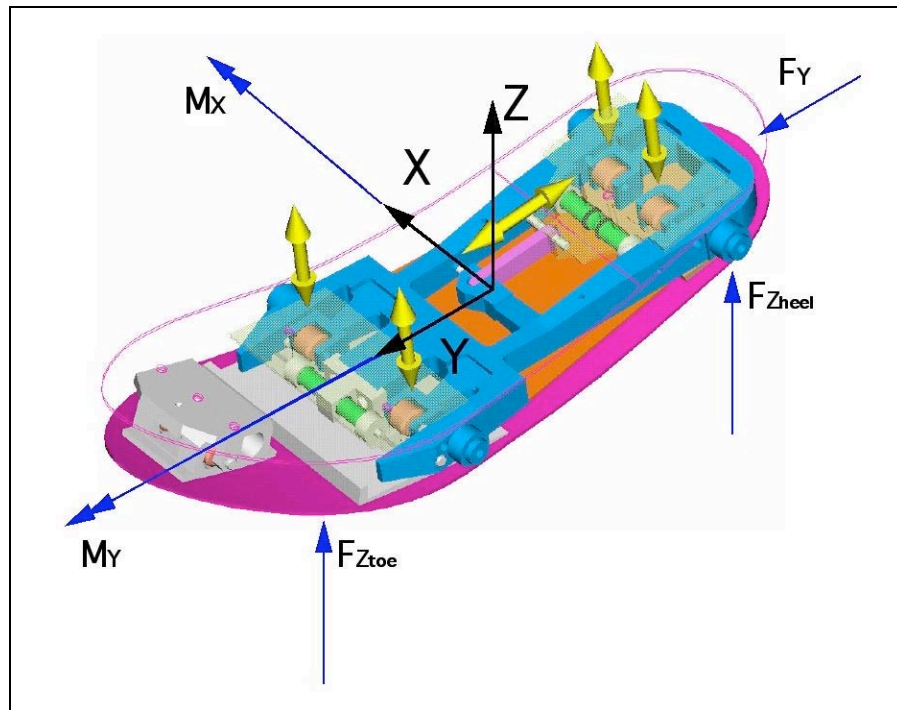
Fig. 13. Measured forces and moments.

The current design does not measure lateral horizontal loads (not a requirement for the exoskeleton application). To add this capability would require the addition of two lateral load cells and linkages or shear pads to transmit the lateral loads. Figure 14 shows a conceptual model of a 7-axis sensor. This design shows ball joint linkages that transmit loads only along their centerline. The ball joint ends are required to accommodate the slight motion that occurs when the top plate flexes. It also shows an optional toe force sensor. Flex angle measurement would also be required to calculate the vector angle of the toe force.
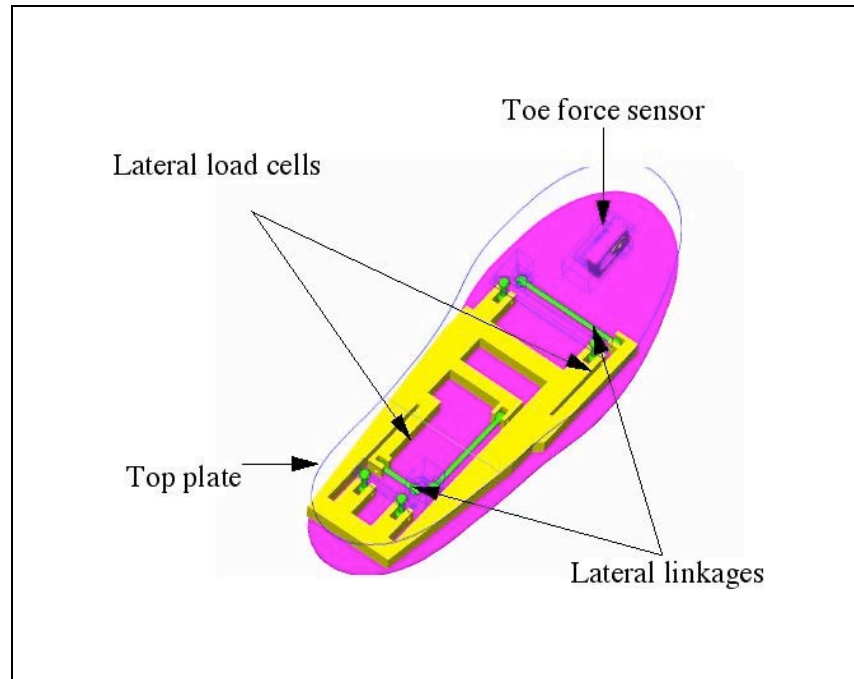
Fig. 14. Conceptual 7-axis foot sensor.

FOOT FORCE-TORQUE SENSOR TESTING

After calibrating the individual load cells, data was collected from the sensor during standing, walking (slow and fast), jumping and jogging. From the five load cells it is possible to measure total vertical (Z) force, ball or heel forces, moment as viewed from the saggital plane, moment as viewed from the frontal plane, and fore/aft horizontal force. Figures 15 through 20 show typical data collected in these activities. The foot sensor data compares favorably with published force data that has been taken from commercial, stationary force plates.
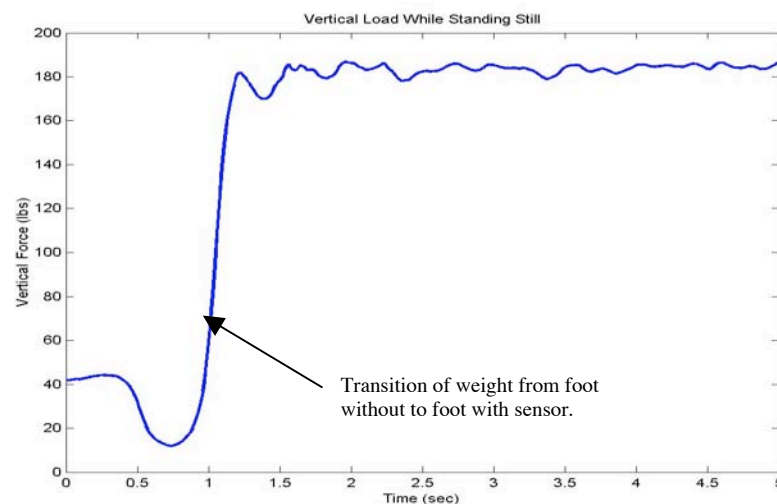
Fig. 15. Standing force data.
(Note variation caused by balancing action of 185 lb subject).

13
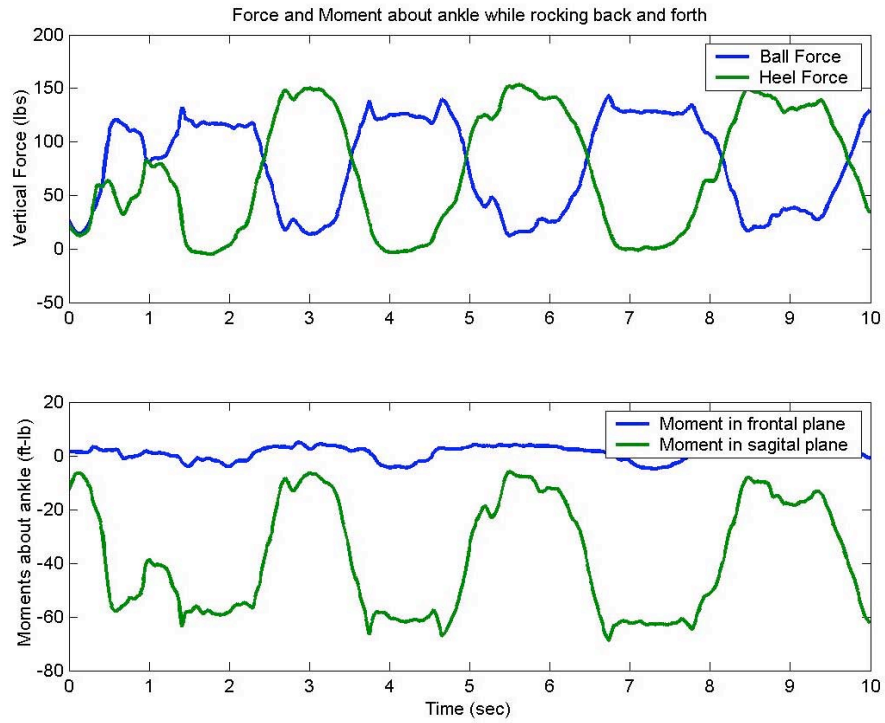
Fig. 16. Standing/rocking force data.
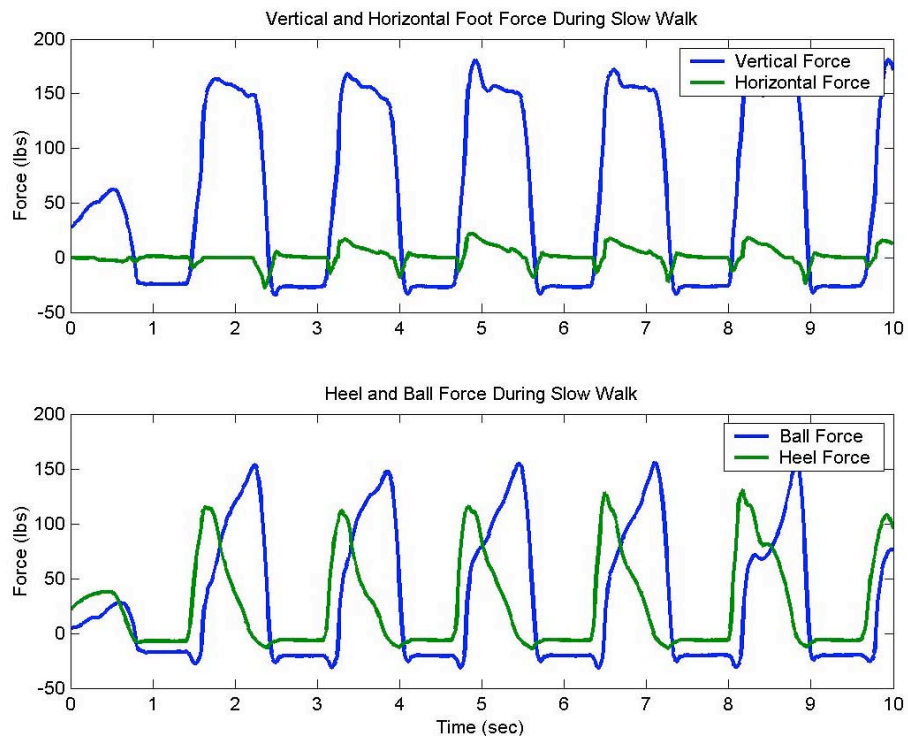
Fig. 17. Slow walk force data.

14
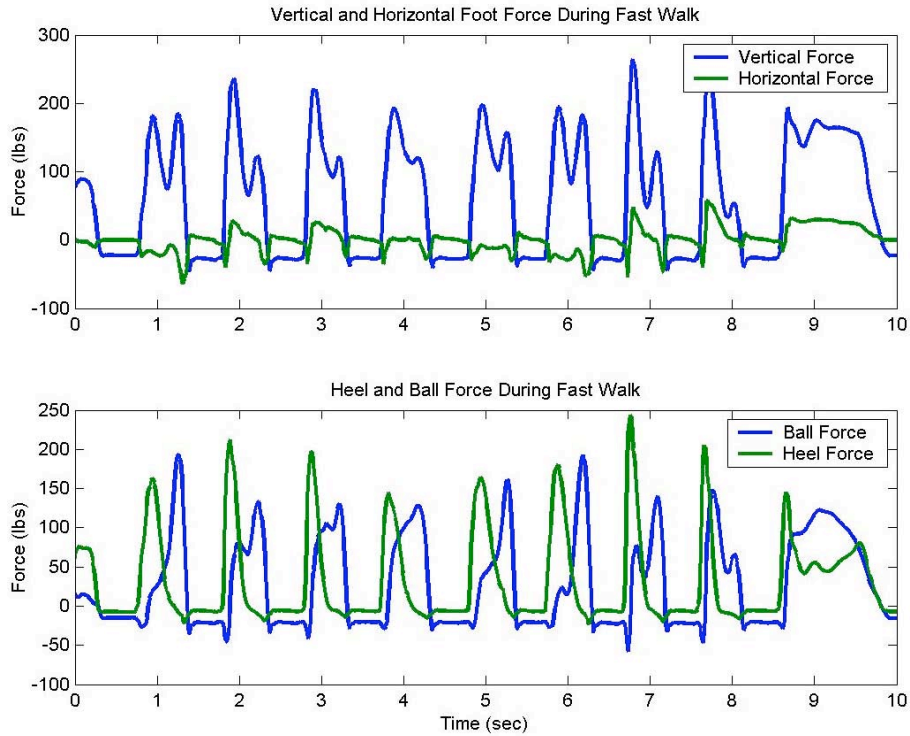
Fig. 18. Fast walk force data.
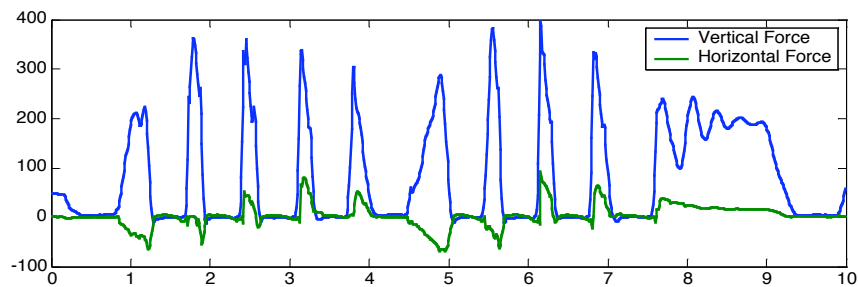
Fig. 19. Jogging force data.

While initial reaction to wearer comfort appears very positive, metrics as to the comfort of this sensor from a soldier's perspective are not yet available. The Army Research Lab (ARL) is currently performing biometric analysis on the effect of an extended sole on soldiers' performance during various tasks such as marching, squatting, and running that will help in quantifying the human response to this sensor.
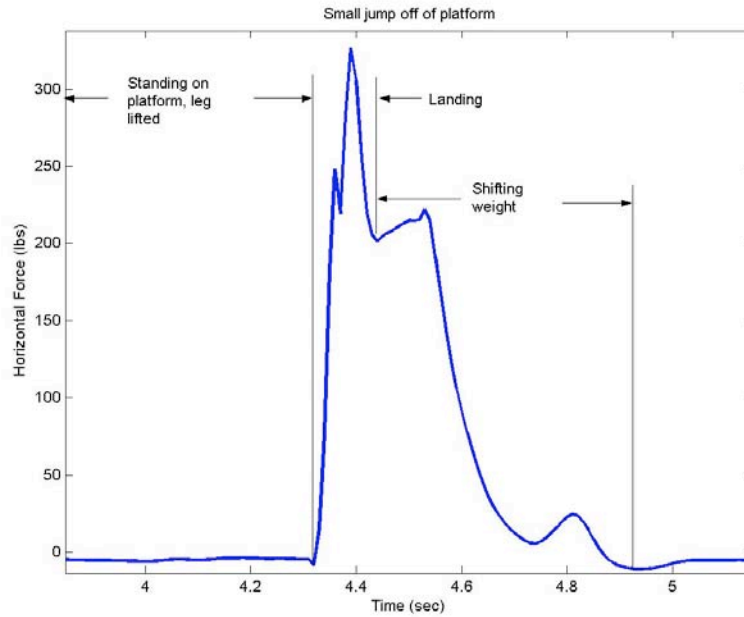
Fig. 20. Jumping force data.

SUMMARY

A foot sensor has been developed at ORNL for an exoskeleton application. The sensor is based on robust foil strain gage technology with five integral bending beam load cells. The sensor is lightweight (2.5!lb) with a low profile (1.75!in including bottom tread) and is designed to interface directly with a typical boot (with minor modifications). Mechanical bosses have been designed to allow ready integration into the exoskeleton support structure.

The sensor is rated for a maximum vertical load of 1200!lb but has a sensitivity of 0.16!lb in the vertical, 0.08 lb in the horizontal directions, and 0.1!ft-lb moment about the ankle. The vertical sensitivity is 7500:1 (i.e., 1200/.16) which is outstanding for a multi-axis force sensor and is achieved by exploiting the entire geometry of the sole volume.

The sensor provides data similar to larger and more expensive force plates with the addition of moment about the ankle roll motion. It is unique in that it can measure vertical forces at the ball or heel of the foot. It conforms to the human foot and appears to be extremely accurate simply because it exploits the full geometry of the sole of the boot. The sensor can be easily scaled either up or down to accommodate the force impact loading. The foot sensor is comfortable to wear, superior to commercial force-torque sensors, unique in design, and will meet the expected stresses encountered by the exoskeleton environment. The design provides space inside the sensor for integration of all necessary signal conditioning electronics. The sensor is readily sealable to prevent moisture and environmental contaminants from entering the device.

SOFT TISSUE INTERFACE

INTRODUCTION

A powered exoskeleton works in intimate mechanical contact with its human user. The design of an effective exoskeleton requires extraordinary attention to the details of this coupling. A well-engineered exoskeleton with compact, efficient power sources, stable control, and dexterous motion can still fail if it does not mesh seamlessly with the user's mobility, if it applies unusual or excessive forces to the body, or if it loads the body in a manner that causes skin irritation or discomfort. The design of an effective human interface has challenged every tool and machine that works in contact with the body, from shoes and boots, to clothing, to prosthetics, to orthotics. The challenge is no less for powered exoskeletons.

Human interface considerations divide roughly into two categories. First are issues related to control and haptic interactions between machine and human. Here, one must pay attention to the dynamics of the control system, where sensors are located and what quantities are being measured, and the dynamics, kinematics, and human motor control of normal posture, motion and gait.

Second are issues related to contact forces, moments and pressures exerted by the machine on the human. Here, the critical factors are the load duration characteristics of the shear and normal forces applied to the skin and bony prominences. Body locations vary widely in their ability to withstand external forces. For example, the heel can tolerate large, steady normal forces and substantial impact loading as it does daily during standing and gait. Bony prominences can only take small normal forces over brief periods of time before blood is squeezed out of the area and the skin starts to break down. Fleshy areas over muscle bellies in the shank and thigh can take a reasonable level of normal load, but offer a highly compliant coupling to the underlying skeleton rendering close, collaborating control between exoskeleton and human skeleton almost impossible. No area of the skin can tolerate shear loads for any reasonable period, which means the direction of the force loading vector applied by the exoskeleton to the body must be known and result from careful design.

All of these considerations regarding human-machine coupling have been known and studied for decades in the design of shoes, athletic footwear, high performance hiking and climbing boots, backpacks, prosthetics and orthotics. Little is known, however, on how these considerations change for active exoskeletons.

For the ORNL exoskeleton human couplings, we developed preliminary concepts and designs while being guided by results from traditional biomechanics research. In parallel, we developed a test plan with the intent of following an informed iteration process as the design was refined. Our objective is to have the exoskeleton fit be equivalent to the fit of a high performance hockey skate. Our target was to achieve "tolerable comfort." Like orthotics, skates must be closely coupled to the body, and must transmit considerable loads between the body and the ground. Skates are not as comfortable as bedroom slippers, but if properly fit, can be worn for long periods while meeting performance requirements. The normal and shear loading of the skin and

underlying anatomical structures by the exoskeleton, however, must be kept within safe limits for all proposed mission tasks.

The remainder of this section briefly reviews relevant prior art in biomechanics research then details the designs for the human couplings

PRIOR ART

Lessons from Biomechanics and Anthropometrics

The dimensions and clearances for the exoskeleton structure were dictated by human anthropometrics. Tabular information on 5-95% body dimensions for adult males was acquired from Woodsen et al. (1992). Human joint range of motion data was taken from Barter et al. (1957) to determine design requirements for the exoskeleton motion and for the placement of mechanical limit stops for safety. The details of human joint motions during gait were taken from Rose and Gamble (2000) for use in designing the exoskeleton degrees of freedom.

Biomechanics studies that measured the frequency content of gait were used to determine the closed-loop frequency response of the exoskeleton system. Studies show that 90% of the signal power of human limb motion during gait is 6!Hz or less (Antonsson and Mann, 1985; Winter, 1990). Most of the force signal content during heel strike is 10!Hz or less, but there are some impulsive loading components during shod walking that can reach 75!Hz (Harris et al., 1996). The addition of padding between the foot and the exoskeleton will filter high frequency impulsive forces but because the exoskeleton controller must be stable for high frequency impulsive disturbances caused by jumping or stomping, it was determined that its closed-loop response should be 10!Hz.

Lessons from Pressure Sore Studies

The physical attachment of machine to human must be designed carefully. There is considerable knowledge and experience embedded in the fields of orthotics and prosthetics which for decades has tackled problems of applying significant forces to the skeleton while keeping skin loading to acceptable levels.

Abnormal loading of skin causes tissue breakdown leading to pressure ulcers. Some adaptation ("skin toughening") is possible through training programs, but the more appropriate solution is to keep loads within safe limits. One problem with exoskeletons is they apply loads in locations on the body that are not intended to carry loads of any magnitude for long duration. The classic example are skin ulcers on the buttocks of individuals with spinal cord injury who are seated in wheelchairs for long periods and who forget to shift their weight. Another example is the skin breakdown that can occur at the socket-skin interface of a prosthesis for above-knee amputees. Practically everyone has experienced a minor example of abnormal loading from wearing poorly fitted shoes. An overview of the skin's response to loading can be found in the review by Sanders (1995).

The literature on acceptable skin loading is sparse, but it is clear that skin breakdown and ulcer formation is a function of load magnitude and duration. While definitive load-duration

thresholds have not been established for human skin, guidelines have emerged from the results of several research projects using animal models or human subjects and those guidelines have been translated into clinical practice for the prevention of pressure sores and design guidelines for orthotics and prosthetics (Sanders et al., 1995). The generally accepted model is that surface tissue pressure leads to ischemia that in turn leads to tissue damage. Reasonable estimates of critical loads are 100!mm!Hg (2!psi) for two hours or 35!mm!Hg for four hours. The implication for the exoskeleton is that modest attachment pressures can be tolerated for long periods while high pressures will lead to skin breakdown.

Tissue damage occurs first in deep tissue. Damage will occur to the muscle before seen on the skin. Poorly designed exoskeletons may cause damage to the user before any external symptoms are noticed. The location of the applied pressure impacts damage. Pressure applied where the bone is near the surface will rapidly break down skin because it is easier to squeeze the blood away from the region. Exoskeletons with attachments at bony prominences in an attempt to couple closely to the skeleton are sure to fail.

Shear loads are equally important although less well understood. Shear loading is particularly disruptive for skin, but a small shear load is acceptable even over many cycles. The friction of the material against the skin has a role in the damage process (Sanders, 1998). It appears that skin tolerates high cycles of low shear loads better than few cycles of high loads which bodes well for an exoskeleton designed with low shear loads which cycle with each step.

Moisture and temperature influence the ability of skin to maintain integrity under load. Our attachment designs will keep the skin dry and cool, through the use of appropriate padding materials drawn from orthotics practice. The exoskeleton attachment points must also be kept away from heat generating sources.

Lessons from Prosthetics and Orthotics

The physical architecture of the exoskeleton is more related to orthotics than to prosthetics. Classical design of orthoses is covered in several clinical textbooks, including Bunch (1985), Nawoczenski (1997), and Redford (1986). Also, a brief review of powered orthotics is provided in Goldfarb (1996). There are a few examples of full-leg orthoses (hip-knee-ankle-foot orthosis [HKAFO]), mostly designed for paraplegic walking systems. The hip guidance orthosis (HGO) was developed in Oswestry, England. The reciprocating gait orthosis (RGO) is a similar product developed at Louisiana State University. Both provide guidance at the hip and knee joints and couple the hip joints for reciprocal motion. Neither has met with widespread clinical success because of their bulk, weight, and difficulty in donning and doffing. One criteria for the exoskeleton is that it can be abandoned rapidly in case of emergency. This will be challenging for designs which transfer power to the body, but simpler for machines which walk along with the human.

There are many examples of commercial knee orthotic braces that are both functional and comfortable. Many athletes wear them for several weeks after sustaining a knee ligament injury. For example, the DonJoy product line of knee braces from Smith and Nephew provide a comfortable yet secure fit to the thigh and calf. Likewise, ankle orthoses designed to limit

motion have been successful in the commercial market and are designed for all-day wearing. Products from Air-Cast, Smith and Nephew and Active Ankle systems provide good design models for the exoskeleton.

Our attachment point designs draw directly from tested designs used in orthotics. To reduce costs, wherever possible we take advantage of off-the-shelf orthoses and athletic equipment.

COUPLING ISSUES

The fundamental concept of the exoskeleton is close operation with, but not exact correspondence to the human skeletal structure. An advantage of this approach is that the exoskeleton attaches to the user only at the foot, waist, and shoulder, which greatly simplifies the task of designing attachment points. A second fundamental concept of the exoskeleton is to couple to the user through force sensors. The controller acts to minimize the loads seen by the force sensors, which results in a gentle coupling to soft tissues.

As with any orthosis, the challenge in designing attachments is the trade-off between rigid coupling to the skeleton and comfort for the user. Because rigid coupling is not feasible, any connection will move relative to the skeleton. Our preliminary designs for attachments minimize this shift to be within the stability limits of the controller while still retaining tolerable comfort for the user. A well-designed attachment point meets these requirements: (1) distributes the load, (2) minimizes shear, (3) avoids bony points, and (4) keeps the skin cool and dry. Another critical design criteria for the attachments are that the exoskeleton be easily donned and doffed.

Foot Interface

The most challenging attachment point is at the foot because space is tight and because the boot needs to incorporate the force-torque sensor. The interface design consists of a boot with the rigid force sensing element sandwiched between the tread components that contact the ground and the sole components that contact the foot. Each component has several layers to satisfy the multiple functions of comfort, flexibility, and accurate force sensing.

Figure 21 shows the stack up of layers at the foot from the ground to the skeleton. Each layer has an essential purpose and both control and comfort are effected by the entire impedance chain. For excellent control, a tight coupling to the skeleton is needed. If control was the only issue, the sensor top plate would be connected directly to the skeleton by bone screws, but this of course is not possible. Because of inherent compliance in soft tissue, the boot can be padded with layers of comfort material that have approximately the same compliance as the tissue in the foot. Compliance between the sensor plate and the skeleton is easier to handle in the controller than a deadband because compliance can be modeled and is relatively well behaved. To eliminate deadband, the boot padding will conform closely to the foot when the boot is closed.

The foot coupling must handle bi-directional forces along the vertical axis because as the foot leaves the ground during the start of the swing phase, the exoskeleton must follow along. Unlike a regular shoe, the boot will be padded under the closure straps and laces as well.

The user effectively is "standing" on the foot plate of the exoskeleton with the 6-axis force-torque sensor fitting in series between the human and machine. Thus, the user is raised off the ground, much like wearing boots with very thick soles. The height off the ground is dictated by the height of the force-torque sensor and related fittings. The target package height specification for the sensor is < 4.5!cm. Testing will be done with standard boots attached to sensor mockups to ensure that normal gait is achievable with this configuration.
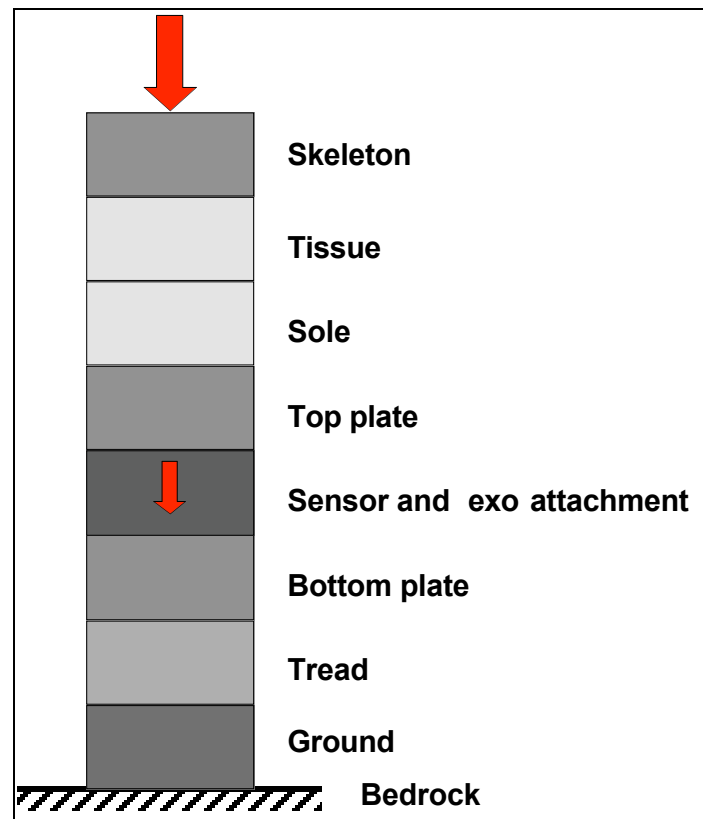
Fig. 21. Layers at the foot coupling.
(Each layer has a compliance that affects comfort and exoskeleton control. The top
arrow is body weight loading. The middle arrow is the load applied by the exoskeleton.)

Waist interface

An off-the-shelf, commercial orthosis will be used to couple the exoskeleton at the waist. Figure!22 shows the device selected, the Model 387x pelvic band component from the Orthomerica Newport 4 Hip Orthosis (www.orthomerica.com). The band has a hard polyethylene outer shell with threaded inserts for mounting components and is lined with soft padding. The band comes in three sizes and the shape of the shell conforms closely to the iliac crest which results in a close, comfortable fit when the component is closed.
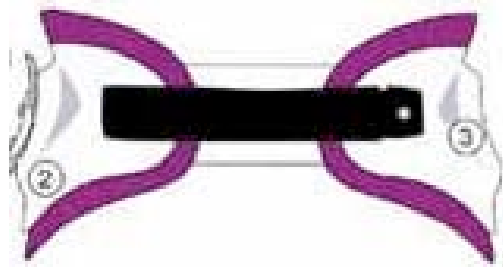
Fig. 22. Waist connection.
(Pelvic band (Model 387x) from the Orthomerica Newport 4 hip orthosis.)

Shoulder Interface

The coupling at the shoulder will use off-the-shelf, high-performance backpack components (Fig. 23). These provide relatively close coupling to the torso. If tighter coupling is needed for control stability, an off-the-shelf trunk orthosis as shown in Fig. 23 will be used.

Fig. 23. Shoulder coupling.
(Standard pack components will be used. If tighter coupling is needed,
an off-the-shelf trunk orthosis will be used.)

Some of the exoskeleton load will appear like a backpack load to the user. From published studies of backpack loading, gait kinematics, and energy use are impacted by pack load with more perturbations for higher load. There are no hard limits on minimum or maximum loads, which means the amount of loading that the exoskeleton applies to the human need not be tightly specified. Published backpack experiments typically used loads ranging from 10 to 30!kg, although one study looked at loads up to 60!kg (Legg, 1992). The distribution of the load is important, and for good balance the load should be relatively constant.

Materials

In addition to standard metal and polymer engineering materials, body attachments will take advantage of the wide range of materials available through the orthosis industry for fitting custom orthotics. Figure 24 shows some of the most useful materials we will use for padding and structural components.
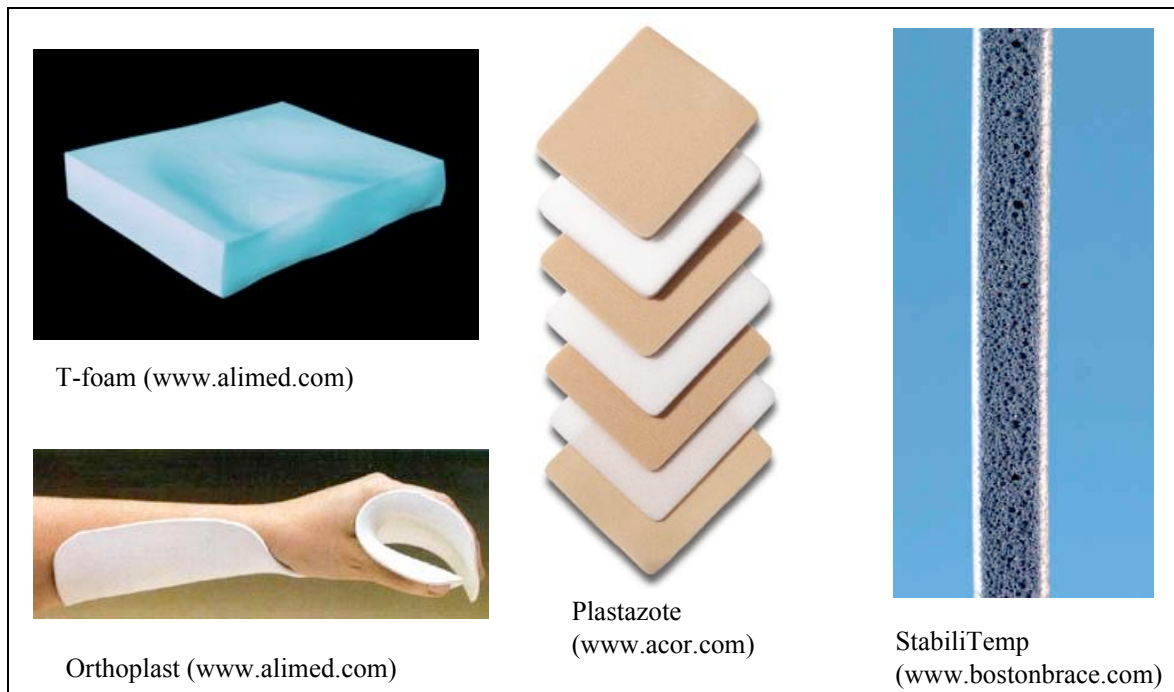
Fig. 24. Common orthotics industry materials.

Polypropylene is the most common sheet material used for rigid cuff and shell type orthotics. Polypropylene can be saw cut, drilled, milled or punched. Drape or vacuum forming is achieved at temperatures of 400°F. Minor modifications are possible with a hot air gun. Boston Brace (www.bostonbrace.com) provides two grades of polypropylene depending on required stiffness and impact resistance. Sheets come in 1/8" to 1/4" thickness.

Low density polyethylene (www.bostonbrace.com) is another common sheet material used in orthotics. Applications are when flexibility and limited strength are needed. Polyethylene can be heat formed at 270°F.

Orthoplast (www.alimed.com) is a low-heat formed, rigid material that is commonly used to fabricate custom splints and braces. Forming is done after soaking the material in very hot water. Orthoplast is extremely easy to work with.

Thermofoam (www.bostonbrace.com) and *Plastizote* (www.acor.com) are lightweight, non-allergenic, closed cell polyethylene cushion foams for direct skin contact. The foam comes in 1/16" to 1/2" thickness and is ideal for padding because it has good load dissipation in all directions. The material can be cut with a knife or scissors, die cut, or punched. It can be formed using heat and pressure and bonded with a variety of adhesives. The foam is used for liners, pads, splints, and fillers and is the material of choice to line shells and cuffs in upper and lower extremity orthosis.

Durofoam (www.bostonbrace.com) is an open cell polyethylene that maintains approximately constant thickness under compressive loads for long periods of time. It is used where load

dissipation is needed along with firm support, for example to form pads under a diabetic's foot. It can be bonded to softer foams for more cushioning effect.

Temper-foam (www.alimed.com) is a visco-elastic, conforming material that is commonly used in seating applications. It slowly forms to whatever shape is applied, but is rigid under impact loads.

StabiliTemp (www.bostonbrace.com) is a 3-ply liner material that forms a cool, dry interface by wicking away moisture from the skin into an absorbent gel.

Other Design Considerations

The coupling of the exoskeleton to the soldier was designed with a quick release feature. For the short-term product development, a quick release coupling simplifies the task of testing exoskeleton prototypes with human subjects. In the long term, a quick release is required should the soldier need to abandon the exoskeleton during emergency situations. For early exoskeleton prototypes, we planned to take advantage of existing quick release products such as the step-in fitting used in high-performance bicycling.

BIOMECHANICS ANALYSIS

POWER AND TORQUE REQUIREMENTS[††]

A study was performed by ARL to provide baseline estimates of the power and torque requirements for the lower limbs of an exoskeleton for two hypothetical dismounted missions. The missions are "movement to contact" and "clear a building." Human biomedical data reported in journal articles and technical reports were used in this study. The purpose of this work was to provide guidance for the design of the lower limbs of an exoskeletal device. In providing design guidance, there were two goals. The first goal was to provide estimates of the angles, torques, and powers for the ankles, knees, and hips of an exoskeleton based on data collected from humans. The second goal was to calculate the mean power required for various tasks and the total peak power needed by the lower limbs of the exoskeletal device for two "typical" infantry missions.

In order to apply human biomechanical data to design guidance for an exoskeleton, six assumptions were made:
1) The size, mass, and inertial properties of the exoskeleton will be equivalent to those of a human.
2) The exoskeleton will carry itself (including power supply) and the soldiers' load.
3) The joint torques and joint powers scale linearly with mass.
4) The exoskeleton's gait will be the same as a human's gait.
5) The exoskeleton will carry a load on its back in the same way that humans carry loads on their backs.
6) The exoskeleton will move at the same speed, cover the same distance, and carry the same load as a soldier who does not have an exoskeleton.

The human biomechanical data used in this analysis came from studies reported in relevant journals and technical reports. These data are from studies of normal walking, walking at various speeds, walking while loads are carried, running at a moderate pace, and running at various speeds. Other activities for which joint angle, torque, and power data were obtained included stair climbing, jumping, and kneeling. The figures in Appendix C show the joint angles, joint moments, and joint powers for walking, walking while a load is carried, running, ascending stairs, descending stairs, and jumping. It is important to note that the joint power data are derived from calculations of the mechanical work done by the lower limbs to move the entire body, as opposed to physiological work based on oxygen consumption.

The calculation of total peak power focused on two hypothetical missions, a movement-to-contact mission and a clear-building mission. These missions represent the kind of diverse missions for which an exoskeleton might be used. Also, the fundamental tasks (e.g.,!walking, jogging, etc.) involved in these missions are the same tasks that occur in other infantry missions (e.g., infiltrate and raid). The movement-to-contact mission took place over a 16-hour period, and the exoskeleton carried the soldier's sustainment load (35!kg) during most of that time. In the clear-building mission, which lasted approximately 2 hours, the exoskeleton carried the

---

[††] This section summarizes the ARL study documented in Crowell et al., 2002.

soldier's fighting load (24!kg). The soldier in these hypothetical missions was a 50th percentile male whose mass was 77!kg.

The data used to calculate total peak power for the movement-to-contact and clear-building missions came from the joint power data in Appendix C. Five simplifying assumptions about gait and the exoskeleton were made in order to calculate peak power. The assumptions were:
1) Increasing the load carried has the same effect on peak power as does increasing body mass.
2) Joint powers in the frontal and transverse planes are small compared to the sagittal plane. Therefore, only sagittal plane peak power profiles were calculated.
3) Normal gait is symmetrical.
4) Peak power values for assuming and leaving kneeling and prone positions, crawling, and climbing a ladder can be approximated with the values for stair ascent.
5) Power values of other lower extremity joints, such as the metatarsophalangeal joint, are small and therefore not included in the peak power calculation.

Then, a four-step process was used to calculate the peak power required by the lower limbs of the exoskeleton during the movement-to-contact and clear-building missions.
1) Spreadsheets that listed each task in chronological order (e.g.,!walking, jogging, jumping, etc.) that occurred during the missions were created. The time required for each task and the load type are listed in Table 1.
2) The powers required at each joint (left and right ankle, knee, and hip) were summed, and peak and average power values were identified for each task and load combination (Fig.!25 and Table 2).
3) The peak power for each task and load combination was entered into the spreadsheet.
4) The peak power and the time required for each task were plotted for each mission (Figs.!26 and 27).
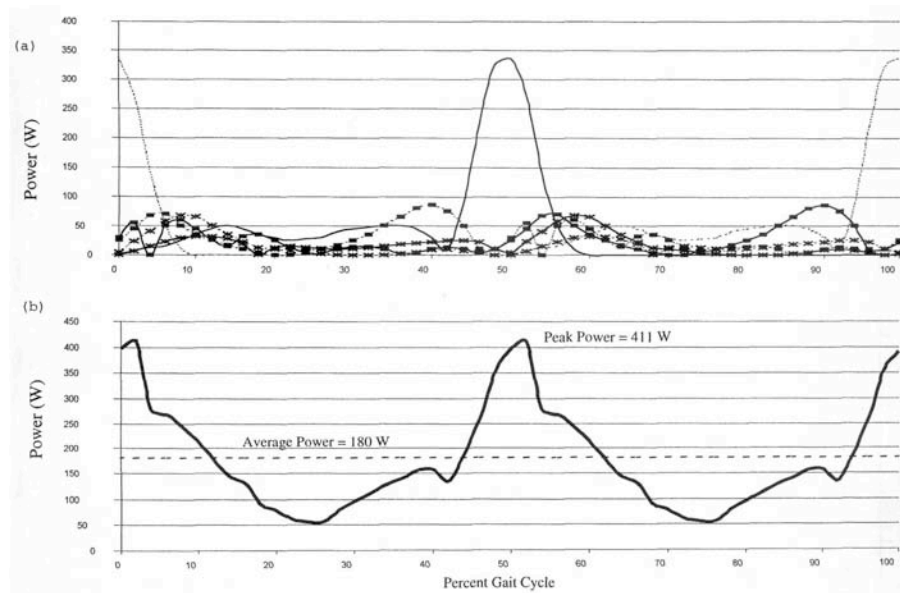
Fig. 25. Peak and average power.
(Example of one cycle of a task and load combination for all six lower limb joints.)

Table 1. Sample time-line of a typical soldier mission

Time (min)	Task	Load
0	Walking	Sustainment
45	Resting	
60	Walking	Sustainment
90	Kneeling and Resting	Sustainment
92	Walking	Sustainment
110	Resting	
120	Walking	Sustainment
130	Kneeling and Resting	Sustainment
124	Walking	Sustainment
150	Prone - Security	Sustainment
152	Walking	Sustainment
170	Resting	
180	Walking	Sustainment
200	Prone - Security	Sustainment
205	Walking	Sustainment
230	Resting	
240	Walking	Sustainment

Table 2. Peak and average power values for typical soldier tasks

Task	Total mass (soldier plus carried load)	
	Fighting (101 kg)	Sustainment (112 kg)
Slow walk (86 steps/min)	283 (119)	314 (131)
Natural walk (105 steps/min)	411 (180)	456 (200)
Fast walk (122 steps/min)	693 (315)	769 (349)
Jog (2.7 m/s)	1966 (1041)	2180 (1155)
Run	3147 (1693)	3489 (1877)
Sprint (7.6 m/s)	5547 (3522)	6151 (3906)
Running vertical jump	3559 (1325)	3947 (1369)
Ascend stairs	501 (229)	556 (254)
Descend stairs	478 (270)	530 (300)

Note: All peak (average) power values are given in watts. All values represent absolute power for all six lower extremity joints (left and right hip, knee, and ankle joints) during the given task and load combination, except for jumping, which assumes a running jump with single-legged take-off.

Fig. 26. Lower limb peak power profile for clear-building mission scenario.

Fig. 27. Lower limb peak power profile for movement-to-contact mission scenario.

28
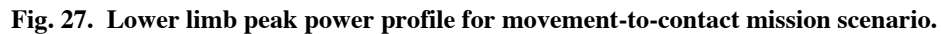
The accuracy of the calculated results is in part a reflection of the accuracy of the original data. When biomechanical data are collected, certain assumptions, limitations, and variabilities affect the accuracy of the data. The accuracy of data collected in biomechanical studies is generally within 20% of their real values. It is likely that when these data are used to calculate kinetic variables such as joint moments and powers, compensating errors keep the overall accuracy of the results within 20% of their true values. Therefore, the power requirements calculated in this report have a tolerance of ±20%.

During most of the movement-to-contact mission, the soldier and exoskeleton walked at a natural pace, and the exoskeleton carried the sustainment load. Although the average power required for this task was 200!W ±40!W, there were peak power requirements of 500!W ±100!W. The peak powers are important because the power supply must be sized to meet the peak requirements. If the power supply cannot meet the peak requirements at the proper frequency, then the exoskeleton may, in contrast to its goal, decrease the soldier's speed, strength, and endurance. The 500!W ±100!W peaks occurred at approximately 2!Hz. This frequency coincides with ankle plantarflexion that occurs during "toe-off" in each gait cycle. When contact was made with the enemy, part of the sustainment load was dropped, and the soldier and the exoskeleton performed a variety of tasks including sprinting. The average power required during this part of the mission was 3500!W ±700!W with peaks of 5500!W ±1100!W that occurred at 4!Hz. The 4-Hz frequency coincides with ankle plantarflexion during toe-off for sprinting.

The power requirements for the clear-building mission were more variable than the power requirements for the movement-to-contact mission. This occurred because the soldier changed his speed many times as he moved to the building and then from room to room. For the clear-building mission, the average power required was 200!W ±40!W to 300!W ±60!W during much of the mission. Peak powers rose to 400!W ±80!W for walking at a natural pace and frequently to 700!W ±140!W for walking at a fast pace. There were several times when the soldier was jogging. At those times, the average power was 1000!W ±200!W, and peak power as 2000!W ±400!W. The highest peak power requirement for this mission (approximately 3000!W ±600!W) occurred at the beginning when the soldier was running up to the building. As with the movement-to-contact mission, the peak powers must be delivered at approximately 2 to 4!Hz.

In conclusion, the data provided through this analysis can be used as a baseline for the initial design of an exoskeletal device. These data can be used to evaluate currently available and near-term technology to determine the feasibility of developing a practical exoskeleton. The joint angles, torques, and powers presented in Appendix C and Table 2 provide a basis for initial design of lower limb joints and actuators, and the peak power profiles (Figs. 25 and 26) provide a basis for initial sizing of the power supply.

HUMAN FACTORS ANALYSIS

SOLE THICKNESS OF THE BOOT INTERFACE[‡‡]

The exoskeleton boot interface, an integral component of the system, is expected to incorporate a 1- to 2-inch thick sole for the containment of force sensors, thus creating a substantial offset of the soldier's foot from the ground. Very little published data exists regarding human factors issues related to footwear sole thickness, therefore, the objective of this investigation was to identify, through analyses of biomechanics data, observations of ability to negotiate obstacles and subjective assessments, potential human factors issues related to the additional sole thickness of an exoskeleton boot interface. The results of this investigation will provide critical guidance to the DARPA EHPA Program for the development of an exoskeleton boot interface that is safe, comfortable, and functional, and may also result in substantial savings of time and money for the EHPA Program.

In this investigation, three-dimensional angles and sagittal plane moments and powers at the right hip, knee, and ankle joints during walking, running, squatting, and right and left kneeling; stride length, velocity, cadence, and percent stance during walking and running; cycle time during squatting and right and left kneeling; time to negotiate obstacles; and ratings of comfort, stability and difficulty during walking, running, squatting, right and left kneeling, and negotiating obstacles were evaluated for three sole thicknesses-baseline (no additional sole), 1-inch and 2-inch. Rubber overboots with detachable wooden soles were used to create the three-sole conditions (Fig. 28). For each of the three-sole conditions, three-dimensional positions of reflective markers placed on the participants' boots and at several anatomical locations (Fig. 29), were tracked by six high-resolution video cameras connected to a computer running EVaRT 4.0 motion capture software (Motion Analysis Corporation, Santa Rosa, California), as participants walked, ran, squatted, kneeled on their right knee, and kneeled on their left knee (Fig. 30) on a force plate (Advanced Mechanical Technology, Inc., Newton, Massachusetts) surrounded by a raised walkway. Biomechanics variables were calculated from ground reaction force and three-dimensional marker position data using KinTrak 6.2 biomechanical analysis software (Motion Analysis Corporation, Santa Rosa, California). Individual completion times under the three-sole conditions were collected for five obstacles on the Army Research Laboratory (ARL) Mobility-Portability course (Aberdeen Proving Ground, Maryland)—log balance, elevated up and down, tires, house, and zig-zag (Fig. 31). Subjective assessments of comfort, stability and difficulty during walking, running, squatting, right and left kneeling, and negotiating the five obstacles under the three-sole conditions were obtained using a questionnaire with a six-point rating scale (very low, low, slightly low, slightly high, high, very high).

Twelve male soldiers (age: 21±3 yr, height: 172.5±8.6 cm, body mass: 76±9 kg), stationed at Aberdeen Proving Ground, were recruited for participation in this study. All participants were first briefed on the objectives of this investigation and procedures to be followed, and then asked to sign a statement of informed consent. After signing the volunteer agreement, height, weight, and shoe size were measured and recorded for each participant. Prior to data collection for each

---

[‡‡] This section summarizes the ARL study documented in Boynton and Crowell, 2003 that is currently in publishing.

sole condition, participants were trained to walk, run, squat, and kneel on the force plate and to negotiate each of the five obstacles correctly, and then permitted to practice until they were able to perform each activity comfortably.

Fig. 28. Overboot and sole set-up.
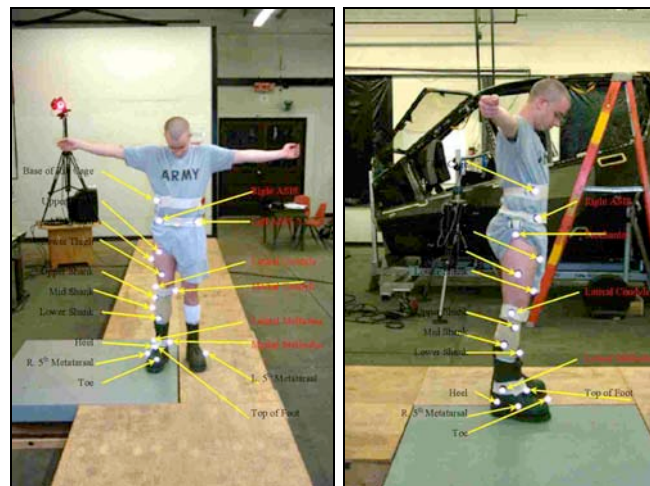
Fig. 29. Reflective marker placement.

| Walking | Running | Squatting | Right kneeling | Left kneeling |
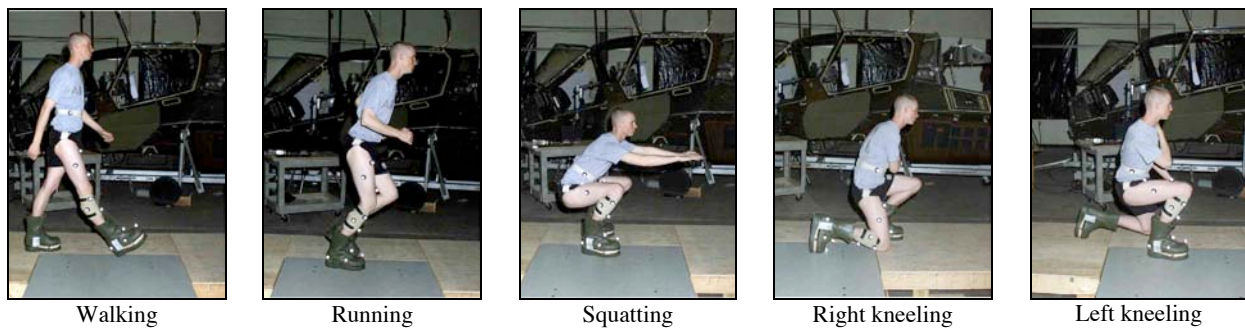
Fig. 30. Activity on the walkway and force plate.

| Log balance | Elevated up and down | Tires |

House   Zig-zag

Fig. 31. Obstacles on the ARL mobility-portability course.

A within-subjects design with a Williams Square counterbalancing scheme for sole condition was used in this investigation. The independent variable was sole thickness, which consisted of three levels: baseline, 1-inch and 2-inch. The dependent variables were:

    a. peak three-dimensional joint angles at the hip, knee, and ankle (degrees),

    b. peak sagittal plane joint moments at the hip, knee, and ankle (N-m/kg),

    c. peak sagittal plane joint powers at the hip, knee, and ankle (W/kg),

    d. peak ground reaction forces (N/BW),

    e. stride length (m),

    f. velocity (m/s),

    g. cadence (steps/min),

    h. percent stance,

    i. cycle time (sec),

    j. obstacle completion time (sec), and

    k. ratings of comfort, stability and difficulty.

A univariate analysis of variance (ANOVA) with main effects for participant, order, and sole conditions was performed on each dependent variable. Those variables significantly affected by sole condition were further analyzed using a Fisher's Least Significant Difference (LSD) post-hoc test in order to identify specific differences between means. ANOVA and Fisher's LSD results were considered significant for values less than 0.05. All statistical analyses were performed using SPSS 10.1 for Windows (SPSS, Inc., Chicago, Illinois).

Summaries of the biomechanics data for walking, running, squatting, and right and left kneeling under each of the three-sole conditions can be found in Tables 7-11 in Appendix D, respectively. Stride length, velocity, cadence, percent stance, and cycle time are reported as mean values. Angles, ground reaction forces, moments, and powers are reported as means of the peak values.

During walking, twelve biomechanics variables were found to be significantly affected by sole condition- peak hip power generation; peak knee flexion, external rotation, power generation and absorption; peak ankle dorsiflexion, abduction, internal rotation, plantarflexor moment and dorsiflexor moment; peak vertical ground reaction force; and peak propulsive ground reaction force (Table 7, Appendix D). Compared to the baseline sole condition, 1-inch and 2-inch sole condition mean values were found to be significantly smaller for ankle abduction (39.6 and 53.0%) and internal rotation (25.6 and 35.6%); knee power generation (22.2 and 34.1%) and absorption (14.1 and 44.1%); and propulsive ground reaction force (8.0 and 16.0%); and significantly larger for ankle dorsiflexion (20.8 and 24.2%), plantarflexor moment (11.8 and 9.7%) and dorsiflexor moment (61.9 and 52.4%). Mean values under the 2-inch sole condition were shown to be significantly smaller than both baseline and 1-inch sole condition means for knee flexion (6.0 and 4.5%) and power absorption (44.1 and 34.9%); hip power generation (20.4 and 17.1%), and propulsive ground reaction force (16.0 and 8.7%). Additionally, compared with the baseline sole condition, knee external rotation under the 2-inch sole condition was found to be significantly reduced by 14.7 percent.

Only one running biomechanics variable, peak ankle abduction, was found to be significantly affected by sole condition (Table 8, Appendix D). Post-hoc test results further revealed that the 1-inch and 2-inch sole condition mean values were significantly reduced below that of the baseline sole condition by 37.3 and 35.8 percent, respectively.

Sole condition was not found to have a significant effect on any of the biomechanics variables for squatting (Table 9, Appendix D).

A significant effect of sole condition was found for nine right kneeling biomechanics variables-cycle time; peak hip flexion; peak knee flexion (maximum) and external rotation; peak ankle abduction, external rotation, internal rotation and power generation; and peak vertical ground reaction force (Table 10, Appendix D). Mean 1-inch and 2-inch sole condition values were found to be significantly larger than mean baseline values for cycle time (10.8 and 19.0%), hip flexion (59.2 and 76.7%), knee flexion (10.2 and 8.3%), and ankle power generation (73.0 and 113.5%), and significantly smaller than mean baseline values for ankle abduction (63.8 and 87.8%) and internal rotation (39.3 and 47.9%). Vertical ground reaction force, knee external rotation and ankle external rotation means under the 2-inch sole condition were also found to be significantly increased over the baseline sole condition by 16.7, 33.8 and 78.3 percent, respectively. Additionally, compared with 1-inch sole condition means, 2-inch sole condition means were significantly larger for cycle time (7.4%) and vertical ground reaction force (11.4%).

Five left kneeling variables were found to be significantly affected by sole condition- peak hip abduction; peak knee flexion (maximum) and external rotation; and peak ankle dorsiflexion (maximum) and external rotation (Table 11, Appendix D). In comparison to baseline sole condition means, 1-inch and 2-inch sole condition means were found to be significantly larger for maximum knee flexion (3.5 and 7.9%) and knee external rotation (15.7 and 26.9%). Mean 2-inch sole condition means for hip abduction, and ankle dorsiflexion and external rotation were

also shown to be significantly increased over those of the baseline sole condition, by 21.9, 14.4 and 35 percent, respectively. Additionally, maximum knee flexion under the 2-inch sole condition was found to be 4.3% larger than that under the 1-inch sole condition.

Mean obstacle completion times under each of the three sole conditions are shown in Table 12 (Appendix D). A statistically significant effect of sole condition on completion time was identified for the Log Balance and Tires only. For the Log Balance, 1-inch and 2-inch sole condition completion times were found to be significantly longer than for the baseline sole condition, by 21.3 and 26.0%, respectively. Additionally, in comparison to the baseline sole condition, the Tires completion time for the 2-inch sole condition was significantly increased by 11.5 percent.

In order to compute mean values and conduct statistical analysis of the questionnaire responses, each response level was assigned a numerical value: 1=very low, 2=low, 3=slightly low, 4=slightly high, 5=high, 6=very high. Mean responses to the comfort, stability and difficulty questionnaire are given in Fig. 101 (Appendix D). With the exception of Squatting, House and Zig-Zag difficulty, all questionnaire responses were found to be significantly affected by sole condition. As a whole, ratings of comfort and stability were found to decrease, while ratings of difficulty were found to increase, with increasing sole thickness.

Few of the biomechanics variables examined were identified as being significantly affected by sole condition (approximately 14.5%). It is especially notable that peak moment and power values at all three joints are similar across sole conditions, with the exceptions during walking of hip power generation and knee power generation and absorption, which decrease, and ankle plantarflexor and dorsiflexor moments, which increase, as sole thickness increases. Thus sole thicknesses up to 2 inches should not have a negative impact on the power requirements of the exoskeleton system, and actuators can be designed to provide additional torque at the ankle joints. Although sole thickness was found to have a significant effect on various joint angles during walking, running, and kneeling, it appears that humans are able to accommodate these differences, maintaining similar values across sole thickness conditions for each of the temporal-spatial variables examined. The significantly longer completion times observed for the Log Balance and the Tires are most likely the result of decreased stability as sole thickness increased. Although sole condition was shown to have a significant effect on perceptions of comfort, stability and difficulty, it should be noted that on average the comfort rating for the 2-inch sole condition was slightly high while that for the baseline condition was high, and the difficulty rating for the 2-inch sole condition was slightly low while that for the baseline was low. The largest disparity was seen for stability with the average 2-inch sole condition rating being slightly low as compared to an average rating of high for the baseline condition. It may be possible to eliminate differences between the baseline and the 1-inch or 2-inch conditions through training or by designing the components of the exoskeleton so that they promote comfort and stability. Overall, it appears that the exoskeleton boot interface could incorporate a sole up to 2 inches in thickness without considerable impact on the human factors issues investigated in this study.

BIOMECHANICS TESTING

CONTROLLER LAG EFFECTS ON AN OPERATOR WALKING

The exoskeleton force-reflecting controller is maximally challenged at heel strike and toe off when rapid dynamics occur. In the event that the controller does not keep up with the human during certain maneuvers when the foot is coming up off the ground, the user will feel a sensation not unlike wearing a pair of sticky boots. That is, the controller may exert brief forces on the foot with the force vector directed towards the ground. This is the same effect that many haptic interfaces have when emulating stiff walls. When the user taps the virtual wall with the haptic interface, he or she may feel a slight "stick" as the controller attempts to emulate the high bandwidth mechanical events that occur during rigid object collisions.

To explore what impact these control delays would have upon gait, and to determine whether padding was required under the tongue of the boot, a simple pilot experiment was conducted. The purpose of the experiment was to see what it was like to walk in a "sticky" boot. Although one could design an exoskeleton with very high bandwidth actuators and control, if the stickiness is tolerable, more cost-effective, lower bandwidth components would be adequate.

A single "sticky" boot was constructed by fastening disk magnets to the underside of a standard hiking boot. The boot was a Cherokee, size 12, right hiking boot purchased from a discount store. The magnets were ceramic pot magnets, 1.4-in dia., 0.281-in thick with a maximum 13-lb pull (McMaster Carr 5685 K26). Magnets were fastened to the sole of the boot with 10-24!x!1/2" machine screws. An 1/8" brad point drill bit was used to make pilot holes in the sole. The screws were self-threaded into the sole, a fastening means that was sufficiently secure for brief experiments. Eight magnets were used, four fastened to the heel and four to the sole. Two sheets of 12"!x!24", 22!g plain sheet steel were taped end to end on the floor to provide a target area for the shoe. Photographs of the apparatus appear in Fig.!32.

A single subject walked, sometimes over the target area and sometimes over the adjacent plain floor. The sticky boot was on the right foot. The left foot wore the matching, but unmodified, left boot. The magnet pull when on the steel sheet varied depending upon how many magnets were in contact and whether the magnets were flat against the plate. With all magnets making good contact and the foot pulling straight up, the release load was 35!lb. When the foot was rolled up, as is normal during gait, the release load dropped to 1-2!lb because it is relatively easy to release the magnets through rotation.

The results of this unstructured pilot showed that small amounts of force keeping the foot on the ground can be tolerated quite well with only a modest impact on gait. Further, only minimal padding is needed under the laces to distribute the extra loads comfortably. Special user training would be required to accommodate the soldier to these unusual forces should they be an inevitable part of the controller. More rigorous human factors testing of "sticky" boots is needed to determine the true impact on gait.
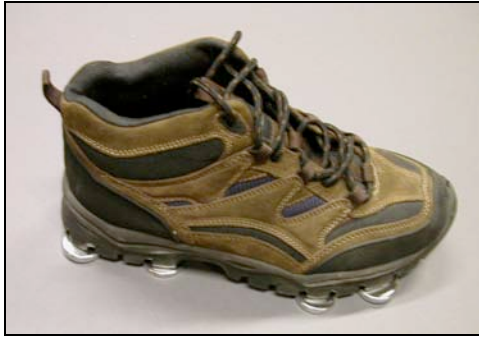
Fig. 32. "Sticky" boot.
(Eight disk magnets attached to sole. Walking over sheet steel with boot.)

EXOSKELETON MOCKUP

To determine whether the selected exoskeleton joints and degrees of freedom would interfere or complement normal gait or mobility maneuvers, a simple mockup of the exoskeleton structure was fabricated. Fabrication materials included aluminum bar and tube, wood dowels, an off the shelf orthotic pelvic band (Newport 4 hip orthosis, Orthomerica, www.orthomerica.com), and a standard hiking boot. Only one side of the orthosis was mocked up. The intent was to produce a structure that was faithful in kinematics to the powered exoskeleton, but not in actuation or load carrying. Figure 33 shows the mockup during quiet standing.

The mockup had an ankle flexion/extension and foot inversion/eversion joints (Fig. 34), a knee flexion/extension joint, and a thigh prismatic joint (Fig. 35), and hip flexion/extension and internal/external rotation joints (Fig. 36). The hip abduction/adduction joint was not implemented in the mockup.

Fig. 33. Exoskeleton mockup.

Fig. 34. Ankle flexion/extension and foot inversion/eversion joints.

Fig. 35. Knee flexion/extension and thigh prismatic joints.
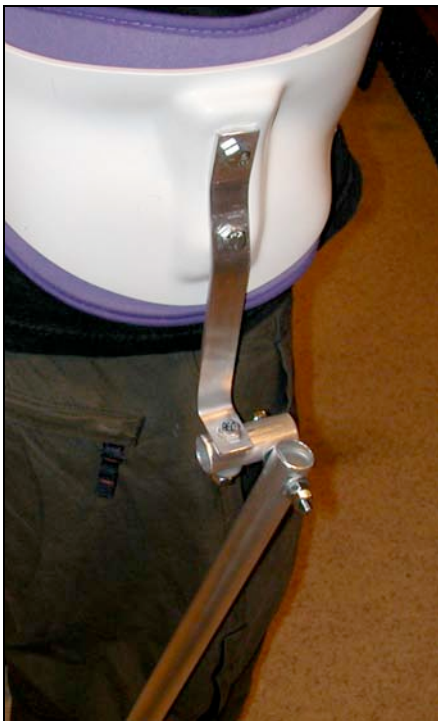
Fig. 36. Hip flexion/extension and internal/external rotation joints.

The mockup was able to follow the body during normal maneuvers. Figure 37 shows the foot and ankle during toe-off of a gait cycle. Figure 38 demonstrates that the kinematics are able to follow a deep knee bend.

Fig. 37. Ankle during toe-off.

Fig. 38. Deep knee bend.

Figure 39 shows foot inversion while Fig. 40 demonstrates ankle flexion/extension maneuvers.
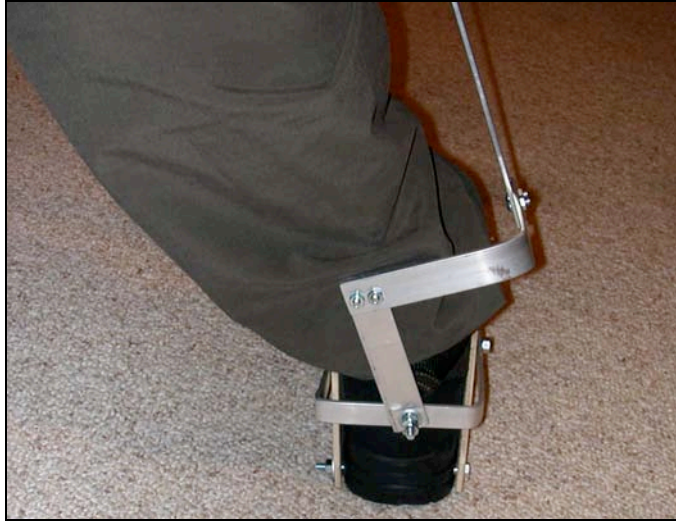
Fig. 39. Foot inversion.

Fig. 40. Ankle flexion/extension motions.

Figure 41 shows hip internal/external rotation and Fig. 42 shows hip flexion/extension motion.

Fig. 41. Hip internal/external rotation.

Fig. 42. Hip flexion/extension.

Results from informal wearing of the mockup verified that the kinematic design chosen for the exoskeleton is viable. Comprehensive human factors testing is needed to confirm these results.

FOOT INTERFACE TESTING

A series of tests have been planned for Phase II, each with another layer of realism added. In the first tests a controlled hydraulic piston will replace the human and will apply accurate force or motion loading profiles to the force sensor. In the second test, a SACH (solid-ankle, cushioned-heel) prosthetic foot (Fig. 43) will be driven by the hydraulic piston. The SACH foot, with a compliance and shape that closely match that of a real foot, offers the highest level of realism without using an actual human. The third test will add a human user exercising the system through a wide range of voluntary motions including standing, weight shifting, stepping, and stomping. The motion limits of the exoskeleton will be constrained with limit stops for safety.

The tests are designed to understand controller properties and are not meant to test comfort. An important objective is to determine the range of acceptable compliance for foot padding and ground contact. Real orthotic padding materials will be used in these tests with the goal of determining the types and thickness of padding that are acceptable for stable control. This will establish the constraints for the final boot design.

Force and position data will be collected for all tests. In addition, internal boot loads against the foot would be tested using individual Flexi-force or distributed pressure sensor arrays from Tekscan (Fig. 44).

Future test beds will include a single-leg, multi degree-of-freedom (DOF) system where the leg can move in all directions and where contact stability for all motions of the foot (heel-strike, toe-off, flat foot, inversion/eversion) can be tested. The single-leg, tethered exoskeleton will next be tested during treadmill walking for loaded and unloaded conditions. Testing of a two-leg exoskeleton prototype is further in the future, and will include testing in-place, on a standard treadmill and on the 2-DOF treadmill at ARL.

Fig. 43. SACH foot for mannequin testing.

Flexi-force pressure sensor
www.tekscan.com

Tekscan distributed pressure array
www.tekscan.com

Measuring foot-shoe interface pressure with Flexi-force sensor
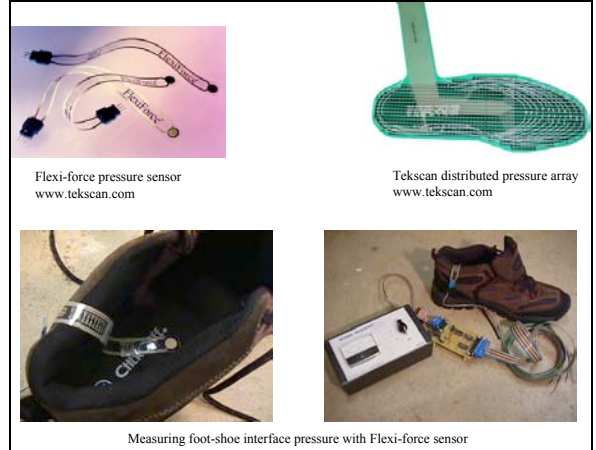
Fig. 44. Testing shoe/foot interface loads.
(Testing thin pressure sensors.)

POWER SYSTEM

BACKGROUND[§§]

For an application such as an exoskeleton, there will be significant differences in the steady-state power requirements and the peak power or transient demands. The power source must, therefore, be able to meet both the energy requirements and peak power demands and comparison of potential power sources must be made with respect to meeting both of these requirements. For an exoskeleton type of system, the specific power (power ÷ weight) and specific energy (energy ÷ weight) are the parameters that are more useful for comparison of potential power systems. Ragone Diagrams (Fig. 45), which plot specific energy vs specific power, provide a means for making broad, general, comparisons between potential power sources. However, it should be noted that Ragone Diagrams provide information on steady-state specific power and specific energy, but they do not provide any indication as to the response time of a power source and thus, its ability to follow demand.

Figure 45 provides a general comparison of typical fuel cells, batteries, internal combustion engines, and super capacitors. It should be noted that on-going research is continuing to expand the capabilities of these power sources. Although other power sources and storage devices, (e.g., compressed gas, thermoelectric devices, and flywheels) are available, they are not considered practical for a remote mobile device, such as an exoskeleton. From Fig. 45, it can be seen that (1) internal combustion engines have relatively high specific power and specific energy and (2) a hybrid system such as a fuel cell and either batteries or super capacitors can also meet the requirement of high specific power and energy.
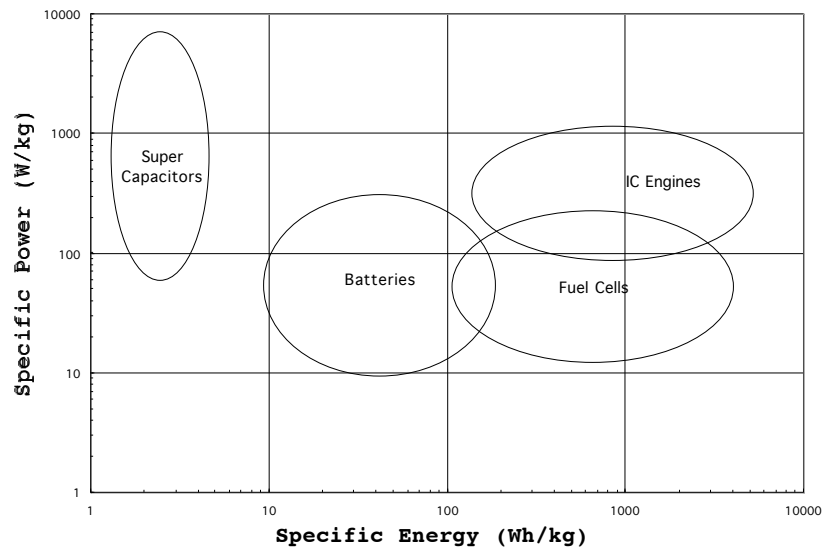
Fig. 45. Comparison of different power sources.

[§§] Appendix E provides additional background details regarding the basis of the approach taken (Jansen et al., 2000).

The power source for an exoskeleton must satisfy both power and energy requirements. With the significant variability in anticipated power demands, the ability of the power source to respond to peak loads without impeding performance is essential. Oversizing a single power source to meet both power and energy requirements is not consistent with the need for efficiency required for this application. A hybrid power system, where transient peak power demands are met with one source and mission energy requirements are met with another source, can enhance efficiency at the expense of a more complicated system. Super capacitors and nickel-metal-hydride (NiMH) batteries are both capable of meeting peak transient load requirements, but they are insufficient as an energy source. A fuel cell fed by hydrogen, which is generated by a chemical reaction and an internal combustion engine (ICE) are both capable of meeting system energy requirements.

Table 3 compares the weight for three possible power sources, diesel engine, fuel cell, and batteries, as well as two possible hybrid systems. While the weights for the ICE are lower than those for the fuel cell, it must be noted that the ICE weights do not include provisions for signature (noise, thermal, and emissions) reduction and vibration damping. These can be compensated for, but at the expense of increased complexity and weight. The weight of the fuel cell and the hybrid fuel cell approach are the same. Should a fuel cell itself be capable of responding fast enough to meet peak transient demands, there would be no inherent advantage to the hybrid fuel cell approach over a fuel cell.

Table 3. Power source comparison

Power Source Type	Specific Power (kW/kg)	Specific Energy (kWh/kg)	Energy/ kg of Fuel (kWh/kg)	Weight for Power (kg)	Weight for Energy [1] (kg)	Total Weight (kg)
Diesel ICE[2]	0.4		3.3	5.0	2.4	7.4
PEM Fuel Cell[2,3]	0.5		1.2	4.0	6.8	10.8
Li Ion Batteries[4]	0.5	0.25		4.0	32.0	32.0
Hybrid						
Fuel Cell[5]	0.5		1.2	2.0	6.8	
Battery (NiMH)[6]	1.0			2.0		
Total						10.8
Hybrid						
Diesel ICE[5]	0.4		3.3	2.5	2.4	
Battery (NiMH)[6]	1.0			2.0		
Total						6.9

Requirements:
    Avg Power (kW) =   1.0
    Peak Power (kW) =   2.0
    Energy (kWh) =   8.0

[1] Based on specific energy <u>or</u> fuel consumption.

[2] Sized to meet peak power and energy requirements, including fuel.

[3] Specific energy based on 39.4 kWh/kg (higher heating value) of H_2. Assumes 6 wt% H_2 b& 50% efficiency.

[4] Total weight based on energy requirements.

[5] Sized to meet average power and energy requirements.

[6] Sized to meet peak power requirements.

Fuel cells allow for more stealthy operation because of their quiet operation, relatively low temperatures, and benign emissions (water). While there are development issues remaining to be solved for fuel cells, primarily regarding the hydrogen source, there appears to be viable options.

These are currently being pursued by commercial suppliers and are already being introduced into the market for niche applications. It should be noted that there have been significant increases in fuel cell power density, with more increases anticipated. Integrating a super capacitor or NiMH batteries for transient response with a fuel cell fed by chemically generated hydrogen offers the potential for best meeting the combination of power, energy, and signature objectives and safely function in close proximity to a human operator. This is the approach (Fig.!46) that has been taken in Phase I and will be discussed in greater detail.

The focus of the Phase I power supply effort was on demonstrating a bench top integrated, hybrid power source that would meet both energy and power needs (including peak transient loads) for an exoskeleton. The system was successfully designed, fabricated, and tested. In addition, the feasibility of water recycling as a means of increasing the energy density was also investigated. Both of these efforts are described in detail below.
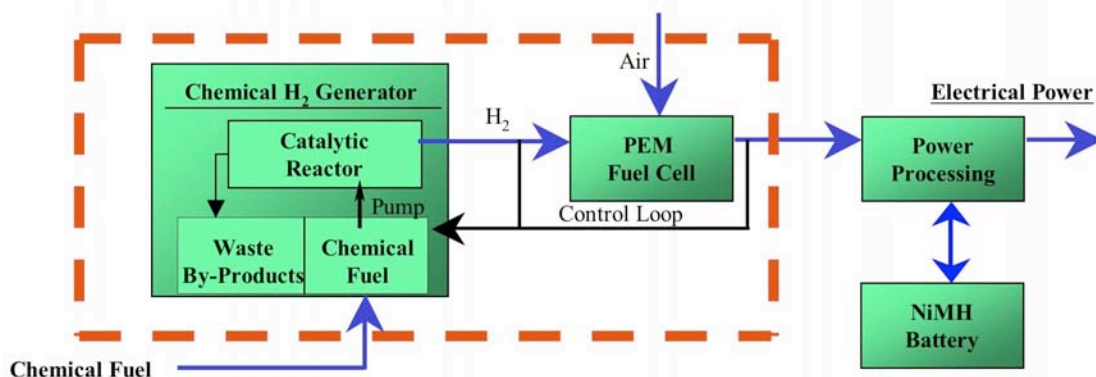
Fig. 46. Power system block diagram.

INTEGRATED POWER SYSTEM[***]

The power source tested was comprised of three basic parts: (1) a proton exchange membrane, hydrogen-air fuel cell as the base power requirement; (2) a battery transient response module to address situations when the power requirements exceed the power deliverable by the fuel cell or in cases where the fuel cell response lags the load, and; (3) an easy method to generate hydrogen, control its flow to the fuel cell, and recycle its by-product.

A five-step plan was employed to allow rapid construction of a demonstration power supply for our chosen hybrid architecture. The first step was to select off-the-shelf components. The second was to design and build the power supply. Third, the power supply was tested, debugged, and integrated into the system. The fourth step was to develop the system controller and the additional hardware to measure and control all system parameters. In the fifth step, the ORNL chemical hydrogen generation subsystem was integrated and the sodium borohydride solutions prepared. The integrated system was fabricated and tested under several upper- and lower-bound power profiles.

[***] This section summarizes the report documented in AeroVironment, 2003, and found in Appendix F.

47

The result of this approach was a prototype system ready to operate from fuel to electricity and demonstrating hybrid system capabilities for the soldier's energy and power requirements. An operating voltage of 48VDC was selected as best for control of the hybrid system. From this voltage, a system control concept was developed and a control circuit was designed. NiMH batteries were selected for the transient handler system. Demonstrations used hardware to analyze and understand the nuances of the chosen hybrid power architecture—placing paramount emphasis on robustness, simplicity, safety, and system sizing flexibility-related issues.

A hybrid system-sizing map (the parameter space) showed optimized system configuration for soldier energy demand average, peaks, and down time (available recharge time). No single power profile could determine base system sizing criteria because a soldier's activity is varied. With the help of ORNL, models were developed for a variety of scenarios and analyzed from a system sizing perspective. Most significantly, a demonstration (portable) system operating under automatic control, from fuel to electricity, was built by adding a hydrogen storage and handling system from ORNL. The system demonstrated the viability of the control concept through both steady state and transient operating parameters defined in the modeling task. It also tested the performance and the transient handling capability of the ORNL hydrogen generator as a fuel source to the baseline hybrid fuel cell system.

The final product was a self-controlled, self-contained system that starts with a push of a button. Figure 47 illustrates best the overall concept. The PC is used for data display and recording only. The electric load is on the bottom shelf and is used for system testing. The fuel cell stack is an off-the-shelf system and no effort has been expended in reducing the size of the stack or the balance of plant components. The whole system is spread out and is not optimized for weight or size. As it is, it can easily be scaled depending upon power needs and energy storage requirements.

The data in Fig. 48 illustrate how the system can deliver peak power to the electric load as needed. When the transient handler state-of-charge dips below 20% the fuel cell starts charging it, whenever there is excess power available.

Fig. 47. Integrated power test bed.
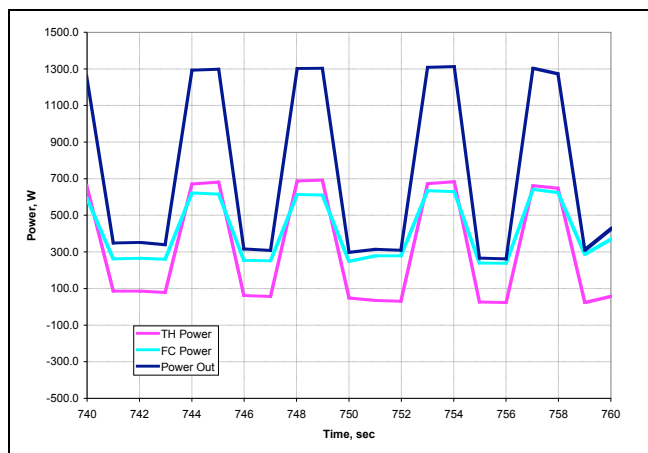
Fig. 48. Power testbed experimental data.
(Fuel cell and transient handler delivering
1.3 kW pulsed power.)

48

Figure 49 shows the power electronics module that is responsible for regulating the output of the energy storage system and controlling the state of charge for the transient handler. Figure 50 is a picture of the system controller. Figure 51 shows the hydrogen generation module, which consists of a catalytic reactor, developed at ORNL, a spent solution chamber and a fresh solution chamber. A small pump pushes fresh $NaBH_4$ solution (<17% $NaBH_4$ in water) through the catalytic reactor. Hydrogen produced is cooled off to stack temperature and fed to the fuel cell. Hydrogen pressure drops prompt new solution to be pumped into the catalytic reactor. The spent solution accumulates in a reservoir, also used as a phase separator, and prevents liquid from entering the fuel cell stack. A fine mesh filter is also used to make sure that the produced hydrogen does not carry any small liquid particles into the fuel cell stack. An off-the-shelf compressor provides air needed for fuel cell operation. The Battery System Controller (BSC) controls its speed, proportional to the fuel cell stack current, and fuel cell stack temperature. Three fan speeds are used, to conserve energy.
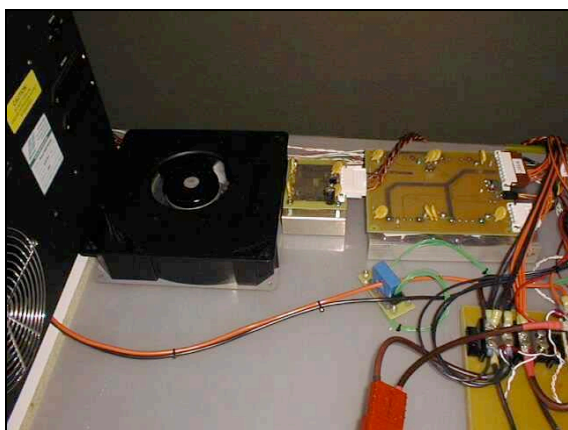
Fig. 49. Power electronics module.
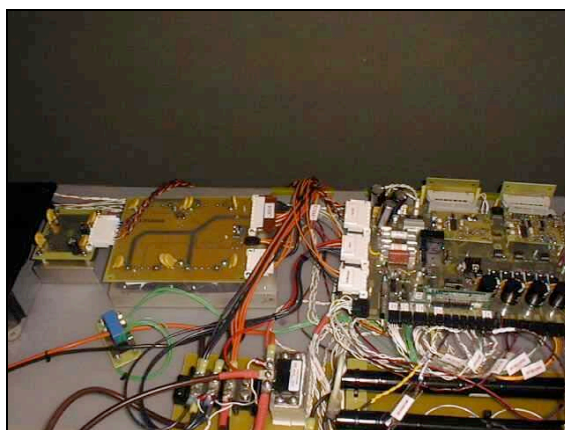
Fig. 50. Power system controller module.

Fig. 51. Hydrogen generation module.

Figure 52 shows the fuel cell stack module with a data acquisition system that measures cell voltage in the stack. The system consists of five FC-SG modules, of 12 channels each. The modules are connected to the system controller via a fast serial bus. The data acquisition system was useful during testing but may not be needed when it is fully developed. Figure 53 shows the

transient handler module, instrumented with voltage and temperature measurement. It is monitored and controlled by the BSC with an elaborate algorithm that inputs temperature, Ah depletion/addition, and average cell voltage.
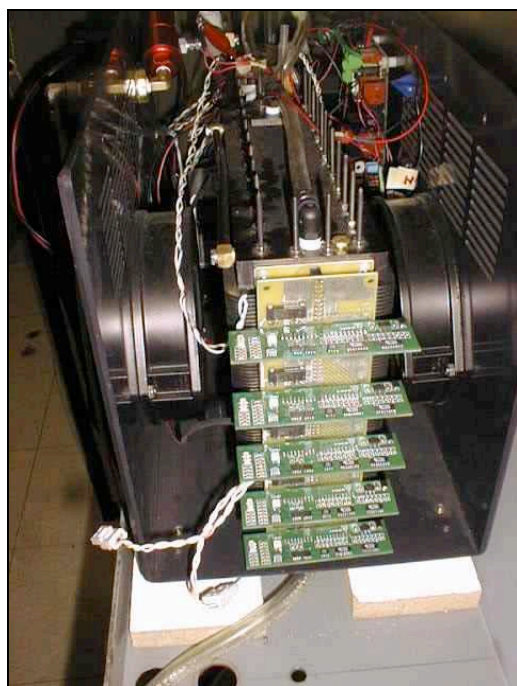
Fig. 52. Fuel cell module.
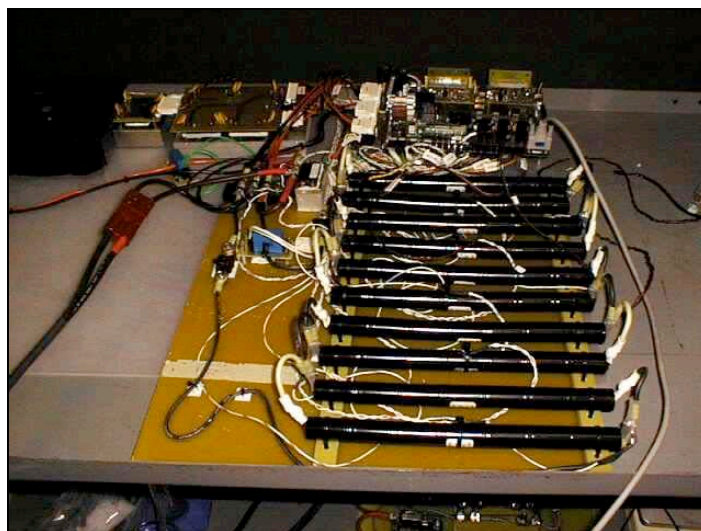
Fig. 53. Transient handler module.

HYDROGEN SOURCE

Mobile and portable power systems, such as required for this application, require high-density energy sources to operate efficiently. One option for achieving this efficiency is to store hydrogen in a hydrolysable compound, couple the hydrolysis reaction with a fuel cell, and recycle excess hydrolysis water and fuel cell product water to the hydrolysis reaction. To maximize net energy production, it is necessary for the reaction to occur exothermically. Selection of hydrides with low molecular-weight, high valence cations are essential to maximize the weight and mole fractions of hydrogen in the feed to the hydrolysis reactor. Reaction systems with fast kinetics are preferable since they facilitate hydrogen generation that is responsive to changes in power demand. Finally, use of a stable hydride that undergoes hydrolysis only in the presence of a catalyst is beneficial from safety and controllability standpoints.

Sodium borohydride was discovered in the 1940s and was first investigated as a portable source of hydrogen for balloons by the U.S. Army Signal Corps (Beatty, 1944; Schlesinger, 1944). The compound has also been investigated as a propellant for rocket engines by various researchers (Beatty, 1944). At present, $NaBH_4$ is used primarily as a reductant in the synthesis of organic chemical compounds and as a bleaching agent in the manufacture of paper.

Sodium borohydride reacts spontaneously with water to generate hydrogen according to the reaction

$$\text{H}_2 \text{ Generation:} \quad \text{NaBH}_4 + 2\text{H}_2\text{O} + x\text{H}_2\text{0} \quad \rightarrow \quad 4\text{H}_2 + \text{NaBO}_2 + x\text{H}_2\text{O} \qquad (1)$$

The overall reaction occurs at a moderate rate initially, quickly slows, and then ceases as the concentration of the basic borate ion in the aqueous product solution increases. Researchers have determined that the duration of the reaction can be increased by the addition of acid to the system to counter the base effect of the borate ion (Schlesinger, 1953). The rate of the reaction and the extent to which the reactants are converted to products can be increased significantly in the presence of catalysts. Specific catalysts that have been investigated include various metal chlorides, noble metals, and precipitates that are formed when metal chlorides are reacted with sodium borohydride solutions (Levy et al., 1960; Kaufman and Sen, 1985; Brown and Brown, 1962). Ruthenium has been found to be the most effective catalyst for promoting hydrogen generation (Brown and Brown, 1962). In our previous work, we confirmed that the hydrolysis of NaBH_4 in aqueous solution is initiated quickly under ambient conditions and proceeds to 100% conversion when the reaction is catalyzed by activated ruthenium. We also determined that the reaction ceases quickly when reactants and catalyst are separated, or when reactant flow through a packed catalyst chamber is terminated, which is extremely important for controllability.

At present, all proposed applications of NaBH_4-based hydrogen generation have been based on reactions using aqueous feed solutions. Because of the limited solubility of the reaction product salt, sodium metaborate, the concentration of NaBH_4 in the aqueous solution is limited to approximately 30!wt!%. As indicated by the stoichiometry in Eq.!(1), the hydrolysis reaction derives half of the product hydrogen from solution water, effectively doubling the storage density of the hydride. Consequently, the effective weight percentage of hydrogen in the feed solution is limited to 6.4!wt!%. In addition, a basic compound (e.g., sodium hydroxide) must be added to the reagent solution to suppress uncatalyzed hydrolysis in the stored reactor feed to prevent loss of hydrogen. The suppressant fraction added to the feed solution replaces part of the water fraction, thereby impacting the solubility of the reaction product and forcing a reduction in the concentration of NaBH_4 solution in the feed. As a result, the practical hydrogen concentration in the borohydride solution is limited to about 4!wt!%.

The catalyzed hydrolysis of NaBH_4 is sufficiently exothermic to vaporize most of the excess water in the feed solution. Vaporization of excess water facilitates its separation from the NaBO_2 waste exiting the reaction chamber. Coupled with the fact that a fuel cell produces water as a by-product, Eq.!(2), it is theoretically possible to continuously segregate and recycle the water in a NaBH_4/fuel cell system. In fact, since for every mole of water consumed in the hydrolysis reaction, the reaction at the fuel cell produces 2 moles of water, the system is a potential net generator of water.

$$\text{Fuel Cell:} \quad 4\text{H}_2 + 2\text{O}_2 \quad \rightarrow \quad 4\text{H}_2\text{O} \qquad (2)$$

Water recycling eliminates the need for on-board storage of any significant volume of water, since solid NaBH_4 reactant can be dissolved on demand into a small volume of water that is continuously replenished during system operation. Consequently, the effective hydrogen storage

density of the fuel is 21 wt % : one half of which comes from $NaBH_4$ and half from the recycled water. With water recycling and the resulting elimination of significant aqueous $NaBH_4$ solution storage, the addition of a suppressant to prevent uncatalyzed hydrolysis is minimized or eliminated.

As discussed previously, there are two potential sources of water, the fuel cell and the hydrogen generation process itself (Eqs. (1) and (2)). The percentage of the available water that must be recovered for full water recycling (i.e., no external water added, dry $NaBH_4$ used) is shown in Fig. 54. The minimum line represents the best-case scenario, which will be discussed in greater detail in the next section. It can be seen that based on the minimum line, and with a 25% $NaBH_4$ solution, ~80% of the available water must be recovered for full water recycling. A series of experiments were set up and conducted for the purpose of evaluating and demonstrating the feasibility of water recycling. Both the recovery of water from the fuel cell and the hydrogen generation were addressed in these experiments.
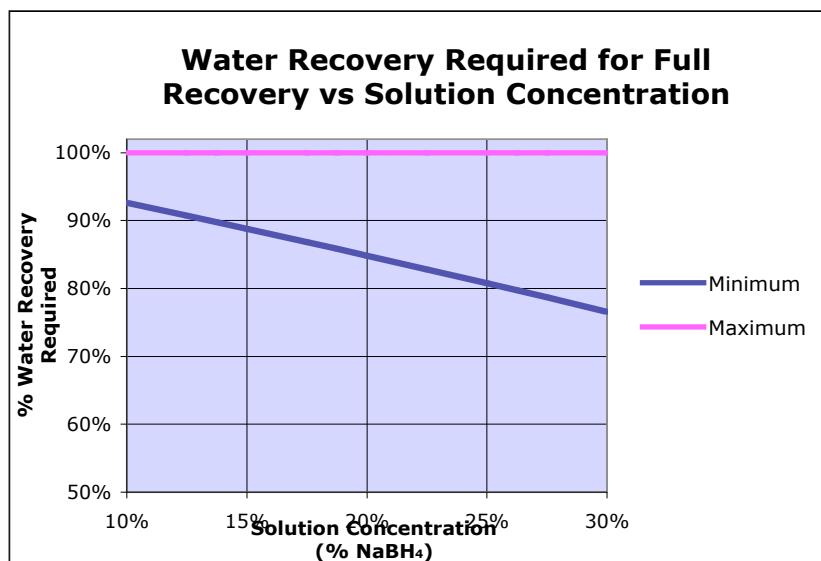
Fig. 54. Water recovery versus concentration.

Fuel Cell Water Recovery

As was seen in Eq. (2), for every molecule of H_2 used by the fuel cell, one molecule of H_2O is generated. Capturing this water provides the opportunity to replace the water consumed in the hydrogen generation reaction (Eq. (1) and potentially to make the system a net water generator. To test how much water could be recovered from the fuel cell an experiment was set up according to Fig. 55. Bottled hydrogen was fed to a commercial fuel cell rated at 500 W that was connected to a simulated load. The output from the fuel cell drain was collected and measured.

Based on these measurements, >80% of the available water was collected. As discussed above, the quantity of water needed for full water recycling with a 25 wt % feed solution is 80%. Based on this simple lab bench test, the recovery of water from the fuel cell is consistent with this target.
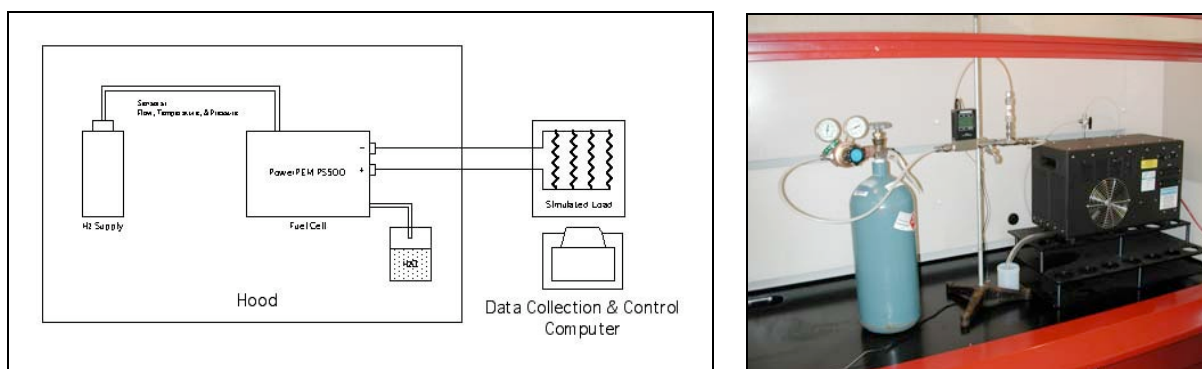
Fig. 55. Fuel cell water recovery test setup.

H_2 Generation Water Recovery

For a 25 wt% $NaBH_4$ solution, there is a total of 6.3 molecules of water per molecule $NaBH_4$. Two of those molecules are consumed in the hydrolysis reaction (Eq. 2), leaving a maximum of 4.3 available for recovery. If all the water was vaporized in the reaction leaving the sodium borate by-product as a solid, plugging of the reaction chamber would obviously occur. Therefore, while it is desirable to recover as much water as possible, it is not possible to recover all of the available water without plugging the reactor. Preliminary testing led to focusing on the form of the sodium borate by-product in order to strike an appropriate balance between recovering as much water as possible and maintaining flow through the reactor.

The form of the by-product that is produced is one of the key issues in obtaining full water recycling. As can be seen from Fig. 56, sodium borate is more hygroscopic at lower temperatures. Operating above 103°C provides the opportunity to generate sodium meta-borate hemi-hydrate ($NaBO_2 \cdot 0.5H_2O$) with only one half molecule of water per molecule of sodium borate as opposed to two or four molecules at lower temperatures. This enhances the ability to recover the higher percentage of water needed for full water recycling. The boiling temperature of the sodium meta-borate hemi-hydrate is 120.2°C. Operating above this temperature while releasing more water vapor will increase the likelihood of plugging.
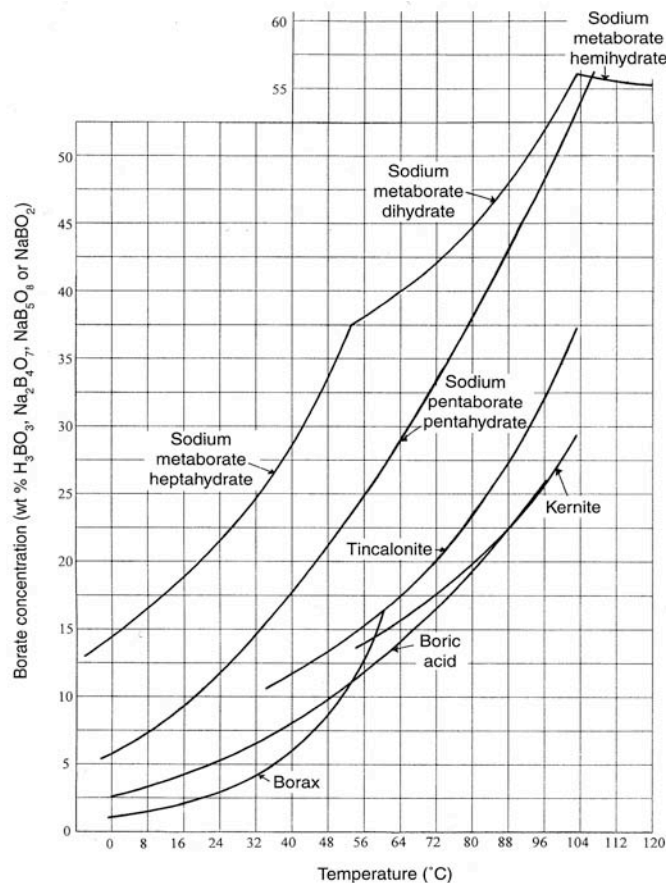
Fig. 56. Solubility of boric acid and several sodium borates.[15]

One of the testing setups for measuring the amount of water that could be recovered from the hydrogen generation reaction is shown in Fig.!57. (Later testing used different vessels that were smaller and much better with respect to leaks, as well as a different reactor design.) The test setup consisted of a hydrogen generator, feed pump, vessels to catch the reaction by-product, a heat exchanger to condense the water vapor, and a vessel to catch the condensate. The generated H_2 was vented into the hood.
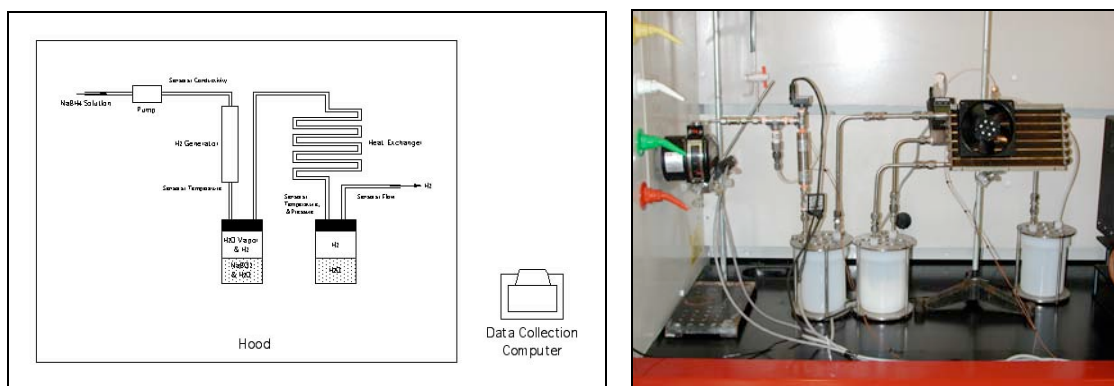
Fig. 57. H_2 generation water recovery test setup.

54

Water recovery test results are listed in Table 4. Two different generator configurations (Fig.!58) were tested along with a glass generator (Fig.!59) for visualization purposes. In addition, tests were conducted with and without preheating. As the tests were of relatively short duration (on the order of 20 minutes), a relatively large percentage of the total test time (~25%) was spent reaching thermal equilibrium. During this transition, the temperature was insufficient to vaporize the excess water, thus limiting the amount of water available for recovery. Tests were also conducted where the system was preheated to the equilibrium temperature to simulate longer duration steady state operation. The results with no pre-heat, where the time spent reaching equilibrium was a high percentage of the overall test time provides more of a worst-case scenario. The results of these tests are encouraging and indicate that full water recycling (i.e., addition of no external water) is feasible. Figure!60 shows the results plotted with the theoretical amount of water recovery needed versus solution concentration.

Table 4. Hydrogen generation water recovery data

Test	Generator	Preheat	Concentration	H_2O Recovered
1	Can	No	23.1%	76.5%
2	Cylinder	No	22.9%	65.8%
3	Cylinder	No	22.9%	70.2%
4	Cylinder	230 °F	20.0%	86.8%
5	Cylinder	230 °F	20.0%	96.1%

Fig. 58. ORNL H_2 generators.
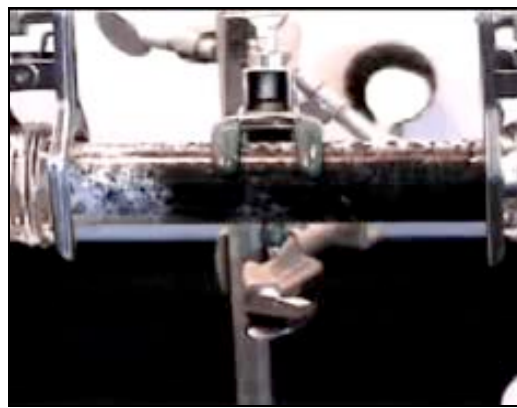
Fig. 59. H_2 generation in glass generator.
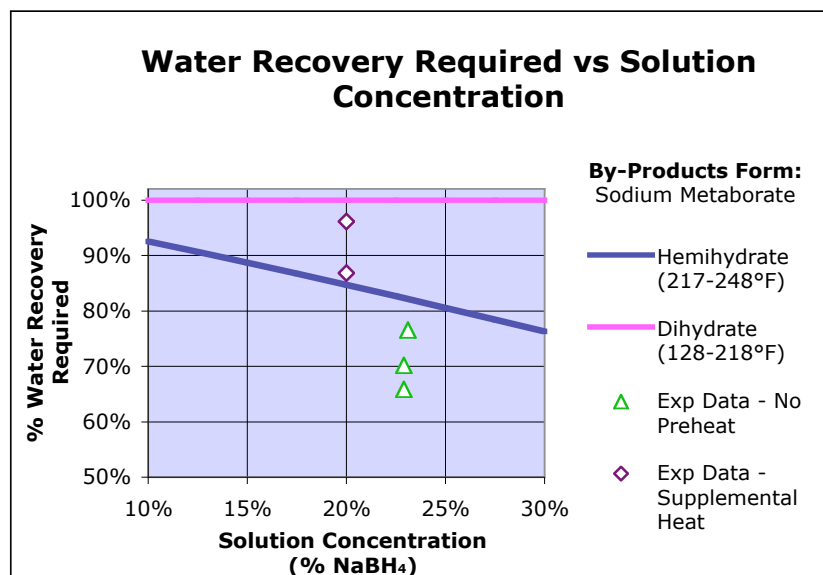
Fig. 60. Test data and water recovery versus concentration.

Other H$_2$ System Testing

In addition to the water recycle testing, testing was conducted to develop understanding on a few key areas relative to implementing a full system. These tests focused on determining how fast sodium borohydride could be expected to dissolve, how much hydrogen would be lost through off-gassing, and how fast the hydrolysis reaction takes place.

Dissolution Rates

There are several parameters that affect the dissolution rates, including the concentration of sodium borohydride, the concentration of sodium hydroxide, and the temperature. The solubility of NaBH4 is shown in Fig.!61. Below 36.4°C represents the solubility of the dihydrate form and above 36.4°C the anhydrous form.

A series of measurements were taken to study parameters affecting the rate at which sodium borohydride can be put into solution and are shown in Fig!62. For the solutions containing sodium hydroxide, the sodium hydroxide was dissolved prior to the addition of the sodium borohydride. As anticipated, higher concentrations of sodium borohydride and the presence of sodium hydroxide both slowed the dissolution. It is also evident that as the temperature approaches 150°F the rates of dissolution converge.
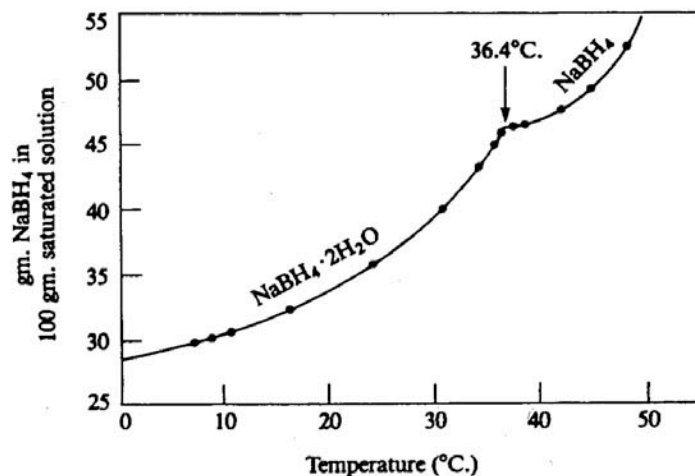
Fig. 61. Solubility of NaBH$_4$ vs temperature.[38]
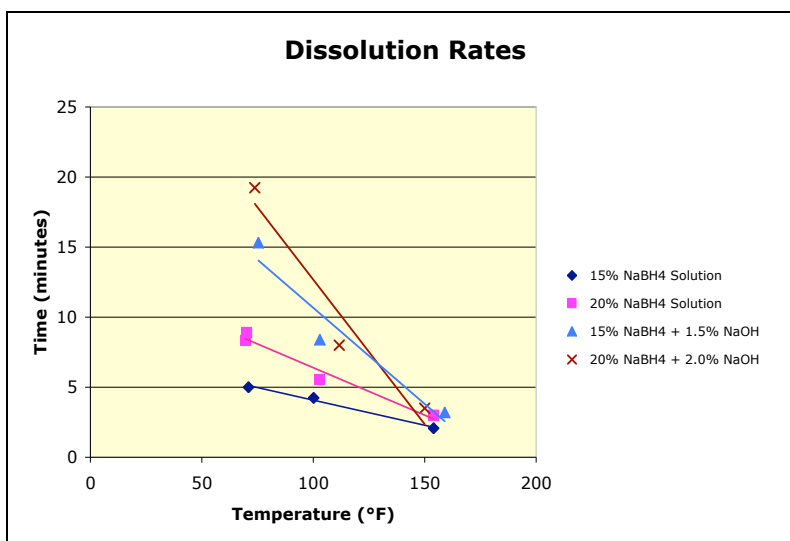
Fig. 62. Dissolution rates of NaBH$_4$.

Reaction Rates

Scoping tests were performed to evaluate the effects of Ru catalyst concentration and NaBH$_4$ feed concentration on the rate of hydrogen generation by NaBH$_4$ hydrolysis. The objective of the test was to determine if the rate of hydrogen generation is limited by the availability of hydrolysis sites on the catalyst or by the rate of diffusion of reactant to these reaction sites. The intent was to determine if operating hydrolysis systems using higher catalyst loadings was an effective means of increasing the hydrogen generation rate. The presumption is that, if the rate of hydrogen release is higher at higher catalyst Ru loadings but is not affected by reactant concentration, the rate of hydrogen generation is limited by the reaction at the catalyst surface. Conversely, if H$_2$ generation increases with increasing reactant concentration in the feed solution but is unaffected by Ru loading, the rate is controlled by the rate of diffusion of the reactant to the catalyst surface.

57

Tests were performed under three sets of conditions. In the first test, the Ru loading on the carbon substrate was 1% (w/w) and the NaBH$_4$ concentration in the feed solution was 20%!(w/w). In the second test, the Ru loading was 2% (w/w) and the feed solution NaBH$_4$ concentration was 20%!(w/w). In the third test, the Ru catalyst loading was 1%!(w/w) and the NaBH$_4$ concentration in the feed solution was 25%!(w/w). NaOH was added to the feed solution used in all tests to a concentration of 1%!(w/w) to suppress uncatalyzed hydrolysis. The system was not preheated, and no attempt was made to control the temperature of the experimental system during testing.

The test configuration used is shown in Fig. 63. In each test the feed solution was added to a stirred vessel containing catalyst chips. In each test the mass of catalyst present in the reactor was 0.5!g. At the start of each test, 20 ml of feed solution were introduced to the reaction chamber through a valved feed tube. The feed tube was valved closed immediately after the solution was delivered. The solution and catalyst were agitated continuously using a magnetically-driven stirring bar. The volume of gas evolved was measured in terms of the volume of water displaced from a tank that was connected to the reactor outlet.

The results of the test are presented in Fig.!64. Under each test condition the rate of gas generation increased after an initially slow rate of evolution. The low initial rate reflects two aspects of the test system. First, an amount of gas had to be generated initially in order to pressurize the system enough for water to be displaced and collected. Second, the rate of the reaction increased after initiation as the temperature of system increased due to the exothermic nature of the reaction.
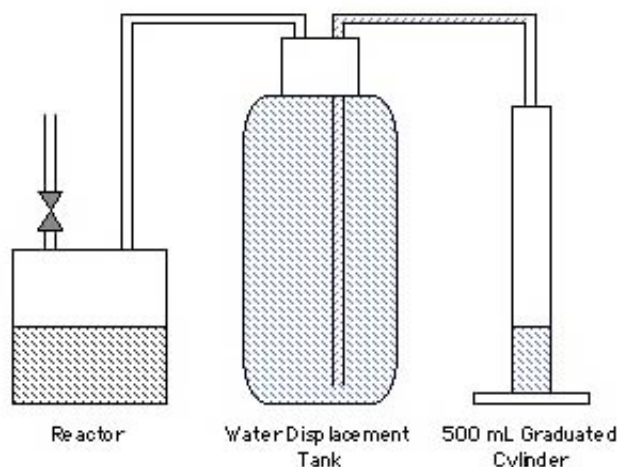
Fig. 63. Experiment configuration.

Significant differences are apparent in the rate of hydrogen generation as a function of catalyst loading. At the 1% Ru, 20% NaBH$_4$ condition the maximum rate of generation was approximately 1 L/min, occurring between 13 and 14 minutes after feed introduction. At the 2%!Ru, 20% NaBH$_4$ condition the maximum rate is approximately 2!L/min, occurring between 10 and 11 minutes after introduction of feed. Other than a slight offset, little difference is apparent in results obtained at different feed concentrations when the catalyst loading was unchanged.

The results of the test indicate that the hydrolysis rate is affected by the loading of the catalyst. Since the same mass of catalyst was used in all three tests, and since the substrate surface areas should be approximately equal, it is also apparent that the substrate surface is not completely occupied by Ru at the lower (1%) loading, and that increased loadings are needed to optimize the reaction rate.
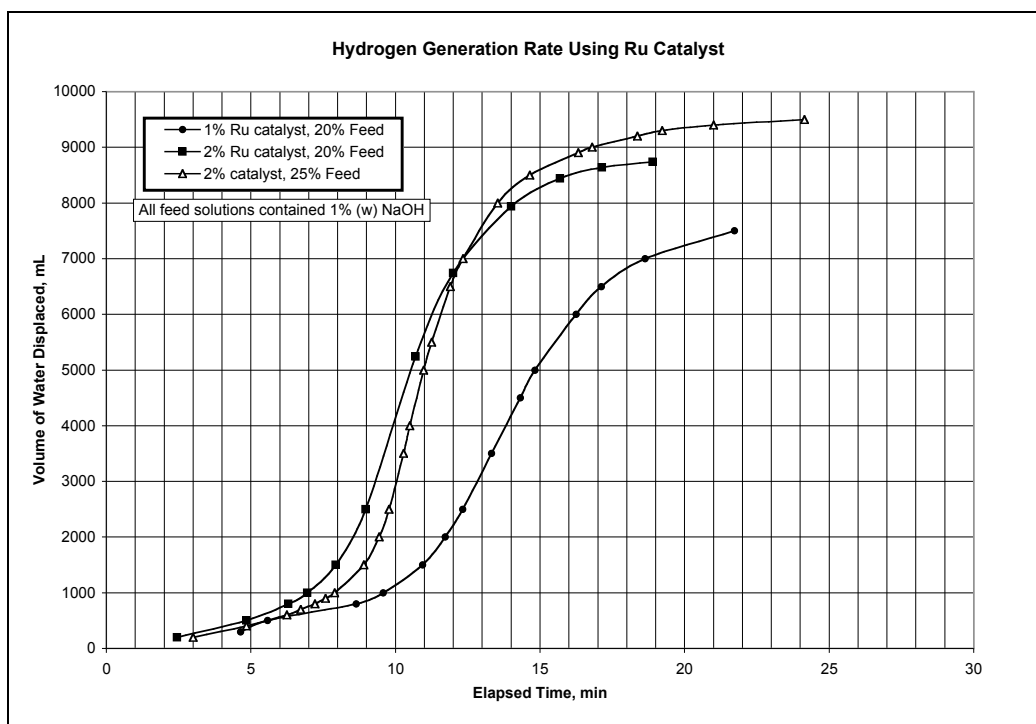
Fig. 64. Hydrogen generation reaction rates using ruthenium catalyst.

Off-Gassing

Spontaneous hydrolysis of sodium borohydride solution occurs over time, with the rate dependent on concentration, pH, and temperature. The hydrolysis in water causes a rise in the pH, decreasing the rate of decomposition. Typically sodium hydroxide is added to increase the pH and slow the hydrolysis. The rate of decomposition can be estimated by:

$$\log_{10} t_{1/2(min)} = pH - (0.034T - 1.92) \tag{3}$$

where $t_{1/2}$ is the half-life in minutes and T is temperature (°K) (Morton International, Inc., 1995).

The dependence of hydrolysis upon various parameters is depicted in the figures below. Figure!65 illustrates the effects of pH on hydrolysis over time. The higher concentrations of sodium hydroxide slow the spontaneous hydrolysis process. The effect of increased solution temperature is shown in Fig.!66. As can be seen, the increased solution temperature results in increased spontaneous hydrolysis. The effects of temperature and the suppression of the reaction with increased pH are also illustrated in Fig.!67.
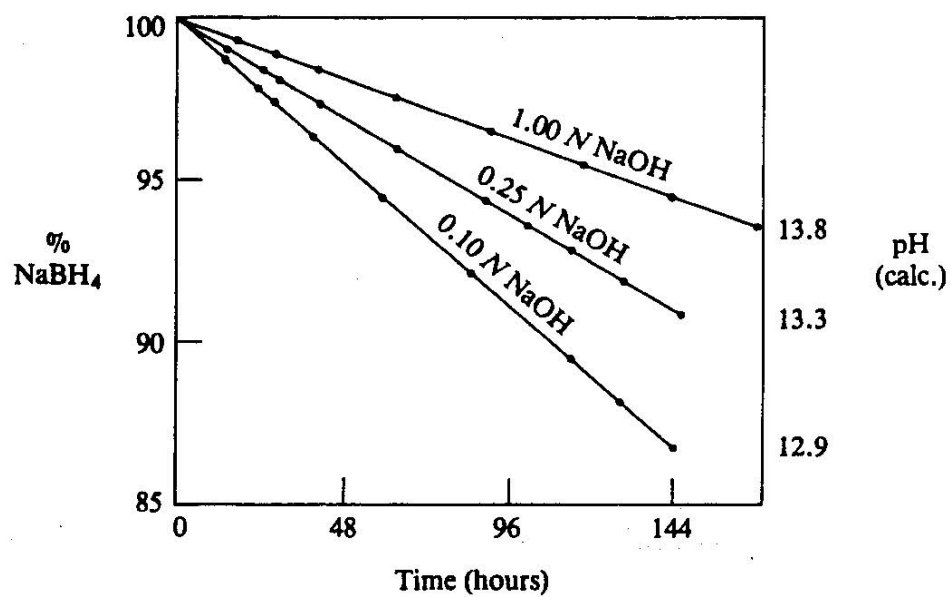
Fig. 65. Stability of NaBH₄ vs pH.[38]
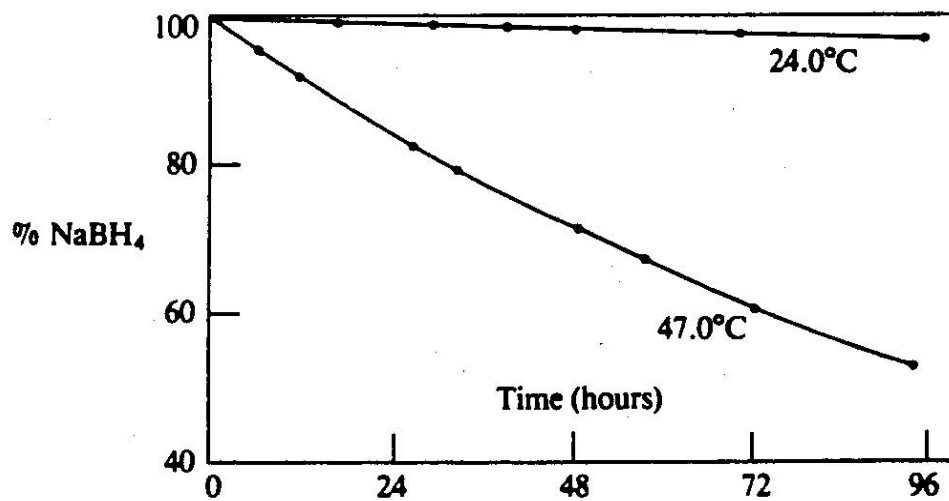
Fig. 66. Stability of NaBH4 solution vs time at different temperatures.[38]
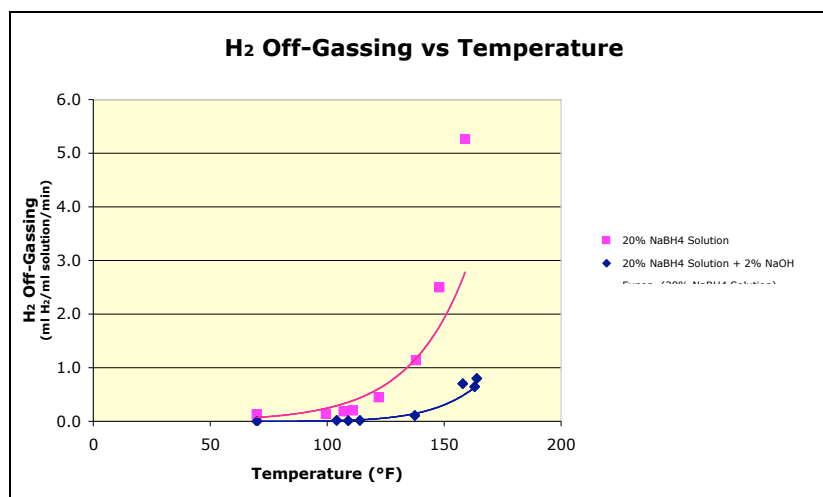
Fig. 67. Hydrogen off-gassing from NaBH₄ solution.

How does this spontaneous hydrolysis affect the design of a hydrogen source for a fuel cell? If solution is to be stored for any appreciable period of time, obviously the solution must be stabilized by the addition of sodium hydroxide. However, a system based on water recycling that mixes the solution and consumes it in a relatively short period of time could avoid having to add the sodium hydroxide, thus simplifying the process and potentially enhancing recycling of the reaction by-products.

POWER SOURCE SUMMARY

This effort successfully demonstrated that a fuel cell hybrid power supply can be a viable option for supplying the power and energy needs of an exoskeleton. In addition, it was shown that the hybrid power supply system is intrinsically safe, and can be operated from hydrogen created on demand by a package of sodium borohydride. The fuel cell was able to deliver power in a pulsed mode, even when operated with an air compressor and hydrogen generated from a chemical hydride.

The next step in refining this system would be to find the lightest, most efficient system components available. There is significant room for size reduction, increased efficiency and simplified operation. The system can be packaged with different form factors.

Fine tuning is needed for the power sharing algorithm and to keep the fuel cell operating at close to full power whenever needed in order to extend the availability of the transient handler. In addition, there is a need for additional work to enhance the stability of the sodium borohydride solution and the pump used to feed the catalytic reactor. In order to increase the specific energy, the design should include a system for fuel cell product water recovery, with the capability to store the sodium borohydride in a dry form and mix it with the product water from the fuel cell, as needed.

A series of experiments were conducted to test the validity of recycling water concept. Tests were conducted to determine the feasibility of recovering water from the fuel cell and the hydrogen generation. Results showed that water recovery is indeed feasible, therefore

demonstrating the potential to increase the hydrogen storage content from ~4!wt!% up to as high as 21!wt% (for full water recovery). An initial system configuration has been conceived (Fig.!68).

The hybrid fuel cell system built and tested has potential for many other uses. For example, with slight modifications the control system could be a component for other projects with similar architecture but in a range of power ratings up to 100 kW.
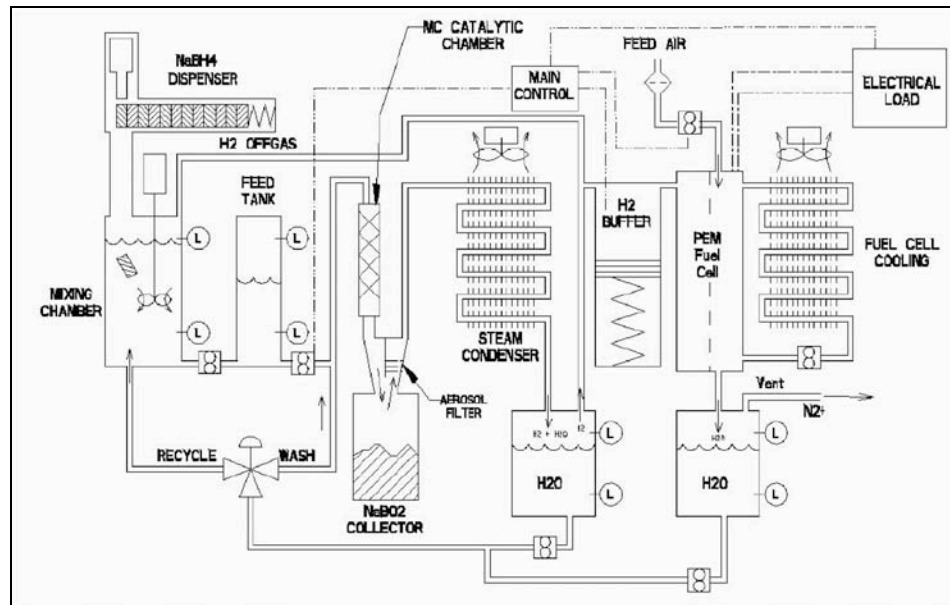
Fig. 68. Hydrogen generation and fuel cell system block diagram (with water recycling).

ACTUATION

BACKGROUND[†††]

As a part of a feasibility study for exoskeleton (Jansen et al., 2000) various types of actuator technologies, subject to their relevance to the exoskeleton project were investigated. A comparison of potential relevant technologies was performed. A designer must make decisions based on critical design parameters such as (1)!power/mass, (2)!power/volume, (3)!stress, (4)!strain, (5)!steady-state efficiency, (6)!power expended during load holding, (7)!bandwidth or tracking performance, (8)!auxiliary transmission system, (9)!auxiliary power modulation equipment, and (10)!ease of controllability. Depending on the type of actuator, some of the critical design parameters will not be applicable or not available due to design specificity. Actuator technologies can be broken down into two major groups: conventional and non-conventional. Conventional actuators are electric motors, hydraulic, and pneumatic. The non-conventional actuators are the piezoelectric and magnetorestrictive. While others have examined these types of actuators in the past, their relevance to the exoskeleton project is the main consideration here.

Of the conventional actuators (Table 5), it appears that hydraulics is the best candidate for an exoskeleton application. The power-to-weight and power-to-volume ratios of hydraulics typically exceed the ratios for electromagnetic actuation by factors of 10 and 5 respectively. The closed-loop bandwidth of pneumatics is typically 5 to 6 times less than that for hydraulics, thus limiting the ability to track at 2 Hz. Based on packaging and the ability to track the human, hydraulics is the preferred conventional actuator.

Table 5. Comparison of conventional actuators

Item	Electromagnetic Actuators	Hydraulic Actuators	Pneumatic Actuators
Bandwidth	Transmission required. Motors sized 10 to 20% larger due to transmission efficiencies.	High performance servos in the 50 to 100 Hz range. Dependent on actuator and controller design.	5 to 6 x less than hydraulics.
Power to Weight	Approximately 1/10 hydraulics ratio.	Excellent.	Elastic type actuators are similar to hydraulics. Hard-shell type actuators are similar to electric actuators.
Power to Volume	Approximately 1/5 hydraulics ratio.	Excellent.	Elastic type actuators are similar to hydraulics. Hard-shell type actuators are similar to electric actuators.
Packaging	Transmission increases vol by 20-50%. Power electronics can exceed size of actuator.	No transmission. Power electronics are inconsequential. Sound proofing pumps difficult.	Similar to hydraulics.
Load Holding	5-10% or rated power required.	No power for linear actuators with asymetrical cylinders. 1 to 10% for symetrical cylinders and rotary actuators.	Similar to hydraulics.

[†††] Appendix F provides additional background details regarding the basis of the approach taken (Jansen et al., 2000).

However, there are issues concerning the use of hydraulics, which must be taken into account. First, the power loss at the servo valves associated with flow control is significant and has a serious impact on the overall power supply sizing. Second, noise is a serious problem associated with hydraulics that can be difficult to mitigate due to the large acoustical wavelengths.

While none of the nonconventional materials have reached the level of maturity achieved with hydraulics, both the piezoelectric and the magnetostrictive materials hold great promise and should be investigated further. In particular, a piezoelectric pump was shown to have the potential for power densities approaching those of hydraulics, as well as high steady-state efficiency, and no wasted power holding a load. The magnetostrictive actuators are similar to piezoelectric actuators, but with lower anticipated efficiencies and load holding capability similar to that of electric motors. Power electronics is an issue for both that is the subject of ongoing research.

At the start of the exoskeleton program, two approaches were proposed by ORNL to address the compact actuator needs of this initiative that could meet the requirements of receiving electrical energy and convert it to mechanical energy through a hydraulic fluid medium. The first was a high-risk, high-payoff path based on utilizing piezoelectric materials as the primary pumping source to control the motion of the associated hydraulic actuators. The second approach was a less risky, but with lower potential performance, based on utilizing high-speed electric motors turning a miniature hydraulic pump which in turn feeds conventional hydraulic actuators. Work on the piezoelectric based actuators will be the main focus of this section; however, at the end of this section there will be a discussion of the progress of the second approach.

PIEZOELECTRIC ACTUATOR APPROACH

Piezoelectric material can convert electrical energy to hydraulic energy and act as a flow control device similar to a hydrostatic pump. Further, the power-to-weight and power-to-volume ratios of this device can be shown to be potentially superior to current methods of placing an electric motor in tandem with a hydraulic pump in tandem with a flow control valve. Presently, lead zirconate titanate (PZT) ceramics are the materials of choice for piezoelectric ceramic actuators. These materials have piezoelectric coefficients d_{33}, around 200 to 750×10^{-12} m/V, and strain levels from 0.05 to 0.1%. However, there is a new family of piezoelectric material that has the potential to change future piezoelectric actuators. One type, a single crystal form of relaxor-based ferroelectric materials, lead zirconate niobate / lead titanate (PZN-PT), has been observed to have piezoelectric coefficients d_{33}, around 2000×10^{-12} m/V, and strain levels from 0.5% to 1.0%, an order of magnitude greater than conventional PZT material. While these materials have been known for several years, their potential for high performance actuators has only recently been recognized. Large forces and small displacements occur in a piezoelectric crystal when an electric field is applied and is the major limitation for their utilization. Compressive stress levels can be as high as 35 MPa (5000 psi), whereas the tensile stress levels can be only 5 to 10% of the compressive stress level. Typically, a mechanical force bias is required to avoid the tensile stress limits. Displacements are typically very small for piezoelectric materials. One difficulty of using piezoelectric material pertains to converting small displacements to large motion (i.e., the transmission problem). Various approaches include the "inch-worm," where micro-stepping

action through rapid lock-and-move sort of motion are used to create a large linear motion. Another concept is that of a piezoelectric hydraulic pump, where small quantities of fluid move at very high frequencies. The accumulation of small drops of fluid at a high rate adds up to a large flow rate. Both of these concepts are based on the idea of the cyclic motion of the piezoelectric material. This latter approach of moving one drop of fluid at a time is the one being taken in this project and has the potential of achieving the radical improvement in motion control for a high-power density actuator. It can be shown that the maximum power per volume of the piezoelectric actuator is directly proportional to the stack operating frequency. At a 1!kHz rate, the power density is approximately 2.7!J/kg per cycle for a single-crystal piezoelectric material, lead zirconate niobate (PZN). Larger energy-storage terms have been reported in the literature, but because of fatigue life limitations (recall that due to the transmission problem, billions of cycles will be required from this material), this reduced value is more reasonable. Power-to-volume for electric motors around the 1!kW level is approximately 1.3!W/cm^3. To obtain a factor of 5 times this value and therefore rival that of hydraulic actuators, the cyclic frequency would have to be around 1!kHz. While the power-to-weight for an electric motor at the 1!kW level is approximately 300!W/kg, the single crystal material would have a power-to-weight about 3 times this value. If one takes into consideration that electric motors are high speed and low torque devices and that some sort of transmission system (which could add up to 50% of additional weight) would be required to connect an electric motor to a hydraulic pump, the power-to-weight value for the piezoelectric materials as compared to an electric motor could easily be 5 times larger.

To attack this problem, two approaches were taken concerning the transmission problem. These two approaches are predominately associated with how the valving of the pumping chamber should be accomplished. While there were other technical concerns pertaining to stack voltage and fluid modulation methodology, valving was the primary demarcation of the two approaches. The first approach was to use very responsive passive valves that allowed fluid into and out of the chamber without significant losses. The second approach was to utilize active valves for the pumping chamber based on piezoelectric actuators. The ORNL focused on the first approach with passive valving and Virginia Polytechnic Institute (VPI) focused on the second approach based on active valving. The target objective, based on early estimates pertaining to the power requirements, was 600!W of mechanical power at an operating pressure of either 1,000 to 2,000!psi.

Passive Valve

ORNL has developed a novel hydraulic pump/actuator test!bed (Fig. 69), building upon the central idea of a distributive passive valving (Fig. 70) scheme to achieve very high frequencies in moving small drops of fluid rapidly in and out of the pumping chamber.

Due to power electronics limitation, the operational frequency of the stack could not exceed 400!Hz. For the final system, frequencies around 1!kHz are required. The following results, which benchmark the performance of ORNL's piezoelectric pump, are linearly scaled to evaluate the overall performance potential of the pump. The first measurement is for no load flow test, where the test fluid is pumped into a fixed volume for 100 seconds. The theoretical and the measured flows are shown in Fig.!71. Approximately 60% volumetric efficiency at frequencies below 300!Hz was achieved. It is apparent from Fig.!71 that significant leakage flows still exist.

Ball check valves on the piston side have significantly reduced the leakage flows from the previous design; however, they have not been placed on the cylinder side of the pump (i.e.,!the outlet valve) due to required modifications of the pumping chamber to support this change. At higher frequencies (around 300!Hz), the results (Fig.!71) suggests that the flappers are not responsive enough. Next, the deadhead pressure was tested by blocking the piston outlet flow. Theoretical pressures should exceed 1000 psi over a much larger frequency band than those shown in Fig. 72 (based on the assumed structural compliance and fluid bulk modulus values).
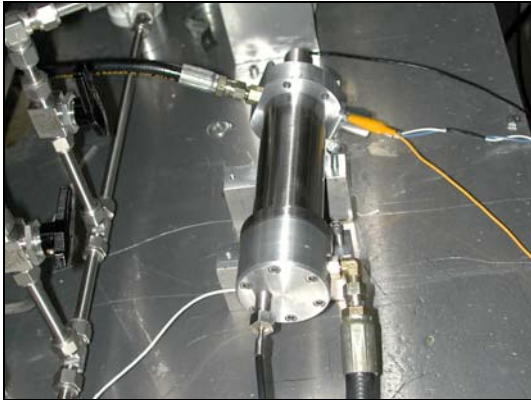
Fig. 69. ORNL's piezoelectric pump.
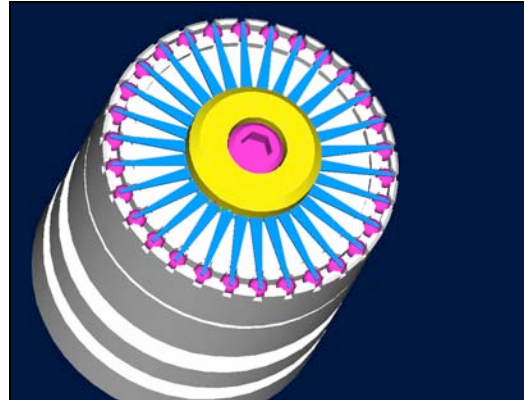
Fig. 70. Distributive valves.
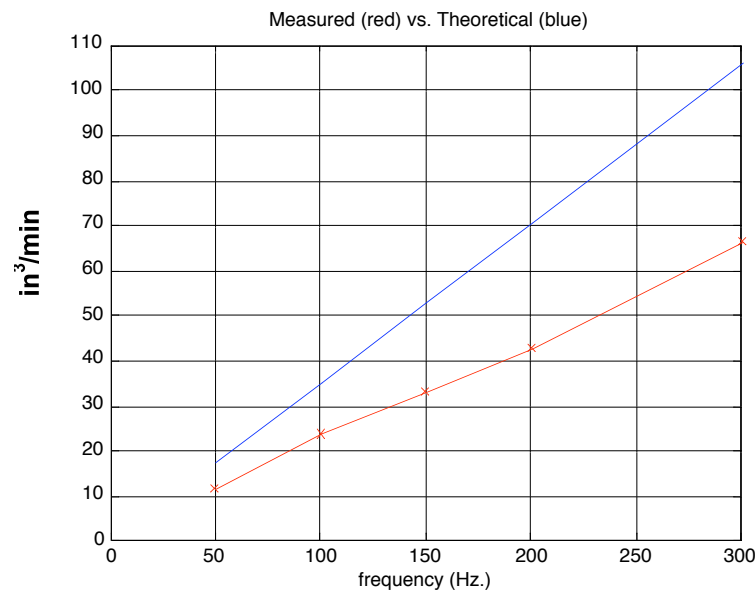
Fig. 71. ORNL piezoelectric pump flow.

66
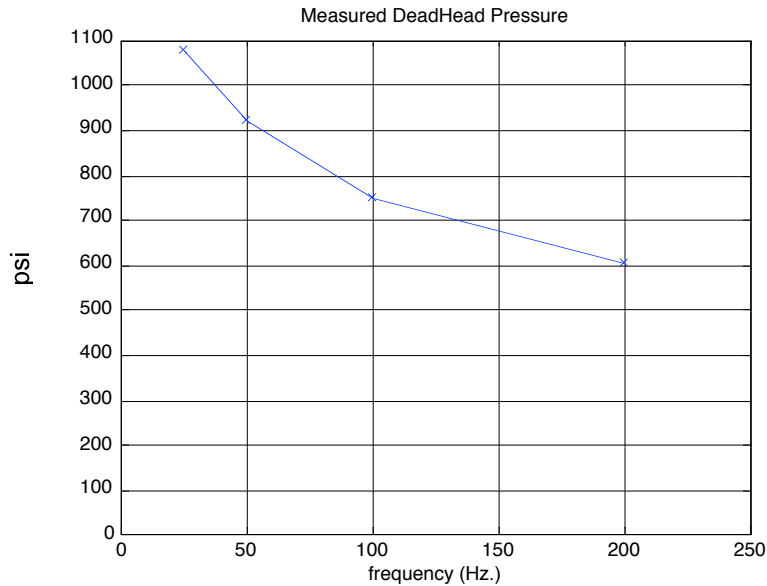
Fig. 72. Deadhead pressure versus stack frequency.

There are two possible explanations for the discrepancies with the theoretical values: leakage and air that has not been properly evacuated or entrained into the working fluid. Again, the ball check valves that we would like to install on the cylinder should eliminate the leakage problem. Finally, the power produced by our pump should be around 200!W at 1!kHz and should scale linearly at lower frequencies. At 300!Hz, the power should be around 67!W. Figure!73 shows the results of a power test we have performed at various stack operating frequencies. This test entailed having the pump move fluid against a constant back pressure. As demonstrated in this figure, we are roughly off by a factor of 4 from the expected value (i.e., roughly 14!W at 300!Hz compared with the theoretical expected 67!W).
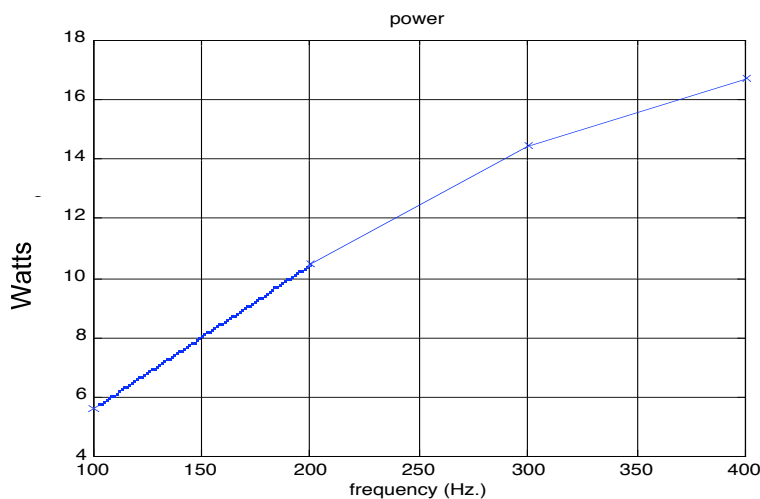
Fig. 73. Power out of the piezoelectric pump.

67

Active Valve

VPI successfully designed, built, and tested a piezo-hydraulic actuator that achieved 3.6!W of mechanical power out. Figures!74 and 75 show the major components and the overall system integration. Further, they developed the system-level models that accurately predicted the performance of the device. Presently, the major system-level limitations were: high current driver requirements for operation in the kHz range which resulted in large drive electronics and viscous losses in the hydraulic circuit and valves limited operating speed of the pump.

Figure 76 shows how velocity varies with both loading and frequency. Studies have demonstrated that the output power was highly dependent on the valve phasing. Power variations of 15-20% were noted by varying the valve phasing about the nominal conditions as can be seen in Fig.!77.

Cylinder velocities of 39!mm/sec were measured under no-load conditions (Fig.!76). Velocities of 10 mm/sec were measured at loads of 22!kg. Maximum output power of 3.6!W was measured at an optimal operating frequency of 140!Hz (see Fig.!77).

For the VPI actuator, the primary limitations to increasing the power output were: viscous losses in the hydraulic circuit limited flow at higher frequencies and decreased power output at frequencies higher than about 140!Hz and kilohertz frequency operation necessitated high current output power supplies and these power supplies proved to be difficult to miniaturize.
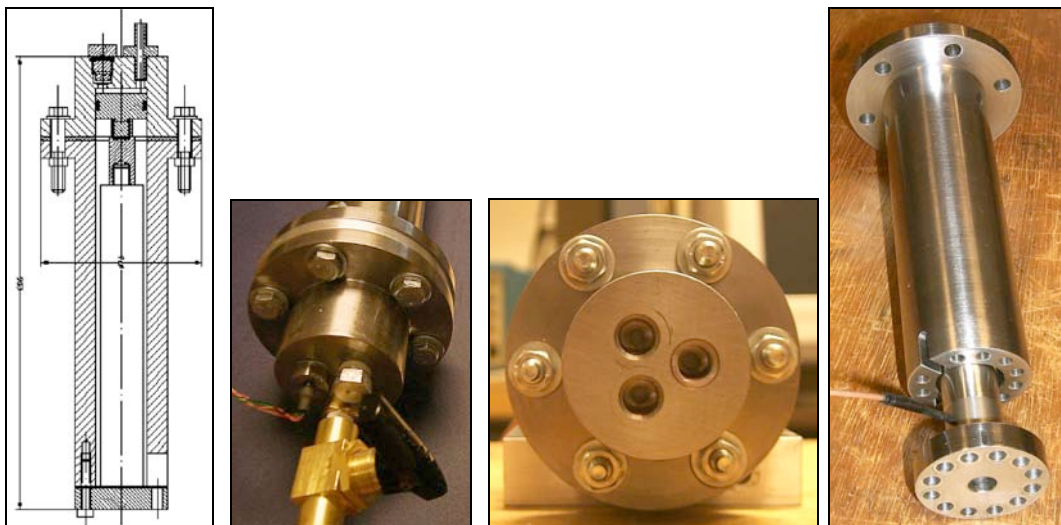
Fig. 74. VPI pump.
(Assembled drawing, assembled pump, chamber outputs, casing.)
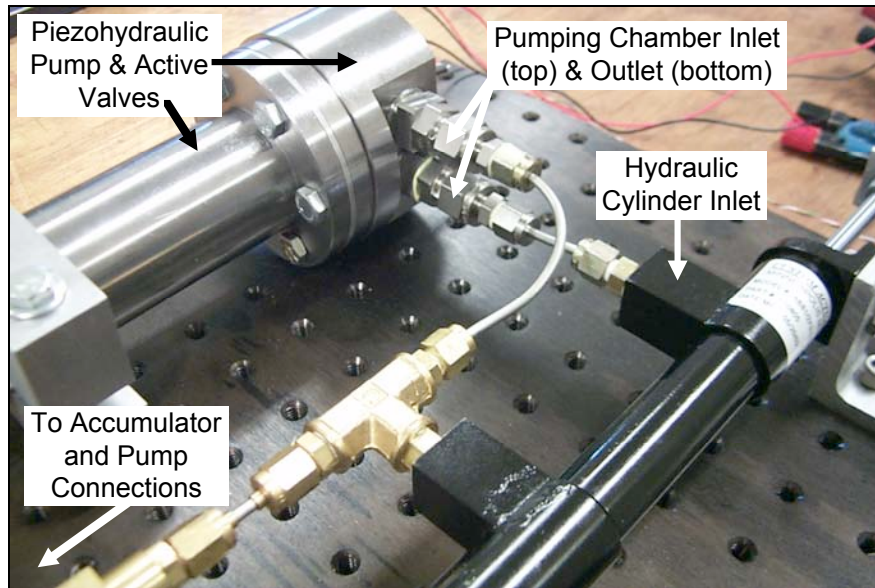
Fig. 75. Integrated system.
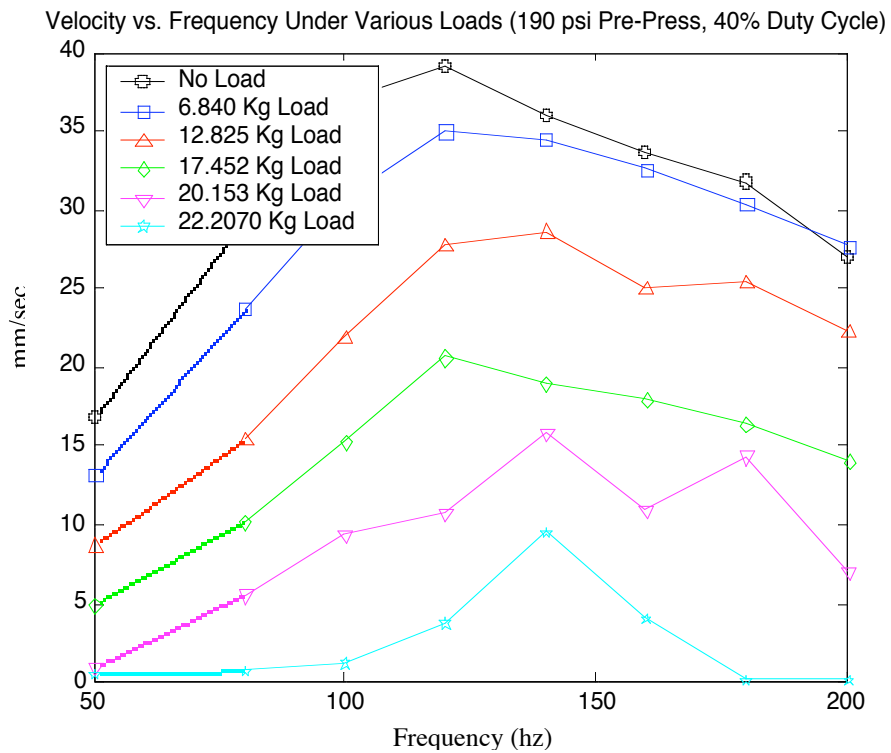
Fig. 76. Velocity vs frequency under various loads.

Power vs. Load at Diff Frequencies (190 psi Pre-Press, 40% Duty Cycle)
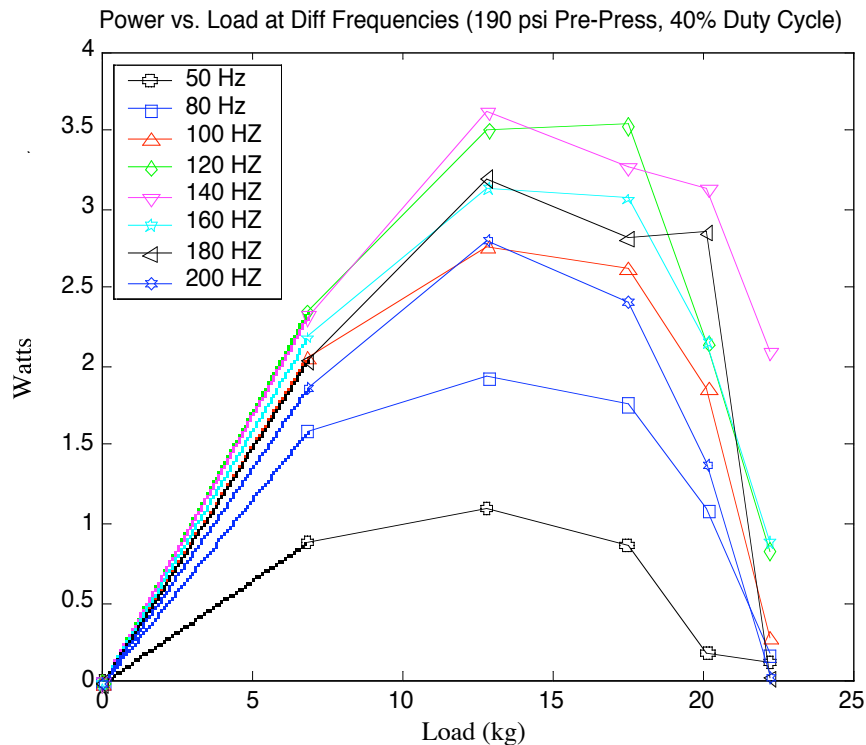
Fig. 77. Power vs load at different frequencies.

Conclusion of Piezoelectric Actuator Initiative

High power densities are theoretically possible only if the piezoelectric stack is driven at high frequencies since the power density is directly proportional to stack frequency. While this approach holds great promise, this technology is currently not going to be available to meet the exoskeleton program needs. A second approach based on a high-performance, high-speed electric motor turning a miniature hydraulic pump will be examined next.

ELECTRIC MOTOR APPROACH

As was previously discussed, ORNL has been investigating two approaches for actuation. The first was a piezoelectric pump scheme that would feed a hydraulic actuator. The second was a high-speed electric motor scheme that drives a miniature hydraulic pump. The piezoelectric pump scheme was based on driving a piezoelectric stack at high frequency allowing fine control of hydraulic fluid (basically a drop at a time). In comparison, the high-speed electric motor/pump is analogically similar to the piezoelectric pump. For the high-speed electric motor/pump, the electric motor turns a miniature hydraulic pump at a high angular velocity allowing fine control of hydraulic fluid. Functionally, the electric motor exerts a very low moment but has a very large displacement. High power densities are possible (and have

been tested) since the electric motor rotor volume is directly proportional to the torque generated. Therefore, power density is roughly proportional to motor speed. For the near term, the high-speed electric motor/pump appears to be most promising and will allow the efficient conversion of electric energy to hydraulic energy.

Without cooling, a frameless brushless electric motor will have a power-to-weight around 300!W/kg. With a well-designed cooling system exploiting the hydraulic fluid as the cooling medium in a heat exchanger, it could be possible to extend the power density up to 3 times these values. With a carefully selected hydraulic pump that is matched to the speed and torque characteristic of the electric motor, a transmission system would be avoided. Preliminary calculations indicate that a small hydraulic pump with 1-2!cc/rev of displacements with high volumetric efficiency would be required. Both the electric motor and the hydraulic pump will be placed inside the reservoir to reduce the overall sound levels and facilitate heat transfer.

Lastly, we will not utilize standard sizing practice for flow control valves (i.e., servo-valves). For hydraulic actuation, servo-valves control the flow by means of large pressure drops across internal orifices, which is analogous to a resistive load for electrical systems. It is not uncommon, due to the size of the servo valves, for up to 33% of the total power transmitted to the load to be lost in the form of heat across these servo valves. Even higher losses are possible in certain loading/flow scenarios. To mitigate losses of the servo valves, servo valves will be rated to operate at significantly lower pressure drops.

To demonstrate the overall size of the components, a computer simulation of ORNL's exoskeleton system was modeled and the hydraulic flows and pressure needs were ascertained for a fast walking scenario of 2.2!m/sec carrying a combined load of 300!lb. The requirements for the hydraulic pump are shown in Figs.!78 to 80. Based on prolonged discussions with a leading aerospace company (Moog,!Inc.), the required hydraulic pump can be built under 2!lb and the electric motor to drive it would be under 4!lb. With an additional 1.5!lb for auxiliary pumping the total weight would be around 7.5!lb.

In summary, by means of operating the electric motor at very high rpm, cooling the electric motor, and allowing lower pressure drop across the fluid control valves, an efficient electrically-driven hydraulic pump can be designed that will both save energy (>30%) and improve power density compared to a conventional constant pressure system. It appears that high-end electric motors, in conjunction with very specialized hydraulic pumps that are now available from industry make it feasible to effectively convert electrical energy from a fuel cell to hydraulic energy.
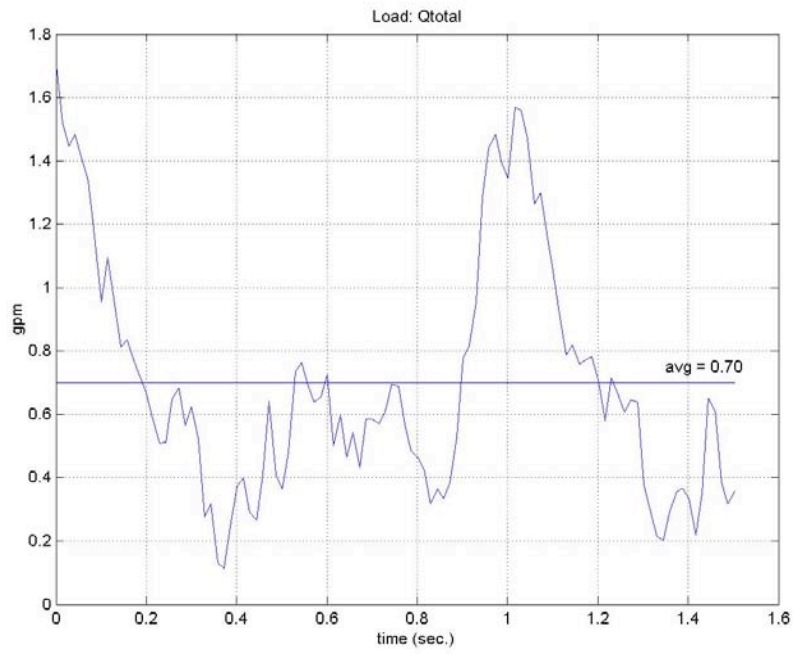
Fig. 78. Flow requirement of pump.
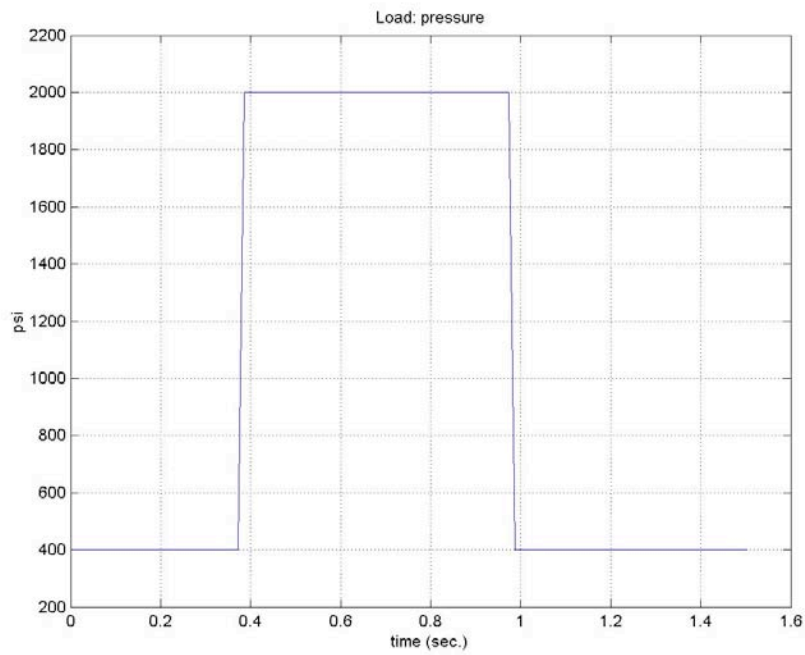
Fig. 79. Pressure requirement of pump.
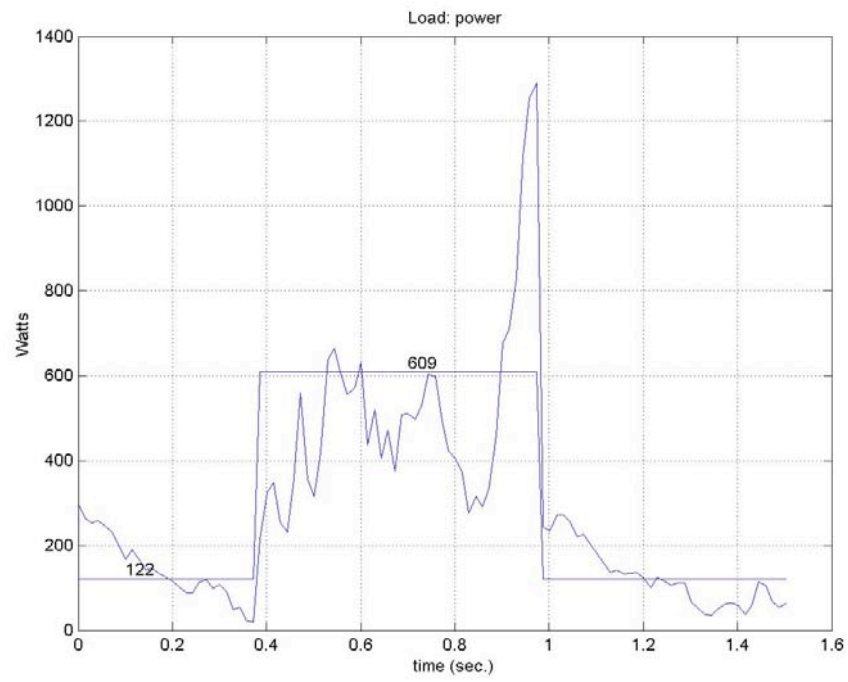
Fig. 80. Power requirement of pump.

ACKNOWLEDGEMENTS

APPENDIX A

FEASIBILITY STUDY - CONTROLLER DESIGN

This appendix is an excerpt from an ORNL exoskeleton feasibility study conducted for DARPA in 2000 (Jansen et al., 2000). This appendix provides background and the rational for the controls approach taken and is included here for completeness and the convenience of the reader.

CONTROLLER ISSUES AND APPROACH

While biped control for autonomous robots is still an active research area, its application to an exoskeleton is almost negligible because the balancing capability of the human operator can be transferred to the exoskeleton. The transfer of balancing capability from the operator to the exoskeleton is based on bilateral force reflection. Historically, the major application of bilateral force reflection controls has been for teleoperator (master-slave) systems. There are three general types of control strategies used in a teleoperator system: (1) position-position, (2)!position-force, and (3) force-force control. The first control strategy, which was used on the Hardiman, position-position control, refers to the type of sensory information (in this case positional information) being used in the "outer" feedback loop of both the master and slave. Position-position control is commonly implemented in most teleoperator systems. Two teleoperators ORNL built in the 1980s, the M2 and the Advanced Servo Manipulators, are examples of this type of control strategy that is common for systems that have kinematically similar master-slave manipulators. For kinematically dissimilar master-slave systems, position-force control is commonly used. For human amplifier (or extender) type systems, where the master and slave are one integral unit such that the human operator and the manipulator are attached to a common point and bilateral force reflection is the primary performance objective, force-force control is commonly used.

The purpose of this section is to define the fundamental control objectives and outline the basic control topology associated with the design of any mechanical exoskeleton system. Issues, such as the amount of mass felt by the human operator, minimum feedback gains, determining the critical sensory feedback signals, and reflection of disturbance forces back to the operator will be discussed.

To avoid undue complexity, a simple 1-DOF system, shown in Fig. 81, will be examined to better understand the salient issues. Figure 81 shows two types of actuators: the first is the human actuator in parallel with the mechanical actuator (such as a hydraulic cylinder). Force sensing is represented by the oval symbols, and force sensing at the human and the mechanical actuator are shown. It should be mentioned that force sensing at the foot instead of at the mechanical actuator is also possible and would be preferred, but for the sake of simplicity, the sensing also shown in Fig. 81, will be useful for discussion. The mass of the human is represented by M_h, the exoskeleton mass is represented by M_{ex}, and the payload mass is represented by M_p.

Three states will be considered in the analysis. The first is when the (mechanical) foot is on the ground with the exoskeleton system at rest. The second is when the (mechanical) foot first impacts the ground and the last when the 1-DOF system is off the ground. Linear analysis (in particular Laplace Transform theory with the s operator) will be assumed to adequately describe the basic physics for a fundamental understanding of a mechanical exoskeleton system. For state 1, where the exoskeleton system is in contact with the ground and initially at rest (i.e., impact is

ignored and the initial velocity is zero), the governing dynamic equations of the overall mechanical system can be described as
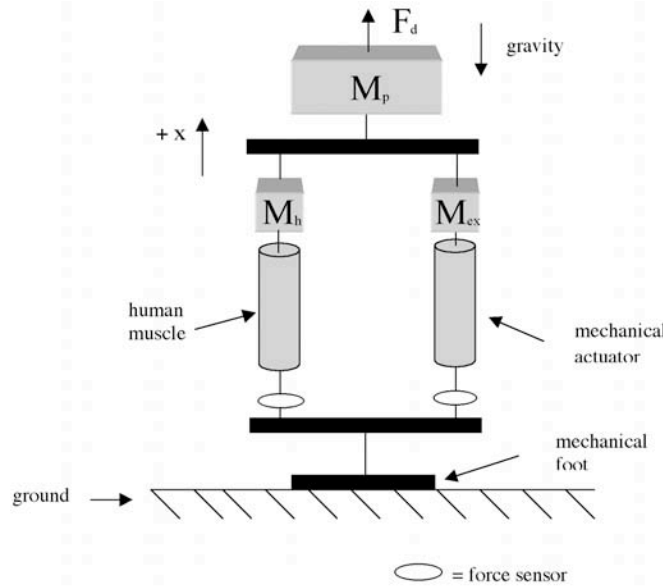
Fig. 81. One DOF exoskeleton system.

$$M_t s \dot{x} = F_h + F_{ex} - M_t g + F_d \qquad (4)$$

where M_t is the total mass and equal to $M_p + M_h + M_{ex}$, g is the gravity constant, and F_d is an external disturbance force. Assuming that the mechanical actuator can be set as a force-based actuator (e.g., current control in an electric motor directly controls the shaft torque), that is, $F_{ex}!=!K_{ex}i_{ex}$ where K_{ex} is the force constant and i_{ex} is the input drive signal.

By defining the desired human admittance, Y_h^{des}, as

$$Y_h^{des} = \left. \frac{\dot{x}}{F_h} \right|_{F_{d'}=0} \qquad (5)$$

where $F_{d'} = F_d - M_t\, g$, the desired human admittance can be thought of as the amount of force a human operator has to apply to achieve a given motion velocity. One would like this admittance to be close to a user specified mass and viscous force value that is limited only by power and bandwidth bounds. If one could achieve an arbitrary human admittance such as

$$Y_h^{des} = \frac{1}{M_{eff}s + K_{veff}} \qquad (6)$$

where M_{eff} is the effective mass and K_{veff} is associated with the effective viscous force, then a detailed understanding of the human neuromuscular control system is unimportant since humans already know how to respond to these environmental forces. To achieve force amplification, an outer control loop will generate an error signal, E, as shown in Fig. 82, where K_h is the force

amplification factor. The goal of the controller is to drive the error term to zero creating a relationship between the human force and the exoskeleton force by the force amplification factor.
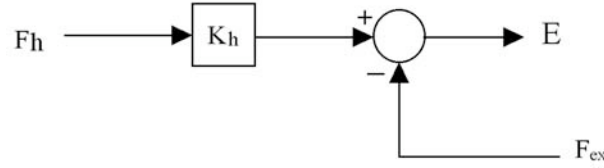
Fig. 82. Outer force control loop.

The remaining issue is the mapping of the error signal, E, to the drive signal, i_{ex}. One possible control topology is shown in Fig. 83, where the controller can be represented as

$$i_{ex} = K_{c2}\left[G_{cl}\left(K_h F_h - F_{ex}\right) - K_p \frac{\dot{x}}{s}\right] \tag{7}$$
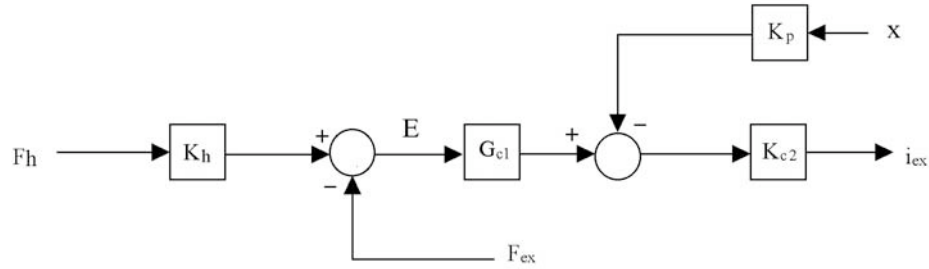
Fig. 83. Exoskeleton controller.

From the combined physical system and controller, the actual admittance of the exoskeleton, Y_h^{ex}, as felt by the human operator, can be shown to be

$$Y_h^{ex} = \left.\frac{\dot{x}}{F_h}\right|_{F_{d'}=0} = \frac{s\left[1+\left(1+K_h\right)G_{cl}K_{c2}K_{ex}\right]}{M_t s^2\left(1+G_{cl}K_{c2}K_{ex}\right)+K_p K_{c2}K_{ex}} \tag{8}$$

If $G_{cl} = 1/s$ and the K_{c2} gain is made large enough (this is where a careful overall design is critical), then it can be shown that over the user-specified frequency range, the actual admittance felt by the human operator is

$$Y_h^{ex}(j\omega) \cong -\frac{1+K_h}{M_t s + K_p} \tag{9}$$

This shows that the effective mass is $M_{eff} = M_t/(1 + K_h)$ and the effective viscous coefficient is $K_{veff} = K_p/(1 + K_h)$. By controlling the value of force amplification gain K_h and the feedback gain K_p, arbitrary amounts of effective inertia and viscous friction forces can be felt by the human operator. As an example, say that we want the human operator to feel only his or her mass and none of the payload or the exoskeleton system mass, then the amplification gain would have to be $K_h = (M_{ex} + M_p)/M_h$. By increasing the force amplification even further, a portion of the human operator mass can also be reduced by energy provided to the exoskeleton actuator.

81

Likewise, it can be shown that the gravitational and disturbance forces that are reflected back to the human operator, called the overall disturbance force (i.e., F_d), and assuming that the exoskeleton system is not moving, is related to the human force by

$$\left.\frac{F_{d'}}{F_h}\right|_{\dot{x}=0} \cong \frac{1}{1+K_h} \qquad (10)$$

over the user-specified frequency range. This indicates that force reflection is simply a function of the amplification gain and is similar to the ratios of the effective mass and viscous forces.

For state 2, where the exoskeleton system impacts the ground, the only difference between state 2 and state 1 is that the initial velocity is assumed to be nonzero. Equation (7) can be modified to show this change

$$M_t s\dot{x} = F_h + F_{ex} - M_t g + F_d M_t \dot{x}(0) \qquad (11)$$

(Note that this equation is in the s-domain and not the time domain). In addition, the disturbance force is modified to

$$F_{d'} = -M_t g + F_d + M_t \dot{x}(0) \qquad (12)$$

All the results for state 1 can now be applied to state 2, while the only change, the additional momentum force, is because of a nonzero impact velocity. This impact force will be felt by the human operator, but at a reduced level, and can be further reduced by means of suitable mechanical compliance in the exoskeleton structure.

If one examines how the disturbance force can affect the exoskeleton velocity, it can be shown through reasoning similar to the discussion for state 1, that

$$\left.\frac{\dot{x}}{F_{d'}}\right|_{F_h=0} \cong \frac{1}{M_t s + K_p} \qquad (13)$$

over the user-specified frequency range, where the benefits of the computer-controlled viscous damping term K_p becomes clear; it dissipates the impact force. Impact forces can be damped to specific target values by the controller; in addition, the mechanical structure can be designed to provide further system damping.

For state 3, where the exoskeleton is off the ground, all ground reactions are obviously zero which forces the governing dynamic equations represented originally by Eq. (7) to change to the following:

$$M_t s\dot{x} = -M_t g + F_d + M_t \dot{x}(0) \text{ and } F_h + F_{ex} = 0 \qquad (14)$$

(Note that these equations are in the s-domain and not the time domain in regard to the initial velocity of the system). The actuator for this 1-DOF exoskeleton system cannot affect the trajectory of the system, and the human and exoskeleton forces add up to zero. The exoskeleton

controller will try to force tracking between the human force and the exoskeleton force, which implies that the effective human force will be about zero (depending on the tracking performance of the controller). When the exoskeleton system is off the ground, the human feels almost no force and cannot affect the trajectory of the system. This is true only for this simple case, where only a 1-DOF example is being considered. For a two-legged system, the leg on the ground would provide the reaction force for the leg that is off the ground.

In summary, a 1-DOF system has been examined to study the feasibility of using a force-based control system to implement performance enhancement. An overview of controller issues, including force sensing, creating a relationship between the human and exoskeleton forces, the use of the human capability to respond to environmental forces, and the damping of impact forces have been addressed. It has been shown that by means of force-based feedback, the effective mass and disturbance and viscous forces as felt by the human operator of an exoskeleton, can be readily controlled. Performance is intrinsically limited only by the mechanical bandwidth and power limitations of the actuators, and the mechanical structure. While examined with a 1-DOF case, these concepts should readily extend to the multiple-DOF case.

SAFETY AND FAULT DETECTION CONCEPTS

Safety will be a prime concern in the eventual deployment of any exoskeleton. A common failure scenario in a hydraulic servomechanism is the failure of either the servovalve, drive electronics, or sensors (say a positional sensor like a resolver) causing a significant flow of fluid to the hydraulic actuator. Detection of this type of fault has to occur quickly because of the high-bandwidth of an exoskeleton, which could result in significant motion within 150!ms. For example, the required dynamic response could result in 80° movement of the knee in 150!ms or less. The best-case human-reflex response time is 110 to 150!ms. Thus, there is a significant potential for injury without adequate fault detection and response capability. Because of the human reaction times, it is unreasonable to expect that an operator could activate an emergency stop button in the time required to prevent injury in the worst-case scenario.

The general approach to error detection is through model-based anticipatory and trend-forecasting schemes (such as Kalman predictive filtering), which can detect a system error during system transients (Tylee, 1983). Unfortunately, conventional methods cannot distinguish between a fault and system disturbance because of the short decision times available when a failure occurs and the unpredictable nature of disturbances acting on an exoskeleton (such as thermal drift in the drive electronics, mechanical vibrations, impact forces). This explains why such systems are not readily commercially available.

ORNL's approach has been to break apart the disturbance forces acting on the system (such as thermal drift in the drive electronics, mechanical vibrations, impact forces) from the overall nonlinear system response caused by a fault. Preliminary work indicates that this approach of partitioning of these forces on a real system can achieve response times around 200!ms (see Fig.!84). ORNL has demonstrated this approach and 200!ms response times on the Next Generation Munitions Handler (NGMH) system. The response times of the command valves are currently limited around 100!ms by the inductance-resistance time-constants. The eventual goal

of the safety-fault detection system is to reduce the response times to as close to a 50!ms goal as possible.

Analysis of the current system indicates that for a hydraulic system, using special shut-off valves, which have reduced inductance-resistance time-constants, can significantly reduce the response time. Other factors, such as faster processing capabilities have a much less significant impact. Further research is needed regarding issues relating to system safety and approaches for further reducing response times. Current models and simulations, verified by data from an operating system (NGMH), provide a starting point for more detailed study of approaches to ensuring system safety.
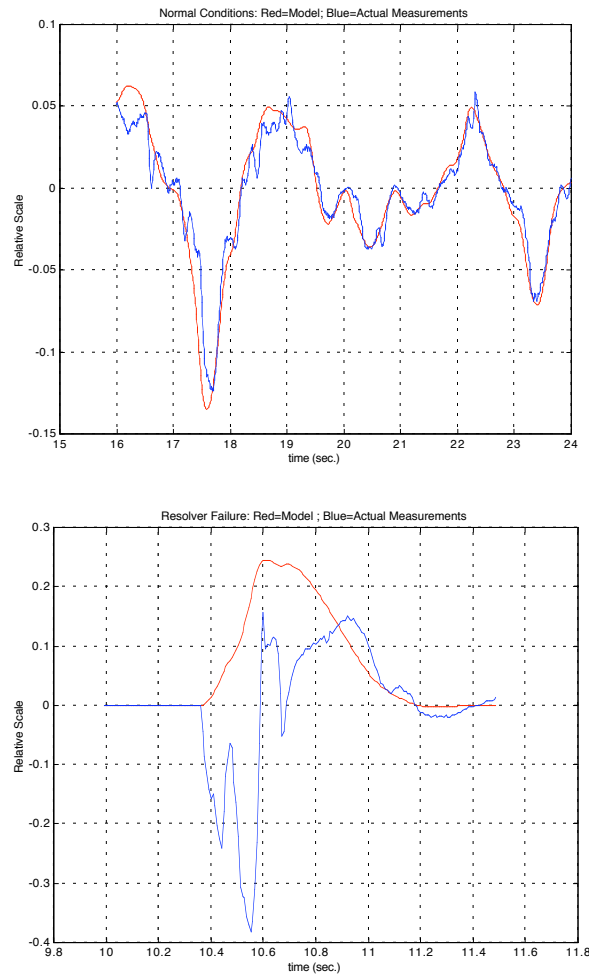
Fig. 84. NGMH fault detection (normal operation and sensor failure).

APPENDIX B

FEASIBILITY STUDY - DESIGN ISSUES

This appendix is an excerpt from an ORNL exoskeleton feasibility study conducted for DARPA in 2000 (Jansen et al., 2000). This appendix provides background and rational for the design approach taken and is included here for completeness and the convenience of the reader.

TECHNICAL APPROACH

The design of the exoskeleton structure must address the fact that the structure's primary function is to support the payload and provide the mechanical interface with the operator, while at the same time, the function must be transparent to the operator and enable overall system energy efficiency. In essence, the exoskeleton is wrapped around the operator and supports the payload as well as its own load with the objective of minimizing disturbances exerted on the operator. Two basic design approaches will be discussed. The first is based on designing the exoskeleton to track the human operator joint by joint. The second approach is based on tracking the limb end-point (foot or hand), but not necessarily matching each joint. Regardless of the approach taken, the design of the exoskeleton should be highly anthropomorphic. While the overall form of the exoskeleton may not differ dramatically based on the approach taken, system complexity, including the number and location of joints, the number and location of attachment points, and the control system complexity, will all be affected.

In comparing these two approaches, consideration of some of the intricacies of human anatomy must be taken into account. First, the human arm and leg have redundant joints; thus, there are multiple joint configurations for each unique hand and foot position and/or orientation. To replicate this capability adds degrees of freedom and increasing system complexity. A study by the ARL detailing requirements for an exoskeleton suggests a minimum number of DOF (Table 6). Note that the recommendation includes 6 DOF for the leg (it does not include ankle abduction-adduction) and 7 DOF for the arm. The addition of a redundant degree of freedom will obviously increase the overall complexity of the control system.

Table 6. Minimum DOF for exoskeleton joints (Crowell, 1995)

Joint	DOF	Description
Foot	1	Extension for metacarpophalangela joint
Ankle	1	Flexion-extension
Knee	1	Flexion
Hip	3	Flexion-extension, abduction-adduction, medial-lateral rotation
Pelvis	3	Coronal, sagittal, and transverse plane rotations
Spine segments	3	Flexion-extension lateral flexion, rotation
Shoulder	3	Flexion-extension, abduction, medial-lateral rotation
Elbow	2	Flexion, forearm pronation-supination
Wrist	2	Flexion-extension, abduction-adduction

Co-locating joints such that both the human joint and the exoskeleton joint rotate about a common axis is difficult, especially at joints with multiple degrees of freedom, such as the hip, shoulder, wrist, and ankle. With a non-co-located joint, the likelihood of the exoskeleton impeding the motion of the operator is increased. This increases the difficulty of the design, especially when combined with the need to accommodate a broad range of operator sizes. The

addition of a redundant joint, while adding complexity, especially to the control system, can aid in avoiding configurations where the exoskeleton does in fact impede the operator.

To follow or track, the human operator on a joint-by-joint basis requires attachment and sensing at or near the joint. For example, to track the knee, attachment above and below the knee would be required. As joint-by-joint tracking implies a position-position control loop, position sensing of both the human and exoskeleton joints would also be required. Complicating this is the fact that the centers of rotation for human joints, such as the knee, are not fixed. Replicating these types of joints mechanically is difficult, and the likely result is tracking errors, which will have some impact on the interface at the attachment points.

The second approach, tracking the limb end-point, has advantages over the joint-by-joint tracking approach. First, attachments are not required at each joint. In particular, no attachment is required for the elbow and knee. The number of degrees of freedom can be limited to 6 for each limb, thus reducing complexity and weight. Accurately tracking of each individual joint is not an issue, eliminating the need to accurately sense the position of each human joint and to accommodate the motion of complex joints such as the knee. Significant reduction in mechanical complexity is achieved in this approach at the expense of increased complexity of the control system. The remaining discussion is based on the results of these comparisons, in an effort to address other design issues affecting feasibility.

STRUCTURE

Design of a transparent exoskeleton is affected by many parameters such as response bandwidth, sensing points, soft-tissue interfaces, and amplification schemes, in addition to key structural parameters, including kinematics, load-transfer points, and the determination of actuated versus non-actuated joints. While the design of the exoskeleton should be highly anthropomorphic, a 1:1 correspondence between each of the exoskeleton and operator joints is not necessary. It is essential, however, that these joints be located in as close of proximity as possible, although not necessarily co-located.

Co-locating joints, such as the hip and wrist, were evaluated to determine the design trade-offs related to the structure. The most significant advantage of co-locating the joints is reduced tracking errors. The trade-off is in the increased complexity, as can be seen in the co-located hip joint as seen in Fig. 85. A special configuration that allows for remote centers of rotation (which are co-located with the body's center of rotation), limits the range of motion achievable without interfering with the body, and greatly increases the difficulty in the design of bearings. The fact that the hip requires the simultaneous co-location of three DOF, adds tremendously to the mechanical complexity in achieving the desired range of motions. Figure 85 shows the medial and lateral rotations, as well as the hip abduction. It can be seen in the hip abduction (third frame) that the motion causes an interference with the body. After investigating a number of options, it became apparent that co-locating a joint as elaborate as the human hip was extremely difficult, with complexity that rendered such a design impractical. A non-co-located hip design, with linear actuators, is shown in Fig. 86. It should be noted that these figures represent concepts and that further detailed design would obviously be required.
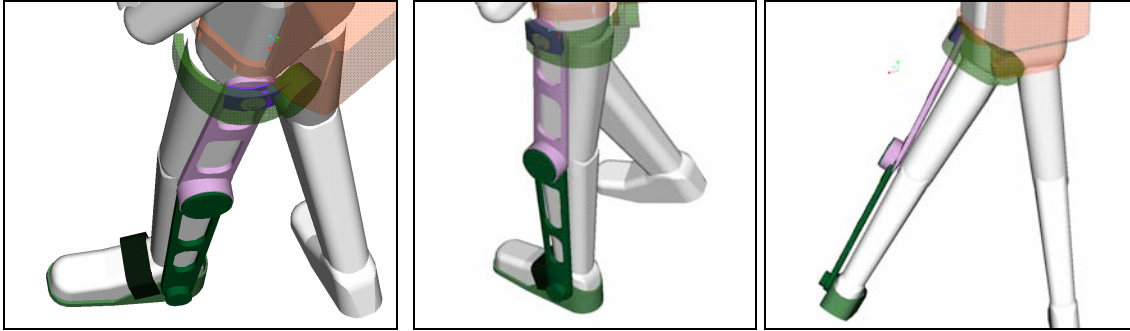
Fig. 85. Co-located hip.
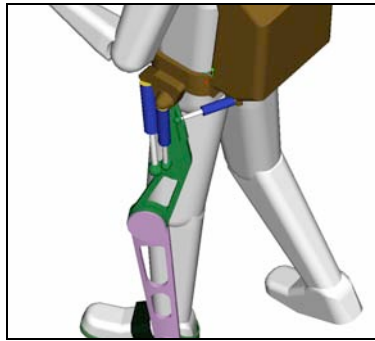
Fig. 86. Non-co-located hip with linear actuators.

Co-locating of joints is also an issue with the arm design as well. Due to complexity and range of motion limitations, the shoulder does not lend itself to co-location, similar to the hip. However, examination of the elbow joints forearm pronation-supination, which gives the wrist roll type of motion, indicates that co-locating of that joint can be accomplished while simplifying the design (Fig. 87).
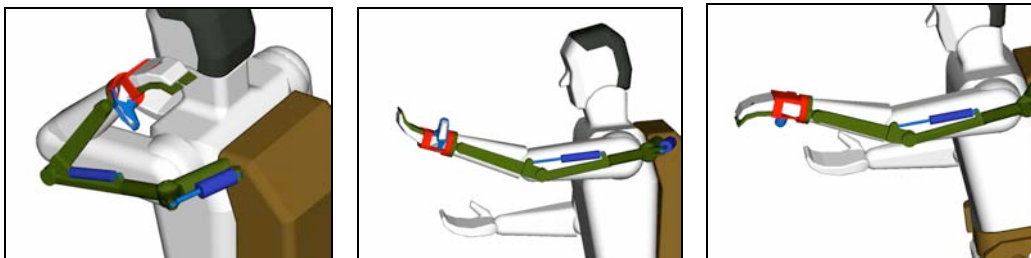
Fig. 87. Shoulder and arm structure.

Table 6 lists a minimum of 6 DOF per leg. A couple of points can be made concerning the number of DOF. It may be tempting to eliminate the hip medial-lateral rotation to simplify the design, as has been done in some proposed concepts. This, however, introduces a complication that would require further evaluation. Without this DOF and likewise, without the ankle abduction-adduction, the foot is constrained to remain in the same plane as the leg. This has implications with regards to changing direction, and at the very least will require slipping of the foot and may in fact alter the normal manner in which one changes direction.

Joint design type was also investigated. The issue is to determine where to use rotary or linear actuators. Compactness of the design and range of motion are the determining criteria. The selection of either rotary or linear actuators is highly dependent on the joint. In general, rotary actuators appear to be more applicable to joints where more than 90° range of motion is required. Linear actuators have an advantage with respect to the ease of measuring force. The knee flexion, for instance, could be done using either type of joint. The ankle flexion-extension, although it is less than 90° may be more appropriately done with a rotary joint (Fig.!85). Ball and socket joints such as the hip in Fig.!86 would require linear joints.

As stated previously, minimization of power and energy requirements is crucial to the development of a truly "fieldable" exoskeleton system. An emphasis on optimizing the design of the structural elements to minimize system weight is an important aspect in the overall systems approach. The criteria for sizing the structural elements must take into consideration not only stresses, but structural stiffness as well. For the anticipated load range, stiffness is the determining factor in the sizing of the structural elements. Thus, minimizing the size of structural elements must be traded off with the requirement of maintaining structural stiffness.

While detailed modeling and analysis will be required to optimize this trade-off, preliminary analysis indicates that adjustable aluminum channel members can be used for the upper and lower links, respectively. Based on this analysis, assuming a 136!kg (300!lb) payload and a minimum structural natural frequency of 10!Hz, an approximate weight for the structural system was calculated to be on the order of 12!kg (excluding actuators). The payload included the weight of the exoskeleton, assumed to be on the order of 32!kg (70!lb) and an effective payload of 105!kg (230!lb). The effective payload, which could take the form of either a backpack or an item manipulated using the exoskeleton arms, was used to size both the arms and the legs, which must transmit the load in either case. A study on the effects of increased payload showed that doubling of the payload had the affect of increasing the approximate weight of the structure by about 40% (excluding actuators).

For an exoskeleton to move from the laboratory to the field, the structure must be adjustable to accommodate a wide range of operator sizes. The goal should be able to accommodate from the 5% female to the 95% male. Adjustments will be required for both the upper and lower leg and arm links. Adjustment will also be required to accommodate for variances in torso proportions as well.

ATTACHMENT

Attachment of the exoskeleton is extremely difficult because of the close coupling required between the machine and the operator and the sensitivity of soft tissues, which are susceptible to bruising and damage with pressures as low as 0.1!atm over a few hours. There are considerable knowledge and experience embedded in the fields of orthotics and prosthetics, which have been addressing the problems of applying significant forces to the skeleton while keeping skin loading to acceptable levels.

As stated previously, the exoskeleton should be highly anthropomorphic—that joints should be located in as close of proximity as possible, although not necessarily co-located and that a 1:1

correspondence between each of the exoskeleton and operator joints is not necessary. Therefore, the number of attachment points can be kept to a minimum by attaching at the limb extremities (feet and hands) and at the waist and shoulder. Thus, the leg or arm would be controlled based on the force input at the extremities as opposed to matching positions of each joint. By minimizing the number of attachment points, the total number of required DOF and actuators can be reduced, and the difficult task of mechanically replicating the motions of the human knee, which does not have a fixed center of rotation, can be avoided. The trade-off for simplifying the mechanical design is increased difficulty in the design of the control system (i.e., going from a joint-to-joint to a Cartesian control scheme).

It is important to provide a reliable and comfortable attachment at the human foot to the exoskeleton (Fig. 88). In this concept, soldiers outfitted for exoskeleton augmentation will wear boots that have built-in rapid-release attachment points. The boots will permit normal bending of the foot at the toes and will not create any additional human-tissue contact points. When not attached to the exoskeleton, the boots will feel and perform like ordinary boots. The coupling at the foot includes sensing of both the operator and the total system forces. These forces will be measured using multi-axis, force-torque sensors. The design will ensure that forces transmitted from the human foot to the exoskeleton can be accurately and unambiguously measured. The role of this force sensor was discussed in greater detail in the control section.
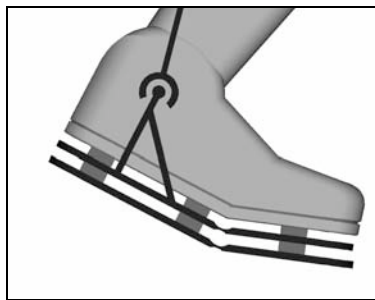
Fig. 88. Foot attachment schematic.

Attachment at the waist and shoulder areas would use a belt and shoulder straps, which are normal contact pressure areas. A major design issue would be to maintain comfort and acceptable loading over extended periods of time.

CONCEPTUAL ENHANCEMENTS

Some additional conceptual ideas that could enhance the design of an exoskeleton and thus potentially increase the likelihood of successfully developing an exoskeleton have been considered: first, the concept of using passive joints to reduce system complexity, and next, the concept of reconfiguration and multiple mode operation.

Passive Joints

While this study is focused on determining the feasibility of a powered exoskeleton, there may be opportunities to use passive joints as opposed to actuated joints in certain instances. Obviously, there is a significant advantage in weight and energy savings and reliability and cost

in using passive joints where appropriate to simplify the system. While the actual determination of the joints that could be made passive would require more detailed analysis than the scope of this study allows, there are two joints that stand out as possible candidates. The metacarpophalangeal joint, as seen in Fig. 85, is the most likely candidate to be made passive. The hip-rotation joint is another possibility.

Reconfiguration and Multiple Mode Operation

The possibility of a modest reconfiguration of the system to allow a low power mode of operation was also investigated. In particular, a lower power, ballistic-type walking mode was investigated. Such mode would be advantageous for tasks such as long marches and could enhance operating times. Emulating a straight-leg ballistic mode is shown in Fig. 89. In this mode, the knees would essentially be locked and a thigh prismatic joint would be used to lengthen and shorten the legs, which would be moving with a pendulum type motion. Obviously, in such a mode close tracking of the knee is not a concern, but conservation of energy is the primary motivation. The trade-off for energy efficiency is the addition of the prismatic joint.

Fig. 89. Straight-leg ballistic mode.

The addition of a thigh prismatic joint (Fig. 90) could add other advantages. These include the minimization of tracking errors between the operator and exoskeleton legs, thereby reducing the risk of the exoskeleton impeding operator motion and allowing for a "tighter fitting" exoskeleton. The prismatic joint also compensates for pelvic-tilt-type motions, which were not easily accommodated with rotational joints.
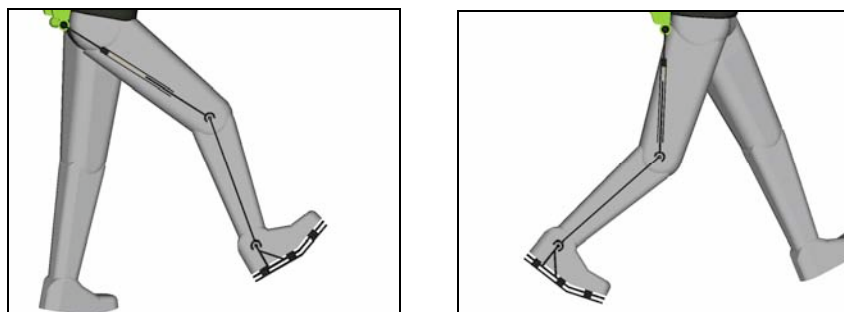
Fig. 90. Leg structure schematic demonstrating thigh prismatic joint.

APPENDIX C

POWER AND TORQUE DATA

This appendix contains the data from the biomechanics analysis performed to determine exoskeleton power and torque requirements that was conducted by ARL (Crowell, et al., 2002).
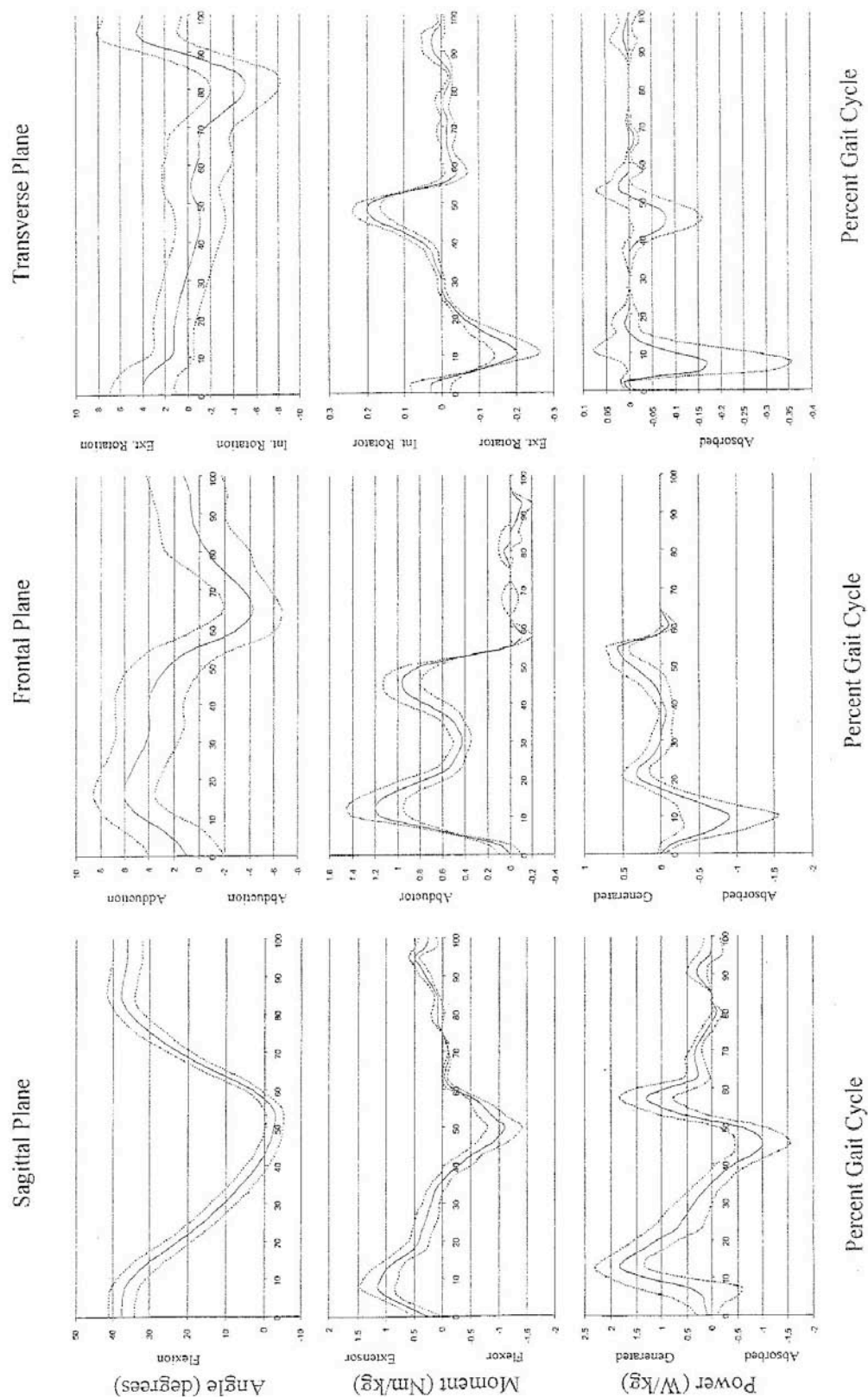
Fig. 91. Hip joint angles, moments, and powers - walking.
(Saggital, frontal, and transverse planes during one cycle of normal walking. Solid lines are mean values and dotted lines are ± one standard deviation.)

95
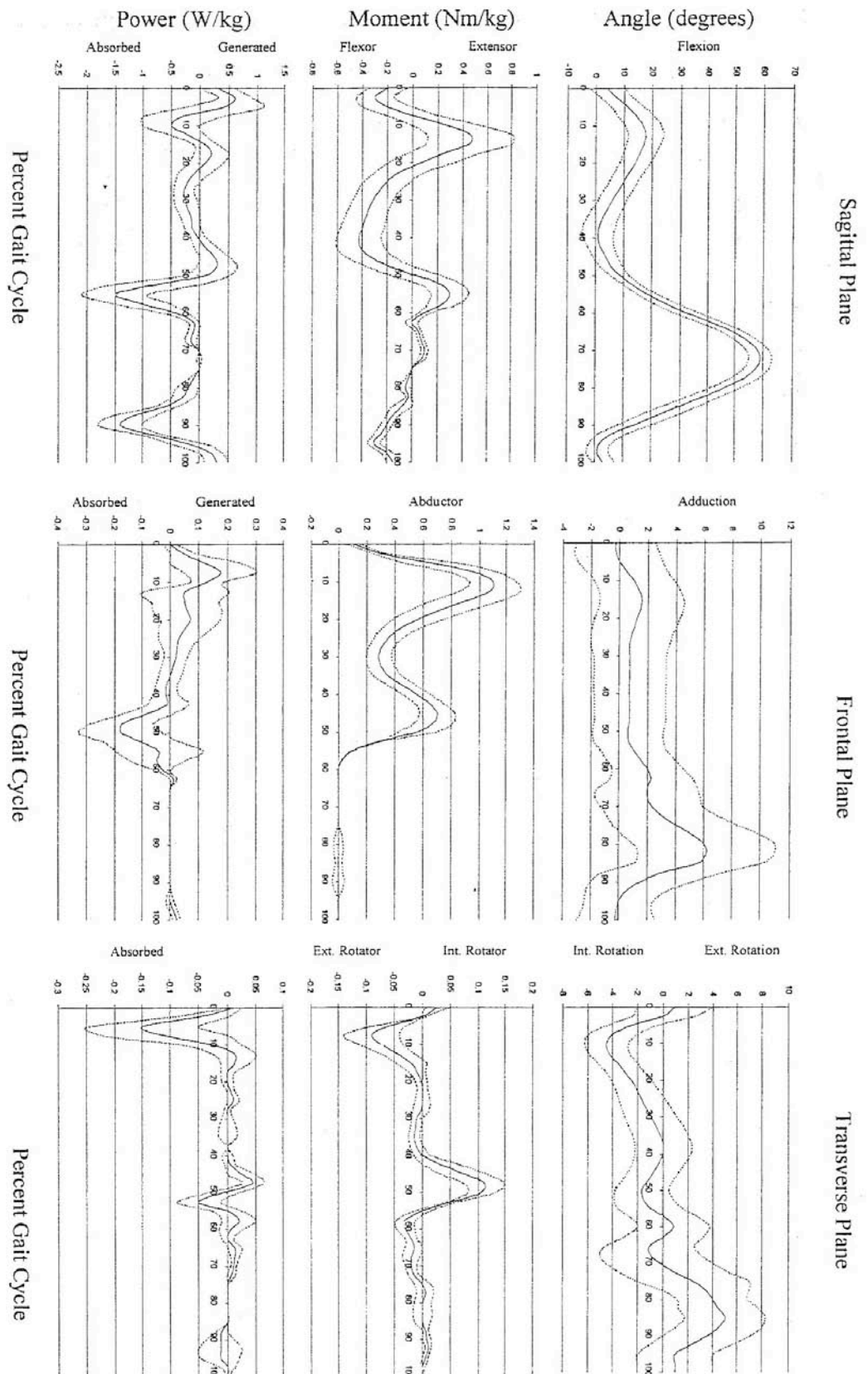
Fig. 92. Knee joint angles, moments and powers - walking.
(Saggital, frontal, and transverse planes during one cycle of normal walking.
Solid lines are mean values and dotted lines are ± one standard deviation.)

96
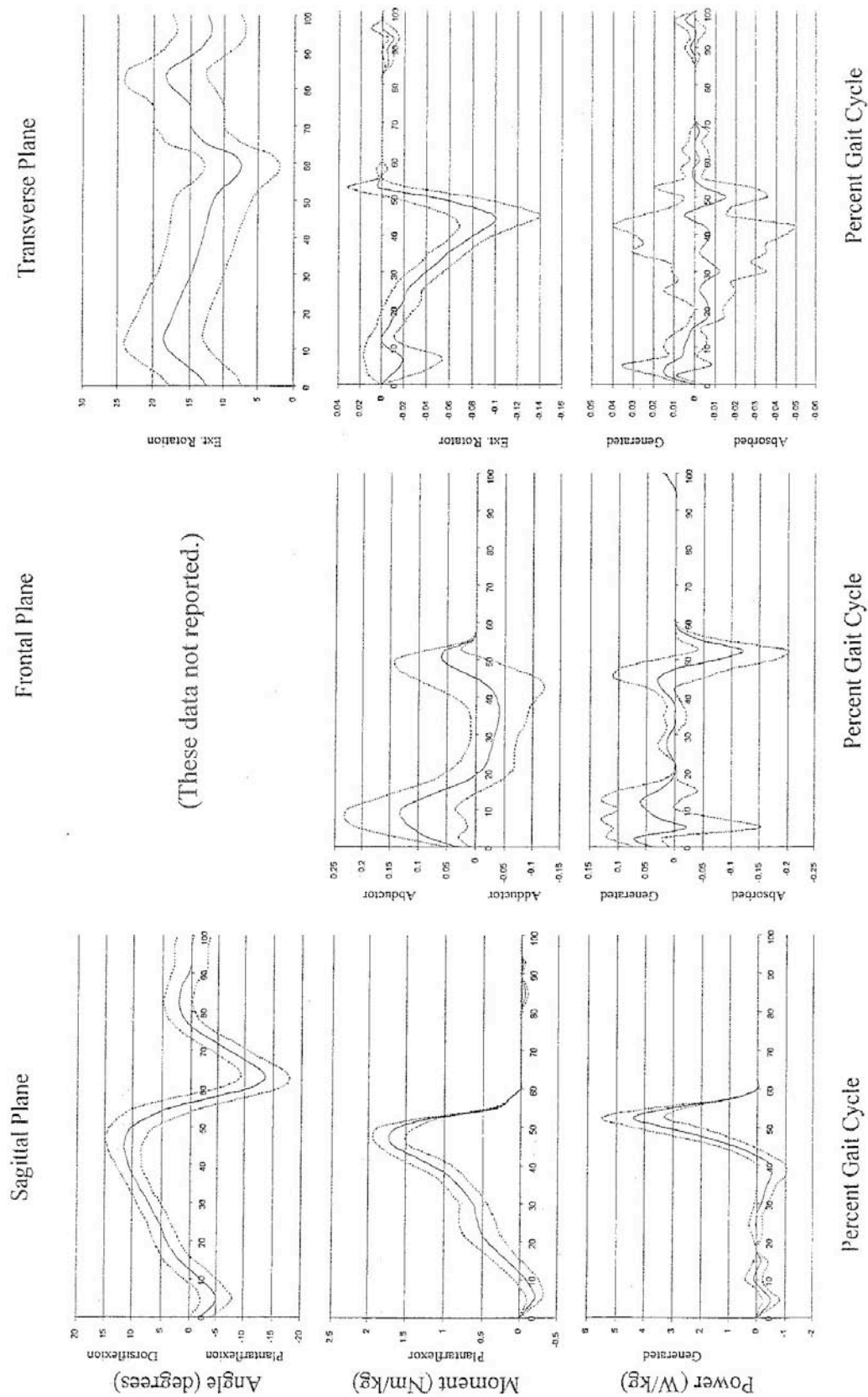
Fig. 93. Ankle joint angles, moments and powers - walking.
(Saggital, frontal, and transverse planes during one cycle of normal walking.
Solid lines are mean values and dotted lines are ± one standard deviation.)

97
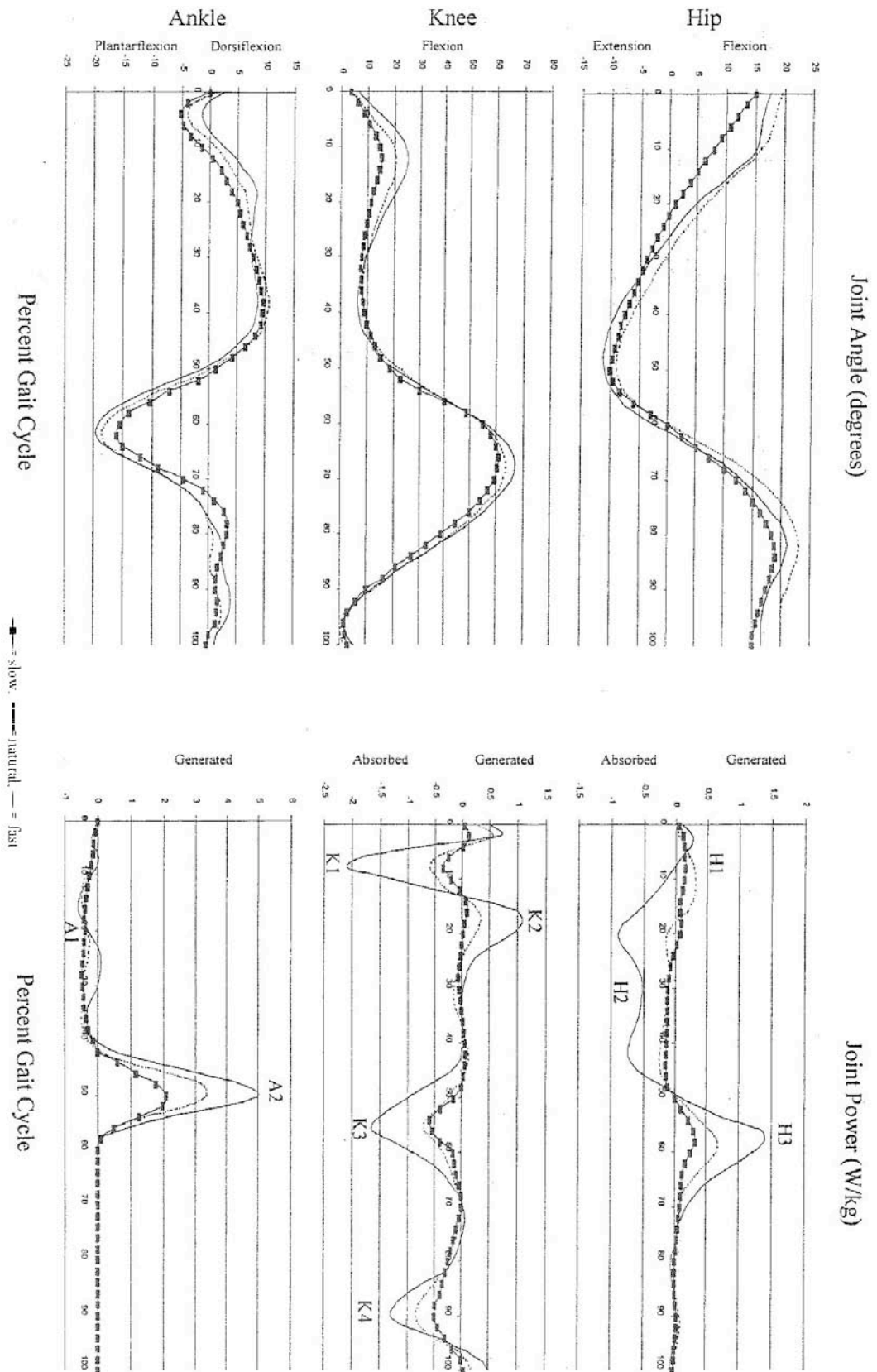
Fig. 94. Joint angles and powers - walking.
(Saggital plane joint moments and power during one cycle of walking at three cadences.)
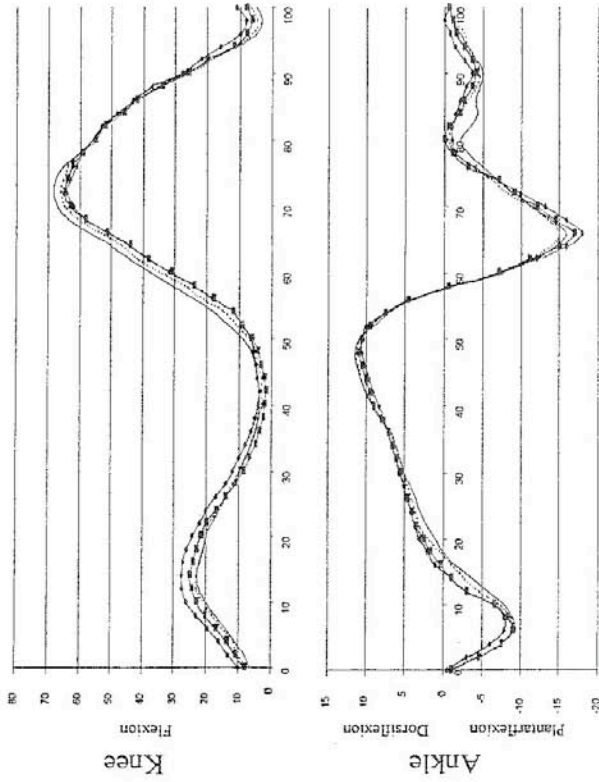
98
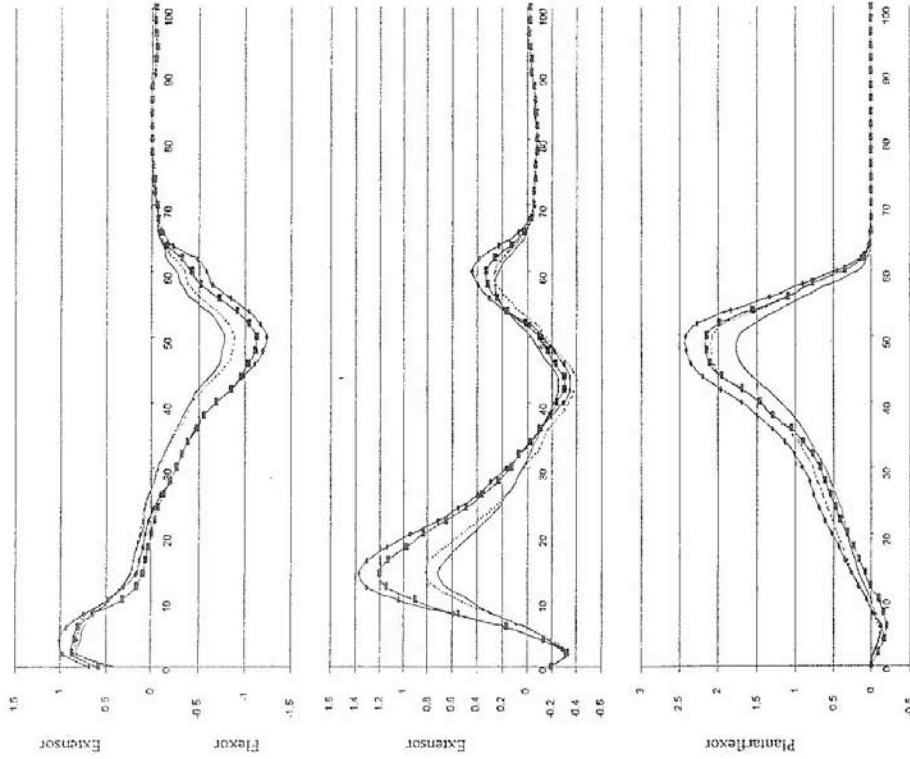
Fig. 95. Joint angles and powers – walking with various loads.
(Saggital plane joint moments and power during one cycle of walking at 1.33 m/s
with four different backpack loads.)

99
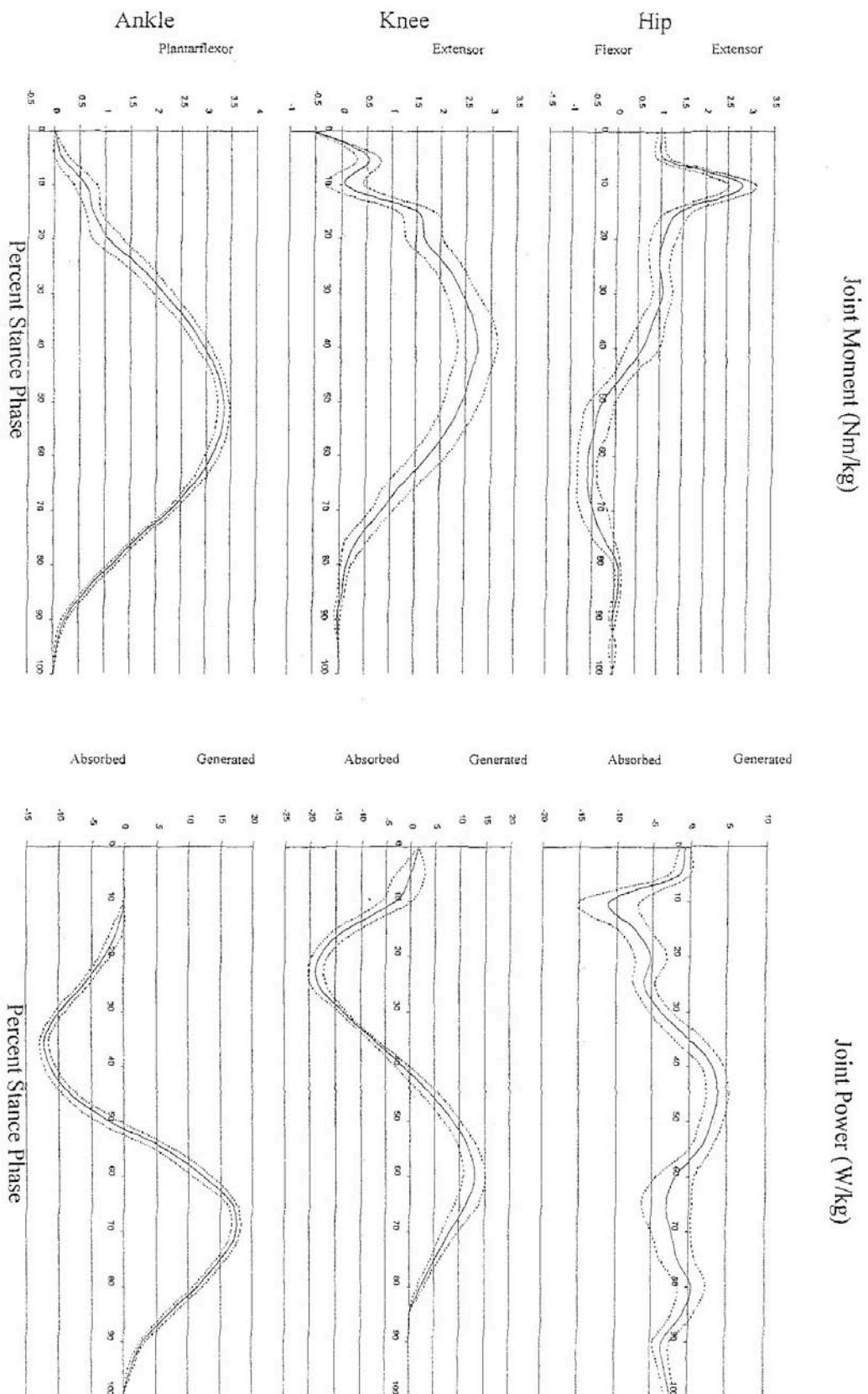
Fig. 96. Joint moments and powers – moderate running.
(Saggital plane joint moments and power during the stance phase of running at 3.8 m/s.
Solid lines are mean values and dotted lines are ± one standard deviation.)

100
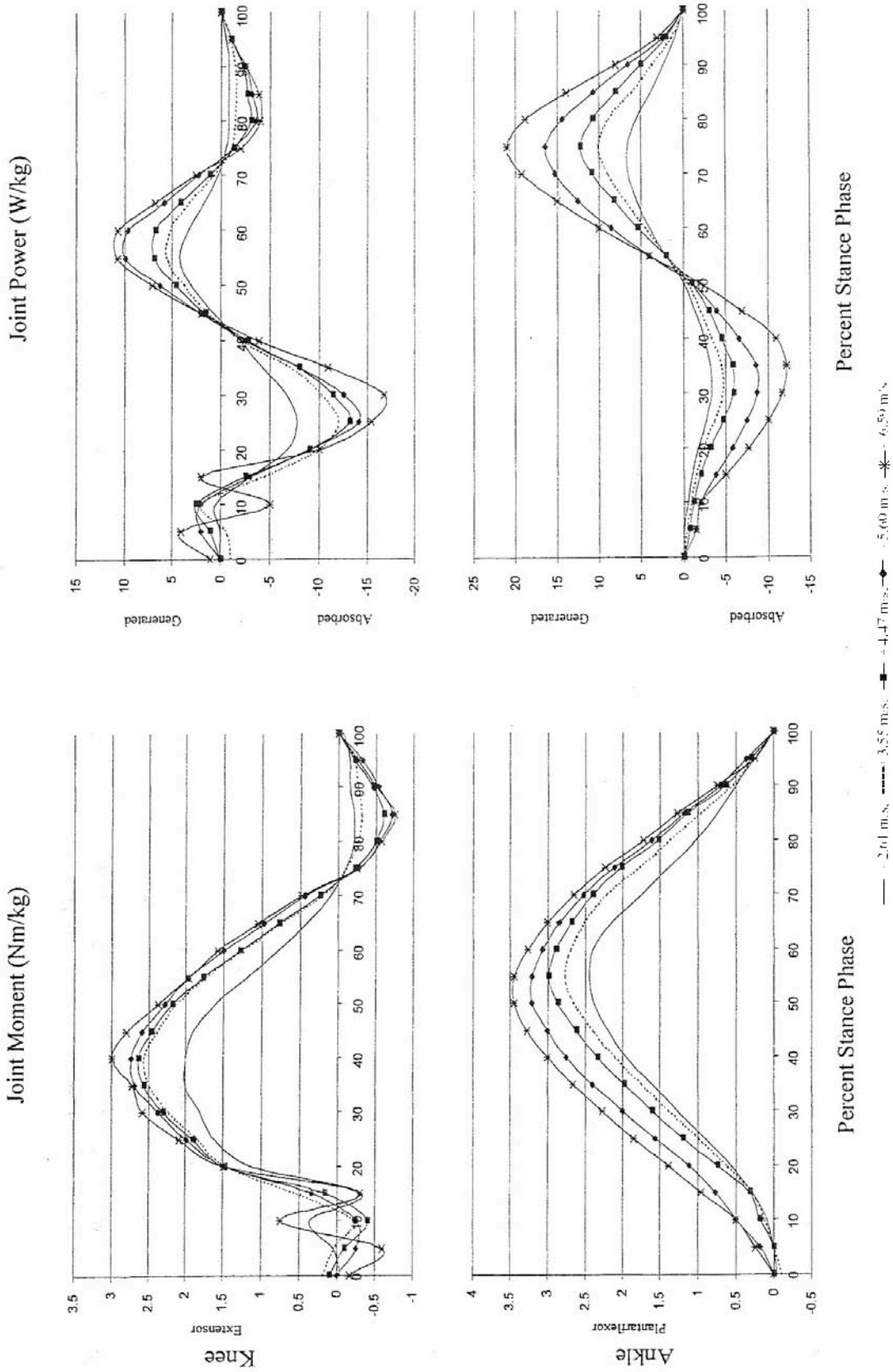
Fig. 97. Joint moments and powers - running at varying velocity.
Saggital plane joint moments and power during the stance of running at five velocities.

101
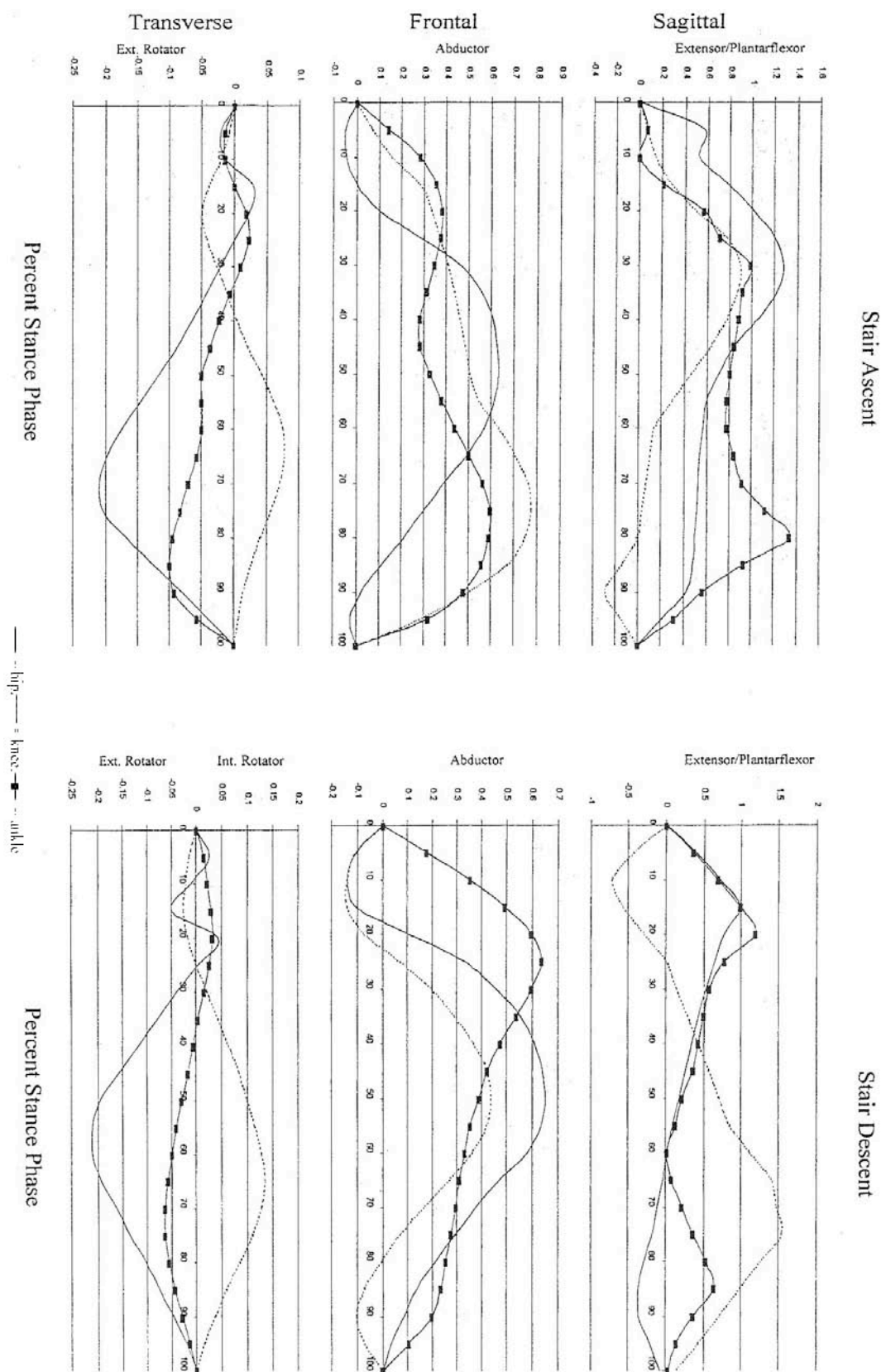
Fig. 98. Joint moments - stair ascent and descent.
(Joint moments in the saggital, frontal and transverse planes during stance phase of stair ascent and descent.
Values are in newton-meters per kilogram).

102
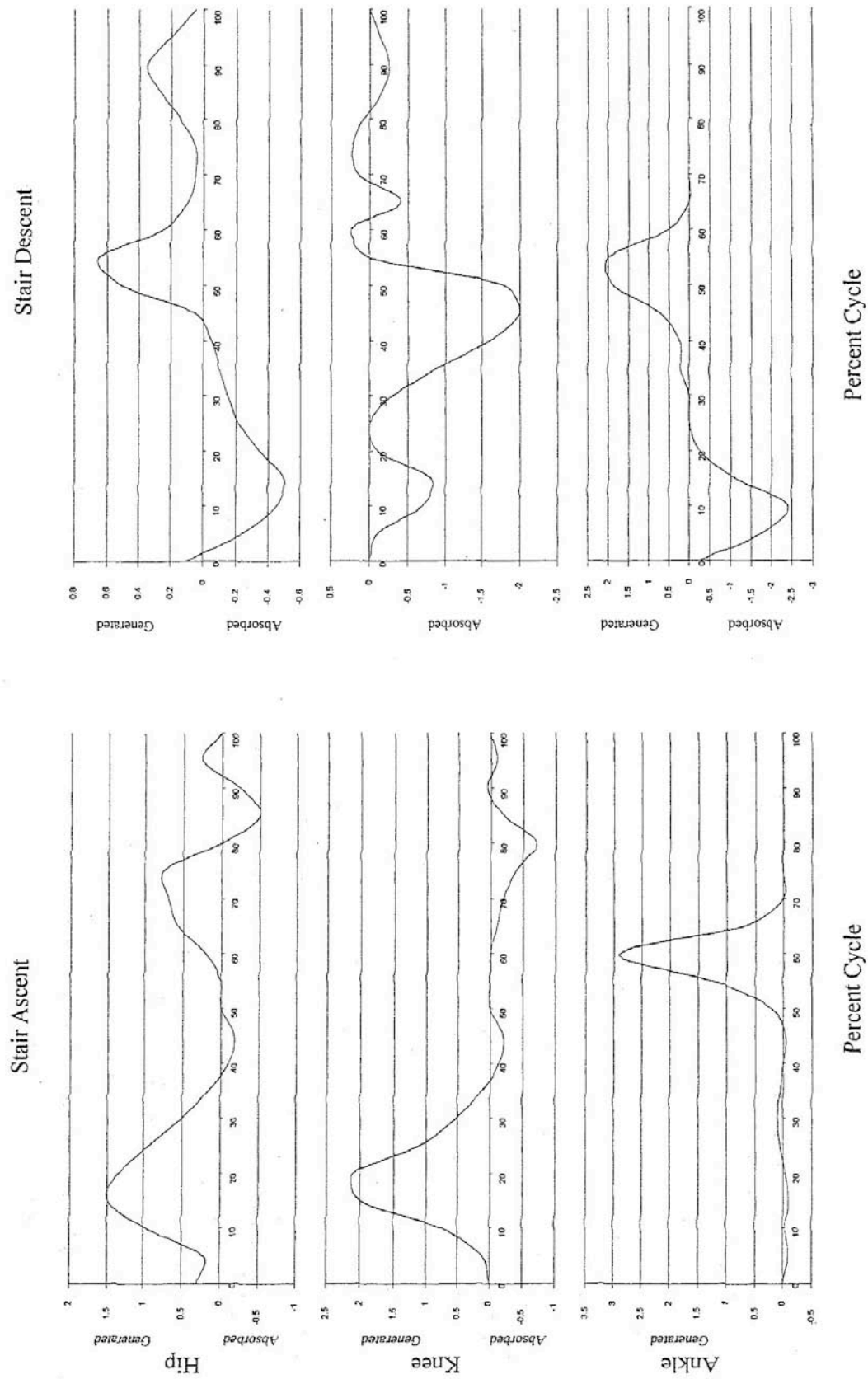
Fig. 99. Sagittal plane joint powers - one cycle of stair ascent and descent. (Values are in watts per kilogram.)

103
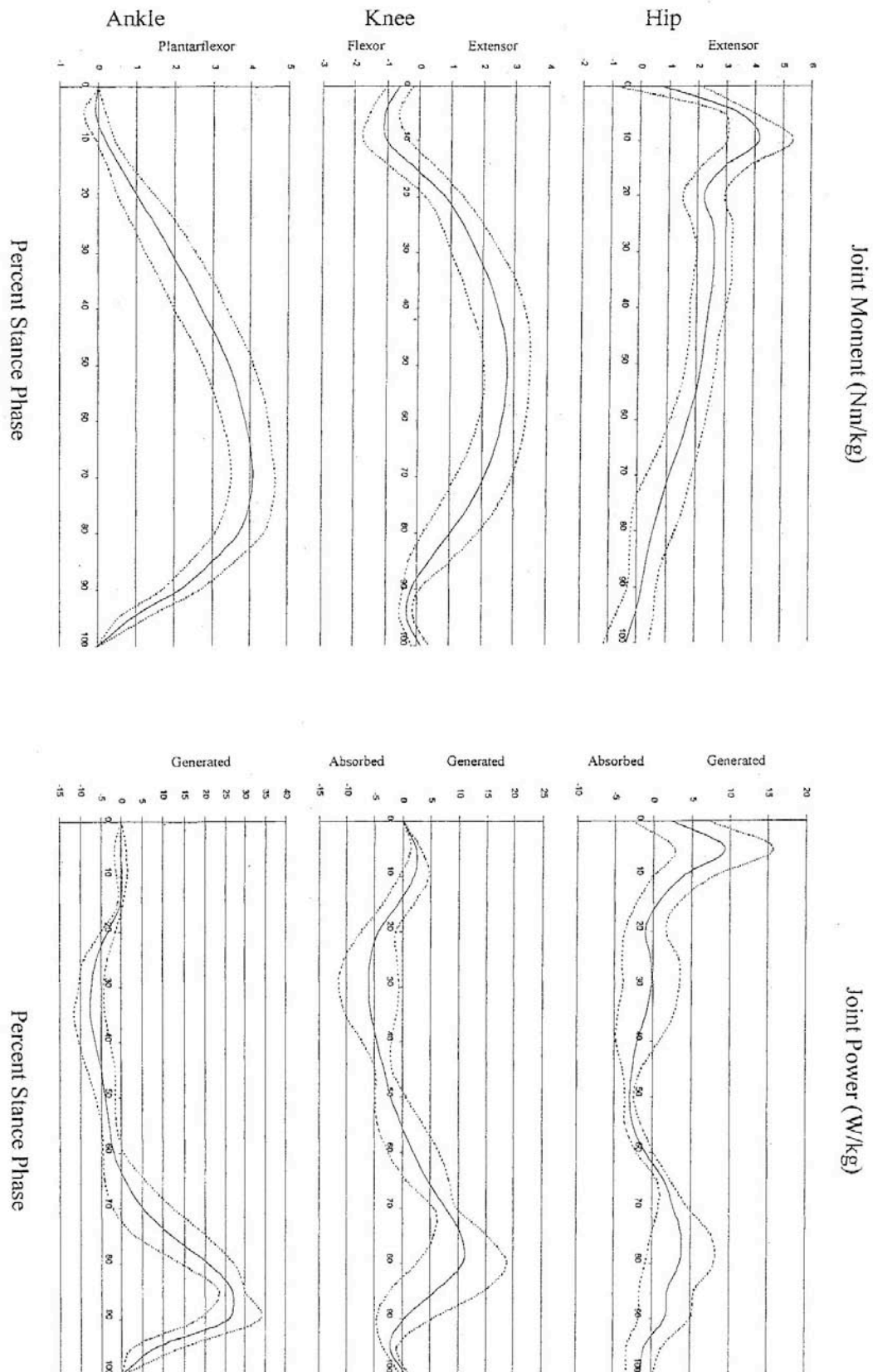
Fig. 100. Joint moments and powers – running vertical jump.
(Saggital plane joint moments and power during the stance phase of before toe-off of a running vertical jump. Solid lines are mean values and dotted lines are ± one standard deviation.)

104

APPENDIX D

SOLE THICKNESS TEST DATA

This appendix contains the data from the human factors analysis on the effects of sole thickness of the boot interface. This study was performed by ARL and is documented in Boynton and Crowell, 2003.

Table 7. Biomechanics variables for walking

Variable			Sole Condition			p
			Baseline	1-inch Sole	2-inch Sole	
	Stride Length (m)		1.575 (0.111)	1.607 (0.134)	1.597 (0.114)	0.15
	Velocity (m/s)		1.396 (0.094)	1.428 (0.145)	1.401 (0.165)	0.79
	Cadence (steps/min)		106 (3)	107 (8)	105 (7)	0.26
	% Stance		63.6 (2.1)	64.9 (3.0)	64.5 (2.3)	0.30
Angle (degrees)	Sagittal	Hip	Maximum	31.7 (4.4)	32.3 (3.5)	30.3 (3.6)	0.38
			Minimum	-19.4 (2.0)	-19.6 (2.8)	-19.6 (2.1)	0.99
		Knee	Maximum	75.1 (5.4)	73.9 (4.3)	70.6 (6.0)	0.00 –
			Minimum	-4.8 (2.3)	-2.3 (2.9)	-4.3 (5.3)	0.16
		Ankle	Maximum	12.0 (3.0)	14.5 (4.2)	14.9 (4.3)	0.02 –
			Minimum	-11.7 (3.2)	-10.3 (2.9)	-10.2 (3.6)	0.21
	Frontal	Hip	Maximum	6.1 (5.0)	6.3 (5.4)	6.7 (4.3)	0.93
			Minimum	-7.2 (4.1)	-7.0 (3.3)	-7.4 (1.9)	0.84
		Knee	Maximum	16.3 (5.6)	16.2 (6.6)	14.8 (3.7)	0.73
			Minimum	3.2 (3.1)	4.0 (3.9)	3.6 (3.9)	0.79
		Ankle	Maximum	4.2 (2.6)	6.3 (2.6)	7.2 (3.7)	0.07
			Minimum	-20.2 (7.4)	-12.2 (4.8)	-9.5 (5.1)	0.00 –
	Transverse	Hip	Maximum	-0.4 (3.6)	-0.1 (2.6)	0.2 (2.5)	0.46
			Minimum	-12.2 (3.9)	-11.3 (3.7)	-11.0 (3.7)	0.12
		Knee	Maximum	12.9 (3.7)	11.9 (3.7)	11.0 (2.3)	0.03 –
			Minimum	-8.2 (1.9)	-8.0 (2.1)	-8.9 (3.6)	0.72
		Ankle	Maximum	4.6 (3.4)	4.8 (3.7)	5.5 (2.6)	0.20
			Minimum	-9.0 (4.9)	-6.7 (4.0)	-5.8 (2.7)	0.01 –
Ground Reaction Force (N/BW)	Vertical	Maximum		1.25 (0.04)	1.28 (0.06)	1.23 (0.06)	0.04 –
	Anterior-Posterior	Maximum		0.25 (0.03)	0.23 (0.03)	0.21 (0.03)	0.00 —
		Minimum		-0.19 (0.03)	-0.19 (0.04)	-0.18 (0.05)	0.74
	Medial-Lateral	Maximum		0.03 (0.01)	0.02 (0.01)	0.01 (0.01)	0.27
		Minimum		-0.09 (0.02)	-0.10 (0.02)	-0.10 (0.01)	0.72
Moment (N-m/kg)	Hip	Maximum		1.20 (0.29)	1.29 (0.30)	1.10 (0.29)	0.08
		Minimum		-0.84 (0.31)	-0.88 (0.23)	-0.79 (0.14)	0.63
	Knee	Maximum		0.35 (0.12)	0.32 (0.09)	0.26 (0.10)	0.12
		Minimum		-0.54 (0.16)	-0.55 (0.16)	-0.60 (0.11)	0.79
	Ankle	Maximum		1.44 (0.16)	1.61 (0.18)	1.58 (0.16)	0.00 –
		Minimum		-0.21 (0.05)	-0.34 (0.10)	-0.32 (0.08)	0.01 –
Power (W/kg)	Hip	Maximum		1.52 (0.49)	1.46 (0.38)	1.21 (0.48)	0.00 –
		Minimum		-0.70 (0.17)	-0.68 (0.35)	-0.53 (0.16)	0.08
	Knee	Maximum		1.35 (0.47)	1.05 (0.42)	0.89 (0.23)	0.01 –
		Minimum		-1.77 (0.45)	-1.52 (0.36)	-0.99 (0.26)	0.00 —
	Ankle	Maximum		2.55 (0.62)	2.12 (0.25)	1.88 (0.52)	0.07
		Minimum		-1.06 (0.47)	-1.38 (0.43)	-1.34 (0.41)	0.07

Note: Values given as mean (s.d.), N=12

　Positive values indicate flexion, adduction, and external rotation; vertical, posterior and medial GRF; extensor moment and power generation

　Negative values indicate extension, abduction and internal rotation; anterior and lateral GRF; flexor moment and power absorption

　‑ statistically significant difference in Baseline and 1-inch Sole condition means (Fisher LSD, p<0.05)

　‑ statistically significant difference in Baseline and 2-inch Sole condition means (Fisher LSD, p<0.05)

　‑ statistically significant difference in 1-inch Sole and 2-inch Sole condition means (Fisher LSD, p<0.05)

Table 8. Biomechanics variables for running

Variable			Baseline	1-inch Sole	2-inch Sole	p
			Sole Condition			
Stride Length (m)			2.435 (0.285)	2.341 (0.392)	2.351 (0.289)	0.43
Velocity (m/s)			3.097 (0.324)	3.012 (0.362)	3.011 (0.327)	0.41
Cadence (steps/min)			153 (7)	156 (13)	154 (10)	0.54
% Stance			39.4 (4.4)	41.5 (4.0)	42.0 (3.3)	0.05
Angle (degrees)	Sagittal	Hip Maximum	38.2 (7.7)	38.6 (7.1)	37.6 (7.9)	0.96
		Hip Minimum	-25.9 (5.4)	-24.9 (3.4)	-25.6 (5.4)	0.65
		Knee Maximum	94.0 (10.9)	96.8 (11.7)	90.3 (10.7)	0.29
		Knee Minimum	7.7 (5.2)	9.7 (4.9)	6.6 (4.4)	0.25
		Ankle Maximum	23.8 (2.7)	26.0 (3.4)	25.4 (3.0)	0.08
		Ankle Minimum	-13.6 (4.2)	-10.0 (5.2)	-11.1 (4.9)	0.07
	Frontal	Hip Maximum	10.5 (3.5)	10.7 (4.9)	10.6 (4.6)	0.94
		Hip Minimum	-5.6 (3.5)	-5.6 (4.6)	-4.5 (3.3)	0.80
		Knee Maximum	18.2 (5.2)	18.2 (6.5)	18.5 (5.0)	0.93
		Knee Minimum	3.8 (3.9)	4.2 (3.5)	3.8 (3.9)	0.46
		Ankle Maximum	12.0 (5.7)	12.8 (3.6)	12.8 (4.3)	0.67
		Ankle Minimum	-13.4 (5.1)	-8.4 (3.9)	-8.6 (3.4)	0.00 ⁻
	Transverse	Hip Maximum	2.5 (4.0)	2.3 (1.8)	1.5 (1.6)	0.90
		Hip Minimum	-9.1 (3.2)	-9.0 (2.9)	-8.6 (3.3)	0.85
		Knee Maximum	18.3 (3.8)	18.1 (5.9)	17.9 (2.9)	0.92
		Knee Minimum	-8.8 (2.0)	-8.4 (2.0)	-8.2 (3.1)	0.73
		Ankle Maximum	6.2 (4.4)	4.2 (2.7)	5.1 (2.0)	0.42
		Ankle Minimum	-5.5 (3.8)	-5.1 (3.3)	-3.6 (2.5)	0.07
Ground Reaction Force (N/BW)		Vertical Maximum	2.45 (0.20)	2.45 (0.18)	2.41 (0.21)	0.99
		Anterior-Posterior Maximum	0.28 (0.03)	0.26 (0.04)	0.25 (0.04)	0.32
		Anterior-Posterior Minimum	-0.23 (0.06)	-0.20 (0.07)	-0.21 (0.05)	0.33
		Medial-Lateral Maximum	0.00 (0.01)	0.01 (0.01)	0.01 (0.01)	0.31
		Medial-Lateral Minimum	-0.23 (0.04)	-0.24 (0.04)	-0.23 (0.03)	0.63
Moment (N-m/kg)		Hip Maximum	2.03 (0.83)	1.76 (0.66)	1.51 (0.39)	0.36
		Hip Minimum	-0.71 (0.17)	-0.70 (0.17)	-0.64 (0.15)	0.75
		Knee Maximum	1.54 (0.49)	1.65 (0.50)	1.58 (0.40)	0.62
		Knee Minimum	-0.43 (0.61)	-0.43 (0.20)	-0.46 (0.22)	0.55
		Ankle Maximum	2.60 (0.30)	2.72 (0.40)	2.64 (0.40)	0.13
		Ankle Minimum	-0.33 (0.19)	-0.41 (0.35)	-0.20 (0.07)	0.13
Power (W/kg)		Hip Maximum	4.66 (2.00)	4.58 (2.28)	3.74 (2.12)	0.06
		Hip Minimum	-1.85 (0.85)	-1.47 (0.78)	-1.67 (0.58)	0.45
		Knee Maximum	3.77 (1.63)	4.25 (1.56)	3.50 (0.85)	0.40
		Knee Minimum	-5.30 (1.56)	-5.57 (1.78)	-4.62 (1.60)	0.43
		Ankle Maximum	8.16 (0.97)	7.75 (1.13)	7.51 (1.30)	0.35
		Ankle Minimum	-7.19 (0.79)	-7.24 (1.55)	-7.17 (1.47)	0.71

Note: Values given as mean (s.d.), N=12

Positive values indicate flexion, adduction, and external rotation; vertical, posterior and medial GRF; extensor moment and power generation

Negative values indicate extension, abduction and internal rotation; anterior and lateral GRF; flexor moment and power absorption

⁻ statistically significant difference in Baseline and 1-inch Sole condition means (Fisher LSD, $p<0.05$)

⁻ statistically significant difference in Baseline and 2-inch Sole condition means (Fisher LSD, $p<0.05$)

⁻ statistically significant difference in 1-inch Sole and 2-inch Sole condition means (Fisher LSD, $p<0.05$)

Table 9. Biomechanics variables for squatting

Variable			Sole Condition			p
			Baseline	1-inch Sole	2-inch Sole	
Cycle Time (sec)			2.428 (0.432)	2.566 (0.444)	2.520 (0.506)	0.52
Angle (degrees)	Sagittal	Hip Maximum	64.6 (5.7)	67.0 (5.1)	65.2 (4.4)	0.40
		Hip Minimum	3.5 (2.5)	4.6 (2.1)	3.8 (2.3)	0.37
		Knee Maximum	139.2 (10.6)	138.5 (10.7)	136.2 (12.2)	0.55
		Knee Minimum	11.6 (7.1)	10.7 (3.9)	10.2 (4.0)	0.69
		Ankle Maximum	31.7 (4.1)	32.1 (4.4)	32.1 (3.8)	0.65
		Ankle Minimum	3.9 (2.3)	3.7 (3.2)	4.3 (2.6)	0.37
	Frontal	Hip Maximum	-2.2 (3.2)	-1.2 (3.7)	-0.9 (3.0)	0.56
		Hip Minimum	-28.7 (5.9)	-27.3 (6.5)	-27.9 (5.8)	0.92
		Knee Maximum	23.8 (7.1)	23.8 (3.4)	23.6 (6.9)	0.90
		Knee Minimum	6.7 (2.7)	7.2 (3.7)	7.3 (3.2)	0.73
		Ankle Maximum	14.2 (5.1)	14.6 (3.8)	14.6 (3.5)	0.54
		Ankle Minimum	-1.7 (4.0)	-2.6 (2.4)	-0.6 (2.3)	0.28
	Transverse	Hip Maximum	-8.6 (3.4)	-8.0 (3.2)	-8.2 (2.7)	0.59
		Hip Minimum	-27.4 (5.5)	-25.3 (5.6)	-26.7 (4.6)	0.56
		Knee Maximum	33.7 (10.0)	33.7 (11.0)	33.7 (12.3)	0.80
		Knee Minimum	-0.9 (2.6)	-1.2 (3.0)	-0.01 (3.3)	0.28
		Ankle Maximum	1.8 (1.9)	1.8 (3.0)	3.5 (3.1)	0.10
		Ankle Minimum	-4.0 (4.0)	-2.5 (3.3)	-1.2 (3.3)	0.08
Ground Reaction Force (N/BW)		Vertical Maximum	0.13 (0.03)	0.15 (0.03)	0.15 (0.03)	0.47
		Anterior-Posterior Maximum	0.01 (0.01)	0.01 (0.00)	0.01 (0.00)	0.58
		Anterior-Posterior Minimum	-0.02 (0.01)	-0.02 (0.01)	-0.02 (0.01)	0.98
		Medial-Lateral Maximum	0.06 (0.02)	0.06 (0.01)	0.06 (0.01)	0.14
		Medial-Lateral Minimum	-0.01 (0.01)	-0.01 (0.01)	-0.01 (0.01)	0.06
Moment (N-m/kg)		Hip Maximum	0.27 (0.22)	0.24 (0.18)	0.11 (0.17)	0.07
		Hip Minimum	-0.41 (0.21)	-0.36 (0.22)	-0.39 (0.19)	0.83
		Knee Maximum	0.37 (0.23)	0.32 (0.17)	0.29 (0.21)	0.77
		Knee Minimum	-0.32 (0.19)	-0.21 (0.11)	-0.10 (0.07)	0.12
		Ankle Maximum	0.45 (0.20)	0.36 (0.23)	0.28 (0.21)	0.10
		Ankle Minimum	-0.24 (0.23)	-0.22 (0.21)	-0.22 (0.19)	0.96
Power (W/kg)		Hip Maximum	0.39 (0.17)	0.30 (0.06)	0.32 (0.28)	0.55
		Hip Minimum	-0.53 (0.20)	-0.56 (0.32)	-0.48 (0.24)	0.65
		Knee Maximum	0.73 (0.27)	0.57 (0.17)	0.38 (0.19)	0.19
		Knee Minimum	-0.54 (0.31)	-0.30 (0.14)	-0.41 (0.26)	0.42
		Ankle Maximum	0.14 (0.05)	0.09 (0.08)	0.09 (0.06)	0.68
		Ankle Minimum	-0.09 (0.03)	-0.10 (0.07)	-0.06 (0.03)	0.82

Note: Values given as mean (s.d.), N=12
Positive values indicate flexion, adduction, and external rotation; vertical, posterior and medial GRF; extensor moment and power generation
Negative values indicate extension, abduction and internal rotation; anterior and lateral GRF; flexor moment and power absorption
- statistically significant difference in Baseline and 1-inch Sole condition means (Fisher LSD, p<0.05)
- statistically significant difference in Baseline and 2-inch Sole condition means (Fisher LSD, p<0.05)
- statistically significant difference in 1-inch Sole and 2-inch Sole condition means (Fisher LSD, p<0.05)

Table 10. Biomechanics variables for right kneeling

	Variable		Baseline	1-inch Sole	2-inch Sole	p
			Sole Condition			
	Cycle Time (sec)		2.985 (0.317)	3.308 (0.431)	3.553 (0.303)	0.00 —
Angle (degrees)	Sagittal	Hip Maximum	12.0 (5.5)	19.1 (6.8)	21.2 (8.8)	0.00 –
		Hip Minimum	-4.7 (4.9)	-3.7 (3.6)	-5.3 (2.9)	0.77
		Knee Maximum	123.5 (10.6)	136.1 (16.3)	133.7 (15.5)	0.00 –
		Knee Minimum	8.3 (7.9)	7.5 (5.0)	4.6 (5.7)	0.33
		Ankle Maximum	33.3 (4.4)	35.6 (4.6)	35.7 (5.5)	0.08
		Ankle Minimum	10.7 (2.0)	9.3 (3.4)	7.3 (3.5)	0.25
	Frontal	Hip Maximum	6.1 (3.4)	6.8 (4.5)	9.0 (5.6)	0.13
		Hip Minimum	-5.9 (5.2)	-9.4 (5.7)	-8.0 (5.7)	0.12
		Knee Maximum	19.8 (5.4)	18.3 (6.9)	19.0 (3.9)	0.33
		Knee Minimum	5.8 (3.8)	4.7 (4.1)	5.2 (3.4)	0.17
		Ankle Maximum	12.4 (4.6)	11.3 (5.3)	15.9 (7.2)	0.10
		Ankle Minimum	-24.6 (9.8)	-8.9 (5.4)	-3.0 (3.8)	0.00 –
	Transverse	Hip Maximum	-1.6 (3.7)	-1.7 (3.7)	-1.5 (2.7)	0.74
		Hip Minimum	-16.4 (5.0)	-15.4 (4.9)	-15.0 (2.9)	0.48
		Knee Maximum	13.0 (7.0)	15.7 (9.2)	17.4 (10.4)	0.01 –
		Knee Minimum	-5.7 (3.2)	-5.0 (3.0)	-5.2 (3.5)	0.83
		Ankle Maximum	4.6 (2.7)	5.5 (5.1)	8.2 (4.6)	0.02 –
		Ankle Minimum	-14.0 (7.0)	-8.5 (4.8)	-7.3 (5.5)	0.01 –
Ground Reaction Force (N/BW)	Vertical	Maximum	0.65 (0.18)	0.70 (0.12)	0.78 (0.10)	0.02 – –
	Anterior-Posterior	Maximum	0.15 (0.03)	0.11 (0.03)	0.12 (0.05)	0.07
		Minimum	-0.04 (0.02)	-0.04 (0.03)	-0.05 (0.04)	0.22
	Medial-Lateral	Maximum	0.03 (0.02)	0.03 (0.01)	0.03 (0.01)	0.96
		Minimum	-0.08 (0.03)	-0.07 (0.02)	-0.09 (0.02)	0.45
Moment (N-m/kg)	Hip	Maximum	0.79 (0.74)	0.97 (0.69)	0.90 (0.76)	0.54
		Minimum	-1.05 (0.74)	-1.78 (0.96)	-1.34 (1.31)	0.38
	Knee	Maximum	1.24 (0.89)	1.76 (0.84)	1.43 (1.13)	0.35
		Minimum	-0.87 (0.86)	-1.00 (0.71)	-0.77 (0.66)	0.72
	Ankle	Maximum	0.81 (0.49)	1.14 (0.64)	1.21 (0.71)	0.72
		Minimum	-0.97 (0.78)	-1.48 (0.89)	-1.33 (1.17)	0.47
Power (W/kg)	Hip	Maximum	0.16 (0.10)	0.65 (0.40)	0.31 (0.19)	0.15
		Minimum	-0.18 (0.07)	-0.28 (0.15)	-0.54 (0.37)	0.28
	Knee	Maximum	1.45 (0.64)	2.02 (0.71)	1.71 (1.49)	0.37
		Minimum	-1.35 (0.48)	-2.96 (1.94)	-1.40 (0.52)	0.09
	Ankle	Maximum	0.37 (0.21)	0.64 (0.24)	0.79 (0.36)	0.05 –
		Minimum	-0.31 (0.11)	-0.66 (0.27)	-0.59 (0.33)	0.39

Note: Values given as mean (s.d.), N=12

Positive values indicate flexion, adduction, and external rotation; vertical, posterior and medial GRF; extensor moment and power generation

Negative values indicate extension, abduction and internal rotation; anterior and lateral GRF; flexor moment and power absorption

– statistically significant difference in Baseline and 1-inch Sole condition means (Fisher LSD, p<0.05)

– statistically significant difference in Baseline and 2-inch Sole condition means (Fisher LSD, p<0.05)

– statistically significant difference in 1-inch Sole and 2-inch Sole condition means (Fisher LSD, p<0.05)

Table 11. Biomechanics variables for left kneeling

	Variable		Baseline	1-inch Sole	2-inch Sole	p
			Sole Condition			
	Cycle Time (sec)		2.798 (0.357)	2.928 (0.430)	3.024 (0.400)	0.16
Angle (degrees)	Sagittal — Hip	Maximum	73.0 (4.9)	71.8 (5.5)	71.8 (5.4)	0.65
		Minimum	2.0 (4.8)	3.5 (2.5)	3.2 (4.1)	0.37
	Sagittal — Knee	Maximum	126.2 (9.4)	130.6 (5.9)	136.2 (8.2)	0.00 —
		Minimum	8.9 (10.6)	8.1 (4.4)	7.9 (5.5)	0.94
	Sagittal — Ankle	Maximum	23.6 (7.5)	25.7 (4.8)	27.0 (5.2)	0.04 ⁻
		Minimum	2.7 (2.6)	2.9 (2.2)	2.8 (2.2)	0.97
	Frontal — Hip	Maximum	4.4 (4.3)	3.2 (4.6)	2.6 (4.9)	0.44
		Minimum	-21.9 (6.5)	-25.5 (4.1)	-26.7 (5.7)	0.04 ⁻
	Frontal — Knee	Maximum	23.5 (4.5)	21.8 (4.1)	22.3 (4.2)	0.61
		Minimum	6.0 (3.7)	6.7 (3.6)	7.1 (3.9)	0.23
	Frontal — Ankle	Maximum	13.0 (4.1)	16.0 (4.4)	16.0 (4.7)	0.08
		Minimum	1.9 (2.6)	2.4 (1.6)	3.1 (2.2)	0.41
	Transverse — Hip	Maximum	-3.7 (3.0)	-2.9 (4.1)	-2.6 (3.5)	0.82
		Minimum	-21.3 (4.1)	-22.7 (4.5)	-23.2 (6.2)	0.19
	Transverse — Knee	Maximum	26.8 (7.3)	31.0 (7.2)	34.0 (5.9)	0.00 −
		Minimum	-4.0 (2.4)	-1.8 (4.2)	-1.7 (2.7)	0.09
	Transverse — Ankle	Maximum	5.7 (3.6)	7.0 (2.7)	7.7 (3.6)	0.02 ⁻
		Minimum	-1.7 (3.7)	-2.2 (2.4)	-1.8 (2.8)	0.78
Ground Reaction Force (N/BW)	Vertical	Maximum	0.55 (0.15)	0.52 (0.18)	0.63 (0.17)	0.20
	Anterior-Posterior	Maximum	0.04 (0.03)	0.03 (0.03)	0.02 (0.01)	0.41
		Minimum	-0.08 (0.03)	-0.10 (0.02)	-0.09 (0.03)	0.20
	Medial-Lateral	Maximum	0.04 (0.02)	0.04 (0.03)	0.01 (0.02)	0.91
		Minimum	-0.06 (0.02)	-0.06 (0.02)	-0.06 (0.02)	0.99
Moment (N-m/kg)	Hip	Maximum	0.66 (0.40)	0.95 (0.27)	0.84 (0.29)	0.24
		Minimum	-0.67 (0.41)	-0.59 (0.56)	-0.29 (0.24)	0.17
	Knee	Maximum	0.62 (0.25)	0.46 (0.09)	0.61 (0.25)	0.37
		Minimum	-0.27 (0.33)	-0.17 (0.22)	-0.09 (0.23)	0.24
	Ankle	Maximum	0.48 (0.30)	0.55 (0.18)	0.64 (0.24)	0.23
		Minimum	-0.39 (0.28)	-0.24 (0.21)	-0.18 (0.16)	0.36
Power (W/kg)	Hip	Maximum	1.07 (0.75)	1.24 (0.64)	1.28 (0.44)	0.45
		Minimum	-0.85 (0.51)	-1.12 (0.38)	-0.84 (0.28)	0.46
	Knee	Maximum	1.15 (0.60)	1.07 (0.62)	1.16 (0.62)	0.99
		Minimum	-1.18 (0.56)	-0.90 (0.30)	-1.06 (0.65)	0.96
	Ankle	Maximum	0.21 (0.15)	0.30 (0.14)	0.29 (0.19)	0.18
		Minimum	-0.19 (0.15)	-0.28 (0.14)	-0.26 (0.21)	0.51

Note: Values given as mean (s.d.), N=12
Positive values indicate flexion, adduction, and external rotation; vertical, posterior and medial GRF; extensor moment and power generation
Negative values indicate extension, abduction and internal rotation; anterior and lateral GRF; flexor moment and power absorption
⁻ statistically significant difference in Baseline and 1-inch Sole condition means (Fisher LSD, p<0.05)
⁻ statistically significant difference in Baseline and 2-inch Sole condition means (Fisher LSD, p<0.05)
⁻ statistically significant difference in 1-inch Sole and 2-inch Sole condition means (Fisher LSD, p<0.05)

Table 12. Obstacle completion times (seconds)

Obstacle	Sole Condition			p
	Baseline	1-inch Sole	2-inch Sole	
Log Balance	12.7 (3.0)	15.4 (3.4)	16.0 (4.4)	0.01 −
Up & Down	5.4 (1.0)	6.0 (2.2)	6.4 (3.0)	0.13
Tires	7.8 (0.9)	8.3 (1.3)	8.7 (1.4)	0.02 -
House	9.3 (0.9)	9.5 (1.2)	9.9 (1.8)	0.07
Zig-Zag	5.9 (0.7)	5.9 (0.7)	6.3 (0.9)	0.12

Note: values given as mean (s.d.), N=12
- statistically significant difference in Baseline and 1-inch Sole condition means (Fisher LSD, p<0.05)
- statistically significant difference in Baseline and 2-inch Sole condition means (Fisher LSD, p<0.05)
- statistically significant difference in 1-inch Sole and 2-inch Sole condition means (Fisher LSD, p<0.05)
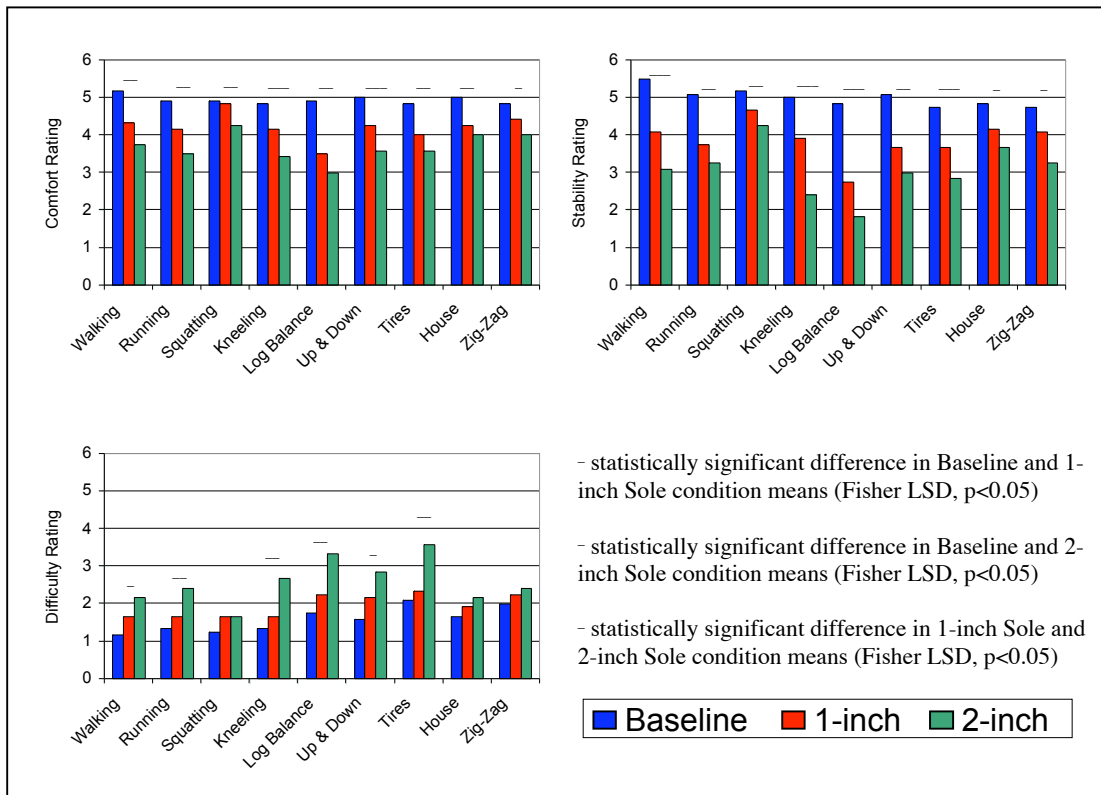
Fig. 101. Mean comfort, stability and difficulty questionnaire responses (N=12).

APPENDIX E

FEASIBILITY STUDY - POWER SOURCE COMPARISON

This appendix is an excerpt from an ORNL exoskeleton feasibility study conducted for DARPA in 2000 (Jansen et al., 2000). This appendix provides some of the background and basis for the design approach taken and is included here for completeness and the convenience of the reader.

Issues relating to potential power sources and both steady-state and transient power requirements will be addressed. While no single power source can meet all the requirements optimally, a hybrid system that can satisfy both steady-state and transient power needs appears to be the most promising approach.

POWER AND ENERGY REQUIREMENTS

To get a rough idea as to the power requirement of an exoskeleton, it is instructive to look at the power requirements of man-made and living vehicles (i.e., animals). Gabrielli and von Karman (Gabrielli, 1950) showed that specific resistance, ε, is an accurate measure of power requirement for a given velocity for a wide range of different types of mechanical locomotion including living organisms. Specific resistance is defined (using the same units used by Gabrielli) as

$$\varepsilon = \frac{P}{W \cdot V} \tag{15}$$

where P = power in units of lb-ft/s, W = weight in lb, and V = speed in ft/s. For a human being walking on level ground, the specific resistance is around 0.06 to 0.09 and increases to 0.12 when running. Bicycles, cars, and horses at low velocities have a specific resistance ranging from 0.01 to 0.05. Since the specific resistance of an exoskeleton is not known, we will assume a conservative range from 0.01 to 0.1. If the exoskeleton and its payload is W_{ex} then the power requirement, P_{ex}, of such a machine must range from $P_{ex} = (.01 \text{ to } 0.1)* W_{ex} V_{ex}$ where V_{ex} is the velocity of the exoskeleton. At a speed of 2 m/s (or 4.5!mph or 6.6!ft/s), P_{ex} would range from 6.6!lb-ft/s to 66!lb-ft/s per 100 lb of load (or 8.9 to 89 W per 100 lb of load). For a 350!lb total load (exoskeleton and payload), the upper power requirement is around 310!W. Standard earth-moving equipment has a payload to weight ratio of 1:2, which implies a conventional hydraulic system and would suggest an exoskeleton weight of approximately 233!lb and a payload of 117!lb. Based on anticipated performance improvements of an exoskeleton in comparison to heavy equipment, the payload to weight ratio is expected to be significantly better.

Two cases will be compared, walking while lifting 100!lb and running. If in addition to walking, the power required to lift 100!lb vertically against gravity at 1!ft/s is added, the additional power is around 140!W. Thus, for an exoskeleton with maximum payload, the total power required could be expected to around 440!W, assuming a worst-case scenario and extrapolating the same power requirements as those for a human. The second case is running. As mentioned above, about 310!W were calculated assuming a speed of 2!m/s (4.5!mph). Increasing the speed to 3 m/s (6.7!mph) and the specific resistance range to 0.01 to 0.12 for running, similarly, gives an estimate of approximately 560!W. Based on these two scenarios, 600!W should be a conservative upper bound for the required steady-state power. Peak power demands could be significantly larger than 600 W and would affect the overall sizing of the power supply, unless temporary energy storage is used to offset peak power demands. For motions such as rapid, deep, knee bends, or climbing stairs, peak power demands could reach as high as 2!kW. It is clear that an exoskeleton power source will have to have both large energy (600!W times operational hours) and peak-power (2!kW, > 3 times the nominal load) capacities.

POWER SOURCES

As discussed above, there could be significant differences in the steady-state power requirements and the peak power or transient demands. The power source must, therefore, be able to meet both the energy requirements and peak power demands and comparison of potential power sources must be made with respect to meeting both of these requirements. For an exoskeleton type of system, the specific power (power ÷ weight) and specific energy (energy ÷ weight) are the parameters that are more useful for comparison of potential power systems. Ragone Diagrams (Fig.!102), which plot specific energy vs specific power, provides a means for making broad, general, comparisons between potential power sources. However, it should be noted that Ragone Diagrams provide information on steady-state specific power and specific energy, but they do not provide any indication as to the response time of a power source and thus, its ability to follow demand.

Figure 102 provides a general comparison of typical fuel cells, batteries, internal combustion engines, and super capacitors. It should be noted that on-going research is continuing to expand the capabilities of these power sources. Although other power sources and storage devices, (e.g.,!compressed gas, thermoelectric devices, and flywheels) are available, they are not considered practical for a remote mobile device, such as an exoskeleton. From Fig. 102, it can be seen that internal combustion engines have relatively high specific power and specific energy and a hybrid system such as a fuel cell and either batteries or super capacitors can also meet the requirement of high specific power and energy. Using a single power source requires sizing the source such that it can meet both steady-state energy needs and peak power loads. For systems such as the exoskeleton, where peak loads can be several times the steady-state loads, this may result in an oversized source (both weight and cube) and a significant reduction in efficiency. Alternatively, a hybrid system can handle large variations in steady-state and peak loads, as one source is sized to provide for power peaks and another to provide steady-state energy. A hybrid system offers the possibility of a more efficient system, optimized for both peak power and steady-state energy needs at the cost of increased complexity. In the following section, potential power sources will be discussed with regard to the exoskeleton specific requirements.
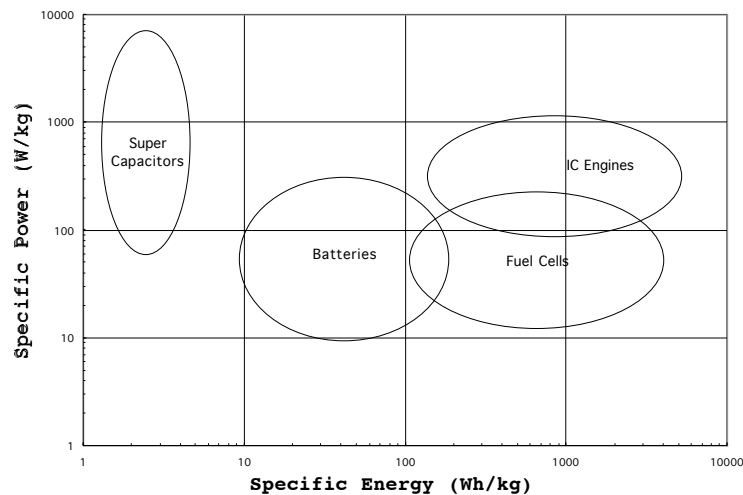
Fig. 102. Comparison of different power sources.

116

Fuel Cells

The National Aeronautics and Space Administration (NASA) demonstrated the potential of fuel cells, originally discovered in 1839, by using them to provide power during space flights in the 1960s. Since then, research has been ongoing with a focus on improving efficiency and economic viability. There are multiple types of fuel cells, typically designated by the electrolyte type, currently in various stages of development (Table 13). These include polymer electrolyte membrane (PEM), alkaline (AFC), phosphoric acid (PAFC), molten carbonate (MCFC), and solid oxide (SOFC). Each has different characteristics and is suited to particular applications. MCFCs and SOFCs operate between 600°C and 1000°C and thus, are not suitable for applications that require close proximity to a human operator. PAFCs, which use concentrated phosphoric acid (up to 100%) for the electrolyte, can operate in temperature ranges from 150 to 220°C, but are poor ionic conductors, susceptible to carbon monoxide (CO) poisoning at the lower temperature range, and also have low power to weight ratios (Hirschenhofer, 1999). AFCs, which operate in the 90 to 100 °C range, have been limited to military and space applications due to the expense of removing carbon dioxide (CO_2) from the fuel and air streams and are generally being phased out (Thomas, 1999). PEM fuel cells have a relatively low operating temperature (about 80°C) and are the most appropriate for portable applications in close proximity to an operator.

Table 13. Comparison of fuel cell types
(Sources: Hirschenhofer, 1999 and Thomas, 1999.)

Fuel Cell Type	Electrolyte	Operating Temperature (°C)	Comments
Alkaline (AFC)	Aqueous solution of potassium hydroxide soaked in a matrix	90–100	Expensive removal of CO_2 required. High performance.
Phosphoric Acid (PAFC)	Immobilized liquid phosphoric acid	175–205	Low power/weight and power/vol. High efficiency. Tolerant of fuel impurities.
Polymer Electrolyte Membrane (PEM)	Ion exchange membrane	60-100	Low temperatures. Quick startup. Sensitive to fuel impurities.
Molten Carbonate (MCFC)	Immobilized liquid molten carbonate	600-1000	High temperatures lead to corrosion and cell breakdown.
Solid Oxide (SOFC)	Ceramic (zirconium oxide based)	800 -1000	High temperature results in higher efficiency, inexpensive catalysts, more fuel options.

While ICEs have superior steady-state specific power, fuel cells are more human-compatible when noise and waste by-products are considered. In particular, PEM fuel cells operate at low temperatures with water as the waste by-product. The PEM fuel cells, however, require careful water management and a particularly clean source of hydrogen (essentially CO and CO_2 free). These fuel cells are susceptible to CO poisoning, which adversely affects the fuel cell voltage, especially at higher current densities (Hirschenhofer, 1999). A major focus of research and development with respect to fuel cells is related to reformer technology, which is being developed to extract hydrogen from hydrocarbon fuels. Significant progress has been made in research concerned with direct methanol PEM fuel cells, which use the methanol directly without

going through a reformer. However, the power density of direct methanol PEMs still lags that of hydrogen/air PEMs due to the need for significantly more of the expensive platinum catalyst (in comparison to hydrogen/air PEMs), and the loss of performance caused by methanol "crossover" (Thomas, 1999). A potential clean source of hydrogen for a PEM is chemical reactions, which are similar to commercially available systems based on a single exothermic sodium hydroxide reaction. The water generated at the fuel cell reaction can be recycled for use in the hydrogen generation, to reduce weight and further increase efficiency.

Commercially available fuel cells in the 500!W to 2!kW range can have specific powers on the order of 50 to 150!W/kg (Ballard and Analytic Power Corporation). AeroVironment, Inc., has developed custom fuel cells for remote power applications in the same range, with specific powers of 675!W/kg for the cells only and on the order of 225!W/kg including ancillary support equipment. The specific power is comparable to that for batteries and below that for super capacitors and internal combustion engines. The overall specific energy of the fuel cell system is highly dependent upon the generating system for hydrogen, which has a specific energy (higher heating value) of 40!kWh/kg.

Chemical reactions as a means to generate a suitable supply of hydrogen for a fuel cell have been examined. Three types of hydrogen-releasing chemical processes have been evaluated as means for feeding a fuel cell that would power an exoskeleton. These processes are the reaction of pure elements (alkali metals, alkaline earth elements, etc.) with water, reaction of alkali and alkaline earth hydrides with water, and the decomposition of metal hydrides. The methods considered are summarized and compared and the relative advantages and disadvantages of each with regard to the proposed application discussed.

Alkali and Alkaline Earth/Water Reactions

The reactions of alkali elements (specifically lithium, sodium, and potassium) with water are rapid, irreversible, and highly exothermic. The general form of the reaction is

$$2M \ + \ 2H_2O \ \rightarrow \ 2MOH \ + \ H_2. \tag{16}$$

As the reactions are irreversible, the rate cannot be altered by controlling the concentration (or the pressure) of the products. The rate of hydrogen generation may be controlled by the rate at which either or both of the reactants are added to the reaction vessel. However, controlling alkali-water reactions by controlling the rate of water addition is impracticable because the amount of heat generated per mass of water added is more than sufficient to increase the temperature of the product to the boiling point of the hydroxide. It is preferable to control hydrogen generation by limiting the rate at which the alkali is introduced to (or comes into contact with) water. Because of the reactivity of alkali elements with water, it is essential that these alkalis be kept in a moisture-free environment before their use. Because of their inflammability, it is also essential that the heat generated by the reaction be removed efficiently.

The primary advantage of alkali-water reactions for hydrogen generation is the relatively low mass of reactants required per mass of hydrogen released, particularly when lithium and water are reacted. Much of this advantage is lost if a large excess of water is needed to effect heat removal from the process. Other advantages of alkali-water reactions are the complete conversion of reactants and a high rate of reaction. In addition to exothermicity, the

disadvantages of these reactions include chemical instability of the reactants, difficulty in regenerating the reactants for reuse, and formation of a corrosive (caustic) by–product.

In addition to alkali elements, reactions of alkaline earth elements (e.g.,!calcium, magnesium) with water have been considered. These reactions take place less rapidly than do alkali-water reactions and they produce somewhat less corrosive bases. However, the mass of reactants required per mass of hydrogen produced is increased over the alkali-water case, because of the need for two molecules of water per atom of alkaline earth element. As with alkali/water reactions, alkaline earth/water reactions are highly exothermic (Table 14).

Table 14. Comparison of hydrogen-generating chemical reactions

Reaction	$\Delta H_{rxn, 298K}$, kcal	$\Delta H_{rxn, 298K}$, kcal/gmol H_2	Mass Ratio Reactants:H_2
$2Na + 2H_2O \rightarrow 2NaOH + H_2$	-87.78	-87.78	40.7
$2Li + 2H_2O \rightarrow 2LiOH + H_2$	-106.38	-106.38	24.8
$Ca + 2H_2O \rightarrow Ca(OH)_2 + H_2$	-103.04	-103.04	37.8
$NaH + H_2O \rightarrow NaOH + H_2$	-30.22	-30.22	20.8
$LiH + H_2O \rightarrow LiOH + H_2$	-31.65	-31.65	12.9
$CaH_2 + 2H_2O \rightarrow Ca(OH)_2 + 2H_2$	-57.94	-28.97	19.4
$B_2H_6 + 6H_2O \rightarrow 2B(OH)_3 + 6H_2$	-107.98	-18.00	11.2
$NaBH_4(aq) + 2H_2O \rightarrow NaBO_2(aq) + 4H_2$	Data not[a] available	Data not available	18.77[b]
$NaBH_4 + 2H_2O \rightarrow NaBO_2(aq) + 4H_2$	-46.68	-11.67	9.16[c]
$2LiH \leftrightarrow Li + H_2$	43.2	43.2	7.9
$CaH_2 \leftrightarrow Ca + 2H_2$	45.1	22.6	10.4
$TiFeH_{1.7} \leftrightarrow TiFe + 0.85H_2$	6.5	7.6	61.5

[a]Enthalpy data for sodium borohydride were not available for the analysis. It is expected that the heat released per g-mole of hydrogen produced will be approximately equal to that released by the hydrolysis of crystalline $NaBH_4$.
[b]Mass ratio assumes that water consumed by the hydrolysis reaction is not replenished.
[c]Mass ratio is based on the necessary replenishment of water consumed by the reaction.

Hydrolysis of Binary Hydride and Tertiary Hydrides

Hydrogen is generated by the reaction of binary hydrides with water according to the general reaction

$$MH_x + xH_2O \rightarrow M(OH)_x + xH_2, \qquad (17)$$
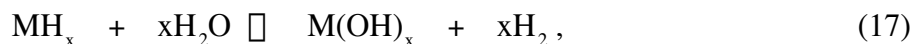
where "x" is the valence of the cation. Reactions of the hydrides of lithium, sodium, calcium, and boron have been considered for the proposed application.

As Eq. (17) indicates, the reactions of alkali and alkaline earth hydrides with water occur irreversibly, and results in the release of hydrogen and the formation of a hydroxide. Relative to the hydrolysis reactions of pure alkalis and alkaline earths, the hydrolysis reactions of binary hydride release less energy per unit of hydrogen released and requires less reactant mass per mass of hydrogen released.

In addition to alkali and alkaline hydride reactions, the reaction of diborane (B_2H_6) with water was evaluated. The hydrolysis of diborane has the advantages of relatively low heat generation and a low mass ratio of reactants-to-hydrogen-generated. The physical state of diborane (a gas at ambient conditions) is both an advantage and a major disadvantage. Control of hydrogen generation by diborane hydrolysis can be accomplished by metering the flow of reactant gas through a water-containing vessel. However, producing hydrogen in a compact processing system would require storage of diborane at high pressure.

The hydrolysis reaction of the tertiary hydride sodium borohydride ($NaBH_4$) has been considered. Millennium Cell Company (MCC) is commercializing a process in which the hydride (in aqueous solution) is hydrolyzed in the presence of a metal catalyst (e.g., ruthenium, nickel, and cobalt) (Amendola, 2000). The MCC process is based on a based on a proprietary catalyst. Initial analysis indicates that the rate of hydrogen generation from the $NaBH_4$ process far exceeds that required to power an exoskeleton and that the rate of H_2 generation decreases with increasing borate concentration. A low percentage of sodium hydroxide may be required in the aqueous feed solution to suppress slow hydrolysis before the introduction of the catalyst.

The use of an aqueous feed solution during the MCC process simplifies control of the reaction rate and provides a heat transfer medium. Using a 25!wt!% feed solution (containing NaOH at 1!wt!%), the total mass of the initial feed solution charge required to generate 1!lb of hydrogen is 18.77!lb. The rate of generation will not remain constant because of disproportionate (by weight) depletion of sodium borohydride and water during the reaction.

To minimize the mass of reactants, the MCC process could be modified so that the solid $NaBH_4$ is blended with water on demand, using water recycled from the fuel cell. The effect on the rate of hydrogen generation is unknown, as is the effect on the rate control scheme. In addition, no heat sink for removal of the heat generated by the reaction is present. This may be a significant problem, as the heat released during the production of one pound of hydrogen from the solid borate is approximately equal to that required to vaporize 11!lb of water at ambient conditions.

Metal Hydride Decomposition

Thermal decomposition of metal hydrides is the most commonly used means of hydrogen release from a chemical storage medium. Decomposition reactions are reversible and endothermic. Consequently, terminating the input of heat to the process can stop the reaction. Adjusting the rate of heat input or the hydrogen pressure can control the rate of hydrogen released over the process. Furthermore, the density of hydrogen stored on metal substrates is greater than the density of pure, liquid hydrogen.

Binary hydrides are not generally suitable for on-demand release because of their thermal stability. For example, hydrides of lithium, sodium, and calcium release hydrogen at significant pressures (i.e., 1!atm) only at temperatures in excess of 300ºC. Transition metal and rare-earth alloy hydrides are better suited for hydrogen release applications since hydrogen is released effectively at temperatures slightly above ambient. As a rule of thumb, in order for hydrogen to be released at 1!atm pressure and at a temperature of about 27ºC, the heat of decomposition should be 9!kcal/gmole for H_2. Of the hydride substrates developed for fuel cell applications, the titanium-iron substrate has undergone the most development. The hydride:hydrogen mass ratio for the $TiFeH_{1.7}$ hydride is about 61.

From a mass conservation standpoint, the hydrolysis of $NaBH_4$ is the most attractive option for hydrogen generation. Generation of 1 lb of hydrogen will consume 9.16 lb of sodium borohydride. At a hydrogen production rate of 1 lb/8 h, heat will be generated at a rate of 1,303 Btu/h.

From a safety standpoint, decomposition of a transition metal hydride (probably a TiFe alloy) is the best option for generating the needed hydrogen. However, the mass of substrate required to support 1 lb of hydrogen may be too great for the exoskeleton application.

Of the individual hydrogen mechanisms considered, no single reaction appears to meet the need for hydrogen generation at a rate of 0.125 lb/h (1 lb over an 8-h period) without presenting significant engineering challenges. The hydrolysis reactions would require design of a compact, low-weight, heat-transfer system to remove the heat produced by reaction and with the exception of the catalytic reaction of sodium borohydride, will result in the gradual build-up of a corrosive hydroxide solution. This corrosive hydroxide solution will eventually have to be disposed of or neutralized.

In addition to the single-step processes evaluated, a two-step operation has been considered in which calcium hydride is hydrolyzed and the hydroxide is then neutralized with nitric acid. The combined heat generated per gram mole of hydrogen generated is 32.96 kcal. The ratio of reactant-to-hydrogen mass is 66.3. Based on the heat released and the mass ratio, this approach is less favorable than decomposition of a transition metal hydride.

ICEs

In general, ICEs are more efficient when the overall energy output is high in comparison to the power output—in other words, the weight of the fuel is high in comparison to the weight of the engine. Although this is not the case for the exoskeleton application, ICEs are still an option worthy of consideration. Reciprocal diesel engines and turbines, in particular, will be discussed. While new developments are currently being pursued for both small diesel and turbines, which will increase their attractiveness for an exoskeleton application, noise, heat, and emissions remain issues that must be confronted, generally at the expense of increased weight. Gasoline engines, which are more readily available in the 1 to 2 kW range, were not considered a viable alternative for a fieldable system due to the hazards associated with gasoline.

The power density of 1 to 40 kW diesel engines typically range from 100 to 400 W/kg, with fuel consumption in the 200 to 300 g/kWh range (Theis, 2000; Heywood, 1988). Fuel consumption is generally increased in smaller scale diesel engines and generators. There are few diesel engines available in the lower power ranges. While a company called D-Star Engineering Corporation is currently making smaller scale diesels and is planning a 1 kW engine and generator set, it is doubtful that these will be available within the next one to two years.

In general, turbine fuel consumption would be anticipated to be from 5 to 15% less efficient than that for reciprocating diesels (Andriulli, 1999; Heywood, 1988). Micro-turbine performance does not scale well below 25 kW and fuel consumption tends to increase more in comparison to piston engines at partial loads (Andriulli, 1999). However, there are micro and mesoscopic turbine generators currently being developed under DARPA sponsorship, which offer the possibilities of compact power sources, which could be advantageous. These turbine generators,

if successful, could potentially have specific powers up to 1,000!W/kg and specific energies to 3,500 Wh/kg.

Batteries

A variety of battery options are currently commercially available. Table!15 and Fig.!103 summarize the specific power and specific energy for a number of available batteries.

The difficulty of meeting both the power and energy requirements while minimizing the weight is a concern with batteries. However, some recent developments could make the use of batteries more desirable for the exoskeleton application. First, AeroVironment, Inc., has recently tested NiMH batteries (both Energizer™ and Panasonic™) that have power densities of 1!kW/kg for up to 10!s with a resulting drop in storage efficiency to only 2.8!Wh/kg. Such a battery could be very useful for meeting peak loads in a hybrid system. Also, another company EVonyx has developed a zinc air power cell (sometimes referred to as a semi-fuel cell) that shows significant promise. The power cell utilizes a replaceable zinc fuel card that can be disposable or rechargeable. If the projected improvements in specific energy and specific power are met, the cell could meet both energy and power requirements at a reasonable weight and could be a viable potential power source for the exoskeleton application.

Table 15. Battery comparison

Type	Specific Energy (Wh/kg)	Specific Power (W/kg)	Cycles to 80%
Pb-acid	30–45	200	200–1000
Ni-Cd	40–55	190–260	500–1000
NiMH	50–70	180–200	500–1000
Li ion	100–250	300–800	500–1200
Ag-Zn	140–200	100–330	100–250
Ag-Cd	55–95	100–220	300–500
Zn-Air	150–300	50–100	
Al-Air	350	500–600	
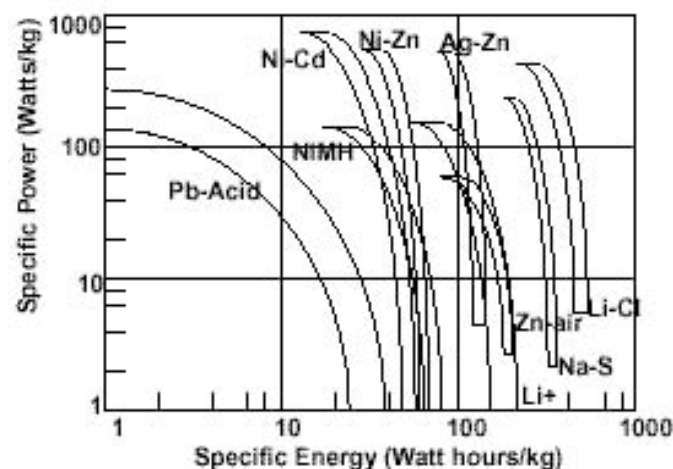
Fig. 103. Battery Ragone Diagram.
(Source: Dowling, January 1997.)

Super Capacitors

Super capacitors could also be used in a hybrid system to meet peak power demands. Figures!104 and 105 show the energy stored as well as the peak power available in super capacitors (data taken from Maxwell Technologies' Ultra Capacitor Series). From the figures, it can be seen that a relatively high specific power of 7!kW/kg and a relatively low specific energy of 3.5!Wh/kg are available. Thus, the super capacitors can provide a significant amount of power over a short period of time and could be extremely useful for load leveling in hybrid systems.
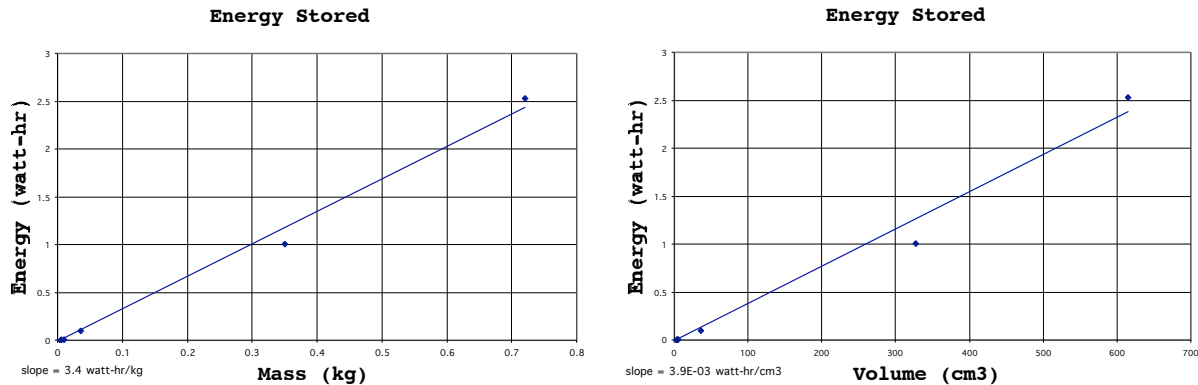
Fig. 104. Super capacitor energy storage vs mass and volume.
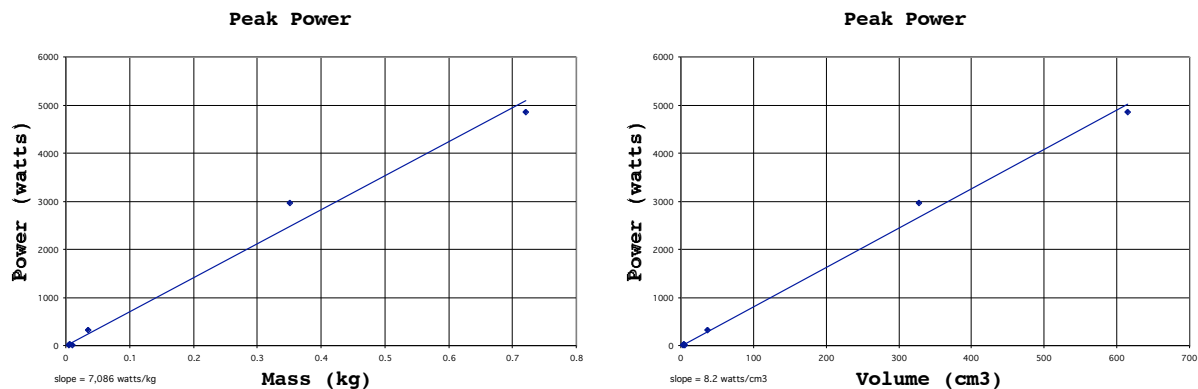
Fig. 105. Super capacitor peak power vs mass and volume.

POWER SOURCES SUMMARY

A power source for an exoskeleton must satisfy both power and energy requirements. With the significant variability in anticipated power demands, the ability of the power source to respond to peak loads without impeding performance is essential. Over-sizing a single power source to meet both power and energy requirements is not consistent with the need for efficiency required by this application. A hybrid power system, where transient peak power demands are met with one source and mission energy requirements are met with another source, can enhance efficiency at the expense of a more complicated system. Super capacitors and NiMH batteries are both capable of meeting peak transient load requirements, but they are insufficient as an energy

source. A fuel cell fed by hydrogen, which is generated by a chemical reaction and an ICE both are capable of meeting system energy requirements.

Table 16 compares the weight for three possible power sources, diesel engine, fuel cell, and batteries, as well as four possible hybrid systems. While the weights for the ICE are lower than those for the fuel cell, it must be noted that the ICE weights do not include provisions for signature (noise, thermal, and emissions) reduction and vibration damping. These can be compensated for, but at the expense of increased complexity and weight.

Fuel cells allow for more stealthy operation because of their quiet operation, relatively low temperatures, and benign emissions (water). While there are development issues remaining to be solved for fuel cells, primarily regarding the hydrogen source, there appear to be viable options. These are currently being pursued by commercial suppliers and are likely to be readily available in the near future. Integrating a super capacitor or NiMH battery with a fuel cell fed by chemically generated hydrogen appears to be the most promising system, which can best meet the combination of power, energy, and signature objectives and safely function in close proximity to a human operator.

Table 16. Power source comparison

Power Source Type	Specific Power (kW/kg)	Specific Energy (kWh/kg)	Energy/ kg of Fuel (kWh/kg)	Weight for Power (kg)	Weight for Energy[1] (kg)	Total Weight (kg)
Diesel ICE[2]	0.4		3.3	5.0	1.4	6.4
PEM Fuel Cell[2,3]	0.225		1.4	8.9	3.4	12.3
Li Ion Batteries[4]	0.5	0.25		4.0	19.2	19.2
Hybrid						
Fuel Cell[5]	0.225		1.4	2.7	3.4	
Battery[6]	1.0			2.0		
Total						8.1
Hybrid						
Fuel Cell[5]	0.225		1.4	2.7	3.4	
Super Capacitor[6]	7.0			0.3		
Total						6.4
Hybrid						
Diesel ICE[5]	0.4		3.3	1.5	1.4	
Battery[6]	1.0			2.0		
Total						4.9
Hybrid						
Diesel ICE[5]	0.4		3.3	1.5	1.4	
Super Capacitor[6]	7.0			0.3		
Total						3.2

Requirements:
    Avg Power (kW) =   0.6
    Peak Power (kW) =   2.0
    Energy (kWh) =   4.8

[1] Based on specific energy or fuel consumption.
[2] Sized to meet peak power and energy requirements, including fuel.
[3] Specific energy based on 40.0 kWh/kg (higher heating value) of H_2. Assumes 7% H_2 by wt & 50% efficiency.
[4] Total weight based on energy requirements.
[5] Sized to meet average power and energy requirements.
[6] Sized to meet peak power requirements.

APPENDIX F

INTEGRATED POWER SYSTEM DEVELOPMENT

AeroVironment,!Inc. has documented the development of an integrated power system in a final report (AeroVironment,!Inc., 2003) for the ORNL Subcontract 4000007000. This appendix provides the details regarding the design and development and is included here for completeness and the convenience of the reader.

TECHNICAL APPROACH

Objective

Our objective was construction of a demonstration power supply for our chosen hybrid architecture. We developed a five-step work plan to do so.

The first step was to compare and contrast off-the-shelf components in order to select the best possible components and system configuration. Second, we proceeded to design and build the power supply. We procured off-the-shelf components and combined them into subassemblies. The two main subassemblies were the battery pack and the fuel cell plus ancillaries. As a third step we tested, debugged, and integrated the power supply, and then carried out a series of tests performed in a manual mode where some portions of the control were done by hand.

Once convinced that the key subsystems work properly, the next step (Step 4) was to develop the system controller, and the additional hardware to measure and control all system parameters. In Step 5 we also added the chemical hydrogen generation subsystem from ORNL, prepared the sodium borohydride solution and started operating the system.

The result of the five-step approach was a prototype system ready to operate from fuel to electricity, capable of demonstrating hybrid system capabilities for the soldier's energy and power requirements.

The project finished with a preliminary CAD design of the integrated system. This preliminary design included a packaging design and analysis to support material selection and geometric layout of the system. We then fabricated the integrated system and tested it under several upper and lower bound power profiles.

Approach Details

The following details our technical approach.

- *Step 1: Performance models*

  Component level: Simple spreadsheet level models for each component were constructed and evaluated in a system model. These models were mainly needed to evaluate the control algorithms.

  System level: This model included steady state evaluations and transient effects and allowed for trade-off between different components and control strategies. Important conditions to model included base-load power at steady state, the intermediate power interval, the recharge transient, the peak pulse event, the startup event, and the shutdown event. Outputs included power and heat flows, required voltages and currents, energy levels, temperatures, mass flows, and voltages as a function of time.

Control algorithms: The System level model was exercised to evaluate component options and control strategies. The results were performance plots used to help down-select components, system configuration, and control algorithms.

Step 2: Hybrid Battery Pack - Fuel Cell System Design and Assembly

Board design selection: The analysis described above provided the necessary information and data to choose the system configuration and components.

Drawings of brass board parts and manufacture: The brass board was laid out in a 2D fashion on a single test bench. Plumbing, wiring, and position of components were designed in a 2D-drafting package.

Energy management system: Using a commercially available programmable controller we programmed the control algorithms determined in Step 1.

Battery pack assembly: The selected unit cells were integrated into a pack that fit with the board layout.

Battery pack testing: The test load profiles were determined based on the system modeling done in Step 1. Next, the pack was tested using our in-house battery test equipment and temperature effects were modeled.

Fuel cell assembly and related ancillaries: As with the battery, test load profiles were determined based on the system modeling done in Step 1. Then, the fuel cell was tested using in-house battery test equipment and temperature effects were modeled.

Fuel cell testing: The fuel cell was tested over all of the operational conditions.

Hybrid system assembly: Once the subassemblies had been tested and debugged, the entire system was assembled and the system test plan was refined.

- *Step 3: Testing*

Evaluation of component and system options: First, the assembled system was tested under manual control using simple load resistors. Next, full steady state polarization, peak pulse and recharge events were measured using a PC based A/D converter and fast FET power switch. Startup and shutdown sequences were tested manually.

Mechanical and analog electrical issues: Hardware modifications were made in response to mechanical, electrical, or data acquisition system exercises.

Control algorithm adjustments: Control logic was refined based on manual testing.

- *Step 4: Digital Control*

Testing - digital control: The full board was tested under digital control using baseload power, intermediate power, peak pulse, shutdown and startup sequences.

Digital control issues: Remaining controls, hardware, or electrical issues were addressed.

- *Step 5: Hydrogen System Integration*

Acquisition and Assembly: The hydrogen generation catalytic reactor was obtained from ORNL. A layout was made for subassemblies necessary to integrate this reactor into the prototype system.

Fuel Mix: An investigation was made of the mixture start points for the sodium hydroborohydride solution.

Integration: The system, including its controllers was assembled into the prototype.

Testing: The full prototype was tested under digital control using baseload power, intermediate power, peak pulse, shutdown and startup sequences.

RESULTS

Battery Component, Model and Results

Selection

NiMH batteries were chosen because of the combination of high specific energy and high power density for this type of battery. The same battery technology is being used in several models of hybrid electric vehicles. In a hybrid application, these batteries can perform hundreds of thousands of load-leveling transient cycles over years of vehicle operation, so there is little doubt that it will be sufficient for the exoskeleton power supply.

Batteries can be ranked by their ability to deliver peak specific power. For NiMH batteries, most of the resistance is taken to be Ohmic, so that ranking by peak power also ranks the batteries in order of power deliverable at a given efficiency. The peak power rating is given by

$$\frac{P_{max}}{m} \sim \left(\frac{V_0}{2}\right)^2 \frac{1}{R\,m}, \tag{18}$$

where m is the cell mass, V_0 is the effective open circuit voltage, R is the effective cell resistance, and V is the voltage. The fraction of peak power can be computed from the discharge/charge voltages via

$$\frac{P}{P_{max}} = 4\frac{V}{V_0}\left(1-\frac{V}{V_0}\right). \tag{19}$$

The V_0 and R are functions of the given state of charge, temperature, and sign of current (i), and satisfies the V, current relationship for the battery,

$$V = V_0 - R\,i \tag{20}$$

in the state of charge range from 60 to 80%.

Table 17 ranks some commercially available NiMH batteries at 20 C and 80% state of charge. The resistance of a NiMH battery varies with temperature and is mainly a function of temperature, and to a lesser degree a function of state of charge and current draw. Since the batteries will operate in a higher temperature environment, we can extrapolate the performance by noting that there is probably a 30% increase in power at 40 C vs at 20 C. In hybrid applications, these batteries are typically not run below 0.95V (or 75% of peak power), or above 1.4V for efficiency and thermal reasons. Miscellaneous losses associated with interconnections, and battery variations are on the order of 20%. Packaging adds 10% to the weight and decreases the specific power by 10%. Taking all of these factors into consideration, the *rated* power (i.e.,!he power we are willing to use) at 40 C is approximately 74% of the *peak* power at 20 C.

As can be seen from the Table!17, each company's smallest cells have the highest power to weight.

Table 17. Peak specific power of various commercial NiMH Cells
(At 20 C and 80% state of charge, based on data from manufacturers' literature.)

Vendor	Model	Effective Open Circuit Voltage, V_0 (V)	Effective Internal Resistance, R (mOhm)	Bare Cell Mass, m (g)	Peak Specific Power @ 20 C, P/m (W/kg)	Design Specific Power @ 40 C, P/m (W/kg)
Panasonic	HHR200SCP	1.27	10.0*	42	914	677
Panasonic	HHR300SCP	1.27	8.5*	55	863	638
Panasonic	HHR650D	1.27	3.5*	170	678	501
Moltech	EMH-1550C	1.27	14.0	40	720	533
Moltech	EMH-2200C	1.27	11.5	53	662	490
Moltech	EMH-2500C	1.27	11.0	58	632	468
Moltech	EMX-7000D	1.27	7.0	160	360	266

*Estimated from discharge curves on data sheets.

The highest power cells from Panasonic (HHR200SCP and HHR300SCP), and Moltech (EMH1550C and EMH2200C) were purchased for testing.

The testing range chosen for charge and discharge power at states of charge was 20 to 100% and temperatures were 20 to 45 C. This test matrix provided sufficient information for creation of a look-up table model to be used for simulation.

Modeling

The component model for the battery included state variables of current, i, state of charge, σ, and temperature, T. All other quantities are derived from these. The voltage for a NiMH battery was estimated using the equation

$$V = V_0(\sigma, T, i) - R(\sigma, T, i)i \tag{21}$$

to relate the voltage to the state variables. The effective open circuit voltage, V_0, and effective cell resistance R are functions of the state of charge and were, for our purposes, computed *via* look-up tables derived from experimental data. For battery operation around a specific temperature and state of charge, the equations were also linearized.

a) State of charge calculation: The state of charge was computed by amp-hour integration of the battery current. It is assumed that there were no coulombic losses in the state-of-charge range of interest so that,

$$\frac{d\sigma}{dt} = -\frac{1}{3600s}\frac{i}{i_c} \tag{22}$$

where i is the current through the battery that is positive on discharge, and negative on charge, and i_c is the 1C (or 1 hour) discharge current. The factor of 3600!s assumed that the units of time are seconds.

b) Cell temperature calculation: The battery heat generation assumed only i^2R losses, and was estimated as a multiple of the output power using, for example,

$$\frac{q_{ohmic}}{P_{out}} = \frac{i^2R}{Vi} = \frac{iR}{V} = \frac{V_0}{V} - 1. \tag{23}$$

The battery heat was assumed to be generated uniformly within the volume of the battery, and lost from the surface. The temperature, T_{cell}, is the state for the thermal model of the battery, simply put, the rate of temperature change is proportional to the net increase in heat so that,

$$\frac{dT_{cell}}{dt} = \frac{1}{m\,c_{p,battery}}\left\{i^2R - hA_{cell}\left(T_{cell} - T_{air}\right)\right\}, \tag{24}$$

where T_{cell} is assumed uniform over the cell, T_{air} is the average of the inlet and outlet air temperature, and $c_{p,battery}$ is the heat capacity of the battery. The first term in the brackets is the ohmic heating of the cell, the second is the heat removed by forced convection. The heat capacity of the battery was estimated to be close to that of water, on a <u>volume</u> basis (i.e.,!4.2!kJ/LK). A NiMH battery is approximately ~3.3!kg/L, so that the heat capacity was estimated to be 1.3!kJ/kgK.

c) Convection cooling calculation: For the convective heat transfer (cooling), we assumed that the cells were arranged side-by-side, end-on into the flow so that the exposed surface area of a cylindrical cell included the ends and thus,

$$A_{cell} = \pi\,DL + \frac{\pi}{2}D^2 = \pi D^2\left(\frac{L}{D} + \frac{1}{2}\right). \tag{25}$$

If fins are used, then this area is increased by the fin area. For small temperature differences, the heat transfer coefficient was estimated using,

$$h \sim 1.86\left(\frac{Re\,Pr}{L/D_h}\right)^{1/3}. \tag{26}$$

The hydraulic diameter, D_h, is defined as four times the ratio of the open area to the wetted perimeter. For the current geometry that does not use fins, this is

$$D_h = D\left(\frac{4}{\pi} - 1\right) \sim 0.27D. \tag{27}$$

The Reynolds number is,

$$Re = \frac{UD_h}{\upsilon} \tag{28}$$

where U is the average flow speed in the channels, and υ is the kinematic viscosity.

To keep a high heat exchanger effectiveness, we wanted the (average) flow rate to be sufficient to carry the heat from the cell,

$$\rho\,A_{cs}Uc_{p,air}\Delta T_{air,out-in} \sim q_{ohmic}, \tag{29}$$

where A_{cs} is the cross-sectional or open flow area, and $c_{p,air}$=1KJ/kgK is the heat capacity for air.

The pressure rise through the battery pack is dominated by abrupt expansion losses and is on the order of,

$$\Delta p_{cool} = 0.25 \rho \overline{U}^2, \tag{30}$$

and the minimum cooling power (not including blower efficiencies) is then,

$$P_{cool} = 0.25 \rho \overline{U}^3 A_{cs}. \tag{31}$$

d) Calculation of temperature variation within the cell

We assumed a simple one dimensional scaling, the maximum temperature difference from the center of the battery to the walls given by the steady state temperature distribution for uniform heating and cooling,

$$\Delta T_{max,cell} \sim \frac{q}{4\pi\, k\, L} \tag{32}$$

where q is the net heat generation by the cell, k is the thermal conductivity of the cell, and L is the cell length.

For the 4/5 Sub-C cell, we estimated the order of magnitude conductivity to be greater than 1!W/mK, so that for the small cells, with q~30,and L ~ 3.3cm, the maximum temperature difference is

$$\Delta T_{max,cell} < \frac{30W}{4\pi\, 10\, \frac{W}{mK}\, 0.033m} \sim 7K, \tag{33}$$

We chose to neglect this for our purposes, as we expected the thermal resistance at the cell-air interface to be much larger than the internal thermal resistance, so that the steady state temperature distribution would not be reached, and the internal temperature would be close to uniform.

Testing

Four battery packs, one for each battery model, were tested to determine their performance and to obtain modeling data. Each battery pack consisted of 12 cells connected in series, shrink-wrapped, with leads and a connector. Twelve cells were used (as opposed to single cells) so that realistic interconnect resistance, and packaging weight would be taken into account.

The current draw, during ten-second high rate charge (at 1.45!V) and high rate discharge (at 0.85!V) pulses, was measured at state of charge (SOC) levels from 100% to 10%. In-between SOC levels, the batteries were charged and discharged at a nominal "base load" current. The test data are summarized in Figs.!106 through 109 and Tables!19 through 21.

These tests were performed at room temperature (22°C) and 45°C for all four of the candidate battery packs, and at (50°C) for the Moltech EMH-2200C (Table!19) that is specified to operate at a somewhat higher temperature.
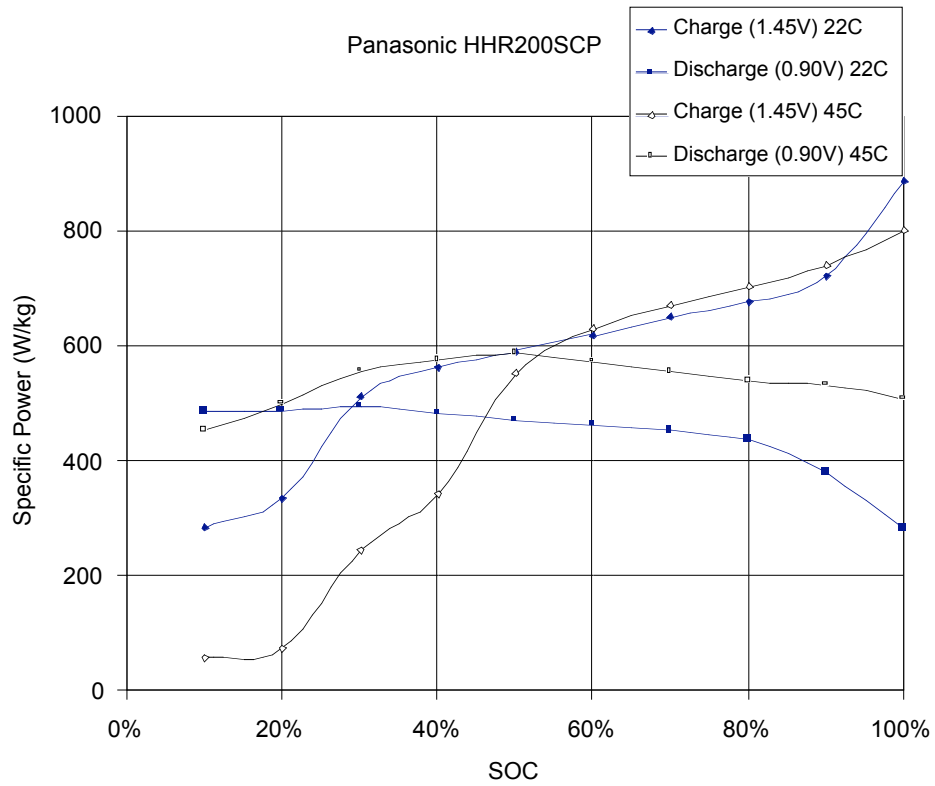
Fig. 106. Specific power curves for Panasonic HHR200SCP batteries.
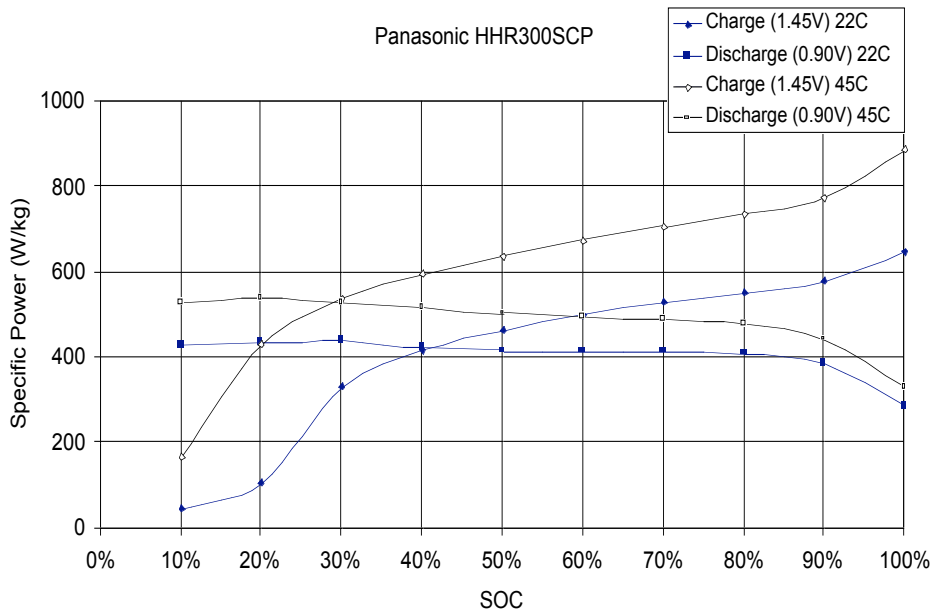

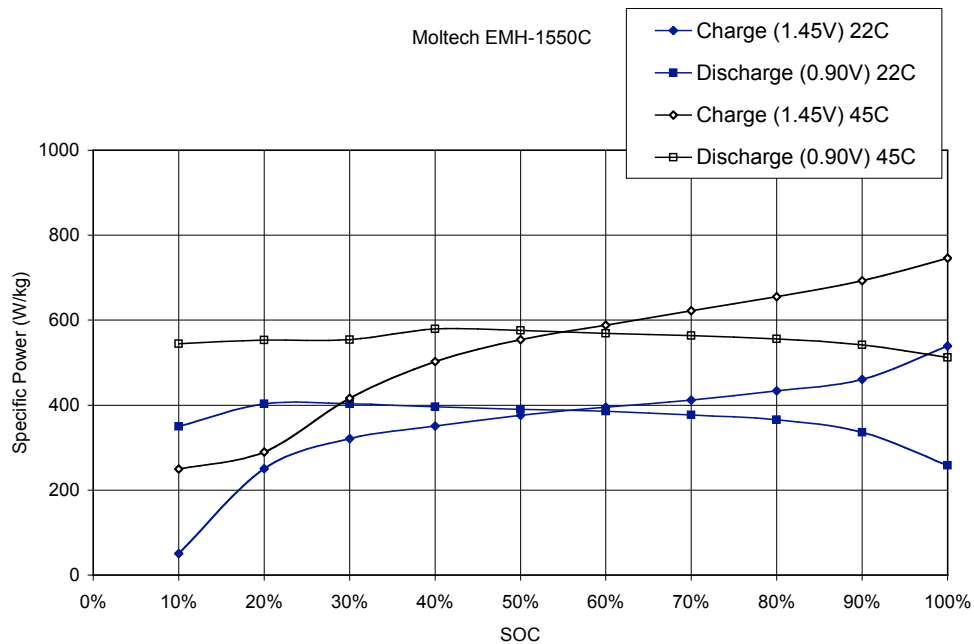**Fig. 107. Specific power curves for Panasonic HHR300SCP batteries.**

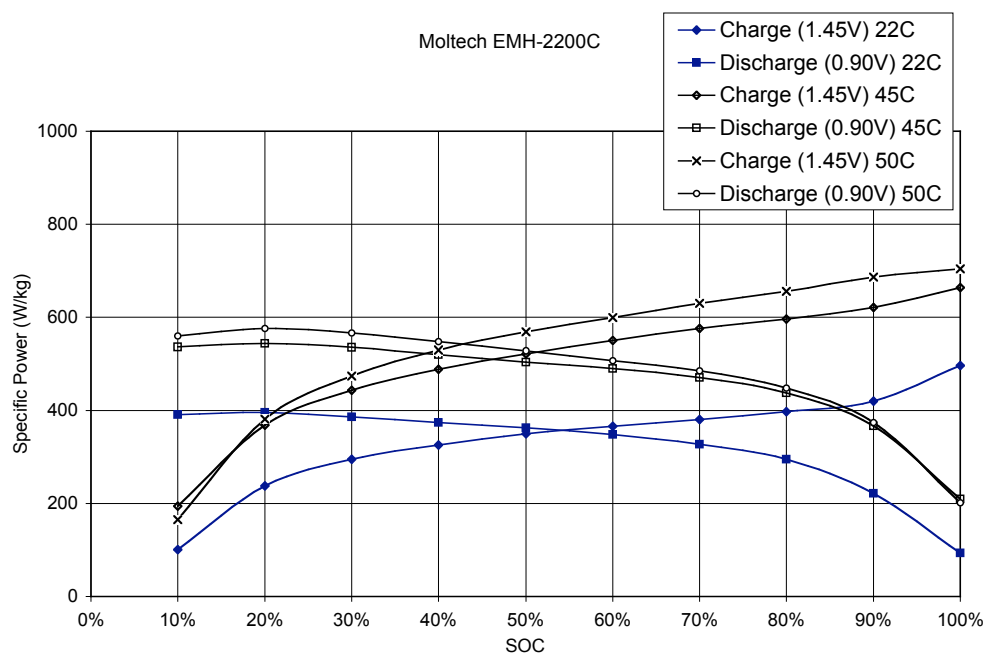**Fig. 108. Specific power curves for Moltech EMH-1550C batteries.**

Fig. 109. Specific power curves for Moltech EMH-2200C batteries.

134

Table 18. Pack voltage for 1.5 kW discharge capabilities
(Battery pack is 2.3kg, which assumes a 650W/kg specific power.)

Battery	Number of Cells	Pack Voltage At 0.9 V/Cell	Pack Voltage At 1.45 V/Cell
H-HR200SCP	51	46	74
HHR300SCP	39	35	57

Table 19. Panasonic HHR200SCP data
(Data is for packs of 12 cells, but is presented on a per-cell basis.)

		Discharge (Per Cell)										Charge (Per Cell)								
Battery		High Power Discharge			Low Power Discharge			Discharge Parameters		Peak Specific Power	Predicted Specific Power at 0.9	High Power Charge			Low Power Charge			Charge Parameters		Predicted Specific Power at 1.45
Panasonic HHR200SCP "4/5 Sub-C"	SOC	Voltage	Current	Power	Voltage	Current	Power	Resistance	Vo			Voltage	Current	Power	Voltage	Current	Power	Resistance	Vo	
	%	V	A	W	V	A	W	Ohm*1000	Vo	W/kg	V	V	A	W	V	A	W	Ohm*1000	Vo	V
22C	100%	0.845	49.020	41	1.398	1.900	3	11.7	1.42	956	887	1.445	-8.460	-12	1.343	-0.820	-1	13.4	1.33	-284
	90%	0.845	40.640	34	1.311	1.900	2	12.0	1.33	822	722	1.445	-11.480	-17	1.299	-0.800	-1	13.7	1.29	-381
	80%	0.845	38.600	33	1.272	1.900	2	11.6	1.29	800	678	1.445	-13.220	-19	1.281	-0.780	-1	13.2	1.27	-438
	70%	0.845	37.240	31	1.260	1.880	2	11.7	1.28	779	652	1.446	-13.780	-20	1.273	-0.820	-1	13.3	1.26	-455
	60%	0.845	35.480	30	1.254	1.920	2	12.2	1.28	745	620	1.445	-14.080	-20	1.266	-0.800	-1	13.5	1.26	-465
	50%	0.845	33.860	29	1.248	1.900	2	12.6	1.27	714	591	1.445	-14.320	-21	1.259	-0.760	-1	13.8	1.25	-472
	40%	0.846	32.360	27	1.242	1.920	2	13.0	1.27	685	564	1.445	-14.720	-21	1.250	-0.820	-1	14.0	1.24	-485
	30%	0.845	29.540	25	1.232	1.900	2	14.0	1.26	629	513	1.445	-15.080	-22	1.239	-0.800	-1	14.4	1.23	-497
	20%	0.846	19.320	16	1.215	1.880	2	21.2	1.25	413	335	1.445	-14.860	-21	1.230	-0.820	-1	15.3	1.22	-489
	10%	0.845	16.600	14	1.192	1.980	2	23.7	1.24	360	286	1.446	-14.820	-21	1.213	-0.820	-1	16.6	1.20	-486
45C	100%	0.845	45.520	38	1.287	1.840	2	10.1	1.31	936	801	1.444	-15.280	-22	1.286	-0.920	-1	11.0	1.28	-509
	90%	0.845	42.360	36	1.264	1.880	2	10.4	1.28	884	740	1.444	-16.020	-23	1.274	-0.920	-1	11.3	1.26	-533
	80%	0.845	40.420	34	1.257	1.860	2	10.7	1.28	848	706	1.445	-16.300	-24	1.265	-0.940	-1	11.7	1.25	-540
	70%	0.845	38.540	33	1.249	1.900	2	11.0	1.27	813	671	1.444	-16.760	-24	1.255	-0.940	-1	11.9	1.24	-556
	60%	0.845	36.320	31	1.239	1.900	2	11.4	1.26	772	631	1.445	-17.360	-25	1.242	-0.920	-1	12.3	1.23	-574
	50%	0.847	31.960	27	1.222	1.920	2	12.5	1.25	691	554	1.447	-17.960	-26	1.225	-0.940	-1	13.0	1.21	-588
	40%	0.848	19.920	17	1.199	1.900	2	19.5	1.24	436	345	1.447	-17.700	-26	1.212	-0.900	-1	14.0	1.20	-577
	30%	0.849	14.360	12	1.162	1.900	2	25.1	1.21	324	247	1.448	-17.180	-25	1.185	-0.900	-1	16.2	1.17	-557
	20%	0.849	4.740	4	1.001	1.920	2	54.0	1.10	126	76	1.448	-15.460	-22	1.163	-0.980	-1	19.7	1.14	-502
	10%	0.850	3.520	3	1.001	1.880	2	92.1	1.17	83	60	1.450	-14.060	-20	1.169	-0.960	-1	21.4	1.15	-454

Table 20. Panasonic HHR300SCP data
(Data is for packs of 12 cells, but is presented on a per-cell basis)

		Discharge (Per Cell)										Charge (Per Cell)								
Battery		High Power Discharge			Low Power Discharge			Discharge Parameters		Peak Specific Power	Predicted Specific Power at 0.9	High Power Charge			Low Power Charge			Charge Parameters		Predicted Specific Power at 1.45
Panasonic HHR300SCP "SUB-C"	SOC	Voltage	Current	Power	Voltage	Current	Power	Resistance	Vo			Voltage	Current	Power	Voltage	Current	Power	Resistance	Vo	
	%	V	A	W	V	A	W	Ohm*1000	Vo	W/kg	V	V	A	W	V	A	W	Ohm*1000	Vo	V
22C	100%	0.848	46.780	40	1.336	3.000	4	11.2	1.37	719	648	1.450	-11.500	-17	1.320	1.560	2	10.0	1.34	-286
	90%	0.848	42.720	36	1.259	3.000	4	10.3	1.29	687	580	1.450	-15.420	-22	1.285	1.500	2	9.7	1.30	-383
	80%	0.848	40.920	35	1.242	2.980	4	10.4	1.27	667	552	1.450	-16.500	-24	1.274	1.580	2	9.7	1.29	-410
	70%	0.848	39.440	33	1.238	3.000	4	10.7	1.27	644	532	1.450	-16.700	-24	1.269	1.500	2	9.9	1.28	-414
	60%	0.848	37.140	31	1.232	3.000	4	11.2	1.27	608	500	1.450	-16.700	-24	1.262	1.500	2	10.3	1.28	-415
	50%	0.847	34.540	29	1.222	3.020	4	11.9	1.26	569	463	1.450	-16.760	-24	1.253	1.480	2	10.8	1.27	-416
	40%	0.848	31.220	26	1.206	3.040	4	12.7	1.24	521	417	1.450	-17.020	-25	1.237	1.460	2	11.5	1.25	-423
	30%	0.847	25.200	21	1.175	3.000	4	14.7	1.22	431	333	1.450	-17.740	-26	1.208	1.480	2	12.6	1.23	-441
	20%	0.847	8.180	7	1.086	3.000	3	46.2	1.22	139	108	1.450	-17.540	-25	1.149	1.520	2	15.8	1.17	-435
	10%	0.847	2.920	2	1.000	3.020	3	-1522.5	-3.60	-36	45	1.450	-17.300	-25	1.125	1.500	2	17.3	1.15	-429
45C	100%	0.845	64.040	54	1.374	3.000	4	8.7	1.40	967	888	1.446	-12.700	-18	1.338	1.520	2	7.6	1.35	-329
	90%	0.845	56.980	48	1.292	3.040	4	8.3	1.32	896	775	1.446	-17.320	-25	1.300	1.500	2	7.8	1.31	-444
	80%	0.845	54.580	46	1.267	2.960	4	8.2	1.29	872	737	1.446	-18.760	-27	1.288	1.520	2	7.8	1.30	-479
	70%	0.845	52.360	44	1.259	2.980	4	8.4	1.28	841	705	1.446	-19.180	-28	1.281	1.500	2	7.9	1.29	-489
	60%	0.845	50.020	42	1.254	3.000	4	8.7	1.28	806	673	1.446	-19.460	-28	1.274	1.500	2	8.2	1.29	-496
	50%	0.845	47.480	40	1.247	3.040	4	9.0	1.27	768	637	1.446	-19.780	-29	1.265	1.460	2	8.5	1.28	-503
	40%	0.845	44.620	38	1.236	3.000	4	9.4	1.26	728	597	1.446	-20.300	-29	1.253	1.480	2	8.8	1.27	-516
	30%	0.845	40.500	34	1.218	2.980	4	9.9	1.25	669	538	1.446	-20.860	-30	1.234	1.480	2	9.5	1.25	-528
	20%	0.845	32.760	28	1.186	3.000	4	11.5	1.22	555	430	1.446	-21.300	-31	1.204	1.500	2	10.6	1.22	-538
	10%	0.845	12.820	11	1.121	3.040	3	28.1	1.21	221	167	1.446	-20.900	-30	1.157	1.520	2	12.9	1.18	-527

Table 21. Moltech EMH-1550C data
(Data is for packs of 12 cells, but is presented on a per-cell basis.)

Battery	SOC	Discharge (Per Cell)								Peak Specific Power	Predicted Specific Power at 0.9	Charge (Per Cell)								Predicted Specific Power at 1.45
		High Power Discharge			Low Power Discharge			Discharge Parameters				High Power Charge			Low Power Charge			Charge Parameters		
Moltech EMH-1550C "4/5 Sub-C"		Voltage	Current	Power	Voltage	Current	Power	Resistance	Vo			Voltage	Current	Power	Voltage	Current	Power	Resistance	Vo	
22C	%	V	A	W	V	A	W	Ohm*1000	Vo	W/kg	V	V	A	W	V	A	W	Ohm*1000	Vo	V
22C	100%	0.847	27.460	565	1.339	1.420	2	18.9	1.37	600	539	1.449	-7.300	-11	1.307	-0.680	-1	21.5	1.29	-258
	90%	0.847	23.980	493	1.259	1.420	2	18.3	1.28	549	461	1.449	-9.520	-14	1.271	-0.680	-1	20.2	1.26	-336
	80%	0.847	22.760	468	1.234	1.400	2	18.1	1.26	531	433	1.450	-10.360	-15	1.256	-0.720	-1	20.0	1.24	-365
	70%	0.847	21.700	446	1.224	1.460	2	18.6	1.25	511	412	1.450	-10.680	-15	1.248	-0.700	-1	20.2	1.23	-377
	60%	0.847	20.860	429	1.218	1.420	2	19.1	1.24	493	395	1.449	-10.920	-16	1.242	-0.700	-1	20.3	1.23	-386
	50%	0.847	19.880	409	1.211	1.420	2	19.7	1.24	473	376	1.450	-11.060	-16	1.234	-0.680	-1	20.8	1.22	-390
	40%	0.847	18.600	383	1.201	1.440	2	20.6	1.23	446	350	1.450	-11.240	-16	1.224	-0.700	-1	21.4	1.21	-396
	30%	0.847	17.160	353	1.187	1.440	2	21.6	1.22	416	321	1.450	-11.420	-17	1.212	-0.700	-1	22.2	1.20	-403
	20%	0.848	13.480	277	1.162	1.420	2	26.1	1.20	334	251	1.450	-11.440	-17	1.191	-0.720	-1	24.1	1.17	-403
	10%	0.848	2.580	53	1.085	1.440	2	208.6	1.39	56	51	1.450	-9.920	-14	1.183	-0.720	-1	29.0	1.16	-350
45C	100%	0.845	38.860	797	1.280	1.440	2	11.6	1.30	878	746	1.446	-14.220	-21	1.270	-0.700	-1	13.0	1.26	-512
	90%	0.845	36.380	747	1.256	1.400	2	11.7	1.27	837	693	1.446	-15.060	-22	1.258	-0.700	-1	13.0	1.25	-542
	80%	0.845	34.540	708	1.246	1.400	2	12.1	1.26	800	655	1.446	-15.460	-22	1.250	-0.760	-1	13.3	1.24	-556
	70%	0.845	32.820	673	1.239	1.420	2	12.5	1.26	764	622	1.446	-15.680	-23	1.242	-0.760	-1	13.6	1.23	-563
	60%	0.845	31.140	639	1.232	1.420	2	13.0	1.25	729	588	1.446	-15.860	-23	1.235	-0.760	-1	13.9	1.22	-569
	50%	0.845	29.400	603	1.224	1.400	2	13.5	1.24	693	554	1.446	-16.040	-23	1.227	-0.760	-1	14.3	1.22	-575
	40%	0.845	26.760	549	1.215	1.460	2	14.6	1.24	634	503	1.446	-16.160	-23	1.218	-0.720	-1	14.8	1.21	-579
	30%	0.845	22.240	456	1.204	1.400	2	17.2	1.23	531	416	1.446	-15.460	-22	1.215	-0.700	-1	15.6	1.20	-554
	20%	0.845	16.780	344	1.084	1.440	2	15.6	1.11	477	290	1.446	-15.500	-22	1.129	-0.660	-1	21.3	1.11	-553
	10%	0.845	14.660	301	1.070	1.400	1	16.9	1.09	429	250	1.446	-15.280	-22	1.103	-0.720	-1	23.6	1.09	-544

Table 22. Moltech EMH-2200C
(Data is for packs of 12 cells, but is presented on a per-cell basis.)

Battery	SOC	Discharge (Per Cell)								Peak Specific Power	Predicted Specific Power at 0.9	Charge (Per Cell)								Predicted Specific Power at 1.45
		High Power Discharge			Low Power Discharge			Discharge Parameters				High Power Charge			Low Power Charge			Charge Parameters		
Moltech EMH-2200C "SUB-C"		Voltage	Current	Power	Voltage	Current	Power	Resistance	Vo			Voltage	Current	Power	Voltage	Current	Power	Resistance	Vo	
22C	%	V	A	W	V	A	W	Ohm*1000	Vo	W/kg	V	V	A	W	V	A	W	Ohm*1000	Vo	V
22C	100%	0.84	33.9	28	1.43	2.0	3	18.4	1.46	525	497	1.44	-3.3	-5	1.38	-1.0	-1	26.4	1.36	-94
	90%	0.84	29.6	25	1.29	2.0	3	16.4	1.32	483	421	1.44	-8.0	-12	1.31	-1.0	-1	19.3	1.29	-222
	80%	0.84	28.5	24	1.24	2.0	2	15.3	1.27	480	398	1.44	-10.9	-16	1.27	-1.0	-1	17.3	1.26	-295
	70%	0.84	27.5	23	1.22	2.0	2	15.0	1.25	471	381	1.44	-12.1	-17	1.26	-1.0	-1	16.8	1.24	-328
	60%	0.84	26.6	22	1.21	2.0	2	15.2	1.24	459	366	1.44	-12.9	-19	1.24	-1.0	-1	16.7	1.23	-348
	50%	0.84	25.4	21	1.20	2.0	2	15.4	1.23	444	350	1.44	-13.4	-19	1.24	-1.0	-1	16.7	1.22	-363
	40%	0.84	23.9	20	1.19	2.0	2	16.0	1.22	420	326	1.44	-13.8	-20	1.22	-1.0	-1	17.0	1.21	-374
	30%	0.84	21.8	18	1.17	2.0	2	16.9	1.21	389	295	1.44	-14.4	-21	1.21	-1.0	-1	17.7	1.19	-386
	20%	0.84	17.8	15	1.15	2.0	2	19.5	1.19	326	238	1.44	-14.8	-21	1.18	-1.0	-1	18.9	1.16	-396
	10%	0.84	7.5	6	1.10	2.0	2	46.8	1.19	137	101	1.44	-14.6	-21	1.15	-1.0	-1	21.2	1.13	-391
45C	100%	0.86	44.1	38	1.39	2.0	3	12.7	1.42	716	664	1.46	-8.5	-12	1.34	-1.0	-1	15.1	1.33	-210
	90%	0.86	42.3	36	1.29	2.0	3	10.8	1.31	719	621	1.46	-14.4	-21	1.29	-1.0	-1	12.3	1.28	-367
	80%	0.86	41.0	35	1.26	2.0	3	10.2	1.28	717	596	1.45	-17.1	-25	1.27	-1.0	-1	11.5	1.26	-438
	70%	0.85	40.2	34	1.24	2.0	3	10.2	1.26	703	576	1.45	-17.9	-26	1.26	-1.0	-1	11.3	1.25	-471
	60%	0.85	38.6	33	1.23	2.0	2	10.4	1.25	680	550	1.45	-18.7	-27	1.25	-1.0	-1	11.4	1.24	-490
	50%	0.85	36.6	31	1.22	2.0	2	10.7	1.24	652	522	1.45	-19.3	-28	1.24	-1.0	-1	11.6	1.23	-504
	40%	0.84	35.2	30	1.21	2.0	2	11.1	1.23	619	489	1.44	-19.3	-28	1.22	-1.0	-1	11.9	1.21	-520
	30%	0.84	32.1	27	1.20	2.0	2	11.7	1.22	573	444	1.44	-19.9	-29	1.21	-1.0	-1	12.4	1.20	-536
	20%	0.84	27.0	23	1.17	2.0	2	13.1	1.20	494	368	1.44	-20.3	-29	1.18	-1.0	-1	13.4	1.17	-544
	10%	0.84	14.4	12	1.13	2.0	2	22.7	1.17	273	194	1.44	-20.1	-29	1.15	-1.0	-1	15.4	1.13	-536
50C	100%	0.85	47.7	40	1.41	2.0	3	12.2	1.43	754	704	1.45	-7.4	-11	1.35	-1.0	-1	14.6	1.34	-202
	90%	0.85	47.6	40	1.31	2.0	3	10.1	1.33	786	686	1.45	-13.9	-20	1.30	-1.0	-1	11.4	1.29	-374
	80%	0.85	46.0	39	1.27	2.0	3	9.6	1.29	779	656	1.45	-16.7	-24	1.28	-1.0	-1	10.8	1.27	-448
	70%	0.85	44.4	38	1.25	2.0	3	9.6	1.27	761	630	1.45	-18.1	-26	1.26	-1.0	-1	10.6	1.25	-486
	60%	0.85	42.4	36	1.24	2.0	2	9.8	1.26	733	599	1.45	-19.0	-27	1.25	-1.0	-1	10.7	1.24	-507
	50%	0.85	40.4	34	1.23	2.0	2	10.1	1.25	703	568	1.45	-19.8	-29	1.24	-1.0	-1	10.8	1.23	-528
	40%	0.85	37.8	32	1.22	2.0	2	10.4	1.24	666	530	1.45	-20.5	-30	1.23	-1.0	-1	11.1	1.22	-547
	30%	0.85	34.1	29	1.20	2.0	2	11.0	1.22	611	475	1.45	-21.2	-31	1.21	-1.0	-1	11.6	1.20	-566
	20%	0.85	27.7	23	1.17	2.0	2	12.7	1.20	511	382	1.45	-21.7	-31	1.18	-1.0	-1	12.8	1.17	-576
	10%	0.85	12.2	10	1.12	2.0	2	26.7	1.17	232	165	1.45	-21.2	-31	1.14	-1.0	-1	15.2	1.12	-560

The effective resistance (R) and offset voltage (V_0) were estimated from the data for charge and discharge at each SOC level, so that the simple equation,

$$V = V_0 - R\,i, \tag{34}$$

yielded the correct V-i (*i.e.,* Voltage-current) relationship at each SOC level. For simulation purposes, V_0 and R were computed using a look-up table that is a function of SOC and temperature.

The estimated charge and discharge specific powers are also presented in the Tables!18 through 21 and Figs.!106 through 109. The peak discharge power was of academic interest, but showed that these batteries approached 1000!W/kg power capability (for 10 second pulses). However,

this level of power was only realized with a fully charged battery, and that was not an appropriate condition when these batteries are to be used for load leveling. The specific powers computed at 0.9!V (discharge) and 1.45!V (charge), and 60%-80% state of charge more closely represented the normal allowable range of operation. We noted that the specific power computed below was based on the battery pack weight including interconnects and packaging.

The shaded areas of the tables indicated the specific power for charge and discharge in the normal range of operation. As seen from the data, all of the batteries performed well, and better at the higher temperatures. On average, the Panasonic batteries performed somewhat better than the Moltech batteries, with the Panasonic HHR200SCP besting the Panasonic HHR300SCP in charge performance, and in discharge performance at room temperature. Interestingly, the HHR200SCP performed somewhat worse than the HHR300SCP at the higher discharge temperature, but not significantly. The performance at lower temperatures was not tested, but it was known that the performance decreases similarly at even lower temperatures. We noted that the batteries could be heated up relatively easily, so operation at higher temperatures was preferred.

Table 17 illustrated the pack voltage that was implied by a 1.5!kW power requirement assuming a 650!W/kg battery pack. The obvious implication was that there needed to be a DC/DC between the fuel cell and battery pack. For a high efficiency lightweight, DC/DC conversion, we could expect 10!W/g, or 60!grams for a 600!W fuel cell.

Parameters to simulate the charge and discharge (electrical) characteristics of the present NiMH batteries were determined experimentally. Either of the Panasonic batteries were recommended for use in transient handling. We also found that almost 1kW/kg is realizable with these batteries, and this was the figure used for the original performance estimates. However, we found that 600–650!W/kg (on discharge) and 400–500!W/kg (on charge) were more realistic for the present transient handling application.

Results: Fuel Cell Component

Selection

A nominally 500!W Fuel cell system from H-Power (PowerPPM-PS500) was selected for testing. The purpose of the energy storage system is to provide a lightweight refuelable electric power source for a human exoskeleton or enhanced mobility device described above.

Modeling

The performance of a fuel cell operating with pure hydrogen as fuel and air as oxidant at a given constant temperature can be modeled using the following equation (Wakizoe, 1995),

$$E = E_0 - b \log_{10}\left(\frac{i}{i_o}\right) - Ri + b \log_{10}\left(\frac{p}{p_0}\right) \quad , \tag{35}$$

where i is the current density in A/cm^2, i$_o$=0.001 A/cm^2 is the exchange current density, E$_0$ is the open circuit voltage, b is the rate of decrease of voltage with current density in V/decade, and R

is the cell internal resistance per unit area, $\Omega.cm^2$, p is the operating pressure, and $p_0 = 14.7$ psi is the reference pressure.

This equation assumes that a sufficient amount of hydrogen and air are supplied to the fuel cell. When the cell gets starved its behavior becomes more complicated and cannot be described by such a simple equation.

For the purposes of our first approximation model, we wanted to be conservative so we required that the fuel cell operate within the assumptions of the equation above, i.e., power would not be drawn in excess of the available reactants. The flow rate of hydrogen and of the air supply were used to define the peak power possible at any moment, so time response of the fuel cell would be determined by the time response of the fuel and air supplies.

At pressures close to ambient ($p=p_o$) the equation above leads to the polarization curve shown in Fig. 110 (the values of the parameters used for the curve in are typical for state-of-the art fuel cell stacks produced by several manufacturers).

Fuel Cell Performance Model

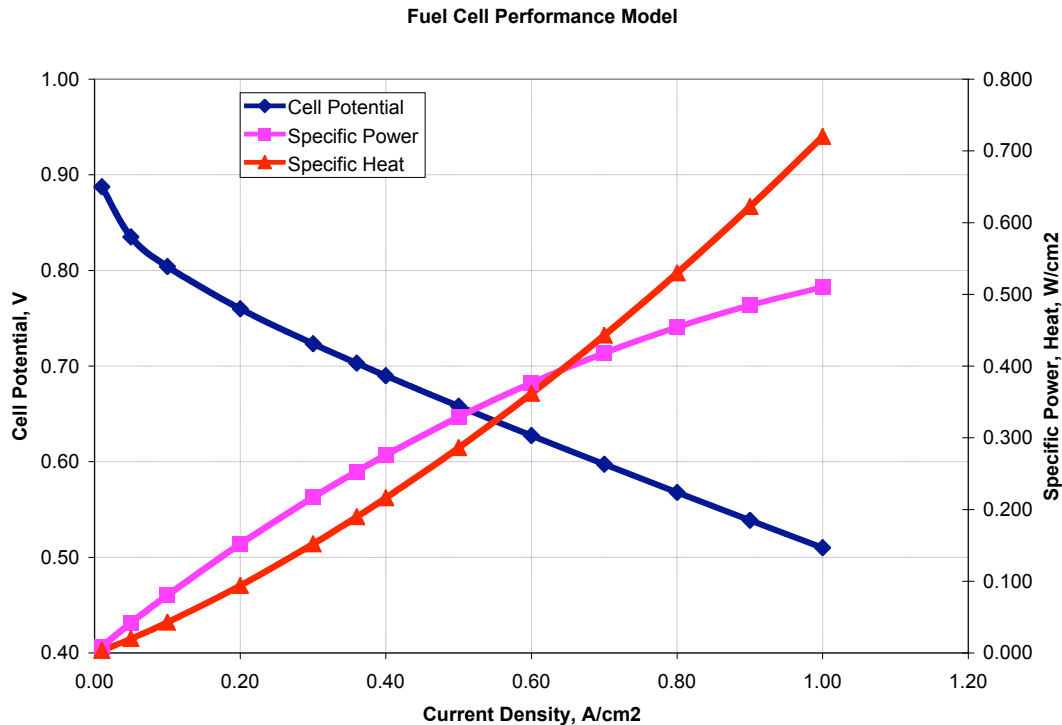**Fig. 110. Polarization curve for E_0=0.95, b=0.06 V/dec, R=0.26 $\Omega.cm^2$, p=p$_0$**

For mechanical design purposes, the weight, volume, and power were computed as function of the active cell area, so that,

Weight:	8 –50 kg/m^2
Volume:	29 L/m^2
Design Power (0.7 V/cell):	2.8 kW/m^2
Peak Power (0.6 V/cell):	3.8 kW/m^2

138

Note that the huge weight range was due to a wide range of technologies used by different manufacturers.

The volume figure assumed that there was a cooling cell (heat exchanger) integrated with every power producing cell, so the cell thickness was roughly 0.3!cm/cell. We could expect half that value for water cooling, but the heat exchanger would have to exist somewhere.

Fuel Requirement

When dealing with fuel cell and hydrogen consumption, it was convenient to put everything in terms of current because then we would just have to make sure that we had 1 electron for each hydrogen atom. I.e., we knew that 1 Amp!=!1!C/s and the charge on an electron was 1.6e-19!C, and that, in a fuel cell, we generate 6.022045e23 electrons per mole of Hydrogen atoms, so that! we would have! 1!Amp!=!1!Coul/s!=!1!atoms of H/1.6e-19!s!=!1!mole of H/(1.6e-19*6.022045e23)s!=!1.04e-5!moles of H/sec!=!1.05e-5!g/s!=!0.0378 g/hr, so hydrogen consumption is, $0.0378 \dfrac{\text{g}}{\text{Ah}}$, or $10.5 \dfrac{\mu g/s}{\text{A}}$.

Air Requirement

Air contains 21% oxygen by volume. Since every molecule of oxygen exchanges four electrons during the electrochemical process occurring in the fuel cell reaction, a flow of 2.59e-6 moles/s of oxygen gas at 100% utilization was needed to support 1 A of current per cell. This translated into 1.23e-5 moles/s of air at the same conditions.

Unfortunately, the presence of nitrogen and other inert gases in the air stream made it impossible to utilize all the oxygen from air, and a utilization of 50 to 30% of the inlet oxygen gave optimal performance. The minimum air-flow at 50% utilization would then be 2.47e-5 moles/s of air.

Another complication of the mass balance on the oxygen side of the fuel cell came from the need to remove the water produced during fuel cell operation. Almost all the water is produced on the oxygen (air) side of the fuel cell, and it is of paramount importance for stable operation to maintain balanced water removal. On the other side, when too much water is removed from the fuel cell—the membrane loses its conductivity and the fuel cell performance rapidly deteriorates.

Chemistry, Cooling

The fuel cell converts the chemical energy of the reaction of hydrogen with oxygen into electrical energy and heat, while producing water.

$$H_2O_2 \rightarrow H_2O + Q \tag{36}$$

Q = W+q

$W = E_{cell}I$ – electrical power

$Q = (E_{tn}-E_{cell})I$ – heat flux

Depending on the state of the water exiting the fuel cell (liquid or vapor), the amount of heat needed to be dissipated by the cooling system differs. When all the product water is removed

139

from the cell in liquid form then $E_{tn} = E_{hhv} = 1.48$ V. When the product water exits the fuel cell with the outlet stream of air in a vapor form, $E_{tn} = E_{lhv} = 1.23$ V at standard conditions.

Thermal Model

For our component model purposes it is assumed that the fuel cell was at constant temperature and pressure and that the product water exited the fuel cell in the form of vapor. The heat generation for each cell is computed using the difference between the lower heating value voltage, and the cell voltage via the following equation:

$$q = (1.23 - E)\,i. \tag{37}$$

We further assumed that the heat carried by the exiting product air stream, and the hydrogen stream was negligible, and that all the heat was dissipated through the fuel cell cooling loop. Figure 111 represents the steady state model of the fuel cell. The data in Table 23 gives the calculated flows and generated power and heat for a fuel cell stack with 20 cells of 200 cm^2 active area, assuming that 100% of the supplied hydrogen was used and 50% of the oxygen from the supplied air was consumed in the reaction.
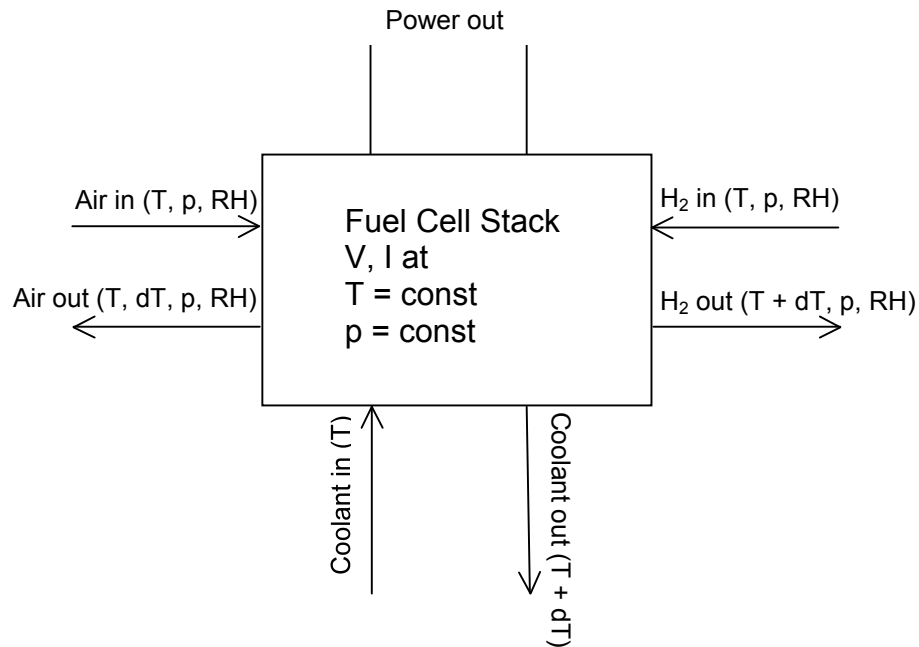

Fig. 111. Steady state model of the fuel cell.

Table 23. Calculated electrochemical fuel cell parameters.

(Performance, generated power and heat, required reactants and water cooling flows for a fuel cell stack with 20 cells of 200 cm^2 active area at steady state conditions and 50% utilization of Oxygen from air.)

Current Density	Cell Potential	Specific Power	Specific Heat	Stack Current	Stack Voltage	Stack power	Heat generated, LHV	Moles of H$_2$	Hydrogen Flow	Moles of O$_2$	AirFlow, 50% O$_2$ utilization	Cooling Water flow, dT=10°C
I, A/cm^2	V	W/cm^2	W/cm^2	A	V	W	W	1/min	SLM	1/min	SLM	l/min
0.01	0.89	0.009	0.003	2	17.75	35	14	0.012	0.3	0.006	1.3	0.02
0.05	0.84	0.042	0.02	10	16.7	167	79	0.062	1.4	0.031	6.6	0.11
0.1	0.8	0.08	0.043	20	16.08	322	170	0.124	2.8	0.062	13.3	0.24
0.2	0.76	0.152	0.094	40	15.2	608	376	0.249	5.6	0.124	26.5	0.54
0.3	0.72	0.217	0.152	60	14.47	868	608	0.373	8.4	0.187	39.8	0.87
0.36	0.7	0.253	0.19	72	14.06	1012	759	0.448	10	0.224	47.8	1.09
0.4	0.69	0.276	0.216	80	13.8	1104	864	0.497	11.1	0.249	53.1	1.24
0.5	0.66	0.329	0.286	100	13.16	1316	1144	0.622	13.9	0.311	66.3	1.64
0.6	0.63	0.376	0.362	120	12.55	1506	1446	0.746	16.7	0.373	79.6	2.08
0.7	0.6	0.418	0.443	140	11.95	1672	1772	0.871	19.5	0.435	92.9	2.54
0.8	0.57	0.454	0.53	160	11.36	1817	2119	0.995	22.3	0.497	106.1	3.04
0.9	0.54	0.485	0.622	180	10.77	1939	2489	1.119	25.1	0.56	119.4	3.57
1	0.51	0.51	0.72	200	10.2	2040	2880	1.244	27.9	0.622	132.7	4.13

Testing

A fuel cell stack with the necessary auxiliary support equipment was procured for this project from H-Power. We verified the performance of the fuel cell system using the experimental setup shown on Fig. 112. The source of hydrogen for these experiments was a pressurized tank. The pressure supplied to the fuel cell was further regulated down to 20!psig. The system had an internal pressure regulator that further reduced the pressure supplied to the fuel cell to less than 5!psig. The hydrogen side of the fuel cell operated in a dead-end mode with periodic purges, necessary to vent any inert impurities and water accumulating during fuel cell stack operation. The air is supplied to the fuel cell using a pump, which was internal to the system. A microcontroller, supplied with the system, monitored internal temperature, pressure, fuel and oxidant flows. The fuel cell system was supplied with eight AAA size alkaline batteries for bootstrapping the system during start-up. An ABC-150 was used as a load for the performance evaluation. The ABC-150 is a very versatile computer controlled power processor, designed for testing all types of energy storage systems. It has the capabilities to deliver very fast transients, in power, current or voltage modes. Its internal data acquisition system can collect current and stack voltage data at 0.1!s intervals.

The fuel cell start-up is quick. The system is capable of delivering 80% of its full rated power in less than one minute.
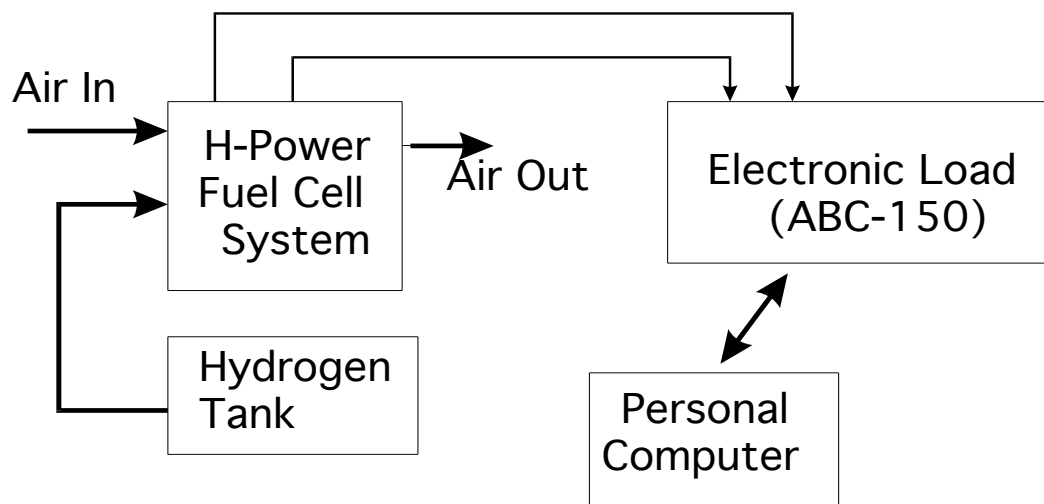

Fig. 112. Schematic diagram of the experimental set-up.

The data from the steady state performance of the fuel cell system are presented in Fig.!113. The data were recorded after the stack was operated in a steady state mode for 30 minutes in order to bring it to optimal conditions. The filled triangles represent stack voltages after 2-minute dwell time at a given stack current. The filled rhomboids are the measured stack voltages with five second dwell time at each current. The solid lines are polynomial approximations of the stack voltage and delivered power as a function of stack current. An unusual instability of the stack performance was observed repeatedly in the range of current densities between 5 and 8!A.
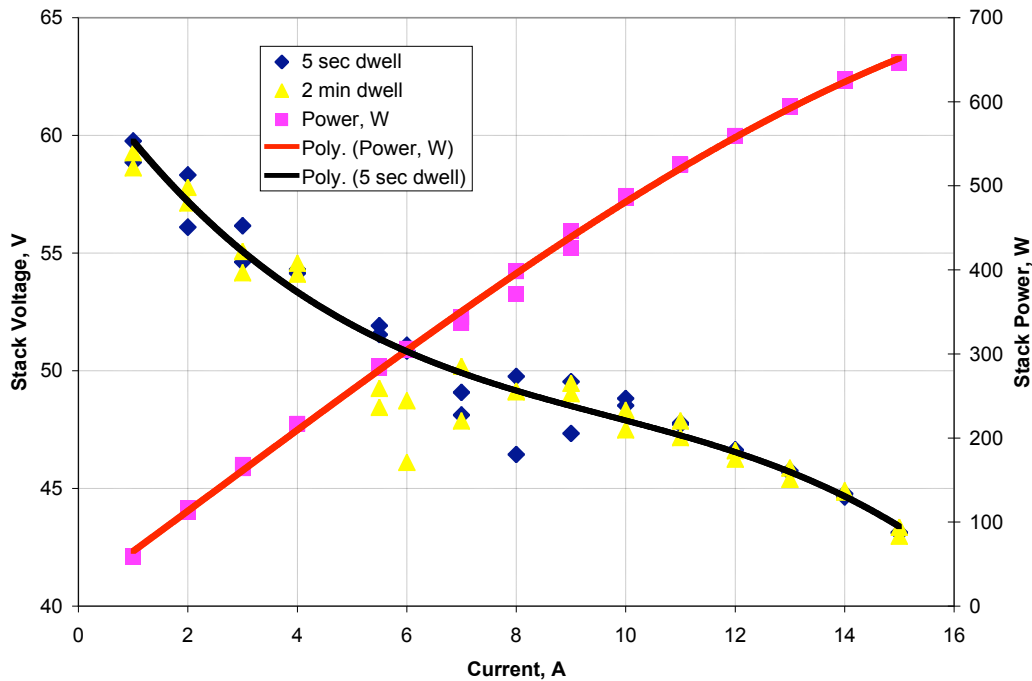
Fig. 113. Typical measured dependence of stack voltage.
(As a function of stack current at optimal system conditions.)

After we convinced ourselves that the fuel cell system performance was very close to the performance described in the technical manual we proceeded with an effort to characterize the system with pulse loads. After a short period for fuel cell conditioning we requested stack current of 2!A for the low power level and 15 A for the high power level. The length of the high power level pulse was set at 20 s. Data for voltage and current were collected at 100 ms intervals. From the graph in Fig.!114 it is evident that the load following capabilities of the fuel cell in this mode are excellent. To illustrate better this point the first and last pulses are presented in a larger scale graph in Fig.!115. One can see that the transition between operation at 100!W and 650!W is instantaneous and there is no deterioration in performance (see Fig.!116 for comparison).

Since the exact power profile for the exoskeleton as a function of time is not known at this time we decided to verify one more mode of pulsed operation – with much longer pulses. Results from an experiment with 3 minute long power pulses are presented in Fig.!117 and Fig.!118. It was evident that even with the long pulse the fuel cell system was able to maintain steady performance at the maximum power level.

It is important to note that the behavior of the fuel cell stack in pulse mode was strongly dependent on the method of fuel and oxidant delivery to the stack. For these experiments hydrogen was readily available, and the air pump was also operating constantly.
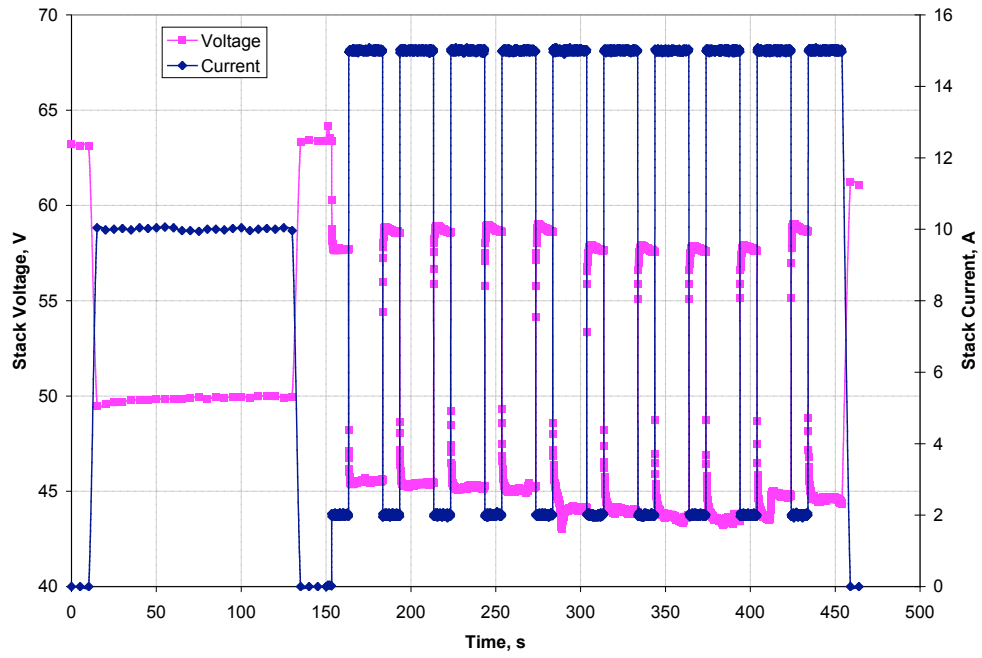
143

Fig. 114. Stack voltage and current as a function of time. Pulse width 20 s.
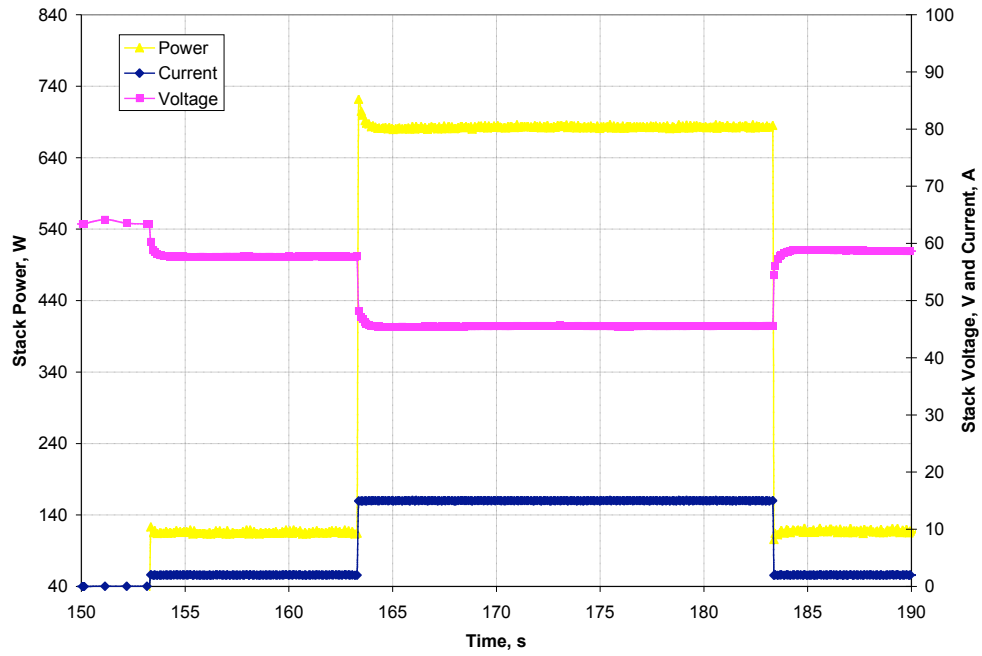

Fig. 115. Stack power, voltage and current as a function of time. Pulse width 20 s
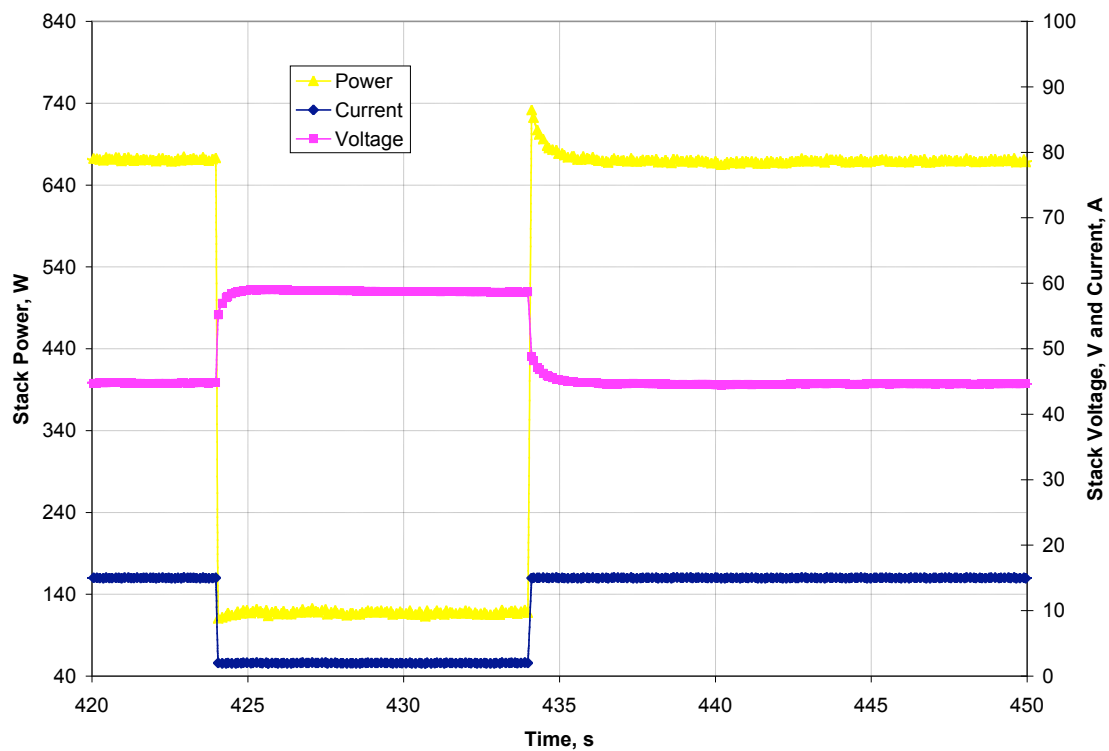(Beginning of the pulse sequence.)

144

Fig. 116 Stack power, voltage and current as a function of time. Pulse width 20 s.
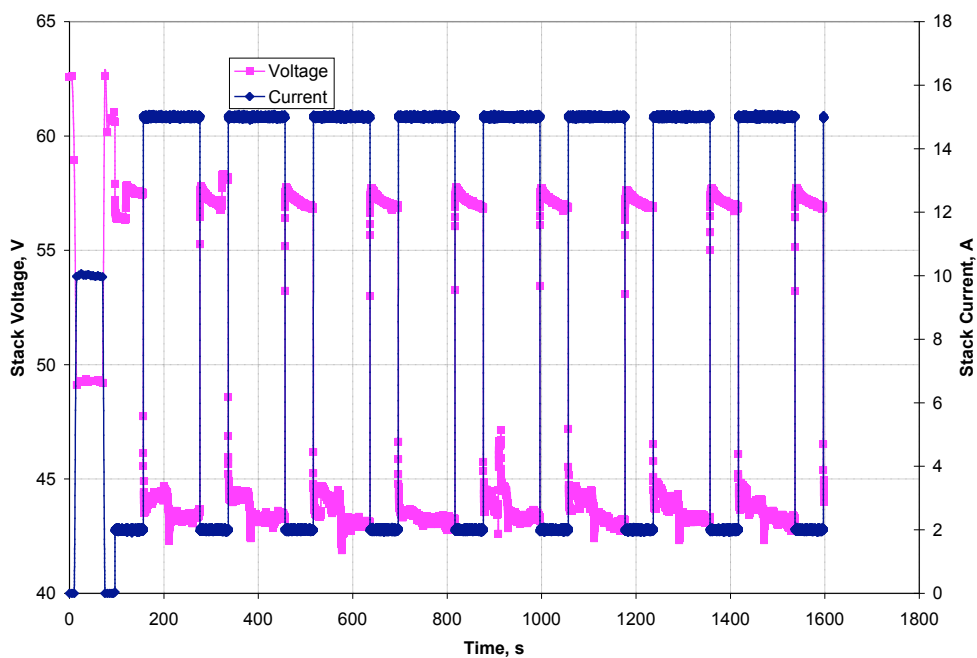(End of the pulse sequence.)

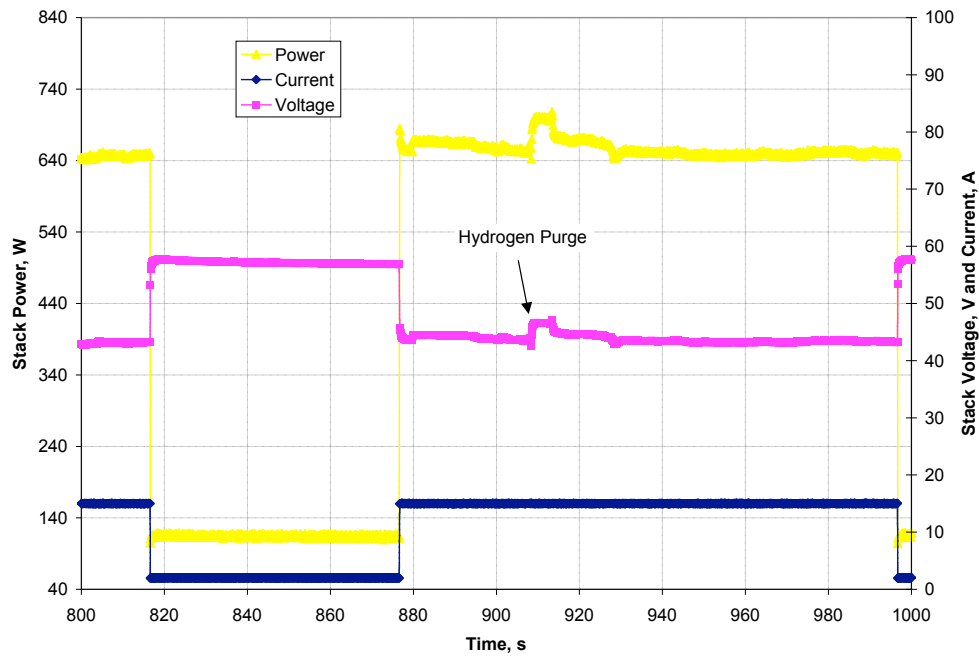**Fig. 117. Stack voltage and current as a function of time. Pulse width 180 s.**

145

Fig. 118. Stack power, voltage and current as a function of time. Pulse width 180s
(Single pulse.)

Results: Digital Data Acquisition and System Control

Layout

The data acquisition and control system was based on the Battery System Controller (BSC) developed at AeroVironment over several years, and used in numerous energy storage systems based on battery packs, fuel cells, microturbine, flywheels etc. A schematic of the system architecture is shown in Fig.!119. The BSC monitors all cell voltages of the fuel cell stack, the transient handler pack voltage and temperature, the FC current, the transient handler current and the temperatures of the hydrogen generator. It sends commands to the cooling fans, the air compressor, the solution pump of the hydrogen generator and the solenoid valves. It also output all the data via a serial port for monitoring and recording.

Several software and hardware modifications and enhancements were required in order to meet the specific objectives for the exoskeleton energy storage system.
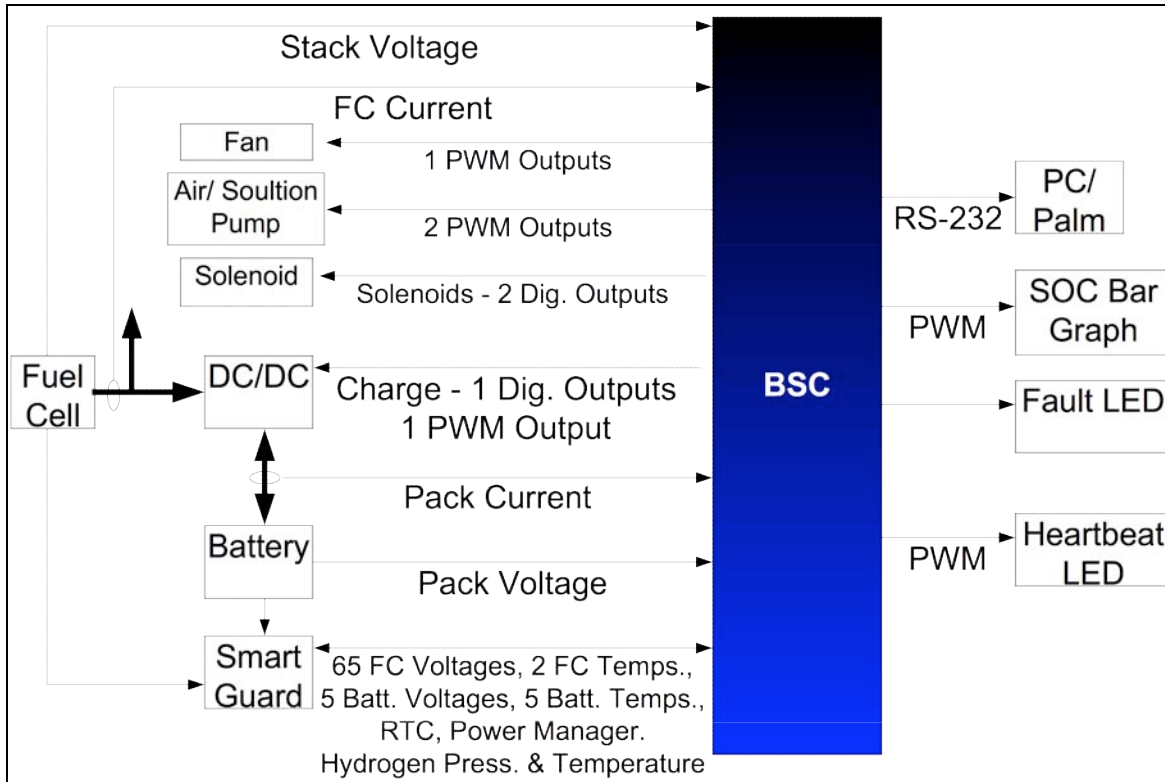
146

Fig. 119. Energy storage system control diagram.

Results: Hybrid System Configuration

With the components exercised, our next step was to see if the main components of the hybrid system could be scaled to an established duty or known range of operating conditions for future exoskeleton work.

Selection

An operating voltage of 48VDC was established to be the best voltage to allow for the hybrid system to be controlled. From this operating voltage a system control concept was developed and a control circuit was designed around this concept. Based upon our previous test data from the battery testing, it was decided that the Panasonic NiMH batteries were the best choice for the transient handler system. From there the system was broken into three main parts:

1. Fuel Cell System - the H-Power Fuel Cell, pressure regulator, and high pressure hydrogen supply

2. Transient Handler System - DC/DC converters, control logic circuit, diodes, NiMH battery sticks, fuses, terminal block, and thermal switch

3. Load System - an on/off switch, timer relay, relays, 150!W load for continuous load to system, 1850!W load on relays as a pulse load.

The control concept, as shown in Fig.!120 for the hybrid configuration of the fuel cell system was as follows:

1. As a pulse load that is greater than the power capability of the fuel cell system is sensed by the control circuit of the transient handler system, it "turns on" the DC/DC converters. This then pulls power from the transient handler system and fuel cell system in parallel.

2. This continues until the pulse load stops, the transient handler system is to a level that requires it to be recharged (battery cell voltage <=1.0 VDC), or the transient handler system is to a level that it is considered fully charged (battery cell voltage >=1.5 VDC).

3. At this point the fuel cell system handles the entire load until the pulse load exceeds the fuel cell system power and the cycle of maintaining the transient handler system's state of charge starts over. In this way the fuel cell always operates at rated power and system controller regulates the transient handler voltage in a way that it will not damage itself and also maintain a high state of charge.

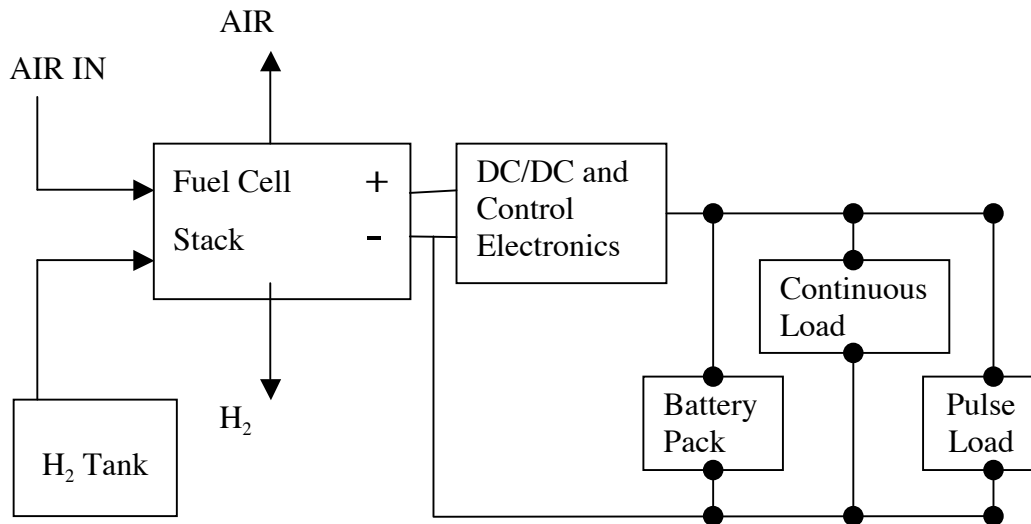**Fig. 120. Hybrid fuel cell system diagram.**

The Transient Handler parts, shown in Fig. 121 consisted of the following:

10 NiMH cell "sticks" (7 elements in a "stick", 5 "sticks" in a series, 2 parallel groups)
DC/DC converter mounted on an Aluminum heat sink
Transient Handler control circuit
Components for circuit measurements and protection
Thermal switches mounted to sticks for cell protection

Fig. 121. Transient handler system.

The Pulse Load parts (Fig. 122) consisted of the following:

       150!W continuous load (halogen automotive light bulbs)
       On/off switch
       Variable time delay relay to control pulse load relays
       Load relays for pulse loads
       1850!W pulse load (off-road high intensity light bulbs)

Instrumentation for the testing consisted of clamp-on style ammeters, voltmeters, and thermocouples. The testing was videotaped with a clock in the background to show the duty cycle times. The pulse loads were also run at varying times to observe the transient handling capabilities of the system. To have the load be "visual" high intensity automotive lights were chosen to be the load so that the load and the representative duty cycle tested could be observed. Fig. 123 presents the bench test setup that was used to check the system.
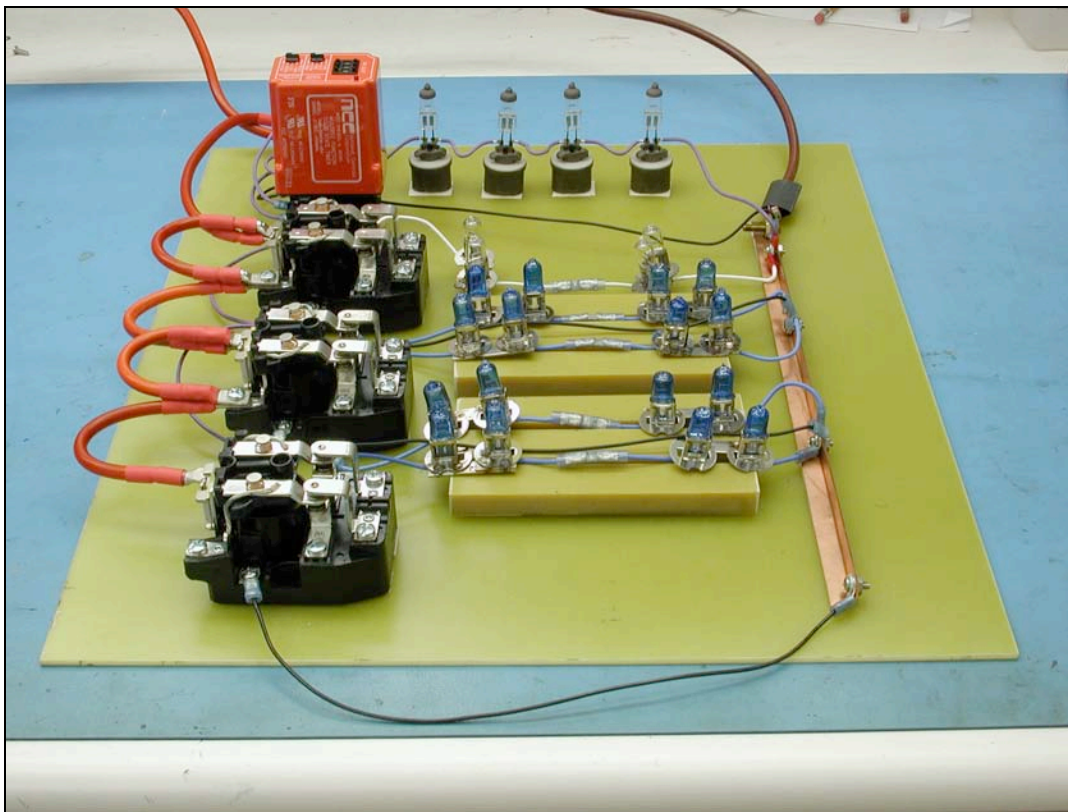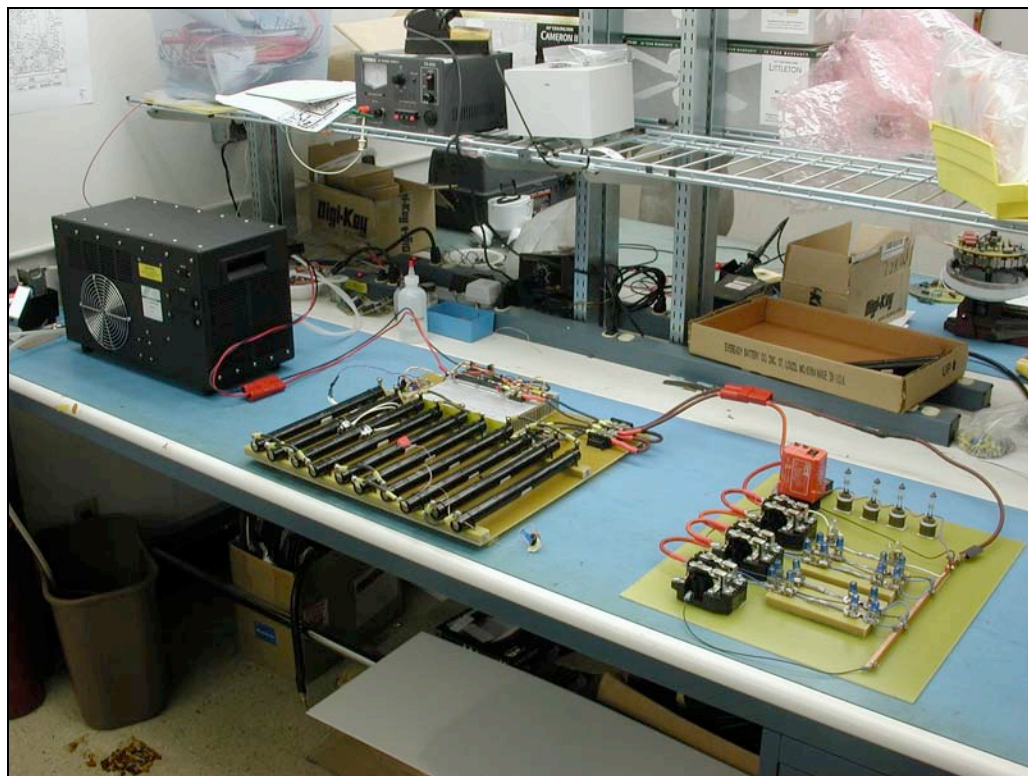
Fig. 122. Pulse load system.

Fig. 123. Hybrid fuel cell system bench test set-up.

150

Testing

The following tests were performed:

LOAD/CYCLE	DURATION/CONCLUSION
150!W Continuous (Fuel Cell only)	PASS
150!W continuous w/~400!W pulse load	PASS – no affect from varying pulse@ listed time cycles (Fuel Cell only)
.5 sec pulse load 1 sec pulse load 2 sec pulse load 9 sec pulse load	
150!W continuous w/~1850!W pulse load @ cycles (Fuel Cell and Transient Handler)	PASS – note varying duration listed time
.5 sec pulse load	~13 min. cycle
1 sec pulse load	~13 min. cycle
2 sec pulse load	~12 min. cycle
5 sec pulse load	~10 min. cycle
9 sec pulse load	~9 min. cycle

Time between cycles to recharge Transient Handler was about 15 to 18 minutes.

Results

Included in the Appendices of this report is a video demonstrating that the system was capable of handling the various input cycles listed below:

> Validation of the system approach and its components
> Transient response of Fuel Cell to loading
> Transient Handler system capable of sustaining 2!kW pulse loads
> Hybrid system capable of maintaining loads at a derived duty cycle.

Hydrogen Generation and Control

The hydrogen storage chemistry used for the Exoskeleton Power System was a solution of sodium-borohydride ($NaBH_4$) and water (H_2O) that was then passed over a catalyst to initiate the production of hydrogen. The catalytic chamber for this project was supplied by ORNL and was proprietary in nature. The physical size of this catalytic chamber can be seen in the following Figs.!124 and 125. It is 1" in diameter, and approximately 6" in length.
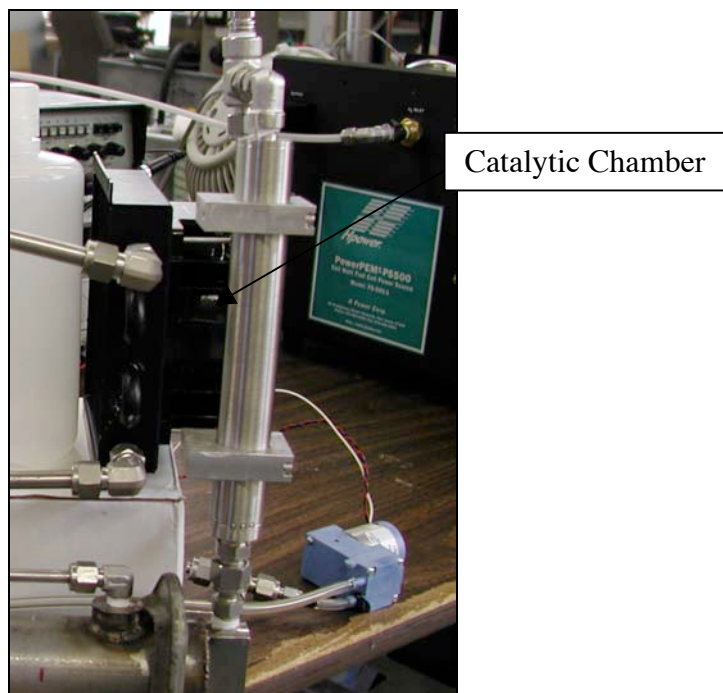
Fig. 124. The catalytic chamber.

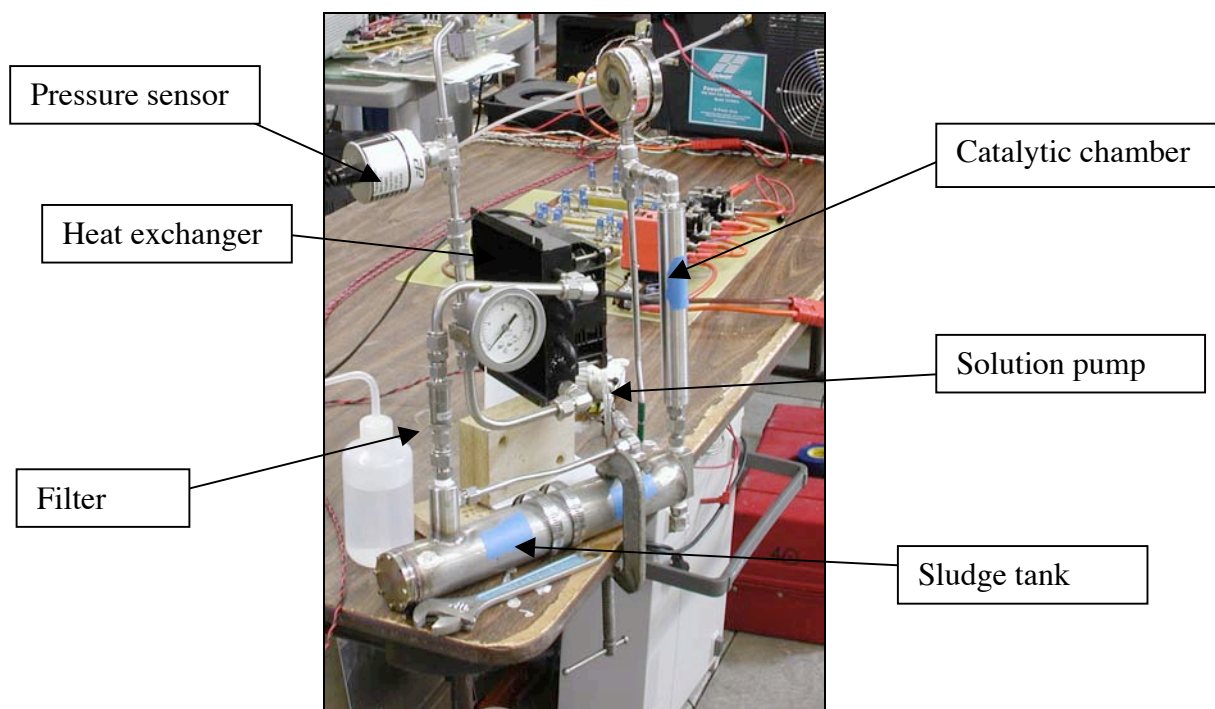**Fig. 125. System components.**

ORNL also suggested that we use the solution of sodium-borohydride and water, based upon the percentage by weight of sodium-borohydride to the water. The recommended mixture start point was 17%. If the percentage of $NaBH_4$ were made much higher than 17%, it would tend to clog the catalytic chamber after very short periods of time, and also demonstrate a significant amount

of spontaneous hydrolysis. The chemical equation for the process as it is passed over the catalyst is shown below.

$$NaBH_4 + 2H_2O = 4H_2 + NaBO_2 + 74kJ/mole \text{ of heat} \qquad (38)$$

A spread sheet analysis tool was used to predict: (1) the amount of hydrogen required from a known duty cycle, (2) the effect of that duty cycle on the state of charge on the hybrid system, (3) heat rejected from the fuel cell and hydrogen generator, (4) water produced, (5) $NaBH_4 + 2H_2O$ solution needed, (6) sludge solution produced, and (7) air requirements for the PEM fuel cell stack.

From this we were able to estimate weights and sizes of a viable power system for the Exoskeleton system, and it gave us parameters and levels to test to during the operation of the system.

As an example, a 630 W PEM fuel cell demonstration system required the following:

Hydrogen flow rate	6.78 SLM
Air flow rate	33.92 SLM
$NaBH_4 + 2H_2O$ solution flow rate	17.15ml/min
Individual fuel cell stack cell voltage	0.65 volts
Heat generated by fuel cell stack	563 W
Heat generated by hydrogen generator	380 W

As we first started to develop the system, we used these parameters for sizing of system components. After operating the system we found that finite control of the solution pump for the hydrogen generation system was not really required. The system operated in a mode of "self regulation". As the solution pump fed solution to the catalytic chamber and hydrogen gas was produced, the pump stalled at a certain gas pressure, regardless of flow rate, and filled up the volume of sludge tank and tubing leading up to the hydrogen inlet of the fuel cell stack. The fuel cell then used up this hydrogen, the gas pressure dropped, the pump was no longer stalled, and solution would flow again. The system seemed to regulate itself to an operating pressure between 15–25 psig. The percentage of $NaBH_4$ in the solution seemed to have a drastic effect upon system performance. At the base line of 17%, we experienced a serious amount of hydrolysis, which had a large effect on the pump performance (i.e., pump cavitation due to hydrogen bubbles in the solution). When we made up solutions of 10%–13%, we no longer experienced the cavitation problems, and the system seemed to operate very well.

We operated the power system multiple times for up to 30 minutes (at which point the system ran out of solution, and sludge tank storage). It would track whatever load was placed on the system with the light load bank. The fuel cell performance never seemed to be affected by, or have an effect upon the hydrogen generation system. More tests will have to be done to help optimize the system, but all in all, it tended to work very well, with very simple elements of control and monitoring.

Once the key subsystems were working properly, we added the system controller and the additional hardware to measure and control all system parameters. We also added the chemical

hydrogen generation subsystem, prepared the sodium borohydride solution and started operating the system. The prototype system was ready to operate. The system starts with a push of button and is all self controlled and self contained. The picture in Fig.!127 illustrates best the overall concept. The PC is used for data display and recording only. The electric load is on the bottom shelf and is used for system testing. The fuel cell stack is an off the shelf system and no effort has been expended in reducing the size of the stack or the balance of plant components. The whole system is spread out and is not optimized for weight or size.
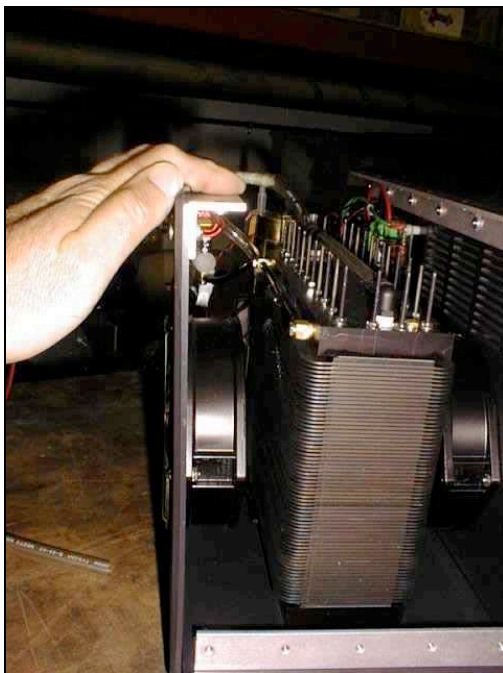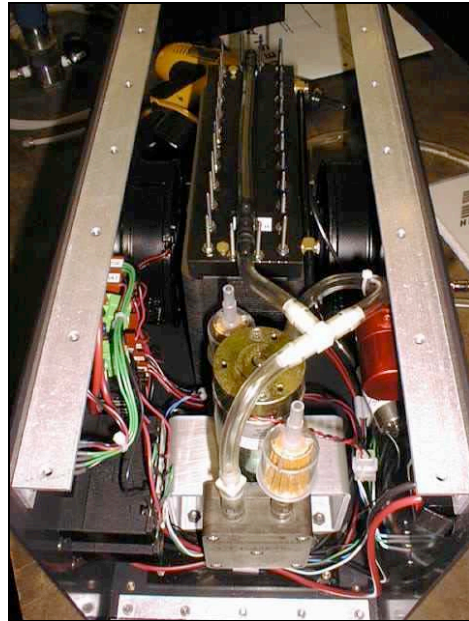
Fig. 126. H-Power fuel cell stack – nominal power 600 W.

Fig. 127. Overall system.

The data in Fig.!128 illustrate how the system can deliver peak power to the electric load as needed. When the transient handler state-of-charge dips below 20% the fuel cell starts charging it, whenever there is excess power available.
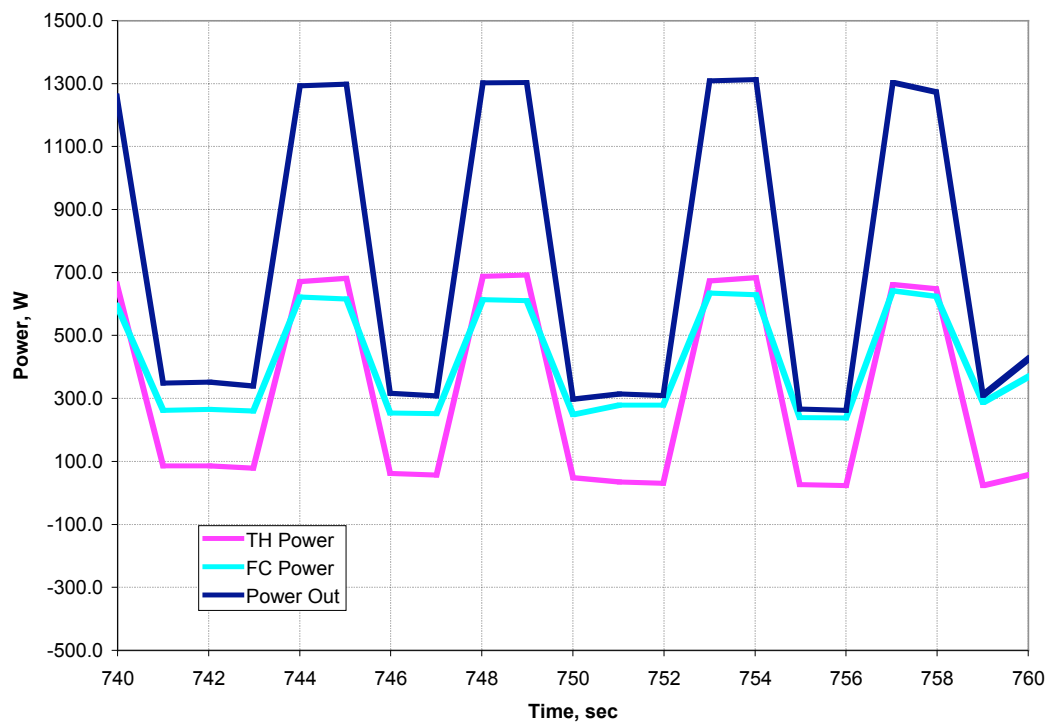

Fig.!128. Experimental data of fuel cell and transient handler.
(Working together to deliver 1.3 kW of pulsed power.)

155

Figure 129 shows the power electronics module that is responsible for regulating the output of the energy storage system and controlling the state of charge for the transient handler. Figure!130 is a picture of the system controller. Figure 131 shows the hydrogen generation module – it consists of a catalytic reactor, developed at ORNL, a spent solution chamber and a fresh solution chamber. A small pump is used to pump fresh $NaBH_4$ solution through the catalytic reactor. The hydrogen produced is cooled off to stack temperature and fed to the fuel cell. Whenever the hydrogen pressure drops below a set value, new solution is pumped into the catalytic reactor. The spent solution accumulates in the reservoir that is also used as a phase separator and prevents liquid from entering the fuel cell stack. A fine mesh filter is also used to make sure that the produced hydrogen does not carry any small liquid particles into the fuel cell stack. The air needed for fuel cell operation is provided by an off-the-shelf compressor. Its speed is controlled by the BSC and is proportional to the fuel cell stack current. The fuel cell stack temperature is also under control of the BSC – in four stages – the fan speed can be set at zero, low, medium and high in order to conserve energy.
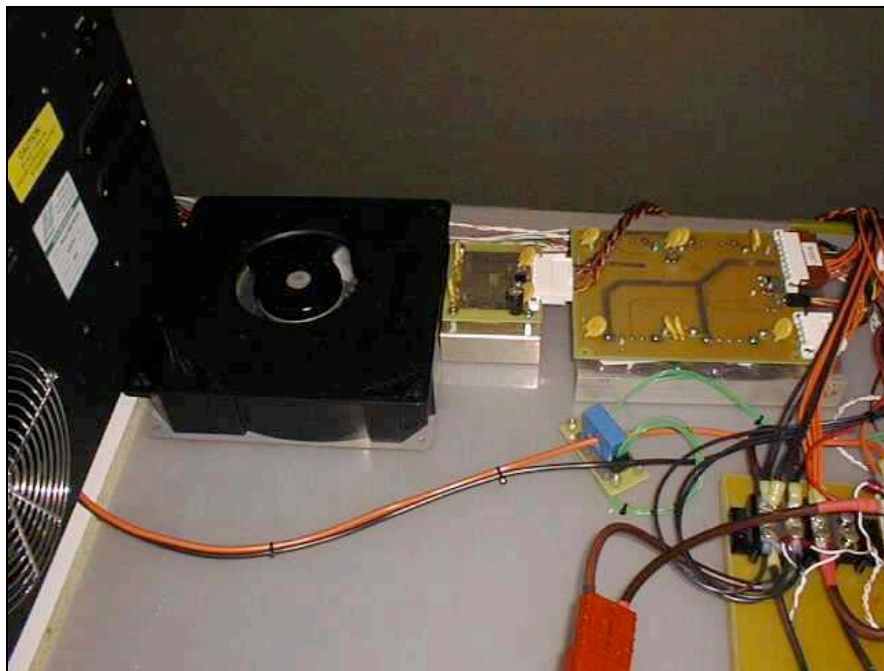
Fig. 129. Power electronics module.
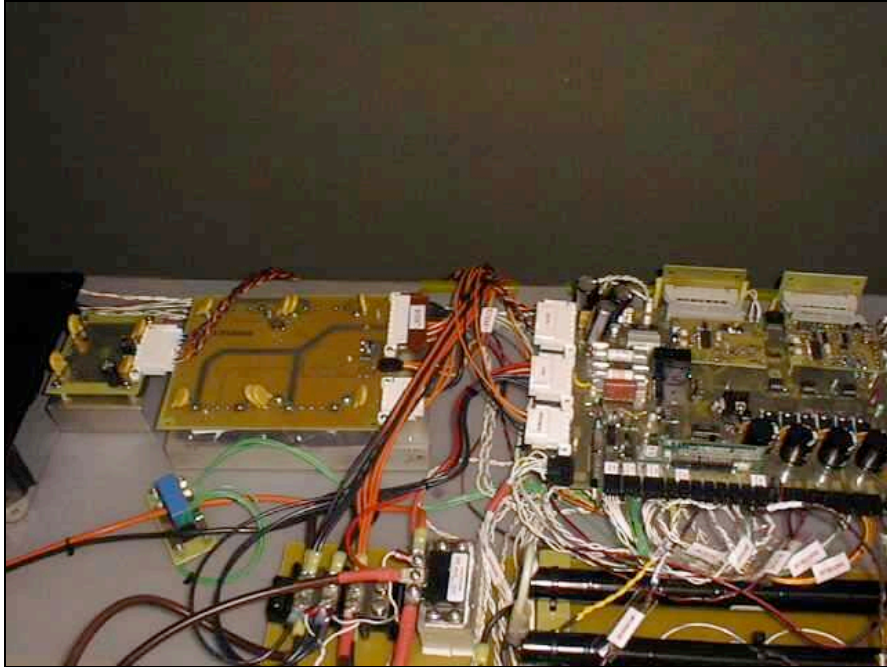
Fig. 130. System controller module.

Fig. 131. Hydrogen generation module.

Figure 132 shows the fuel cell stack module with a data acquisition system that measures every cell voltage in the stack. The system consists of five FC-SG modules, of 12 channels each. The modules are connected to the system controller via a fast serial bus. The data acquisition system was very useful when tuning of the system was performed but may not be needed when it is fully developed. Figure 133 shows the transient handler module. It is also instrumented with voltage and temperature measurement devices so that it's state-of-charge and health can be tracked. The

state of charge of the transient handler is monitored and controlled by the BSC with an elaborate algorithm that takes into account temperature, Ah depletion/addition, and average cell voltage. As can be seen in Fig. 127, all the components can fit on a small cart—and can be easily scaled—depending on the power needs and energy storage requirement imposed on the system.

All experiments with the current system were performed using a diluted solution of less than 17 wt % of $NaBH_4$ in water.

Fig. 132. Fuel cell module.

Fig. 133. Transient handler module.

CONCLUSIONS AND RECOMMENDATIONS

General Findings

The project was very successful in showing that a fuel cell hybrid power supply can be a viable option for supplying the power and energy needs of an exoskeleton. In addition, the project demonstrated that the hybrid power supply system is intrinsically safe, and can be operated from hydrogen created on demand by a package of sodium borohydride.
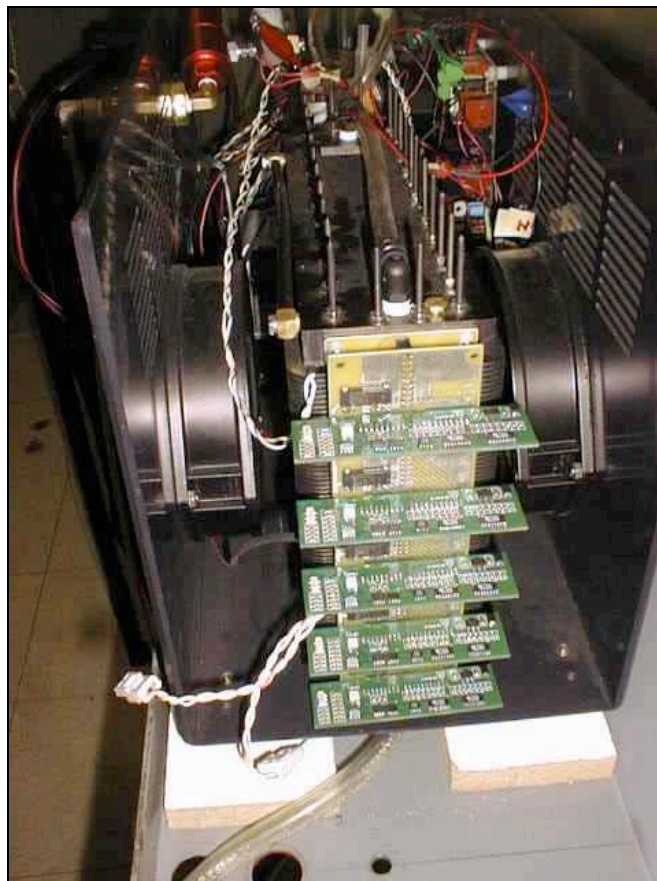
What worked and what did not – the system met all requirements of the project. There could be more tuning of the algorithm for power sharing and keeping the fuel cell operating at close to full power whenever needed in order to extend the availability of the transient handler. We had some difficulties with the stability of the sodium borohydride solution and the pump used to feed the catalytic reactor. It is desirable to reuse the water produced in the fuel cell and react it with dry sodium borohydride in order to increase the specific energy of the system.

Expected results and surprises – it is important to note that the fuel cell could successfully deliver power in a pulsed mode, even when operated with air compressor and hydrogen generated from chemical hydride.

General Recommendations

Recommendations for future work – the system described in this report is a brass board system built with mostly off-the-shelf components. The next task would be to find the lightest, most efficient components. There is significant room for size reduction, increased efficiency and simplified operation. The system can be packaged with different form factors.

159

In order to increase the specific energy of the system, a fuel cell product water recovery system should be incorporated in the design, with the capability to store the sodium borohydride in a dry form and mix it with the product water from the fuel cell, as needed.

Applicability to other projects/uses - The hybrid fuel cell system built for this project has potential for many other uses. For example, with slight modifications the control system could be a component for many other projects with similar architecture but in a significantly wide range of power ratings – up to 100 kW systems.

APPENDIX G

FEASIBILITY STUDY - ACTUATOR COMPARISON

This appendix is an excerpt from an ORNL exoskeleton feasibility study conducted for DARPA (Jansen et al., 2000). This appendix provides some of the background and basis for the design approach taken and is included here for completeness and the convenience of the reader.

The purpose of this section is to compare various types of actuator technologies subject to their relevance to the exoskeleton project. This section is not meant to be a primer about actuators but a comparison of potential relevant technologies. A designer must make decisions based on critical design parameters such as (1) power/mass, (2) power/volume, (3) stress, (4) strain, (5) steady-state efficiency, (6) power expended during load holding, (7) bandwidth or tracking performance, (8) auxiliary transmission system, (9) auxiliary power modulation equipment, and (10) ease of controllability. Depending on the type of actuator, some of the critical design parameters will not be applicable or not available due to design specificity. Actuator technologies will be broken down into two major groups: conventional and non-conventional. Conventional actuators are electric motors, hydraulic, and pneumatic. The non-conventional actuators are the piezoelectric and magnetorestrictive. There will be a brief discussion of the shape memory alloy and polymers. While others have examined these types of actuators in the past, their relevance to the exoskeleton project will be the main focus on this section. Before comparisons can be made, a brief description of the demands that will be imposed on the actuators of an exoskeleton will be given.

EXOSKELETON ACTUATOR DEMANDS

To understand the magnitude of torques and power required for exoskeleton actuators, loads for a human will be scaled to account for the higher weight of a loaded exoskeleton system. The loads are based on the assumption of a 150 lb individual with a 150 lb load to represent a 300 lb exoskeleton system (exoskeleton plus load). Only two joints, the hip and knee joints, will be considered to understand the load and power required for an exoskeleton actuator. Studies at ORNL, which looked at a variety of poses, showed a kneeling pose yielded the largest loads of 1,350 in-lb (153 N-m) for hip joint and 6300 in-lb (712 N-m) for knee joint. Examination of a simple knee-bend-type of movement, where the human and load are moving vertically up and down with respect to gravity with 17.5 in of motion in 1 s, shows power levels for the knee joint can approach 600 W and for the hip joint around 120 W. Peak knee-joint velocities can approach almost 200°/s and for the hip peak velocities around 100°/s are possible. For walking and running, peak joint velocities can go up by a factor of three times these numbers.

Based on human-motion profiles for simple ballistic-type of walking (McMahon, 1984), a periodic gait pattern of around 2 Hz can easily be seen, and even higher numbers are possible for other types of motions (e.g., running). Power requirements for simple ballistic walking will be significantly lower than for a deep-knee-bend-type of movement; however, the actuator would have to be rated for the worst-case scenario.

To evaluate different types of actuators, actuators around the 500 to 1000 W levels will be discussed with thousands of in-lb of torque capability and with the closed-loop bandwidth to accurately track a 2 Hz gait.

CONVENTIONAL ACTUATORS

Conventional actuators are those that are common for robotic manipulators. Basically, there are three major types: electromagnetic (electric motors), pneumatic, and hydraulic. For the electromagnetic category, only brushless dc motors will be examined since they are the closest match to the intent of this project. Reluctance-based motors such as those from Nippon Seiko (NSK) called Motornetics Megatorque™ motors will not be examined because, while they have a somewhat higher torque to mass ratio than do standard brushless dc motors, their overall larger diameters and associated power electronics puts them at a disadvantage pertaining to packaging. Pneumatic and hydraulic actuators based on classical servovalve control will be examined and will be compared to each other.

Electromagnetic Actuators (Brushless Motors)

About 50 motors from Inland Motors, Inc., were examined. All were high-end frameless, brushless motors. A plot of the continuous power versus mass is shown in Fig.!134. For electric motors (specifically those around 0.5!kW to 1!kW level) the power-to-mass ratio can be bounded by a line, which has a slope of roughly 500!W/kg. The continuous torque out of an electric motor per unit total motor volume is shown in Fig.!135.
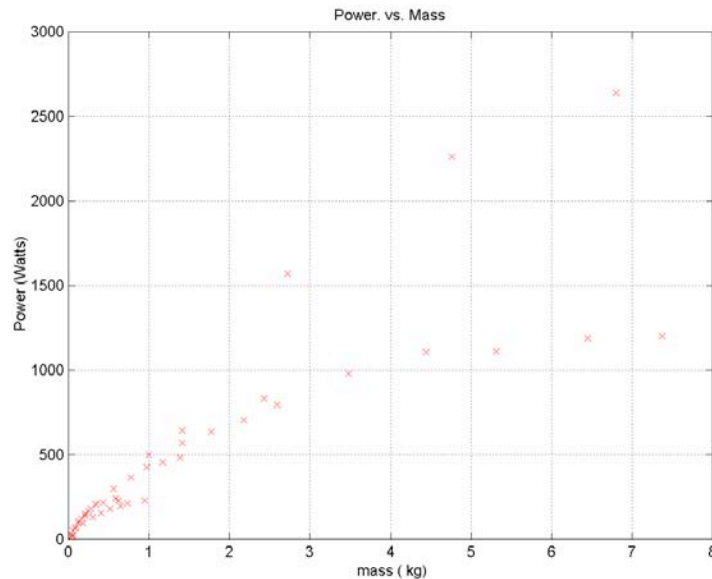
Fig. 134. Power vs mass for frameless brushless dc motors.

164
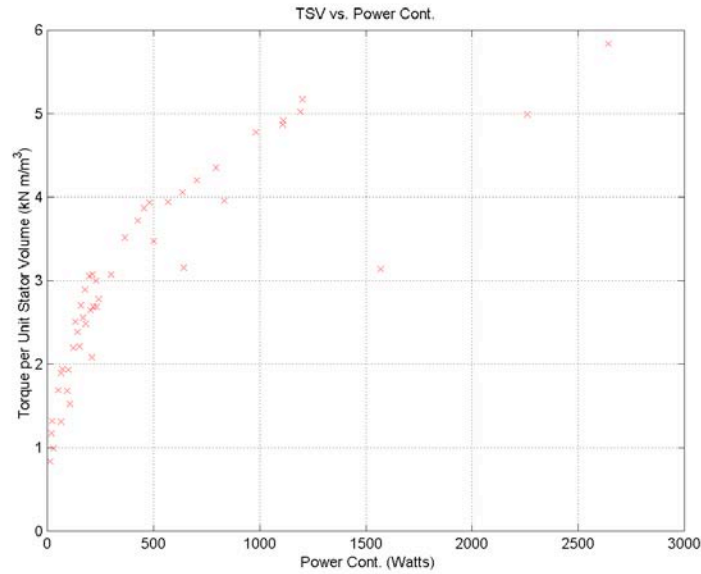
Fig. 135. Torque per unit motor volume vs continuous power.

For 500- to 1000-W motors, the continuous torque per unit motor volume varies from 4 to 5 KN/m^3. Figure 136 shows the continuous torque per mass for the same power range, which is under 3 Nm/kg. The continuous torque per unit volume and continuous torque per unit mass ratios will increase if the thermal operating range of the motors can be exceeded (e.g., air cooling, special higher temperature rated wires). Some researchers cite numbers twice as high as the ones given (Hollerbach, 1992), which can be obtained by the so-called megatorque motors, which are manufactured by NSK; however, as previously mentioned, the package volume of these motors are probably unsuitable for an exoskeleton.
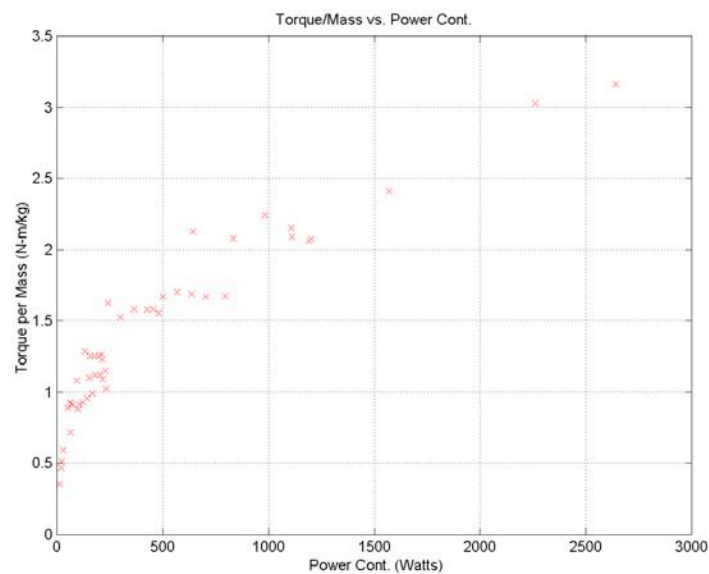
Fig. 136. Torque per mass vs power continuous.

165

Upper values for the shear stress over the rotor surface of an electric motor have been reported to be under 5 psi (higher values are possible if a cooling system is added). These low values of shear stress are not subject to significant improvements and are currently limited by heat transfer and the magnetic saturation limits of supporting ferrous structure (Miller, 1989). Steady-state electromechanical efficiency is around 85 to 95%. The power required for holding rated torque at stalled conditions can range from 5 to 10% of the power rating of the motor. Basically, this means that while no mechanical power is being expended, significant power is required to merely hold the load. Mechanical brakes are typically not an option for a high-performance servo system.

Based on the 600!W required for the knee-joint actuator and the 120!W for the hip joint, and using a 500!W/kg value for actuator mass sizing, a 1.2!kg actuator for the knee and 0.24!kg actuator for the hip would be required. The equivalent torque rating for these actuators, based on the 3!Nm/kg torque sizing value, would be 3.6!N-m for the knee joint actuator and 0.72!N-m for the hip joint actuator. Since we need a 712!N-m for the knee joint, a transmission system (e.g., gearbox) with about a 200:1 ratio is needed for the knee joint. Likewise, for the hip joint we need 153!N-m, and a transmission system again of about a 200:1 ratio will be required. Steady-state transmission efficiencies are typically 80 to 90%, which means that the motors would have to be 10 to 20% larger from a power perspective. Depending on the type of transmission system, such as a harmonic to a planetary type of gearhead, the transmission system can increase the overall package volume by 20%–50%. For simplicity, the impact of the actuators and transmission system on the overall weight of the exoskeleton, while not insignificant, has been ignored in terms of the joint velocity.

From Fig. 137, we see that the maximum unloaded speed of an electric motor is under 75!revolutions/s. When divided by the 200:1 gear ratio, the maximum unloaded angular velocity is 123°/s. Since running will require significantly higher peak joint velocities, a significantly larger motor size will be required by roughly a factor of 2 (i.e.,!the power density will decrease by a factor of 2) to achieve adequate joint velocities. In summary, a transmission system is needed for an electric system, and it can significantly impact the overall package volume and efficiency. To track peak joint velocities, the motor size will have to be increased significantly because of the high gear ratios required.

The volume and mass of the power electronics associated with an electric motor vary greatly depending on the power source (i.e., dc or ac) and how close the voltage of the supply is to the voltage needed by the motor. Typically, on industrial robotic manipulator systems (where weight is not a major concern), the power electronics can easily exceed the weight and volume of all the actuators. Power-to-volume densities are typically in the 2- to 40-W/in^3 range (as compared to around 25!W/in.^{3} for electric motors). By judicial design, the volume and mass of the associated power electronics can be significantly reduced, but not without a significant design effort.
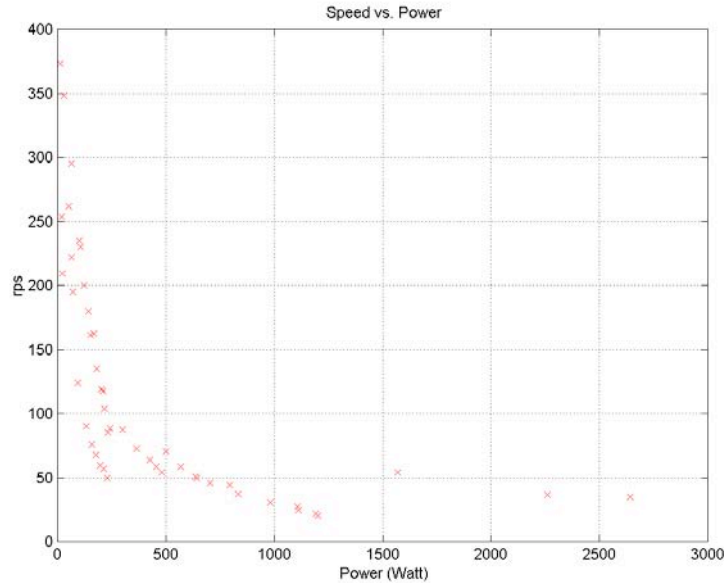
Fig. 137. Speed (revolutions/s) vs continuous power.

Hydraulic Actuators

Hydraulic actuators are fundamentally different than electric motors in that the amount of flow into a hydraulic actuator is limited by the maximum amount of flow possible from the pumping source and any flow restrictions caused by flow control elements such as servo valves. Thermal limitations associated with electric motors do not apply to hydraulic actuators since the hydraulic fluid cools and lubricates the system. Material restrictions are based only on pressure limits. As a rule of thumb, the power to mass ratio is about five times that of an electric motor and the power to volume ratio is about ten times that of an electric motor for many applications. Again, these numbers could be higher or lower depending on the particular application. The pressure levels are from 3,000 to 5,000 psi (or 21 to 35 MPa), with 3,000 psi being an industrial standard. Maximum strain levels correspond to the stroke length over the total actuator length, which can range from 0.5 to 0.8 for most actuators. For rotary actuators, the maximum strain levels do not apply. Unlike the electric motor, the force or torque that can be produced can be easily matched to the application simply by changing the effective area for a linear actuator or the effective displacement for a rotary actuator. Therefore, a transmission system is typically not required. Only the friction at the seals and leakage affects limit the steady-state mechanical efficiency. For linear actuators, high, steady-state mechanical efficiencies are possible and are in the upper 90% range. Rotary actuators range from 80 to 90%. For load-holding applications, zero power is expended for linear actuators with asymmetrical cylinders and a small amount of power is expended in the 1 to 10% range because of leakage for symmetrical cylinders and rotary actuators.

The bandwidth of a hydraulic actuator can be derived based on a few simplifying assumptions; (1) only a symmetrical cylinder design will be assumed; (2) fluid volume outside of the cylinder will be ignored; and (3) half of the system pressure is used to hold the load against gravity. In addition, the fluid bulk modulus will be assumed to be at 100,000 psi (or 689 MPa) and the

system pressure is set at 3000 psi (21!MPa). Starting with the natural frequency, f_o (in Hz), the derivation of a hydraulic cylinder is (Viersma, 1980)

$$f_o \geq \frac{1}{\pi}\sqrt{\frac{A\beta}{MS}} = \frac{1}{\pi}\sqrt{\frac{A\beta g}{MgS}}$$

or

$$f_o \geq \frac{1}{\pi}\sqrt{\frac{\beta g}{\frac{Mg}{A}S}} = \frac{\sqrt{2}}{\pi}\sqrt{\frac{\beta g}{P_s S}}$$

which can be further simplified to

$$f_o\sqrt{S} \geq \frac{\sqrt{2}}{\pi}\sqrt{\frac{\beta g}{P_s}} = 8.1 \tag{39}$$

where

M = load mass (kg),

A = effective stroke area (m^2),

P_s = supply pressure (3000 psi),

S = stroke length (m),

g = gravity constant = 9.807 m/s^2, and

β = fluid bulk modulus constant (100,000 psi).

As an example for a stroke length of 6!in (0.1524!m), the natural frequency would be above 21 Hz. Depending on the type of controller (i.e., position or pressure acceleration and type of feedback), the closed-loop bandwidth could be as low as 0.15 [for positional feedback, (Merritt, 1967)] to 0.5 [for acceleration feedback, (Viersma, 1980)] of the natural frequency value with 0.15 typical for industrial applications. For this example, the closed-loop bandwidth would typically be greater than 3!Hz.

Control of a hydraulic actuator for high-precision applications is typically through a servo valve. The bandwidth for most high performance servo valves that would be applicable to the exoskeleton project would be typically from 50 to 100 Hz (see Moog's model 30 valves at www.moog.com). Losses associated with a servo valve could be as high as about 1/3 of the maximum power to the hydraulic actuator since most servo valves are rated for a 1,000-psi drop across their orifices. Reliability of a hydraulic actuator is mainly limited by seal and/or gland wear and impact loads. Servo valves associated with a hydraulic actuator are more likely to fail. However, with suitable control of the overall filtration levels of hydraulic fluid, servo valves can have a long service life (exceeding over one quarter million hours mean time before failure for valves such as the deflector jet type) as noted by their application in the commercial aircraft industry.

The power electronics associated with the hydraulic servo valve and actuator can be inconsequential. For a two-stage servo valve, the drive current for the torque motor is typically well within the linear operational amplifier range (e.g., the Moog's model 30 is typically rated around 16!mA). This again adds to the advantage of hydraulic actuators as compared to electric motor actuators.

One final point associated with hydraulic servo systems which needs to be mentioned, is the noise problem associated with the pumping system. Hydraulic pumps are typically noisy at fairly low frequency, thus making sound proofing at reasonable packaging volumes difficult because of the large acoustical wavelengths.

Pneumatic Actuators

Pneumatic actuators are very similar to the hydraulic actuators in many respects. However, a few exceptions are especially noteworthy. Air is typically a poor lubricating and cooling medium, as compared to a hydraulic fluid medium. Losses are higher because of fluid leakage through seals. Furthermore, air is significantly more compressible than a hydraulic fluid medium. Compressibility of air will significantly lower the natural frequency of a pneumatic control system. Significant energy can be stored in this medium, which can be used to one's advantage, such as mitigating impact loads, or it can be a safety problem because of the possible burst hazard it presents. In comparison, hydraulic fluid has no significant energy storage capability. Also, as a practical limitation, the supply pressure for a pneumatic storage device is limited to 100 to 150 psi as compared to 3,000 to 5,000 psi, for a hydraulic system. Power to weight and power to volume for pneumatics can vary depending on the type and application. For elastic-type pneumatic actuators, such as the McKibben muscle (Chou, 1996), these ratios can rival hydraulic actuators. For hard-shell-type pneumatic actuators, these ratios are closer to electric actuators; however, the pneumatic actuators are only limited by the mass flow from the pump and any flow restrictors such as a servo valve.

While at first glance pneumatic actuators hold many advantages such as (1)!high power to weight and power to volume (for elastic type pneumatic actuators), (2)!good impact load mitigation, and (3)!energy storage capability; there are some important limitations. While losses are typically higher than hydraulic and safety is always a concern, the main barrier for pneumatic types of actuators is the bandwidth caused by the compressibility of the air. Based on similar assumptions made for a hydraulic actuator and starting with the basic natural frequency formulation!of a pneumatic cylinder (Andersen, 1967)

$$f_o \geq \frac{1}{\pi}\sqrt{\frac{k_p}{M}} = \frac{1}{\pi}\sqrt{\frac{4nP_sA_p^2g}{MgV_t}}$$

or

$$f_o \geq \frac{1}{\pi}\sqrt{\frac{nP_sg}{\dfrac{Mg}{A_p}\dfrac{V_t}{A_p}}} = \frac{1}{\pi}\sqrt{\frac{ng}{S\dfrac{\dfrac{Mg}{A_p}}{P_s}}} = \frac{\sqrt{2}}{\pi}\sqrt{\frac{ng}{S}}$$

169

which can be further simplified to

$$f_o \sqrt{S} \geq \frac{\sqrt{2}}{\pi} \sqrt{ng} = 1.4 \quad \text{to} \quad 1.7 \tag{40}$$

where

n = polytropic exponent which can vary from 1 to 1.4 (ratios of specific heat for air),

k_p = effective stiffness of gas in cylinder, and

A_p = effective area of pneumatic cylinder.

Comparison of the natural frequency of hydraulic and pneumatic actuators by means of Eqs. (39) and (40), clearly shows that for a given stroke length the natural frequency of hydraulics is 5 to 6 times higher than pneumatic actuators. Regardless of the type of feedback scheme, since whatever can be applied to a pneumatic servo can be applied to a hydraulic servo, the closed-loop bandwidth of a hydraulic system will be 5 to 6 times higher than a pneumatic servo-system for the same stroke length. For the example in the previous section, the hydraulic closed-loop bandwidth was calculated to be greater than 3!Hz, while for pneumatics, it would be anticipated to be greater than 0.5!Hz. Closed loop tracking at 2!Hz, for this example, can only be achieved with hydraulic actuators.

NON-CONVENTIONAL ACTUATORS

Non-conventional actuators are those that are typically described as associated with smart materials, such as piezoelectric, magnetostrictive, shaped memory alloys, and electroactive polymers. While there are others (such as those associated with magnetorheological and electrorheological fluids, and electrostrictive materials), only a few of these materials are seriously being considered as viable candidate for the exoskeleton project. In the future and after more research, these other candidates could play an important role in actuator applications.

Piezoelectric Actuators

Large forces and small displacements occur in a piezoelectric crystal when an electric field is applied. Compressive stress levels can be as high as 35!MPa (5,000!psi), whereas the tensile stress levels can be only 5 to 10% of the compressive stress level. Typically, a mechanical force bias is required to avoid the tensile stress limits. Displacements are typically very small for piezoelectric materials. Currently, PZT ceramics are the materials of choice for piezoelectric ceramic actuators. These materials have piezoelectric coefficients d_{33}, around 200 to 750!pC/N, and strain levels from 0.05 to 0.1%. However, there is a new piezoelectric material that has the potential to change future piezoelectric actuators. This new material, a single crystal form of relaxor-based ferroelectric materials (PZN-PT), has been observed to have piezoelectric coefficients d_{33}, around 2,000!pC/N, and strain levels from 0.5 to 1.0%. While these materials have been known for several years, their potential for high performance actuators has recently been recognized (Park, 1997). Applications that require high forces and small displacements, such as those in acoustic applications are immediate application areas. However, ferroelectric

crystals experience a hysteresis effect, which make them difficult to control for high-precision applications.

One difficulty of using piezoelectric material pertains to converting small displacements to large motion (i.e., the transmission problem). Various ideas include the "inch-worm," where micro-stepping action through rapid lock-and-move sort of motion are used to create a large linear motion. Another concept is that of a piezoelectric hydraulic pump (Nasser, 2000), where small quantities of fluid moves at very high frequencies. The accumulation of small drops of fluid at a high rate adds up to a large flow rate. Both of these concepts are based on the idea of the cyclic motion of the piezoelectric material. A simplified electromechanical model is shown in Fig.!138. The left-side ports are the electrical ports where a voltage is applied and current is injected into the crystal. The right-side port is where force represents the equivalent voltage and velocity represents the current. A mechanical load, Z_m, is shown attached to the mechanical port.
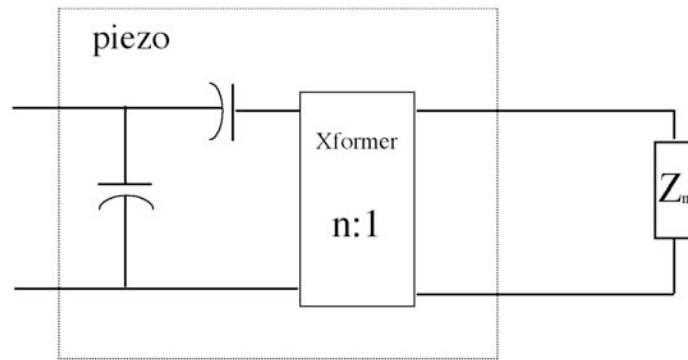

Fig. 138. Electromechanical model of piezoelectric actuator with mechanical load.

If the mechanical load can be represented as a purely resistive load that has been optimized to achieve maximum power transfer at a given frequency, ω, then it can be shown that the power per volume of the piezoelectric actuator can be approximated to

$$\frac{\text{power}}{\text{volume}} = \left(\frac{1}{2}\varepsilon_{33}^{T}E^{2}\right)k^{2}\omega \qquad (41)$$

where

$\quad$ E = electric field, typically under 10^6 V/m,

$\quad$ ε_{33} = electric permittivity, and

$\quad$ k^2 = electrical to mechanical conversion constant (0.75 for PZN).

The term in parenthesis is the electrical energy density stored in the piezoelectric material, and for modest electric fields, this term could have values of 0.02!J/cm^3 (or 2.7!J/kg for a typical density value of 8,200!kg/m^3) for the single-crystal piezoelectric material PZN. Larger energy-storage terms have been reported in the literature, but because of fatigue life limitations (remember that because of the transmission problem, billions of cycles will be required from this material), this reduced value is more reasonable. To obtain over 2,500!W/kg (which is a factor of 5 times that of an electric motor and would therefore rival that of hydraulic), the cyclic

frequency would have to be over 200!Hz. Because of the nonlinear nature of the load expected for the "inch worm" or the piezoelectric pump, a much higher frequency (maybe around 1!kHz) would be required. The steady-state efficiency of running the actuator around 1!kHz would be approximately 85%. The load-holding capacity of the piezoelectric material is excellent—no power is wasted.

The final major challenge associated with piezoelectric actuator is the associated power electronics to control it. Typical piezoelectric actuators are driven by high-voltage power sources of around 400 to 1,000!V. The size of the drive electronics frequently exceeds the overall packaging volume of the actuator by one order of magnitude if not larger. The basic problem of power transfer can be seen in Fig.137. How one can transmit charge readily to the mechanical load without wasting the energy stored in the two capacitors is the salient design problem and is still under research (Newton, 1996).

Magnetostrictive Actuators

Magnetostrictive actuators are very similar to piezoelectric actuators. Applying a magnetic field creates high forces and small displacements. The magnetic domains in the material rotate causing significant dimensional change in the material. Currently, Terfenol-D is the magnetostrictive material in common use. Large strains are typically reported, but in practice values under 0.2% are commonly observed. Stress values, while reported to be higher than piezoelectric materials, are commonly below commercial PZT values when a direct comparison is done (see www.etrema-usa.com for Terfenol-D actuators and www.physikinstrumente.com/pztactuators for the PZT actuators). All of the issues associated with piezoelectric actuators also apply to magnetostrictive actuators. The simplified electromechanical model of the magnetostrictive actuator is shown in Fig.!139, where the left port is the electrical port with current and voltages as inputs and the output port is the mechanical port with velocity and force. The load-holding capability of the material is limited by the i^2R losses associated with generating a magnetic field and is similar to electric motors with a range of 4 to 8% of the continuous power rating for maximum load. Overall efficiency numbers are hard to obtain, but due to the highly nonlinear nature of the hysteresis of the magnetic material and the i^2R losses associated with the electrical coils, efficiencies should be less than those for PZT materials.
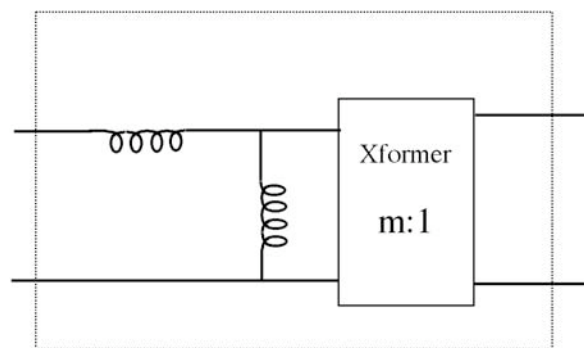

Fig. 139. Magnetostrictive electromechanical model.

The issues associated with the power electronics also apply to the magnetostrictive materials. The basic problem of power transfer can be seen in Fig.!139. How one can transmit current readily to the mechanical load without wasting the energy stored in the two inductors is the salient design problem and is still under research (Kellogg, 1996).

Shaped Memory Alloys (SMAs) and Electroactive Polymers (EAPs)

Shared Memory Alloys (SMAs) (NiTi), while having impressive compressive stresses of 200!MPa (i.e., they can pull but not push), have overall energy efficiencies under 3%. Without large amounts of cooling, overall bandwidth will be below 1!Hz. SMA are not serious contenders for the exoskeleton application unless the overall efficiencies and bandwidth issues can be seriously extended.

Electroactive Polymers (EAPs) are an exciting new material that has many anthropomorphic characteristics similar to muscle. In the majority of EAP actuators, the actuation mechanism is based on ionic species movement in a polymer network (Wax, 1999). EAP actuators can be characterized as gels; ionic polymer metal composites; perfluorinated, ion-exchanged, membrane platinum; or conductive polymers. EAP actuators hold tremendous potential especially for microactuation applications. For macroactuation applications, such as for the exoskeleton project, speed of response (i.e., bandwidth) and higher levels of electrical-to-mechanical power conversion ratios are needed. Currently, macro EAP actuators fall well below electric motor power and force (or torque) densities (Wax, 1999).

ACTUATOR RECOMMENDATION

Of the conventional actuators (Table 24), it appears that hydraulics is the best candidate for an exoskeleton application. The power-to-weight and power-to-volume ratios of hydraulics typically exceed the ratios for electromagnetic actuation by factors of 10 and 5 respectively. The closed-loop bandwidth of pneumatics is typically 5 to 6 times less than that for hydraulics, thus limiting the ability to track at 2!Hz. Based on packaging and the ability to track the human, hydraulics is the preferred conventional actuator.

However, there are issues concerning the use of hydraulics, which must be taken into account. First, the power loss at the servo valves associated with flow control is significant and has a serious impact on the overall power supply sizing. Second, noise is a serious problem associated with hydraulics that can be difficult to mitigate due to the large acoustical wavelengths.

While none of the non-conventional materials have reached the level of maturity achieved with hydraulics, both the piezoelectric and the magnetostrictive materials hold great promise and should be investigated further. In particular, a piezoelectric pump was shown to have the potential for power densities approaching those of hydraulics, as well as high steady-state efficiency, and no wasted power holding a load. The magnetostrictive actuators are similar to piezoelectric actuators, but with lower anticipated efficiencies and load holding capability similar to that of electric motors. Power electronics is an issue for both that is the subject of ongoing research.

Table 24. Comparison of conventional actuators

Item	Electromagnetic Actuators	Hydraulic Actuators	Pneumatic Actuators
Bandwidth	Transmission required. Motors sized 10 to 20% larger due to transmission efficiencies.	High performance servos in the 50 to 100 Hz range. Dependent on actuator and controller design.	5 to 6 x less than hydraulics.
Power to Weight	Approximately 1/10 hydraulics ratio.	Excellent.	Elastic type actuators are similar to hydraulics. Hard-shell type actuators are similar to electric actuators.
Power to Volume	Approximately 1/5 hydraulics ratio.	Excellent.	Elastic type actuators are similar to hydraulics. Hard-shell type actuators are similar to electric actuators.
Packaging	Transmission increases vol by 20-50%. Power electronics can exceed size of actuator.	No transmission. Power electronics are inconsequential. Sound proofing pumps difficult.	Similar to hydraulics.
Load Holding	5-10% or rated power required.	No power for linear actuators with asymetrical cylinders. 1 to 10% for symetrical cylinders and rotary actuators.	Similar to hydraulics.

REFERENCES

1. AeroVironment, Inc., *"Final Report for Exoskeletons for Human Performance Augmentation Power System Development,"* AV-50619/03, AeroVironment, Inc., Monrovia, Calif., 2003.

2. Amendola, et al., "An Ultrasafe Hydrogen Generator: Aqueous, Alkaline Borohydride Solutions and Ru Catalyst," *Journal of Power Sources* **85**, 186–189 (2000).

3. Andersen, B. W., *The Analysis and Design of Pneumatic Systems*, Krieger Publishing Co., Malabar, Florida. 1967.

4. Andriulli, J. B., et al., *Advanced Power Generation Systems for the 21st Century: Market Survey and Recommendations for a Design Philosophy,* ORNL/TM-1999/213, Oak Ridge National Laboratory, Oak Ridge, Tenn., November 1999.

5. Antonsson E. K. and R. W. Mann, "The Frequency Content of Gait," *J Biomech* **18**(1), 39–47 (1985).

6. Barter J, I. Emanuel, B. Truett, *A Statistical Evaluation of Joint Range Data*, WADC Technical Note 57-311, Wright Air Development Center, 1957.

7. Beatty, H. A., U.S. Dept of Commerce, PB-6330, 1944.

8. Boynton, A. C., and H. P. Crowell, *A Human Factors Investigation of Exoskeleton Boot Interface Sole Thickness*, U.S. Army Research Laboratory, Aberdeen Proving Ground, Md. (technical report in press).

9. Brown, H. C. and C. A. Brown, *Journal of the American Chemical Society* **84**, 1493 (1962).

10. Bunch, W. H., *Atlas of Orthotics/American Academy of Orthopaedic Surgeons*, Mosby, 1985.

11. Crowell, H. P., A. C. Boynton, and M. Mungiole, *Exoskeleton Power and Torque Requirements Based on Human Biomechanics*, ARL-TR-2764, U.S. Army Research Laboratory, Aberdeen Proving Ground, Md., November 2002.

12. Crowell, H. P., *Human Engineering Design Guidelines for a Powered, Full Body Exoskeleton*, ARL-TN-60, U.S. Army Research Laboratory, Aberdeen Proving Ground, Md., July 1995.

13. Dowling, K., *Power Sources for Small Robots*, CMU-RI-TR-97-02, Carnegie Mellon University. January 1997.

14. Chou, C. P. and Hannaford, B., Measurements and Modeling of McKibben Pneumatic Artificial Muscles. IEEE Transactions on Robotics and Automation, **12**(1), 90–102 (1996).

15. Garret, D. E. *Borates, Handbook of Deposits, Processing, Properties, and Use* Academic Press, San Diego, 1998.

16. Goldfarb, M. and W. Durfee, "Design of a Controlled-Brake Orthosis for FES-Aided Gait," *IEEE Trans. Rehab. Eng.* **4**(1), 13–24 (1996).

17. Harris, G. F., K. R. Acharya, and R. A. Bachschmidt, "Investigation of Spectral Content from Discrete Plantar Areas During Adult Gait: An Expansion of Rehabilitation Technology," *IEEE Trans Rehab. Eng.* **4**(4), 360–74 (1996).

18. Heywood, J. B., *Internal Combustion Engine Fundamentals*, McGraw-Hill, New York, 1998.

19. Hirschenhofer, J. H., D. B. Stauffer, R. R. Engleman, and M. R. Klett, *Fuel Cell Handbook*, Business/Technology Books for the U.S. Department of Energy, 1994.

20. Hollerbach, J. M., I. W. Hunter, and J. Ballantyne, "A Comparative Analysis of Actuator Technologies for Robotics," pp. 299-342 in *The Robotics Review 2*, ed. O. Khatib, J. Craig, T. Perez, The MIT Press, Cambridge, Mass., 1992.

21. Jansen, J. F. et al., *Exoskeleton for Soldier Enhancement Systems Feasibility Study*, ORNL/TM-2000/256, Oak Ridge National Laboratory, Oak Ridge, Tenn., September 2000.

21. Kaufman, C. M. and B. Sen, *Journal of the Chemical Society Dalton Transactions*, 307 (1985).

22. Kellogg, R. and A. Flatau, "Blocked Force Investigation of a Terfenol-D Transducer," *Proc. SPIE Conf. on Smart Structures and Integrated Systems*, Newport Beach, Calif., March 1999, pp. 184–195.

23. Legg, S. J., T. Ramsey, D. J. Knowles, "The Metabolic Cost of Backpack and Shoulder Load Carriage," *Ergonomics* **35**(9), 1063–1068 (1992).

24. Levy, A., J. B. Brown, and C. J. Lyons, *Ind. Eng. Chem.* **52**, 211 (1960).

25. McMahon, T. A., "Mechanics of Locomotion," *The International Journal of Robotics Research* **3**(2), 4–28 (1984).

26. Merritt, H. E., *Hydraulic Control Systems*, John Wiley and Sons, New York, 1989.

27. Miller, T. J., *Brushless Permanent Magnet and Reluctance Motor Drives*, Oxford University Press, Oxford, U.K., 1989.

28. Nasser, K. D., J. Leo, and H. H. Cudney, "Compact Piezohydraulic Actuation System," SPIE Paper Number 3991-41: Annual Symposium on Smart Structures and Materials, 2000.

29. Nawoczenski, D. A. and M. E. Epler, *Orthotics in Functional Rehabilitation of the Lower Limb*, Saunders, 1997.

30. Newton, D. V., J. A. Main, E. Garcia, and L. Massengill, "Piezoelectric Actuation Systems: Optimization of Driving Electronics," pp. 259-266 in *Proc. of SPIE's 1996 North American Symposium on Smart Structures and materials: Smart Structures and Integrated Systems*, Vol. 2717, San Diego, Calif., February 1996.

31. Park, S. E. and T. R. Shrout, "Characteristics of Relaxor-Based Piezoelectric Single Crystals for Ultrasonic Transducers," *IEEE Transactions on Ultrasonics, Ferroelectrics, and Frequency Control* **44**(5), 1140-1146, (1997).

32. Redford, J. B., *Orthotics Etcetera*, Williams & Wilkins, 1986.

33. Rose J. and J. Gamble, *Human Walking*, 2nd ed., Williams & Wilkins, 2000.

34. Sanders J. E., B. S. Goldstein, and D. F. Leotta, "Skin Response to Mechanical Stress: Adaptation Rather than Breakdown – A Review of the Literature," *J Rehab Res. Dev.* **32**(3), 214–228 (1995).

35. Sanders J.E,. J. M. Greve, S. B. Mitchell, and S. G. Zachariah, "Material Properties of Commonly-Used Interface Materials and Their Static Coefficients of Friction with Skin and Socks," *J. Rehabil. Res. Dev.* **35**(2), 161–76 (1998).

36. Schlesinger, H. I., "Final Report to Signal Corps Ground Signal Agency on Contract W3434-SC-174", PB-6331, 1944.

37. Schlesinger, H. I., et al., *Journal of the American Chemical Society* **75**, 215–219 (1953).

38. *Sodium Borohydride Digest*, Morton International, Inc., 1995.

39. Theis, T. J., J. C. Conklin, J. F. Thomas, and T. R. Armstrong, *Comparison of Prime Movers Suitable for USMC Expeditionary Power Sources*, ORNL/TM-2000/116, Oak!Ridge National Laboratory, Oak Ridge, Tenn., March 2000.

40. Thomas, S. and M. Zalbowitz, *Fuel Cells – Green Power*, LA-UR-99-3231, Los Alamos National Laboratory, Los Alamos, N.!Mex., 1999.

41. Tylee, L., "On-Line Failure Detection in Nuclear Power Plant Instrumentation," IEEE *Trans. Automat. Contr.,* **AC-28**, 406–415, March 1983.

42. Wakizoe, M., O. Velev, and S. Srinivasan, *Electrochemica Acta* **40**(3), 335–344 (1995).

43. Wax, S. G. and R. R. Sands, "Electroactive Polymer Actuators and Devices," SPIE Conference of Electroactive Polymer Actuators and Devices, Newport Beach, Calif., March 1999, pp. 2–9.

44. Winter, D. F., *Biomechanics and Motor Control of Human Movement*, Wiley, 1990.

45. Woodson, W. E., B. Tillman, and P. Tillman, *Human Factors Design Handbook*, 2nd ed, Mc-Graw Hill, 1992.

INTERNAL DISTRIBUTION

1. J. F. Birdwell
2. W. E. Dixon
3. E. C. Fox
4. R. G. Gilliland
5. D. J. Hill
6. J. F. Jansen
7. S. M. Killough
8. R. F. Lind
9. P. D. Lloyd

10. L. J. Love
11. M. W. Noakes
12. F. G. Pin
13. B. S. Richardson
14. J. C. Rowe
15. R. B. Shelton
16. ORNL Central Research Library
17. ORNL Laboratory Records – RC
18. ORNL Laboratory Records - OSTI

EXTERNAL DISTRIBUTION

(This document was cleared by DARPA and has been approved for Public Release, Distribution Unlimited.)

19. Army Research Laboratory, AMSRL-HR-SB, Attn: Angela Boynton (Bldg. 459), Aberdeen Proving Ground, MD 21005-5425

20. Army Research Laboratory, AMSRL-HR-SB, Attn: Philip Crowell (Bldg. 459), Aberdeen Proving Ground, MD 21005-5425

21. W. K. Durfee, University of Minnesota – Twin Cities, Mechanical Engineering, Room 210B, 111 Church St., SE, Minneapolis, MN 55455

22. Greg Fischer, Engineering Consultant, Strategic Analysis, Inc., 3601 Wilson Blvd., Suite!500, Arlington, VA 22201

23. John Gongola, AeroVironment, Inc., 825 S. Myrtle Ave., Monrovia, CA 91016

24. D. J. Leo, Virginia Polytechnic Institute and State University, Center for Intelligent Material Systems and Structures, Mechanical Engineering Department, Blacksburg, VA!24061-0261

25. John A. Main, DARPA-DSO, 3701 N. Fairfax Dr., Arlington, VA 22202-1714

26. George Malosh, ORNL Site Manager, U.S. Department of Energy, Oak Ridge National Laboratory, Post Office Box 2008, Oak Ridge, TN 37831-6269

27. Paul McCready, AeroVironment, Inc., 825 S. Myrtle Ave., Monrovia, CA 91016

28. Army Research Laboratory, AMSRL-CI-EE, Attn: Michael Mungiole, 2800 Powder Mill Road, Adelphi, MD 20783-1197

29. O. A. Velev, AeroVironment, Inc., 825 S. Myrtle Ave., Monrovia, CA 91016

30. T. Zambrano, AeroVironment, Inc., 825 S. Myrtle Ave., Monrovia, CA 91016